



Screening of Bacteria using Impedance Flow Cytometry

Bertelsen, Christian Vinther

Publication date:
2021

Document Version
Publisher's PDF, also known as Version of record

[Link back to DTU Orbit](#)

Citation (APA):
Bertelsen, C. V. (2021). *Screening of Bacteria using Impedance Flow Cytometry*. DTU Bioengineering.

General rights

Copyright and moral rights for the publications made accessible in the public portal are retained by the authors and/or other copyright owners and it is a condition of accessing publications that users recognise and abide by the legal requirements associated with these rights.

- Users may download and print one copy of any publication from the public portal for the purpose of private study or research.
- You may not further distribute the material or use it for any profit-making activity or commercial gain
- You may freely distribute the URL identifying the publication in the public portal

If you believe that this document breaches copyright please contact us providing details, and we will remove access to the work immediately and investigate your claim.

Screening of Bacteria using Impedance Flow Cytometry

Industrial PhD Thesis

Christian Vinther Bertelsen



Screening of Bacteria using Impedance Flow Cytometry

Industrial PhD Thesis
May, 2021

By
Christian Vinther Bertelsen
SBT Instruments A/S
Technical University of Denmark

Disclaimer of financial interests and co-ownership:
The author of this thesis, Christian Vinther Bertelsen, is a co-founder of SBT Instruments A/S and own shares in the company.

University supervisors: Professor Winnie Edith Svendsen
Senior Researcher Maria Dimaki

Industrial supervisors: Gustav Erik Skands
Casper Hyttel Clausen

Copyright: Reproduction of this publication in whole or in part must include the customary bibliographic citation, including author attribution, report title, etc.

Cover photo: SBT Instruments, 2020
Published by: DTU, Department of Bioengineering and Biotechnology, Søtofts Plads 221, 2800 Kgs. Lyngby Denmark
www.bio.dtu.dk

ISSN:
ISBN:

Abstract

In this industrial PhD project, an impedance flow cytometer developed by the Danish company SBT Instruments A/S is used to study the enumeration and characterization of bacterial cells. The device can measure the total concentration of bacteria in a liquid sample in 5 minutes. This is opposed to the growth-based methods used today, which usually take 1-3 days to provide a result. The slow response time is a problem in multiple industries that rely on fast measurements of the microbial burden for quality and hygiene control, such as in food production, health care environments and at drinking water plants.

The technology employed for bacteria characterization is called Impedance Flow Cytometry (IFC). In IFC a liquid containing bacterial cells is continuously injected across a set of detection electrodes placed on the top and bottom of a microfluidic channel. The changes in current during the passing of a bacterium are measured simultaneously at two frequencies probing different parts of the bacteria structure. The technology has been implemented in a tabletop device developed by SBT Instruments called BactoBox and is used to experimentally investigate the impedance response of bacterial cells and other particles.

BactoBox has been used to investigate the impedance response of six different bacteria species to determine if specific cell characteristics can be extrapolated directly from the impedance measurements. Differences between the species were observed, but it was not possible to correlate the differences to the bacteria shape or the gram-type, which emphasize the complexity and variation of bacterial morphology.

BactoBox has also been used to probe the viability state of *E. coli* bacteria after inactivation with three common disinfection and sterilization methods, ethanol, heat and autoclaving. The results show that the viability of *E. coli* bacteria can be determined using IFC, but that the sensitivity and selectivity of the classification depends considerably on the inactivation method. For example, prolonged exposure during heat inactivation improved the viability classification with IFC significantly.

Finally, BactoBox was used to evaluate the antibiotic susceptibility of two known colistin-sensitive strains of *E. coli* and *Pseudomonas aeruginosa* as well as a known colistin-resistant *Pseudomonas aeruginosa* strain. The impedance response of the cells changed as they were exposed to increasing concentrations of colistin and the change in impedance happened at higher antibiotic concentrations for the resistant *Pseudomonas aeruginosa* strain.

The thesis presents this experimental work together with the theoretical models needed for dielectric modelling of bacterial cells in an impedance flow cytometer system. In the thesis a walk-through of the functional parts of the flow cytometer (microfluidic chip, electronics, sample handling and data analysis) is also presented and their function and interrelation are discussed.

The work presented in this thesis will appeal to anyone interested in novel methods for bacteria detection and enumeration focused on electrical characterization of the cells, and to anyone excited by the technology development happening on the border between academia and industry.

Dansk resumé

Et impedans flow cytometer udviklet af det danske firma SBT Instruments A/S er i dette erhvervs-PhD-projekt blevet brugt til at kvantificere og karakterisere bakterier. Cytometret kan måle den totale koncentration af bakterier i en væskeprøve og resultatet foreligger efter ca. 5 minutter. Dette er i skarp kontrast til de eksisterende dyrkningsbaserede metoder, der anvendes i dag, hvor det almindeligvis tager 1-3 dage før der foreligger et resultat. Den langsomme responstid er en stor udfordring i mange brancher, hvor hurtige målinger af den mikrobielle belastning har væsentlig betydning for kontrollen af kvalitet og hygiejne, fx i fødevarerproduktion, sundhedsvæsenet og på drikkevandsanlæg.

Den teknologi, der anvendes til bakteriekarakterisering, kaldes impedans flow cytometri (IFC). IFC bygger på et princip, hvor en væskeprøve med bakterier, løbende pumpes ind mellem et sæt måleelektroder placeret på toppen og bunden af en mikrofluid kanal. Den elektriske strøm mellem elektroderne, målt ved to eller flere frekvenser, ændres, når en bakterie passerer mellem dem på baggrund af cellens elektriske egenskaber. Denne ændring i strøm kan derfor bruges til indirekte at karakterisere bakteriens struktur og opbygning. Denne teknologi er implementeret i apparatet Bactobox udviklet af SBT Instruments, som i dette projekt bruges til at undersøge forskellige bakterier og andre partikler.

I projektet indgår studier hvor BactoBox er blevet brugt til at undersøge impedansresponsen fra seks forskellige bakteriestammer for at vurdere om den målte impedans kan relateres til specifikke bakteriekarakteristika. Der blev observeret forskelle mellem de forskellige stammer, men det var ikke muligt at relatere denne forskel til stammernes form eller Gram-type. Dette illustrerer den store kompleksitet og variation, der findes indenfor de forskellige bakteriestammer.

BactoBox blev også brugt til at undersøge *E. coli* bakteriers levedygtighed efter inaktivering med tre desinfektions- og steriliseringsmetoder, ethanol, varme og autoklaving. Resultaterne af forsøgene viste, at levedygtigheden af *E. coli* -bakterier kan bestemmes ved hjælp af IFC, men at klassificeringens følsomhed mellem levende og døde bakterier afhænger af inaktiveringsmetoden. For eksempel så vi at længden af eksponeringstiden ved varmeinaktivering af *E. coli* medførte en markant forbedring af klassificeringen mellem døde og levende bakterier.

Det blev også undersøgt om BactoBox kan bruges til at evaluere følsomheden overfor antibiotika. Som model blev benyttet antibiotikummet colistin, som blev undersøgt overfor to kendte colistin-følsomme stammer af *E. coli* og *Pseudomonas aeruginosa* samt en kendt colistin-resistent *Pseudomonas aeruginosa* stamme. Resultatet af undersøgelserne viste, at impedansresponsen fra bakterierne ændrer sig, efter de er blevet udsat for stigende koncentrationer af colistin, samtidig med at ændringen i impedans afhænger af bakteriernes resistens overfor colistin.

I denne afhandling præsenteres det eksperimentelle arbejde sammen med de teoretiske modeller, der er nødvendige at kende til for at forstå den elektriske modellering af bakterier i et IFC-system. Afhandlingen indeholder også et kapitel med en gennemgang af de funktionelle dele af flowcytometret (mikrofluidchip, elektronik, prøvehåndtering og data-analyse), hvor deres funktion og indbyrdes relationer diskuteres.

Dette arbejde vil appellere til alle der er interesserede i nye metoder til kvantificering og

karakterisering af bakterier med fokus på elektriske egenskaber, og til alle der er begejstrede for udviklingen af nye teknologier og produkter på grænsen mellem den akademiske og industrielle verden.

Preface and acknowledgements

This thesis is submitted as a partial fulfillment of the requirements for obtaining the PhD degree from the Technical University of Denmark (DTU).

This industrial PhD project has been carried out as a collaboration between the Danish company SBT Instruments A/S and the Technical University of Denmark (DTU). It has been funded by Innovation Fund Denmark under grant no. 7038-00185B. The project has been supervised by Winnie Edith Svendsen and Maria Dimaki from DTU, by Casper Hyttel Clausen formerly SBT Instruments A/S now with Novo Nordisk, and by Gustav Erik Skands CEO from SBT Instruments A/S.

The project started in February 2018 at DTU Nanotech (Department for Micro- and Nanotechnology) as a part of the research group NaBIS (NanoBio Integrated Systems) led by Professor Winnie Edith Svendsen. Due to restructuring at the university it was moved, together with the rest of the research group, to DTU Bioengineering (Department of Biotechnology and Biomedicine) in the first quarter of 2019. The work has been carried out in the offices and laboratory facilities at the university campus in Kgs. Lyngby and at the company offices and laboratories located in Herlev.

I want to thank everyone involved in the project for all their help and support. Most of all I want to thank my supervisors at the university, Winnie and Maria, and at the company, Gustav and Casper. The help and support from each of you in various phases of the project has been invaluable.

Also a big thank you to all of my co-workers. The joy of doing an industrial PhD project is that I have had the opportunity to have two sets of wonderful colleagues. Thank you to everyone, both past and present, in the NaBIS group at DTU and at SBT.

A special thank you to Romén Rodriguez for hosting my stay at the University of Barcelona and to everyone else who helped make my stay there as great as it was.

Finally, thank you to my friends and family. Your support means everything to me.



Christian Vinther Bertelsen
Kgs. Lyngby, 15/05/21

Contents

List of Figures	x
List of Tables	xv
List of Abbreviations	xvii
1 Introduction	1
1.1 What is impedance flow cytometry?	1
1.2 SBT Instruments	3
1.3 Impedance flow cytometry in literature	3
1.4 What is BactoBox?	16
1.5 Objective and outline	17
Part I	19
2 Theory and Modelling	21
2.1 Electrical impedance	21
2.2 Bacteria	22
2.3 Dielectric modelling of biological material	26
2.4 Chapter summary	36
3 The impedance flow cytometer	37
3.1 Flow cell	39
3.2 Sample and fluidics	54
3.3 Electronics	55
3.4 Software and signal analysis	61
3.5 Chapter summary	66
4 Data analysis and visualisation	69
4.1 Plotting the impedance results	69
4.2 Comparing measurements	73
4.3 Chapter summary	79
Part II	81
5 Bacteria characterisation and counting	83
5.1 Manuscript	84
5.2 Influence of effective conductivity relative to the medium	96
5.3 Growth tracking of <i>E. coli</i>	99
5.4 Different bacteria species	99
5.5 Chapter summary	105
CONTENTS	ix

6	Liposomes	107
6.1	Introduction	107
6.2	Manuscript	109
6.3	Chapter summary	113
7	Viability Classification	115
7.1	Introduction	115
7.2	Manuscript - paper 1	117
7.3	Manuscript - paper 2	133
7.4	Additional experiments with <i>Staphylococcus</i>	141
7.5	Using spheres or ellipsoids for modelling	141
7.6	Chapter summary	143
8	Antibiotic susceptibility testing using IFC	145
8.1	Introduction and motivation	145
8.2	Theoretical modelling of surface charge	146
8.3	Experimental methods	151
8.4	Experimental results	154
8.5	Chapter summary	162
9	Conclusion and outlook	163
9.1	Future outlook	165
A	Appendix	179
A.1	Variation between chips	179
B	Appendix	181
B.1	Six bacteria species	181
B.2	ROC comparison of gram-types - Moduli	190
C	Appendix	191
C.1	Drop plate images	191

List of Figures

1.1	Schematic of the basic principle of IFC	2
1.2	Analysis of exponential phase, stationary phase and CCCP treated bacteria cells using FCM (left) and IFC (right)	5
1.3	Schematic of a resonance enhanced flow cytometer	6
1.4	<i>E. coli</i> scatter plots	6
1.5	Fast antimicrobial susceptibility testing using IFC	7
1.6	Photograph of an impedance flow cytometry chip	8
1.7	Schematics of 2D acoustophoretic focusing scheme	9
1.8	Asymmetric measuring scheme	11
1.9	Alternative electrode configuration	12
1.10	Chip design with liquid electrodes	13
1.11	Microdevice for single cell shape-based discrimination	14
1.12	Typical "raw" data from an IFC system	14
1.13	Simulated voltage-time spectra for three horizontal planes	15
1.14	Illustration of type 1, type 2 and type 3 coincidence	16
1.15	Image of the BactoBox	17
2.1	Basic envelope structure of gram-negative and gram-positive bacteria	23
2.2	The route from alive to dead	26
2.3	Sketch of the detection channel with two electrode sets and a single sell sphere between one of them	27
2.4	Sketch of single shelled and multi shelled spherical particles for modelling	29
2.5	ECM and impedance response of two front facing electrodes	30
2.6	Simplest ECM and impedance response of a cell suspended in medium between two electrodes	33
2.7	Impedance response as a function of cytoplasm resistance and membrane capacitance	34
2.8	Impedance response as a function of membrane resistance	35
3.1	Flow cytometer overview - all	37
3.2	Bactobox v1 prototype image	38
3.3	Bactobox v2 prototype image	39
3.4	Illustration of front-facing and co-planar electrode designs	40
3.5	Top view of flow cell	41
3.6	Chip design Q and F	42
3.7	Influence of the open boundary of chip design Q	43
3.8	Flow regions	44
3.9	Exploded view of the flow cell substrates	47
3.10	COMSOL simulation showing the effects of misalignment	49
3.11	Calculated CM-factor for a one-shelled sphere and homogeneous sphere	50
3.12	COMSOL simulation of the effect of DEP forces on particle positions	51

3.13	COMSOL simulation of transition of particles with different cross sectional positions	52
3.14	COMSOL simulation of transition of particles with different cross sectional positions	53
3.15	Flow cytometer overview - sample and fluidics	54
3.16	Flow diagram of the electronics functionality	56
3.17	Measured potential applied to the flow cell after pre-amplification	57
3.18	Block diagram of lock-in amplifier	58
3.19	Signal with and without FIR-filter applied	60
3.20	Frequency sweep of chip with BB and ZI scope	60
3.21	Illustration of the choosing and paring of peaks in the data stream	62
3.22	Illustration of the "gap" in argument due to noise	63
3.23	Compensation of concentration	65
3.24	Distributions used for calculating flow compensation parameters	66
4.1	Scatter plots visualizing impedance data for 2 μm polystyrene beads and <i>E. coli</i>	70
4.2	Histograms showing the cubed modulus and argument of polystyrene beads in 3 sizes	72
4.3	Comparison between scatter plot, heat map and kernel density map	72
4.4	Comparison between 3 kernel density plots with different bandwidths	73
4.5	Example of ROC curves	74
4.6	ROC curves and AUC values for various data transformations for measurements of polystyrene beads and <i>E. coli</i>	75
4.7	Boxplots showing comparisons between polystyrene beads and <i>E. coli</i> compared by their HF argument and opacity	76
4.8	Scatterplots with contours from <i>E. coli</i> measurements from 3 flow cells	78
4.9	Contour comparison of 18 measurements on <i>E. coli</i> performed with 3 different flow cells	79
5.1	Phasor diagram illustrating the shift in differential argument	96
5.2	Sketch showing the 3 primary populations events will take in an differential argument scatterplot	97
5.3	Differential argument measured on polystyrene beads, <i>E. coli</i> and silver coated beads illustrating the 3 dominating positions in the argument plot	98
5.4	Growth tracking of <i>E. coli</i>	99
5.5	Kernel density plot of the low (366 kHz) and high (6.9 MHz) frequency differential argument from measurements of 6 species after 21 hours of growth	101
5.6	Kernel density plot of the low (366 kHz) and high (6.9 MHz) frequency differential argument from measurements of 6 species after 7 days of growth	103
6.1	Illustration of a liposome	107
7.1	Differential argument measured on <i>Staphylococcus</i> inactivated with ethanol	141
7.2	Spherical and rod-shaped bacteria models	142
7.3	Comparison of the shift in differential argument for spherical and rod-shaped models	143

8.1	Antimicrobial mechanism of colistin	147
8.2	Surface charge repels colistin molecules	147
8.3	ECMs used to evaluate changes in impedance due to colistin exposure	148
8.4	Surface layer capacitance and Debye length	150
8.5	Calculated impedance response as a function of diffuse surface layer capacitance	151
8.6	Schematic of the treatment of <i>E. coli</i> with colistin in various concentrations	153
8.7	Scatter plots showing the differential argument (366 kHz on the x-axis and 6.9 MHz on the y-axis) for <i>E. coli</i> samples with increasing concentrations of colistin	155
8.8	Boxplots comparing the shift in low and high frequency argument at increasing concentrations of colistin	156
8.9	Scatterplots showing the shift in populations of colistin susceptible <i>P. aeruginosa</i> (PAO1) at increasing colistin concentrations	157
8.10	Boxplots comparing the shift in low and high frequency argument of colistin susceptible <i>P. aeruginosa</i> (PAO1) at increasing concentrations of colistin	158
8.11	Scatterplots showing the shift in populations of colistin resistant <i>P. aeruginosa</i> (Q5) at increasing colistin concentrations	159
8.12	Boxplots comparing the shift in low and high frequency argument of colistin resistant <i>P. aeruginosa</i> (Q5) at increasing concentrations of colistin	159
8.13	Boxplots comparing the measurements of colistin susceptible (PAO1) and resistant (Q5) <i>P. aeruginosa</i> with no exposure to colistin	160
8.14	Contour comparison of 6 measurements on Q5 and 9 measurements on PAO1.	161
A.1	Argument variation between 3 chips	179
B.1	Kernel density plot of 6 species	181
B.2	Kernel density plot of 6 species	182
B.3	Kernel density plot of 6 species	183
B.4	Kernel density plot of 6 species	184
B.5	Kernel density plot of 6 species	185
B.6	Kernel density plot of 6 species	186
B.7	Kernel density plot of 6 species	187
B.8	Kernel density plot of 6 species	188
B.9	Kernel density plot of 6 species	189
B.10	ROC curves for gram-type classification based on modulus	190
C.1	Drop plating PAO1	191
C.2	Drop plating Q5	191

List of Tables

2.1	Debye lengths	32
3.1	Chip dimensions	43
3.2	Flow regimes	44
3.3	Calculated Reynolds numbers for the detection channel and bypass channel	45
3.4	Hydraulic resistances of the bypass and detection channel	47
3.5	Flow compensation values	65
5.1	Overview of bacteria species	100
5.2	AUC values for comparison between species	105
8.1	Parameters used to calculate the differential impedance response	151

List of Abbreviations

AC	Alternating Current
ADC	Analog-to-digital converter
AMR	Antimicrobial resistance
AST	Antibiotic Susceptibility Testing
AUC	Area under curve
CFU	Colony Forming Unit
DAC	Digital-to-analog converter
DEP	Dielectrophoresis
DOPC	Dioleoylphosphatidylcholine
DPPC	Dipalmitoylphosphatidylcholine
DSL	Diffuse surface layer
ECM	Equivalent Circuit Model
EDL	Electrical Double Layer
FEM	Finite Element Method
FN	False negative
FP	False positive
FPGA	Field-programmable gate array
FPR	False positive rate
HF	High frequency
HFIM	High frequency, imaginary part
HFRE	Low frequency, imaginary part
HMDS	Hexamethyldisilazane
IFC	Impedance Flow Cytometry
IHP	Inner Helmholtz Layer
KDE	Kernel density estimate
LFIM	High frequency, real part
LFRE	Low frequency, real part
LPS	Lipopolysaccharid
MBC	Minimum Bactericidal Concentration
MBD	Micro Broth Dilution
MIC	Minimum Inhibitory Concentration
MMT	Maxwell Mixture Theory

OHP	Outer Helmholtz Layer
PBS	Phosphate-buffered saline
PCB	Printed Circuit Board
PDMS	Polydimethylsiloxane
ROC	Receiver operating characteristic
SNR	Signal to noise
TIA	Transimpedance amplifier
TN	True negative
TP	True positive
TPR	True positive rate
TSA	Tryptic soy agar
TSB	Tryptic soy broth
VBNC	Viable but non-culturable

1 Introduction

Quantification of microbes is extremely important in both industrial and clinical environments for both diagnosis and quality control. Bacterial infections are still one of the most common causes of death and disease across the globe. Especially in industrial settings, microbial quantification has been overlooked and ignored for many years, due to the lack of fast and effective quantification methods. Recently, the role of microbial quantification in providing a safe and stable food and water supply has grown, and today, systematic monitoring of the microbial burden is an irreplaceable part of any quality control system. Additionally, fast and accurate bacteria quantification is not only important in the food and water industry, but also plays a crucial role in pharmaceutical production and R&D, in fermentation processes, and in hygiene control in the health care sector.

Current methods for microbial quantification rely on costly and time-consuming techniques such as growth-based plate counts, microscopy analysis or biochemical assays. Particularly, plate counts on appropriate nutritional media where single bacteria grow into small colonies that can be counted by eye, has long been considered the golden standard of microbial quantification. The main disadvantage of this method is that it requires several days before the single bacteria have grown into colonies that can be counted. This for example means that the quality control manager at the food processing plant or the hygiene responsible at the hospital cannot react immediately to a bacterial contamination and is instead forced to react after the fact.

Therefore, a pressing need exists for a new, fast and easy to use technique for microbial quantification, that can replace the old and slow plate count methods. In this thesis I will describe my work with an instrument for fast characterization and quantification of bacteria based on a technology called impedance flow cytometry (IFC).

1.1 What is impedance flow cytometry?

Impedance flow cytometry (IFC) is an emerging technology for label-free fast enumeration and characterization of single cells and particles in a liquid sample.

In IFC a sample of particles or cells suspended in a liquid electrolyte is continuously injected through a microfluidic channel where a set of micro-electrodes detect changes in impedance during a transition of a cell or particle (as illustrated in figure 1.1). In newer impedance spectroscopy devices two sets of micro-electrodes are used for detection, which allows for measuring the differential current between two identical detection volumes. When no particle is present between the electrodes or when it is exactly in between the two sets, the differential current will be zero. As the particle flows between the electrodes it sequentially changes the impedance between one set of electrodes (ie. A-B in figure 1.1) leading to a non-zero differential current, and then the next set (ie. C-D). The transition of a particle therefore leads to a characteristic double gaussian event in the differential current as seen in figure 1.1. While two sets of micro-electrodes are usually used for detection, systems with a single set or with more than two sets of electrodes also exist. The height of the peaks of the double gaussian event is directly related to the change

in impedance and will depend on the dielectric properties of the passing particle. For bacteria and other cells, this means that properties that affect the impedance such as size, shape, membrane composition and cytoplasmic conductivity can be evaluated individually for each cell that passes between the detection electrodes.

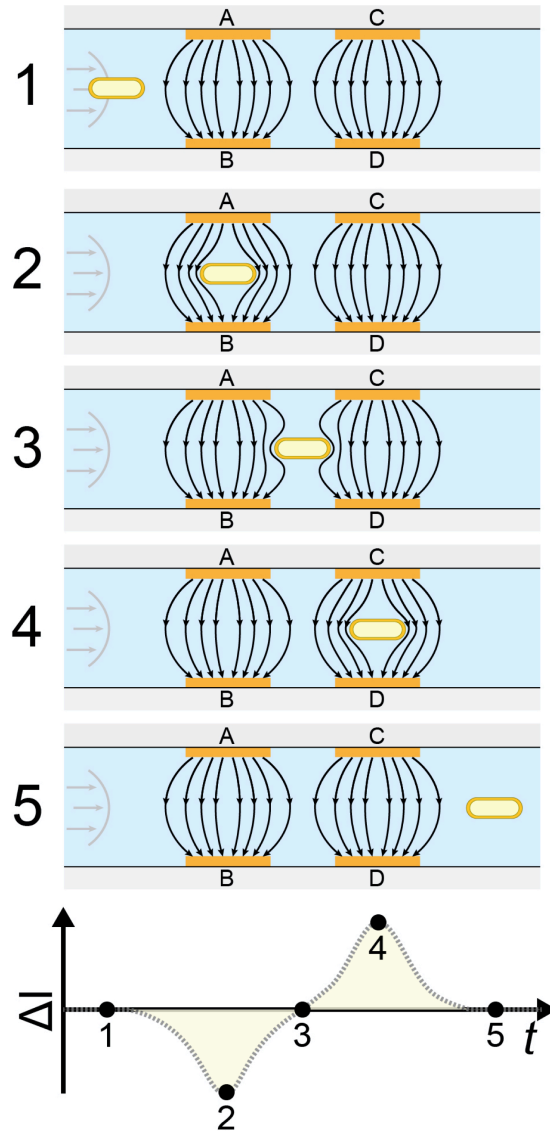


Figure 1.1: Schematic of 5 positions of a transitioning bacteria (1, 2, 3, 4, 5) and the corresponding differential current ($\Delta I = I_{AB} - I_{CD}$). When a bacterium enters the detection area (position 1), the current of the two electrode sets is identical ($I_{AB} = I_{CD}$), resulting in a differential current of zero. When the bacterium moves between electrode A and B (position 2) the electric field is perturbed resulting in a non-zero differential current. When the bacterium is exactly between the electrode sets (position 3) the differential current is again zero. As the bacterium transitions between electrode C and D and further out of the detection area, the electric field is again perturbed giving rise to a differential current (position 4). At position 5 the differential current is again zero as the bacterium exits the detection area. Reproduced from [1].

Usually a multi-frequency AC voltage (consisting of two or more superimposed sinusoidal signals) is applied to the input electrode(s) in the channel. The impedance change induced by a biological cell is different from that of other more homogeneous particles (such as small grains of glass or plastic) due to the cell's unique structure consisting of an electrically isolating membrane and an electrically conducting core. This means that the impedance response of biological cells is highly frequency dependent and that different frequencies can be used to probe different cell properties.

In research applications, IFC setups are custom built using different combinations of amplifiers, signal generators, syringe pumps, tubing and microscopes, very often with the detection channel and electrodes implemented in a custom designed microfluidic chip. In this thesis, I will present my work performed with one of the world's first impedance flow cytometer developed with the intention of commercial sales by the Danish start-up company SBT Instruments A/S.

1.2 SBT Instruments

SBT Instruments is a Danish company located in the greater Copenhagen area. The company was founded in 2014 by myself and two of my fellow graduates from the Technical University of Denmark, Gustav Erik Skands and Fredrik Peter Aalund. Gustav and I had just obtained our master degrees in physics and nanotechnology from the Technical University of Denmark. During our final project, we had built and tested the first iteration of our microfluidic chip meant for IFC detection of bacteria and shown that it could be used to differentiate between bacteria and inorganic particles. Shortly after, Frederik, who has a background in computer science, joined the team and SBT Instruments was founded. In the beginning, we focused on detecting bacteria contaminations in drinking water, but later pivoted to a more general use case for the technology. This resulted in BactoBox, a fully integrated, table-top, impedance flow cytometer capable of measuring the bacteria concentration in liquid samples. Today the company has 14 employees and is actively selling BactoBox to all customers interested in improving their bacteria counting abilities.

1.3 Impedance flow cytometry in literature

Dielectric measurements on cells and other biological material can be traced back to the work of Schwan [2]. Over the last 20 years miniaturized multi frequency impedance flow cytometry has emerged as a popular and well studied technology for non-invasive measurements on single cells, with the first impedance flow cytometers described by Ayliffe [3], Fuller [4] and Gawad [5] around the year 2000. Multiple thorough reviews have been published describing electrical measurements of cells using IFC, e.g. by Xu et al. [6], Chen et al. [7], Petchakup et al. [8], and Sun et al. [9]. I encourage anyone interested in the field to read these reviews.

Here I will focus on systems measuring on bacteria and on different technological considerations and solutions that have been implemented in IFC systems in recent years.

1.3.1 Bacteria measurements with IFC

While IFC has been used to study many different types of cells, the number of publications dealing with the detection and characterization of bacteria cells is quite low. If looking

more generally for work characterizing bacterial cells using dielectric methods, more publications can be found. However, in this subsection I will focus on the publications that I have found that specifically use IFC for single cell detection of bacteria.

Bernabini et al. [10] uses an IFC system that employs an insulating fluid to hydrodynamically focus the stream of particles as they pass by a set of front facing detection electrodes. They use this device for detection and discrimination of 1 μm and 2 μm diameter polystyrene beads and *Escherichia coli* bacteria. Accurate detection and identification of the particles were confirmed by simultaneously measuring the fluorescence emission. They found that they could detect and discriminate between *E. coli* and 2 μm polystyrene beads based on the impedance magnitude at 503 kHz.

Berardino et al. [11] uses an impedance flow cytometer to obtain data from viability studies of yeast (*Saccharomyces cerevisiae carlsbergensis*) and bacteria (*Bacillus megaterium*). The cells were inactivated with heat and anti-fungal or antibiotic substances, respectively. The electrical measurements were performed at 0.5 MHz and 10 MHz. The bacterial viability studies show a shift in the measured phase signal from the heat treated bacteria compared to the untreated. The shift only occurs at 10 MHz, not at 0.5 MHz. Likewise, treatment with both Hygromycin or Kanamycin shows shifts in the measured phase angle. Based on their findings they conclude that the phase angle of the measured signal is important for discrimination of dead and viable cells, and that the best resolution for discrimination was found at 10 MHz. At frequencies below 2 MHz they could no longer discriminate between viable and dead cells. They go on to discuss that the "*advantages of label-free viability analyses of micro-organisms are obvious*" because current fluorescent based flow cytometer solutions have significant sample preparation.

The same group of researchers have written more comprehensively about the viability of *Bacillus megaterium* now with the inclusion of F. David as first author [12]. They compare the results from IFC with fluorescence-based flow cytometry (FCM) and find that the two methods give comparable results, quantitatively and qualitatively. The paper investigates the effect of membrane potential (MP) and viability state on the impedance measurements. The cells are investigated in four different states: exponential growth phase, stationary growth phase, CCCP-treated cells from the exponential phase and 80 °C heat inactivated cells. CCCP (ionophore carbonyl cyanidem-chlorophenylhy-drazone) is a chemical inhibitor that depolarizes the cells.

Comparisons between stationary cells, exponential phase cells and CCCP-treated cells displayed exponential phase cells as highly polarized, while stationary phase cells and CCCP-treated cells only showed low polarization levels (see figure 1.2(a)) at low frequencies (0.5 MHz). Comparisons between stationary cells, exponential phase cells and heat treated cells can be seen in figure 1.2(b) and shows a shift in impedance angle measurement for heat-treated cells compared to viable cells. Investigations of 5 additional frequencies showed that 0.5 MHz and 10 MHz are the best for MP discrimination and viability discrimination, respectively.

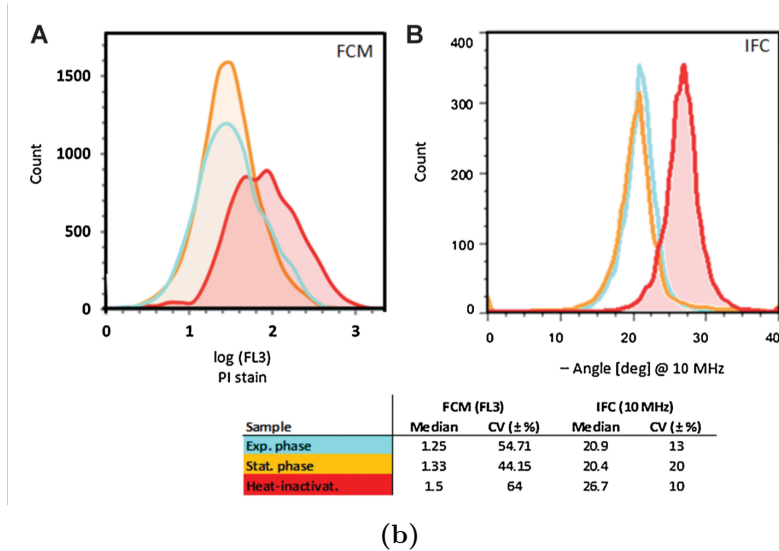
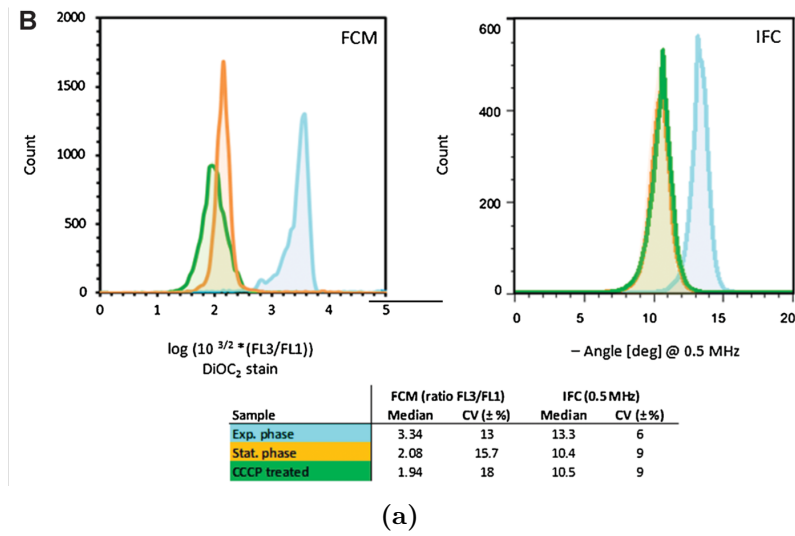


Figure 1.2: (a) Analysis of exponential phase, stationary phase and CCCP treated bacteria cells using FCM (left) and IFC (right). (b) Viability analysis of *B. megaterium* cells by FCM (left) and IFC (right). Adapted from [12] in accordance with the sharing guidelines of Wiley Online Library.

Haandbaek et al. [13] describes an alternative approach to the traditional electronics setup used in IFC, by using an electrical resonator to enable measurements at high frequencies with high sensitivity. They still make use of a lock-in amplifier to detect the signal, but incorporates a resonant circuit in series with the impedance as seen in figure 1.3. At the resonance frequency the impedance of the circuit becomes low and thus increases the sensitivity. When a particle passes the detection electrodes the resonance frequency of the system changes.

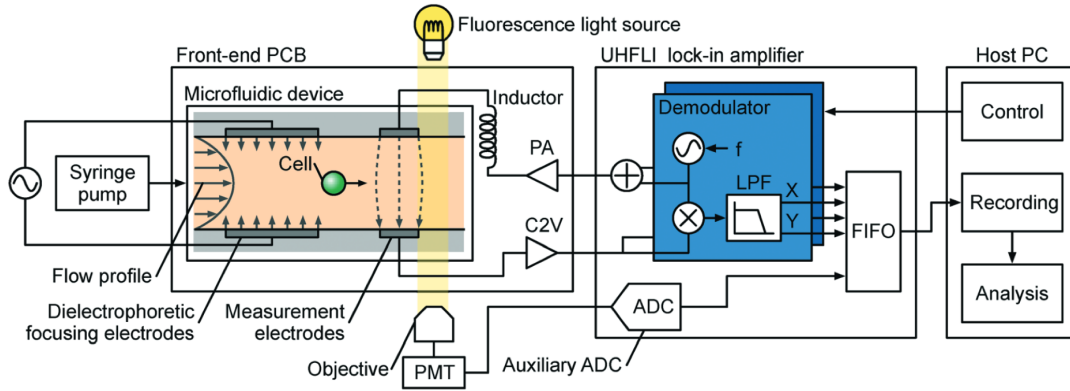


Figure 1.3: Schematic of the complete microfluidic cytometer from [13]. The lock-in amplifier drives a resonance circuit, formed by an inductor and the impedance between the measurement electrodes. Reproduced from [13] with permission from the Royal Society of Chemistry.

The authors write that the improvement in sensitivity arises due to the impedance of the inductor being perfectly aligned with the impedance of the microfluidic channel similar to "a balanced scale, where a small change in weight can make the scale tip to one side or the other, a small change in impedance can give rise to a large change in phase of the current through the resonator". However the high sensitivity and high frequency also makes the system very sensitive to parasitic coupling within the system itself. The authors demonstrate that the device is capable of detection of single *E. coli* and *B. subtilis* cells and that it can differentiate these cells from polystyrene beads as seen in figure 1.4.

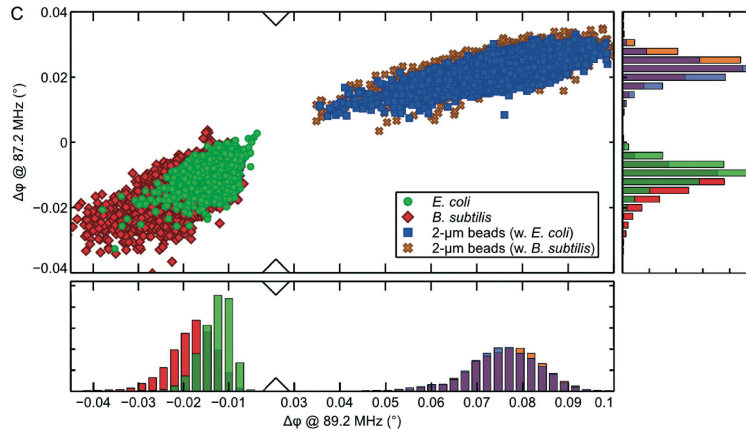


Figure 1.4: Scatter plot of the phase changes measured at 89.2 MHz and 87.2 MHz for two experiments: *E. coli* with 2 μ m beads (green and blue) and *B. subtilis* with 2 μ m beads (red and brown) from [13]. Reproduced from [13] with permission from the Royal Society of Chemistry.

Guler and Bilican [14] has published a paper where they describe a simple coplanar electrode integrated to a simple rectangular PDMS microchannel for the detection of *E. coli*. They enhance the conductivity of drinking water to obtain an optimal conductivity of 2.5

S/m. They perform COMSOL simulations to optimize the conditions of their system and find that the simulation and experiments were well matched when the frequencies were high enough to ignore the electrical double layer effect on the electrode surface. They are able to experimentally differentiate between *E. coli* and 2 μm polystyrene beads.

Last but not least, a recent publication by Spencer et al. [15] presents a label-free method for antibiotic susceptibility testing (AST) based on IFC (see figure 1.5). The method reduces the time consuming growth step in traditional AST to only 30 min. IFC measurements are performed on a bacteria culture before and after exposure to antibiotics and changes in the impedance response reveals if the antibiotic is effective or not. The study is comprehensive, looking at eleven different strains of bacteria and exposure to multiple different drugs. They find that the results obtained using IFC are consistent with those obtained by classical broth microdilution assays for a range of antibiotics and bacterial species.

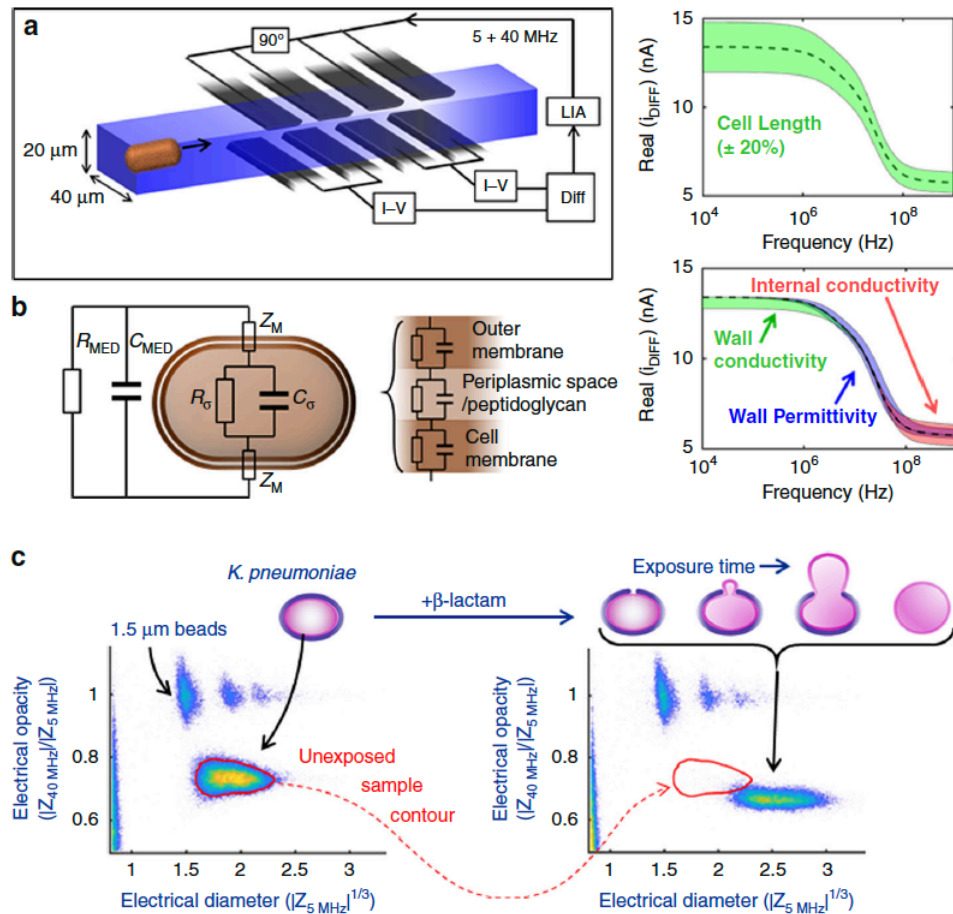


Figure 1.5: (a) Chip schematic, (b) equivalent circuit for gram negative bacteria, (c) impedance scatter plot of *K. pneumoniae* together with 1.5 μm diameter polystyrene beads. After exposure to β -lactam antibiotic, the cell wall breaks down and the bacteria swell causing a shift in the population location. Partially reproduced from [15].

1.3.2 Focusing

In IFC systems, variations and non uniformity in the electric field between the detection electrodes can cause significant variation in the measured impedance response. The size of the variation depends on the electrode design and can cause a serious loss of sensitivity in the IFC system, especially if the electrode layout is co-planar. To address this issue multiple researchers have explored different ways of focusing the cells and particles before measurement.

DEP focusing

Some of the very first microfluidic flow cytometers used dielectrophoretic forces (DEP forces) to focus the cells in the channel [16]. Cottet et al. [17] has described and developed a computational tool for calculating DEP forces of various cells and particles. In Shaker et al. [18] they use an initial region with DEP focusing to focus and re-orient cells and particle in order to determine their shape (see figure 1.11).

Hydrodynamic focusing

Another common way to focus particles to the center of the channel is to use hydrodynamic focusing (as used by Bernabini et al. [10] for bacteria detection). Hydrodynamic focusing uses a focusing liquid (usually non conductive to decrease detection volume) injected on both sides of the main flow. Due to the laminar flow in the microfluidic channel the sample liquid is compressed in the center of the channel.

Winkler et al [19] performs an in-depth system integration study of in-plane hydrodynamic focusing in a microfluidic impedance flow cytometer (see chip design in figure 1.6). They find that ionic diffusion between focusing liquid and the sample is critical as a limiting factor of the system.

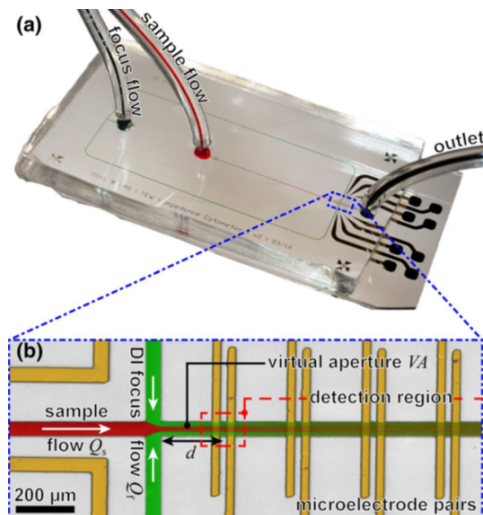


Figure 1.6: (a) Photograph of the impedance flow cytometry chip. The microfluidic channels are filled with dye to enhance visualization. (b) Micrograph of the hydrodynamic focusing region and the detection region. Both from [19].

Acoustic focusing

Grenvall et al. [20] addresses the need for particle positioning by presenting a microfluidic system which positions cells and particles using acoustic forces. The system performs

electrical measurements on the cells after the focusing has occurred. Acoustophoresis uses standing acoustic waves to manipulate the position of cells in a micro-channel. The technique is gentle to the cells and has been used (prior to the authors work) to successfully achieve sample particle focusing, separation, sorting, fractionation, trapping, media switching and in-field cell culturing. Figure 1.7 shows the general principle of acoustic focusing together with some simulation results. By focusing the particles in the center of the channel the variation in height and shape of the pulse curves (events) is greatly reduced.

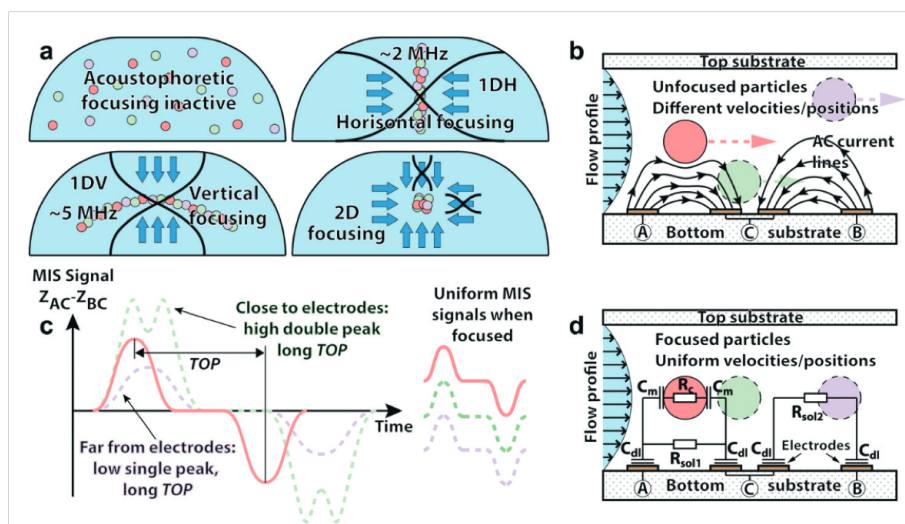


Figure 1.7: Schematics of 2D acoustophoretic focusing scheme from [20]. (a) shows the 1D vertical, 1D horizontal and 2D focusing directions. (b) A schematic illustration of the cause of the variation in measured impedance in a co-planar electrodes layout due to variation in particle position. (c) Illustration of the variation in event signal from positional variation. (d) Equivalent circuit model of the IFC system. Reproduced from [20] with permission from the Royal Society of Chemistry.

7 μm polystyrene beads suspended in a saline solution (0.9 % NaCl in Milli-Q water) were experimentally investigated. Particle position was determined using confocal microscopy. In experiments with 1-dimensional focusing in the horizontal (side wall-side wall) direction the beads were focused in a thin ribbon from top to bottom at the center of the channel, while experiments with 1-dimensional vertical focusing (top-bottom) showed a curved horizontal sheet across the channel. Both these results were in agreement with COMSOL simulations. In experiments with 2-dimensional acoustophoretic focusing the confocal imaging showed articles localized to the superimposed nodal point of the horizontal and vertical focusing sheets. Additionally, experiments with size discrimination of particles (3 μm , 5 μm and 7 μm) were performed. Without acoustic focusing the size populations of the three particle sizes were partly overlapping. In contrast, with 2D acoustic focusing the size histogram displayed fully separated size distributions.

Inertial focusing

The phenomena of inertial focusing has been described by Di Carlo [21]. Inertial focusing is a passive focusing technique that relies heavily on channel geometry and the interplay of various inertial and drag forces acting on the particles in the flow. Tang et al [22] presents

a novel impedance microcytometer integrated with inertial focusing and liquid electrode techniques for high-throughput cell counting and discrimination. They use an asymmetrically curved channel that orders particles into a single lateral equilibrium position due to the balance of transverse inertial lift force and Dean drag force. They go on to use their calibrated microcytometer to investigate the size distribution of human breast tumor cells and leukocytes, and successfully distinguish the tumor cells from the white blood cells

1.3.3 Electrode layout

The layout and design of the detection electrodes in an IFC chip is very important for sensitivity and throughput of the system.

Enhancing sensitivity

Clausen et al. [23] uses the fact that the electric field between the electrodes in a co-planar electrode layout runs parallel to the channel length to increase the sensitivity of the system. By enlarging the perpendicular surface area of the detection electrodes while keeping the general width of the measuring channel fixed, the electric field is forced through a constriction in the exact point of detection. This leads to an improvement in signal-to-noise ratio in the system compared to a conventional straight channel. Using FEM simulations the authors show that the current density running between the detection electrodes is increased when increasing the width of the electrodes. Finally the authors show that the increase in SNR in the improved chip design enables the detection and differentiation of 0.5 μm and 1 μm beads, something that was not possible with the conventional design.

Measuring cell position and orientation

Since positional variation is one of the biggest contributors to variation in IFC systems a lot of effort has been put into either focusing the position (as discussed earlier) or compensating for the position in the measurement. In order to effectively compensate for the positional variation it is of course important to know the position of the particle in the channel. Several approaches to position estimations have been published.

Spencer et al. [24] has developed a solution for position compensation in a front-facing electrodes layout. They present a microfluidic impedance cytometer that uses multiple pairs of electrodes to measure the transit time of particles through the device in two simultaneous differential current measurements. Because of asymmetry in the detection electrode configuration (see figure 1.8) the difference in transition between the two measurements provides a metric ($\Delta X_{TSV} - \Delta X_{OBQ}$) of the vertical position of the particle in channel. The transition time measured on the symmetrical electrodes (ΔX_{TSV}) follows the parabolic profile of the flow in the channel, meaning that the transition time is fastest when the particle is positioned in the center of the channel. The same is true for the transition time measured across the asymmetric electrodes (ΔX_{OBQ}) except that the asymmetry introduces a gradient that depends on the vertical position of the particle. Comparing both transition times therefore allows the authors to calculate the vertical position of the particle.

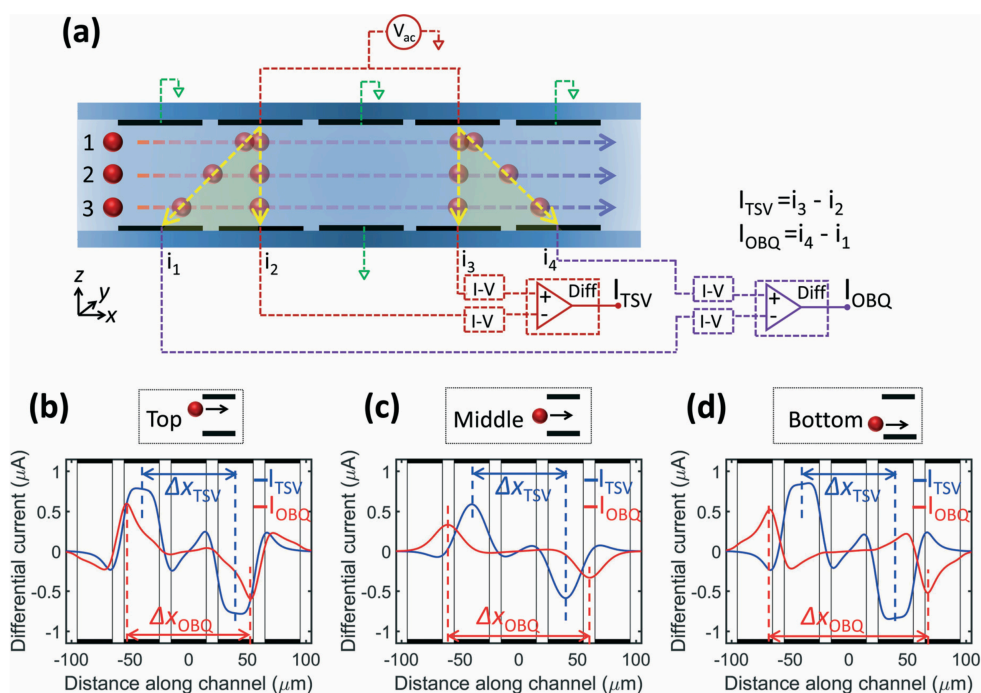


Figure 1.8: Asymmetric measuring scheme from [24]. (a) Multiple pairs of electrodes measure the impedance signal at the same time in the channel; one symmetric pair (i_2 and i_3) and one asymmetric pair (i_1 and i_4). (b-d) Simulated signal events for $7 \mu\text{m}$ bead passing close to the top electrodes, through the centre, and close to the bottom of the channel. Reproduced from [24] with permission from the Royal Society of Chemistry.

Using this metric to compensate the impedance measurements the authors successfully minimise the variation in the measured magnitude of the impedance signal for off-centre particles in experimental data. They go on to say that the technique will eliminate the need for flow focusing and that it only requires trivial calibration of the flow chip with regards to geometry to implement the solution.

If you are not using front-facing electrodes, but instead are using co-planar electrodes De Ninno et al [25] has developed an alternative approach for vertical position determination and compensation for this particular electrode layout. In their design a floating electrode is placed between the excitation electrodes and each of the measuring electrodes (5 electrodes in total). This leads to a characteristic quadruple Gaussian with the orientation of the two first peaks being opposite to the last two peak as seen in figure 1.9.

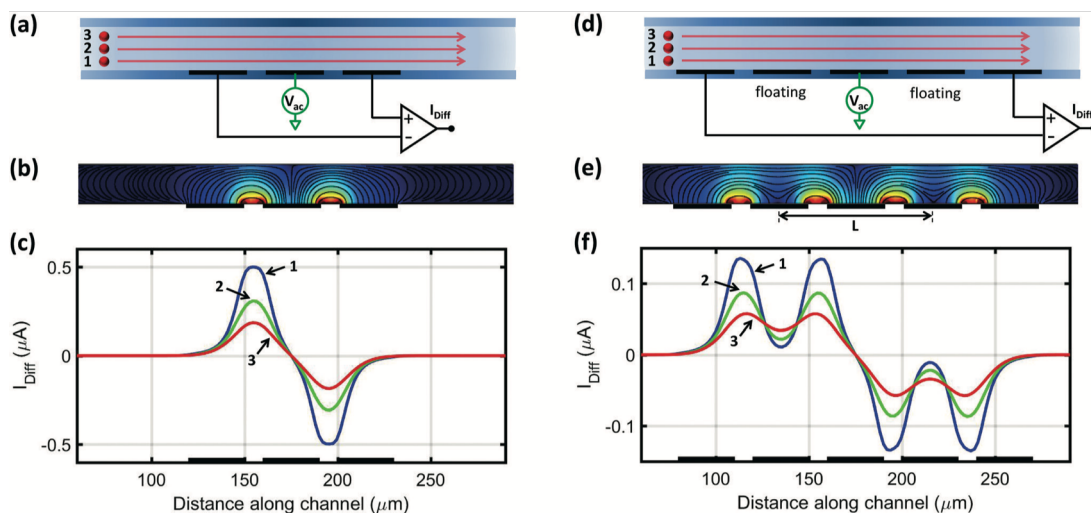


Figure 1.9: Measuring schematics and event signals from [25]. (a-c) Shows the measuring schematic, electric field and differential event signal from a standard configuration of coplanar electrodes. (d-f) Shows the measuring schematic, electric field and differential event signal from the new configuration of coplanar electrodes suggested by the authors. (f) shows the quadruple Gaussian with two saddle points. [25] - Published by The Royal Society of Chemistry.

Because the design is co-planar and all the electrodes are placed on the bottom of the channel, the relative "dip" (saddle point) in current that occurs when the particle passes above the floating electrodes is proportional to the vertical position of the particle in the channel. The authors propose a new metric called the relative prominence (P) defined as $\frac{M-m}{m}$ where M is the signal amplitude at the peak current and m is the signal amplitude in the saddle point. Using the relative prominence to correct the positional variation in the measured signal, the authors successfully separate 5.2, 6 and 7 μm beads based on their size, something that was not possible without the position correction. Similarly, they show that with compensation it is possible to get individual (but still overlapping) populations when measuring the electrical diameter of 6 μm beads and yeast cells.

In Reale et al. [26] (that share co-authors with both of the previously introduced papers [24] and [25]) they combine the designs of Spencer et al and De Ninno et al to build a system capable of determining both vertical and lateral position of a passing particle. The coplanar design of De Ninno et al is used, as is, to measure the vertical position, while the front facing design of Spencer et al is turned 90° on its side in order to measure the lateral position. This is done by incorporating liquid electrodes on either side of the flow channel as seen in figure 1.10. The end result is an impedance flow cytometry system capable of detecting the exact position of any passing particle.

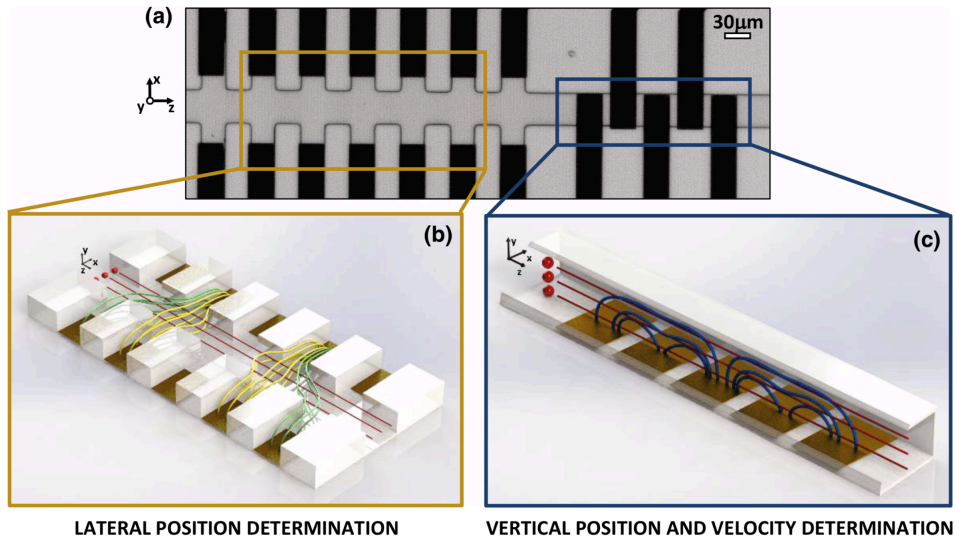


Figure 1.10: (a) Design from [26] with regions for lateral and vertical position determination. (b) 3D render of the region for lateral flow determination. A set of symmetric and asymmetric liquid electrodes allow for determination of the lateral position. (c) 3D render of the region for vertical position determination. Floating electrodes between the measurement electrodes creates a quadruple Gaussian with two saddle point that is used to determine the vertical position. Reproduced from [26] under the terms of the Creative Commons Attribution 4.0 International License.

In Shaker et al. [18] it is not the position of the cell or the particle that it of interest, but the orientation and shape of the cells. Cell shape is related to a number of physiological or pathological cellular conditions and monitoring the cell morphology can be of great importance, particularly during cell division or mitosis. They have developed a non-invasive, label free device capable of single cell morphology discrimination. They do this by having four liquid electrodes in a cross configuration as seen in figure 1.11. Prior to the detection a set of DEP electrodes focuses and orients the cells. As seen in figure 1.11 the detection area consists of four electrodes (1, 2, 3, 4). The AC input signal is applied to electrode 1 and 3, and the resulting currents are measured on electrodes 2 and 4 (I_x and I_y , respectively). They define an anisotropic index (AI) as the ratio of the normalized event current in the longitudinal direction (S_x) and the normalized current in the transverse direction (S_y).

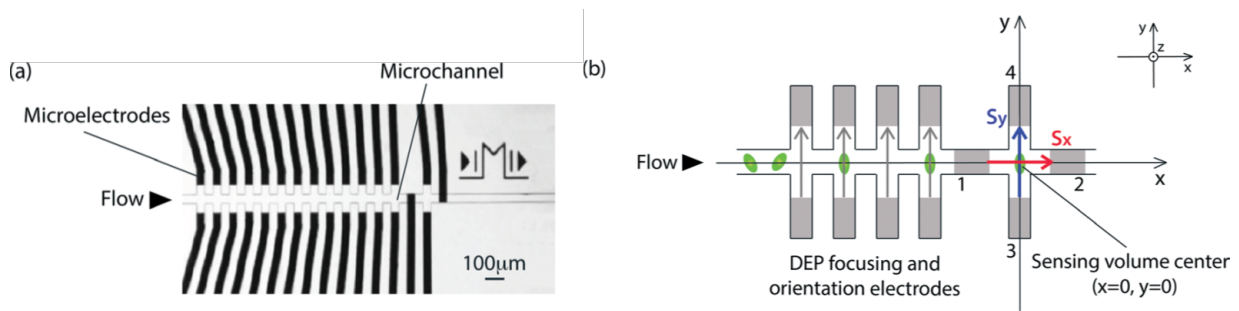


Figure 1.11: A picture of the microdevice for single cell shape-based discrimination with details of the focusing/orientation unit and the shape sensing unit from [18]. (a) Microscope images of the device. (b) A schematic representation of the device and the working principle. Reproduced from [18] with permission from the Royal Society of Chemistry.

For spherical cells the anisotropic index is expected to be 1 due to symmetry. However, for ellipsoidal particles or cells, the AI will be smaller or larger than 1 depending on the morphology and orientation of the cells. The authors demonstrated the efficiency of the device by discriminating the division stage of budding yeast cells.

1.3.4 Event detection and modelling

Typically, "raw" data from an impedance flow cytometry system takes a form like seen in figure 1.12. The data typically contains two time dependent data streams (real and imaginary parts) for each frequency used for measuring. "Raw" data should not be misinterpreted to mean unprocessed data, but rather as data where the characteristic double Gaussian events from the transition of a cell or particle has not yet been identified or analysed. Before the data reaches this form it has already been processed in the lock-in amplifier.

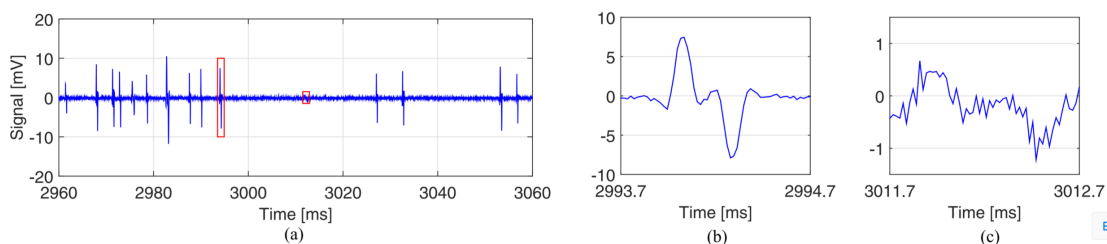


Figure 1.12: Typical "raw" data from an IFC system from [27].

Before any conclusions can be drawn from the raw data, the events in the data stream must be correctly identified. A faulty or imprecise event-detection algorithm will directly impact the results from the experiments. Typically, a differential event is model as a bipolar double Gaussian (or just bipolar Gaussian), but an effective detection algorithm will also be able to handle different event shapes that could arise from different electrode geometries or variations due to asymmetric effects (more on that below).

Caselli et al [27] has presented a simple and robust event-detection algorithm. The algorithm exploits that a differential measuring scheme is typically used and that the events

therefore exhibit an odd-symmetric pattern. The approach uses cross-correlation with a simple asymmetric template followed by a characteristic modulus cross-correlation. The resulting signal is smoothed by a Gaussian smoothing template and the events are singled out by peak finding. In order to reject false positives, the quality of the detected events are assessed. To do this ratio of the even and odd parts of each event is computed. The ratio is denoted E_2O . Do to the odd symmetry of the events the odd part of a true event is expected to be larger than the even part. The E_2O index can therefore be used as a quality indicator where low values indicates high quality events. The authors perform a comprehensive evaluation of the performance of algorithms and find that they have a sensitivity of 94.9 % and a positive predictive value of 98.5 %. As mentioned above the typically expected shape of a differential event is a bipolar double Gaussian, but other shapes might occur. Caselli et al [27] evaluates a shape that occurs if grounding electrodes are placed in between the detection electrodes. This leads to a shape with two primary peak with two smaller peaks in between and on either side (six peaks in total). This shape is brilliantly named the 'bipolar Mexican hat'.

Spencer et al. [28] investigates how the shape of the differential event is affected by the vertical position of the particle in the channel. They find that impedance signal is independent of position over the majority of the channel, but that a large variation occurs when the particle passes close to the electrode surface. They use FEM (finite element modelling) to simulate the passing of a particle at 3 different positions in a microfluidic channel with front-facing electrodes (see figure 1.13). They find that both the amplitude and the shape of the event changes when the particle passes close to the electrode surface at either the top or the bottom of the channel. They conclude that this is due to high electric field densities and edge effect near the edges of the electrodes. Specifically, the top point of the event peak changes its position, leading to an effective change in measured event velocity.

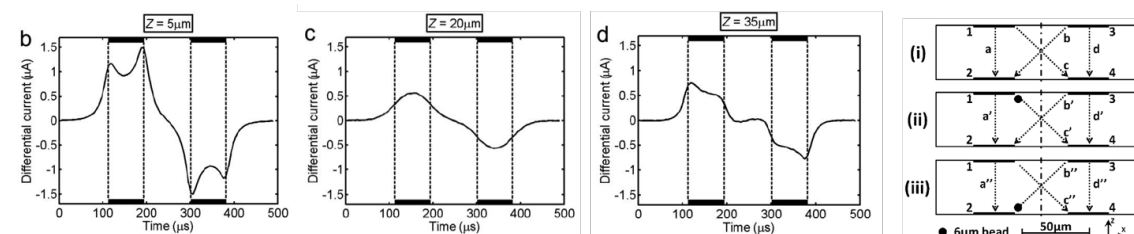


Figure 1.13: (b–d) Simulated voltage-time spectra for three horizontal planes corresponding to the mid-plane, and 5 μm from the top and bottom of the channel from [28]. (i–iii) Diagrams of the current paths between the 4 electrodes in the impedance cytometer with and without a particle (also from [28]). Reproduced from [28] with permission from the Royal Society of Chemistry.

Experimental measurements on polystyrene beads were made to determine the electrical response from particles at different positions in the channel. At low flow rates the particles are positioned across the entire channel cross section and a distribution in both impedance peak values and velocity is observed. By increasing the flow the particles are focused to specific positions in the channel due to inertial focusing. At the high flow rate the variance in the impedance signal is almost eliminated due to the fixed position of the particles.

Another way the amplitude and the shape of the event can be affected is if more than one cell is present between in detection electrodes at the same time (in Hassan et al [29] they call this a coincidence). This is particularly important when counting particles in order to determine the concentration in the sample. If two or more cells are between the electrodes at the same time they will only be counted as one cell leading to misleading concentration measurements. The likelihood of this happening decreases with lower concentrations and larger detection volume (the volume between the detection electrodes). However lower concentration will increase the measurement time while a larger detection volume might decrease the sensitivity of the system. Both of these things are undesirable. In Hassan et al. [29] they have developed a method for coincidence detection and calibration. They show that the coincidence detection of in a co-planar chip measuring on T cells can be characterized into three main types (see figure). Type 1 is characterized by a second cell arriving in the detection area within $\frac{6}{20} \times T$ with T being the total time it takes a cell to move across the electrodes. As the second cell enters the detection volume they predict a sharp increase in amplitude as seen in figure 1.14. Type 2 is characterized by the second cell entering the detection volume between $\frac{6}{20} \times T$ and $\frac{13}{20} \times T$. In this case the width of the event increases by an amount equal to the time delay at which the cell coincidence occurs. As seen in figure 1.14 this can lead to a three peak event. Type 3 is characterized by the second cell entering the detection volume between $\frac{13}{20} \times T$ and T . In this case the distance between the two cells is large enough to get separate peaks from each cell, but due to the closeness of the cells during the passing some interference is still expected. As seen in figure 1.14 this leads to an event with 4 peaks.

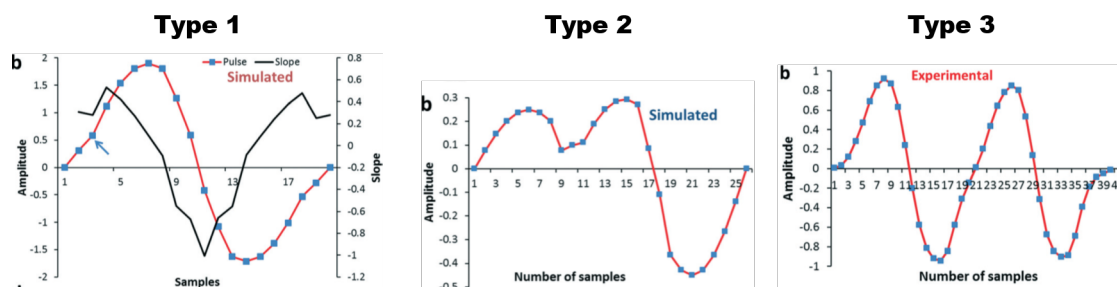


Figure 1.14: Illustration of type 1, type 2 and type 3 coincidence as described in [29]. Reproduced from [29] with permission from the Royal Society of Chemistry.

By taking the three types of coincidence (and combinations there of) into account the authors show that the error in counting T cells due to coincidence is reduced to almost nothing when the counts are compared to counts obtained by regular fluorescence flow cytometry.

1.4 What is BactoBox?

BactoBox is a flow cytometer meant for enumeration of viable bacterial cells in liquid samples based on impedance characterization of the cells. BactoBox is a tabletop device that can be operated without the need for a pc or any other equipment. BactoBox is developed by SBT Instruments as an instrument that will be sold to users in need of more effective quantification of microbiology.



Figure 1.15: Image of BactoBox

The device (as seen in figure 1.15) is operated using 4 buttons (Measurement, Stop, Empty, Clean) and information about the ongoing measurement and the results of the measurement is displayed on a screen on the front of the device. It is not designed as a lab instrument and as such the user only sees the final calculated concentration and does not have access to the guts of the system and cannot change measurement specific settings. Operation of the instrument is straight forward. The user connects a sample vial to the tubing and presses the measurement button. After 3 min BactoBox will show the result on the screen with the measured bacteria concentration. Bacterial samples are suspended in liquid in 7 ml vials that are attached to a cap containing tubing for inflow and outflow of sample. BactoBox contains all the components necessary to run a measurement (ie. pump, memory, CPU, etc.). For development purposes the instrument can connect to a PC through a custom developed web-interface where the expert user can gain additional information about the measurement as it is running and change settings for measurement parameters. BactoBox is meant to replace more traditional methods for microbiology quantification, primarily methods relying on the growth of the bacterial cells for quantification.

1.5 Objective and outline

This thesis describes my efforts from the last 3 years at obtaining a better understating of impedance measurements of bacterial cells. It will focus both on the more fundamental concepts of dielectric measurements of cells, but particularly on how the prototype impedance flow cytometer (ie. BactoBox) developed and produced by SBT performs these measurements. This means exploring the capabilities and boundaries of the device in its current state. BactoBox has been under continual development during the span of this project, with new updates appearing regular to both software, hardware and core technology. Fundamentally the technological concept has been the same throughout the project, but many important details have been tweaked, improved or removed, sometimes based on input from my work, but often also based on input from commercial, user and

customer sources. It is both uniquely challenging and motivating to carry out research in the space between R&D and commercialisation. When developing products, especially in a start-up, you iterate fast, some of the time (maybe most of the time) without knowing the reason why or how a particular feature failed or worked. In my opinion, this is the right way to develop products. Quickly figure out what works and then build upon that. The problem with this approach is that if you continuously skip the step where you actually understand the underlying mechanisms of the technology, you risk ending up not understanding how anything works at all. This industrial PhD project was started as a counter measure to this effect. There is a term that is used in business administration called "absorptive capacity" and it is defined as "*the ability of a firm to recognize the value of new, external information, assimilate it, and apply it to commercial ends*" [30] and it is exactly the absorptive capacity of SBT Instruments that this PhD project will help expand. It is the goal of the PhD project to support the product development of BactoBox by providing more considered answers to why the technology behaves the way it does. More than designing specific improvements to BactoBox, it is my hope that this work will help build the foundation for future improvements of the technology in general and of the product specifically.

This thesis is split into two major parts. Part 1 begins with **chapter 2** and the introduction of the theoretical background for dielectric characterization of bacteria. Next, **chapter 3** gives a more practical presentation of the different functional parts of BactoBox. Both of these areas are hugely complicated and very interdisciplinary, but my hope is that the reader will gain a better understanding of the underlying "hows" and "whys" of the technology that make up BactoBox. **Chapter 4** is the final chapter of part 1 and presents the various ways we will use to analyse and visualise the impedance data obtained from experiments with BactoBox.

Part 2 of the thesis consists of experimental work where I have used BactoBox to investigate the dielectric properties of different bacteria and/or other particles. Chapter 5 presents the results from a few different experiments that illustrate how different bacteria and particles are measured and differentiated with IFC and BactoBox. Most interestingly, it has a comparison between 6 different bacteria strains. Then, **chapter 6** presents a smaller experiment performed during a visit at the University of Barcelona, where we measure the impedance response of samples with custom synthesized liposomes. The idea is that the liposomes can be used as cell models, and by carefully controlling the synthesis we can control properties such as size and membrane composition. The work from these experiments resulted in a manuscript which is presented in this chapter. **Chapter 7** presents work on the classification between viable and inactivated *E. coli*. The work has resulted in two paper manuscripts which are both presented. The first paper takes a general approach to inactivation looking at ethanol, heat and autoclaving as inactivation methods. Based on the results obtained, the second paper looks deeper into the effects of prolonged exposure to heat. As the last chapter of part 2, **chapter 8** describes our efforts at using IFC and BactoBox for fast antibiotic susceptibility testing, looking at the effects of the antibiotic colistin on *E. coli* and *Pseudomonas* bacteria. Finally, **chapter 9** will have my concluding remarks and future outlook.

Part I

2 Theory and Modelling

2.1 Electrical impedance

Electrical conductivity (σ) is a property of every conducting material that describes the materials capacity for conducting electrical current. Furthermore, the conductance (G) describes the current conduction ability of a specific piece of a given material with physical dimensions height (h), length (l) and width (w) and is related to the conductivity in the following way

$$G = \sigma \frac{hw}{l} \quad (2.1)$$

Permittivity (ε) is a property given to dielectric materials (or insulators). Dielectric materials can be polarized due to displacement of charges inside the material in response to an applied electric field. The permittivity describes how easy it is to polarise the material and is often given as a relative value (ε_r) compared to the vacuum permittivity (ε_0)

$$\varepsilon = \varepsilon_r \varepsilon_0 \quad (2.2)$$

Impedance is a measure of the frequency dependent resistance of an electrical circuit to a current when a voltage is applied. Impedance is measured in Ohms (Ω). Impedance is represented by a complex number and can therefore be written as having a real and an imaginary part

$$Z = Z_{RE} + i \times Z_{IM} \quad (2.3)$$

where Z_{RE} and Z_{IM} is called the resistance and reactance, respectively. The complex impedance can also be represented by an amplitude and the phase

$$|Z| = \sqrt{Z_{RE}^2 + Z_{IM}^2} \quad (2.4)$$

$$\arg(Z) = \arctan\left(\frac{Z_{IM}}{Z_{RE}}\right) \quad (2.5)$$

2.1.1 The impedance of electrical components

In electrical circuits, each component of the circuit has its own impedance. The impedance of the three basic circuit components (the resistor, the capacitor, and the inductor) can be calculated from the physical properties of the components.

The impedance of the resistor is independent on frequency and inversely dependent on the conductance of the resistor

$$Z_R = R = \frac{1}{G} = \frac{1}{\sigma} \frac{l}{wh} \quad (2.6)$$

The impedance of a capacitor is inversely dependent on the frequency (ω)

$$Z_C = \frac{1}{i\omega C} \quad (2.7)$$

where C is the capacitance of the capacitor and an expression of the amount of charge that can be stored in the capacitor. The capacitance of a ideal plate capacitor comprised of two parallel plates placed across from each other a a distance (d) with a dielectric material in between is calculated by

$$C = \varepsilon_r \varepsilon_0 \frac{A}{d} \quad (2.8)$$

where ε_r is the relative permittivity of the dielectric material and A is the area of the plates.

Finally, the impedance of an inductor is directly proportional to the frequency

$$Z_L = i\omega L \quad (2.9)$$

2.2 Bacteria

Bacteria make up a very diverse population of cells, both when it comes to cell morphology (e.g., shape and size) and cell activity (e.g. metabolism), and are found in almost all environments and habitats around the world. Understandably, most research and investigations into bacteria in the last 150 years has focused on disease-causing bacteria, resulting in a number of isolated pure cultures used for laboratory work. However, a very large population of bacteria are free-living species (e.g., environmental bacteria or marine bacteria) that researchers have only recently begun mapping and understanding. Therefore, it is impossible to lay down strict rules for bacterial composition or structure, and exceptions exist to any general statement.

Bacteria generally come in three shapes: spherical (coccus), rod-shaped (bacillus), or curved (vibrio, spirillum, or spirochete). Even within these three main groups considerable variation has been observed based on environmental factors and growth conditions, even within the same species of bacteria. Some bacteria naturally form integrated groups of cells such as cocci-species that grow in pairs (ie. diplococcus) and *Streptococci* that grow in long chains.

An average-size bacterium (e.g. the rod-shaped *Escherichia coli*) is about 2 μm long and 0.5 μm in diameter, and the spherical cells of *Staphylococcus aureus* are up to 1 μm in diameter.

Unlike in eukaryotic cells, the DNA in bacteria is not enclosed in a nucleus but instead resides in the bacterial cytoplasm. The cytoplasm makes up most of the volume of the bacteria and is enclosed by a structural shell referred to as the bacterial envelope. The cytoplasm of a bacterial cell consists of 80% water and (besides the genetic material) also holds various enzymes, nutrients, inorganic ions, and many low molecular weight compounds [31].

The bacterial cell envelope is the name given to the membranes and/or shells that surround the cytoplasm [32]. The cell envelope in bacteria is highly complex and plays a crucial

role for the survival of bacteria in hostile and unpredictable environments where other eukaryotic cells would perish. The envelope allows selective crossing of nutrients into the bacteria and also functions as surfaces on which reactions can occur.

Bacteria are generally classified into two groups based on their ability to retain staining with crystal violet stains. This method of classification was developed by Christian Gram in 1884 and the two groups of bacteria are consequently called gram-positive and gram-negative. The reason why some bacteria retain the crystal violet stain and others do not, originates in the essential differences in cell envelope structure of the two groups.

2.2.1 Gram-negative bacteria

The majority of information about the structure of gram-negative bacteria comes from extensive studies of *E. coli*, but the group also contains many other important species such as *Pseudomonas*, *Salmonella* and *Klebsiella*. The gram-negative cell envelope is comprised of 3 main layers as illustrated in figure 2.1: the outer membrane, the peptidoglycan layer and the inner membrane (also called the cytoplasmic membrane or just plasma membrane). Starting from the inside, the first layer is the inner membrane also referred to as the cytoplasmic membrane or just the plasma membrane. The inner membrane is a lipid bilayer made up of phospholipids. Phospholipids are amphiphilic molecules, with a hydrophilic head and a hydrophobic tail (as illustrated in figure 2.1) and are the main component of all biological membranes. The hydrophobic tail is made up of by two hydrocarbon chains while the hydrophobic head constitutes a negatively charged phosphate group which is linked to an organic compound

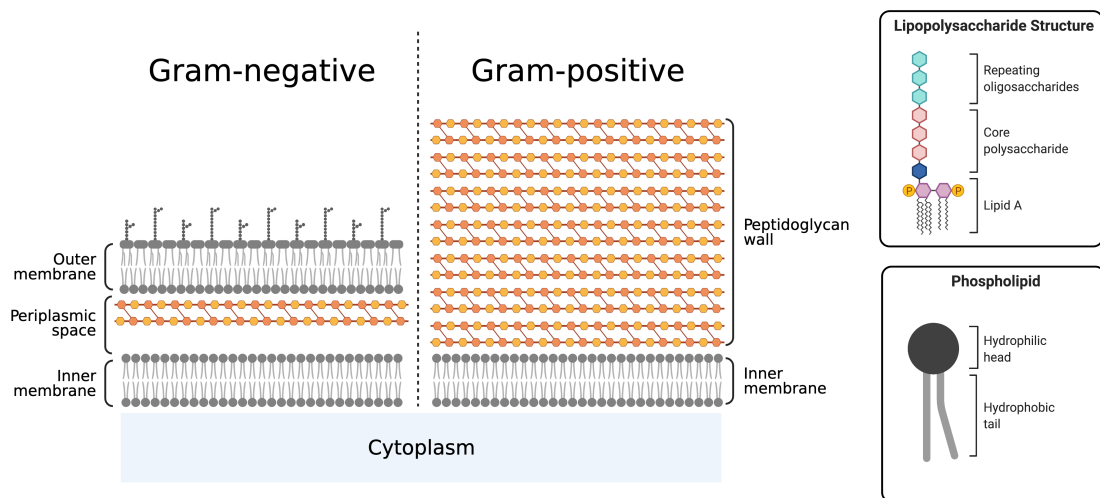


Figure 2.1: Illustration showing the basic envelope structure of gram-negative and gram-positive bacteria. The gram-negative bacteria envelope is made up of three layer: an outer lipid membrane, a periplasmic space that also holds the peptidoglycan layer, and an inner lipid membrane. The gram-positive envelope has a much thicker peptidoglycan layer surrounding a single lipid membrane. Created with BioRender.com.

The inner membrane holds many of the proteins associated with energy production and different biosynthesis processes. The thickness of the inner membrane varies (e.g., depending on species) but is reported to be between 4-10 nm [33–36] .

The aqueous cellular compartment between the inner and outer membrane is called the periplasm or periplasmic space. It is in this space, that the peptidoglycan wall of the gram-negative bacteria is found. Peptidoglycan is made up of repeating units of the disaccharide N-acetyl glucosamine-N-actyl muramic acid, which are cross-linked by pentapeptide side chains [37]. It is a tough and rigid wall compared to the fragile lipid membranes and enables the bacteria to survive in harsh conditions. For example, the peptidoglycan wall prevents the bacteria from swelling under hypertonic or hypotonic conditions and thus helps prevents cell lysis when the cell experience a sudden change in osmotic pressure (e.g., if the cell is put into distilled water). Antimicrobial agents such as β -lactams (e.g., penicillin) inhibits the synthesis of peptidoglycan, leaving the cells vulnerable to external pressure. The resulting cells (i.e. cells without peptidoglycan walls) are called spheroplasts. Spheroplast *E. coli* have been seen to continue their metabolism for hours, even though they are not viable [38]. The last layer in the envelope structure of gram-negative bacteria is the outer membrane. Like the inner membrane, the outer membrane is a lipid bilayer, but unlike the inner membrane it is not primarily made up of phospholipids. Only the inner leaflet (the inner part of the bilayer) is made of phospholipids while the outer part is made of primarily lipopolysaccharides (LPS). LPS are large molecules consisting of three regions: the lipid structure required for insertion in the outer membrane, the core polysaccharide and the polysaccharide chain (see figure 2.1). They are essential to the structural integrity of the outer membrane and play an important role in the pathogenesis of many Gram-negative bacteria. The outer membranes function primarily as a solid barrier, protecting the inner layers of the cell envelope and the cytoplasm of the bacteria from toxic molecules. The outer membrane is a unique feature of Gram-negative bacteria and is not found in gram-positive bacteria.

2.2.2 Gram-positive bacteria

The Gram-positive cell envelope is different from that of gram-negative bacteria in two important ways. The peptidoglycan wall is much thicker in gram-positive bacteria (30-100 nm in gram-positive bacteria compared to a few nm in gram-negative) and they lack the outer membrane (see figure 2.1). The thicker peptidoglycan wall helps gram-positive bacteria survive in harsher environments even without the protective outer membrane. The peptidoglycan wall of gram-positive bacteria is similar in structure to that found in gram-negative bacteria but instead contains multiple stacked layers. Long anionic polymers, called teichoic acids, are woven through the peptidoglycan layers, some of which are attached to the peptidoglycan layers binding them together and others are attached to the surface of the inner membrane. The inner membrane in gram-positive bacteria is largely similar to that found in gram-negative bacteria.

2.2.3 Bacteria viability

Cell viability is of particular interest when evaluating the dielectric properties of bacteria using IFC. Viability is obviously an important factor to consider in risk and contamination assessments. In a production environment (e.g., a food production), an abnormally high concentration of viable bacteria is considered problematic, but if the majority of the cells are dead the risk decreases dramatically.

Even though viability is a frequently used term, its definition is not straight forward. For bacteria and other microbes, even the use of terms like ‘alive’ and ‘dead’ is awkward and the definition of these terms could be considered more of a philosophical challenge than

a technical one. Instead of ‘alive’, we could use terms like healthy, viable or active, and ‘dead bacteria’ could for example be replaced with ‘inactivated bacteria’.

In practice, determination of microbial viability by the plate count method is used every day in microbiology laboratories worldwide and is considered the “gold standard” of viability determination [39]. It is based on the idea that a single bacterium, if viable and placed on the appropriate growth medium under appropriate conditions, can grow and multiply until it forms a colony large enough to be determined with the naked eye. The number of visible colonies, or colony forming units (CFU), on the surface is then counted to evaluate the number of viable cells in the original sample. This makes the plate counting method very sensitive, since it in principle only need one viable bacterium in the sample to produce a result. It is, however, not possible to obtain information about the number of inactivated bacteria in a sample using this method.

Even with its many advantages and widespread use, the plate count method cannot be considered a universal approach to viability determination. In principle, this is because the loss of culturability can be caused by two circumstances [40]:

1. The loss of culturability is a result of cellular deterioration (i.e. cell death, inactivation, etc.)
2. The loss of culturability is an adaptive and programmed survival mechanism of the bacterial cell

The first circumstance can generally be assumed when dealing with standard reference microorganisms acquired from organizations such as the American Type Culture Collection (ATCC) or the German Collection of Microorganisms and Cell Cultures (DSMZ). If microorganisms acquired from such an organization won’t grow when under the prescribed growth conditions, it can be considered inactivated. The second circumstance has led to the term viable but nonculturable cells (VBNC), that describes cells that are metabolically or physiologically active but cannot be cultured on specific media [41]. It is estimated that less than 1 % of the bacteria observable in microscopes in environmental samples can be accurately determined as viable by the plate count method [42]. Furthermore, the bacterial cells can enter states that are described as “dormant” [43], “moribund” (ie. approaching death) [39], or “latent” [44], where they won’t grow easily on an agar plate, but still play some role in disease or fouling processes. Even in cases where the cells do grow, it can be ambiguous to directly relate the CFU count to cell concentration, since a single colony may have formed from 2 or more cells in close vicinity.

It can be problematic to think of viability as an either-or questions, both for single cells and especially for populations of cells. Figure 2.2 shows the range of potential viability states for a microorganism between alive and dead, and illustrates the point that even cells that appear inactivated may recover eventually.

It is generally agreed that disruption of the cell membrane correlates well with viability. Inactivation methods with e.g. surfactants or alcohol causes immediate loss of membrane integrity, resulting in catastrophic loss of homeostasis, cellular functions, and culturability [46]. However, other inactivation methods that will cause immediate loss of culturability (such as inactivation with ultraviolet light) will only later (hours or days) show degradation of cellular components and the cell membrane.

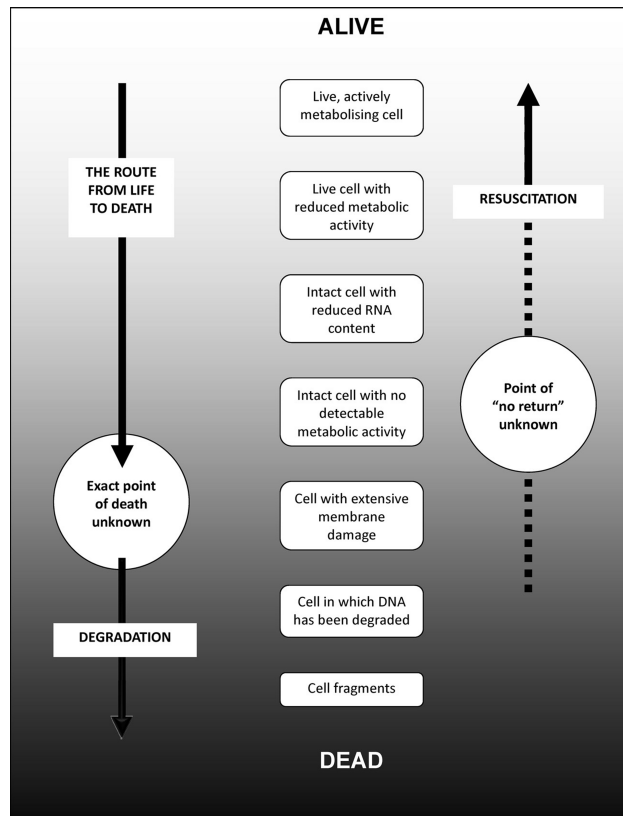


Figure 2.2: The route from alive to dead for a microorganism contains many steps and while the extremes are relatively well defined the steps in between may not be. Figure from [45].

2.3 Dielectric modelling of biological material

The impedance of tissue has been studied for more than a hundred years. Since the beginning of the 20th century researchers have been trying to understand the electrical properties of tissue and biological material. Today we have a much better understanding of the structural building blocks of both eukaryotic and prokaryotic cells, however much of the theoretical and analytical background developed then is still used today.

As early as 1922, Green and Larson were discussing the conductivity of bacteria [47] in relation to assessment of bacterial viability. In the 1930s and 1940s researchers like Kenneth Stewart Cole [48] and Herman P. Schwan [49] developed comprehensive analytical models for the electrical behaviour of biological material. Schwan categorises the dielectric dispersion of biological material into three different ranges; α -, β - and γ -dispersions. α -dispersion is associated with tissue interfaces, β -dispersion is related to the dielectric relaxation and polarisation of biological membrane or what we today would refer to as phospholipid bilayers in cells. Lastly, γ -dispersion is related to the dielectric relaxation of water molecules. We are primarily concerned with β -dispersion.

2.3.1 Mixture theory

Maxwell mixture theory (MMT) takes an effective medium approximation approach to the overall impedance of a suspension of spherical particles dispersed in medium.

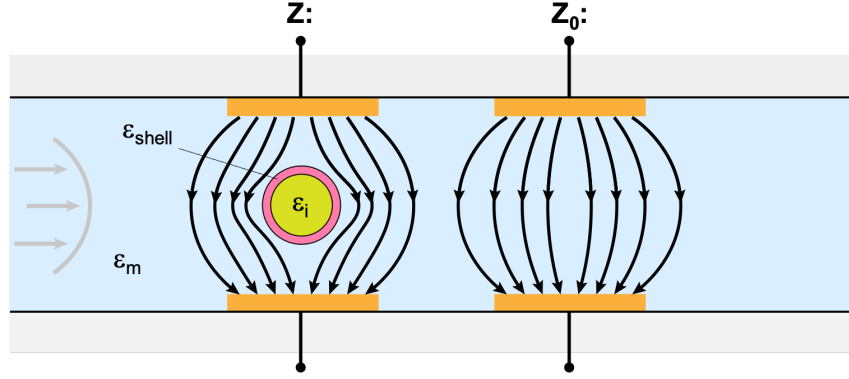


Figure 2.3: Sketch showing the detection channel with two electrode sets (Z and Z_0) and a single-shelled sphere with dielectric properties ε_i and ε_{shell} suspended in the electrolyte medium (ε_m) between one of them. The electric field between the first electrode set is perturbed by the presence of the sphere.

Figure 2.3 show a sketch of the detection channel of the microfluidic chip with two sets of detection electrode and a cell present between one of the sets. Let's call the impedance between the electrode pair with the cell Z and the impedance between the set with no cell Z_0 .

The complex impedance between the electrode sets is calculated using

$$Z^* = \frac{1}{j\omega\varepsilon_{mix}^*l\kappa} \quad (2.10)$$

and

$$Z_0^* = \frac{1}{j\omega\varepsilon_m^*l\kappa} \quad (2.11)$$

where j is the imaginary unit, ω is the angular frequency, κ is a corrected cell constant that depends on the geometry of the electrodes, l is the electrode length perpendicular to the flow, ε_m^* is the complex permittivity of the suspending medium, and ε_{mix}^* is the effective complex permittivity of the mix of medium and particle between the electrodes.

The complex permittivity depends on the relative permittivity (ε_r) conductivity (σ) and the angular frequency (ω) in the following way

$$\varepsilon^* = \varepsilon_0\varepsilon_r - j\frac{\sigma}{\omega} \quad (2.12)$$

The complex permittivity of a dilute suspension of particles between two electrodes is given by MMT as

$$\varepsilon_{mix}^* = \varepsilon_m^* \frac{1 + 2\phi f_{CM}}{1 - f_{CM}} \quad (2.13)$$

where ε_{mix}^* is the complex permittivity, ϕ is the ratio of the particle volume to the detection volume and f_{CM} is known as the Clausius–Mossotti factor calculated as

$$f_{CM} = \frac{\varepsilon_p^* - \varepsilon_m^*}{\varepsilon_p^* + 2\varepsilon_m^*} \quad (2.14)$$

with ε_p^* and ε_m^* as the complex permittivity of the particle and medium. The complex differential current (ΔI) between Z and Z_0 at a given applied potential is calculated as

$$\Delta I^* = I^* - I_0^* \quad (2.15)$$

with I and I_0 calculated using Ohms law from Eq. 2.10 and Eq. 2.11

The Clausius-Mossotti factor also plays an important role in the field of dielectrophoretic manipulation of dielectric particles. Dielectrophoresis, or DEP, is defined as the movement of polarisable particles in a non-uniform electric field. In an AC-field the time averaged DEP force on a particle is given by

$$F_{DEP} = K_{geo} \times \varepsilon_m \varepsilon_0 \times \text{Re}[f_{CM}] \times \nabla |E|^2 \quad (2.16)$$

The magnitude of the DEP force is therefore related to the field strength and the Clausius-Mossotti factor and the direction of the force depend directly on the sign of the real part of the Clausius-Mossotti factor. K_{geo} is a geometry factor that depends on particle geometry (for a sphere the geometry factor is $2\pi r^3$).

Non-spherical cells

Many bacterial cells are not spherical but instead rod-shaped (e.g., *E. coli*, *Listeria* and *Bacillus* species). For these cases, a modified Clausius-Mossotti has been derived [50] that defines the it for each principal axis of an ellipsoidal particle

$$f_{CM} = \frac{\varepsilon_p^* - \varepsilon_m^*}{3(A_n(\varepsilon_p^* - \varepsilon_m^*) + \varepsilon_m^*)} \quad (2.17)$$

where A_n is called the depolarisation factor and depends on the orientation of the particle in relation to the electric field calculated as

$$A_n = \frac{1}{2} a_1 a_2 a_3 \int_0^\infty \frac{ds}{(s + a_n^2) \sqrt{(s + a_1^2)(s + a_2^2)(s + a_3^2)}} \quad (2.18)$$

where s is an arbitrary distance for integration and a_1 , a_2 and a_3 are the half length for the three principle axis of the the ellipsoid. In the case where $a_1 \gg a_2 = a_3$, the depolarisation factor along the major axis (a_1), is given by the relationship

$$A_1 = -\frac{1 - e^2}{2e^3} \left[2e - \ln \left(\frac{1 + e}{1 - e} \right) \right] \quad (2.19)$$

where e is the eccentricity given by

$$e = \sqrt{1 - \left(\frac{a_2}{a_1}\right)^2} \quad (2.20)$$

The sum of the depolarisation factors for the principal axis is always 1 ($A_1 + A_2 + A_3 = 1$), which means that in the case of an ellipsoid where $a_1 \gg a_2 = a_3$, the depolarisation factor for the remaining 2 principle axis can be calculated as

$$A_2 = A_3 = \frac{1 - A_1}{2} \quad (2.21)$$

Shelled particles

Even the simplest cell can not be represented adequately as a homogeneous sphere. A more appropriate model consists of a homogeneous sphere (or core) with one or more concentric shells of various thicknesses surrounding it representing the cell envelope as shown in figure 2.4. Each layer has its own permittivity and conductivity but the entire structure (shells and core) can be modelled as a homogenous particle with an effective complex permittivity that relates to each shell of the original particle.

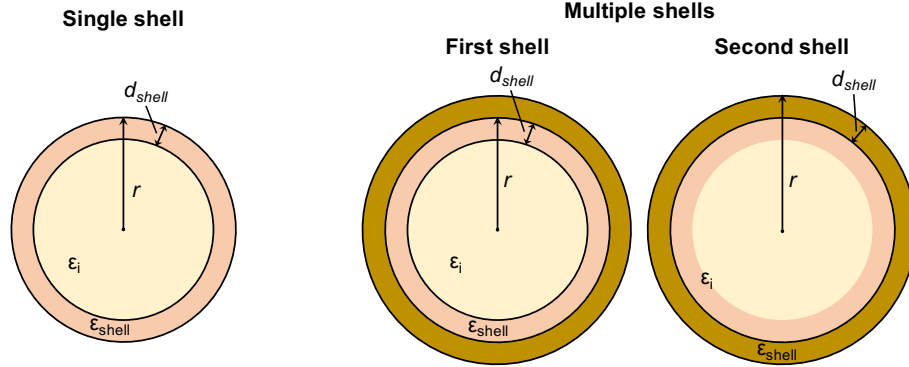


Figure 2.4: Sketch of a single shelled and multi shelled spherical particles for modelling. To calculate the effective permittivity of a multi shelled particle, first calculate the effective permittivity of the interior and the first shell. Then, using the just obtained effective permittivity, calculate the permittivity including the second shell.

For cells modelled as spherical single-shelled particles the effective complex permittivity is found using

$$\epsilon_{eff}^* = \epsilon_{shell}^* \frac{\left(\frac{r}{r-d_{shell}}\right)^3 + 2 \left(\frac{\epsilon_i^* - \epsilon_{shell}^*}{\epsilon_i^* + 2\epsilon_{shell}^*}\right)}{\left(\frac{r}{r-d_{shell}}\right)^3 - \left(\frac{\epsilon_i^* - \epsilon_{shell}^*}{\epsilon_i^* + 2\epsilon_{shell}^*}\right)} \quad (2.22)$$

with r being the particle radius including the shell, d_{shell} is the shell thickness, ϵ_i is the complex permittivity of the interior sphere and ϵ_{shell} is the complex permittivity of the shell. The model can be extended to multiple shells by using Eq. 2.22 for each shell,

starting from the innermost shell and continuously calculating a new effective permittivity from the previous effective particle permittivity and adding the new shell as illustrated in figure 2.4. Each membrane is in itself a complex biological system and specific values for conductivity and permittivity are not necessarily easy to find for every variation of bacteria.

If the shelled particle is an ellipsoid oriented along the axis k , the effective permittivity can be calculated in a similar way using [51, 52]

$$\varepsilon_{eff}^* = \varepsilon_{shell}^* \frac{\beta_k(1-\gamma)\varepsilon_{shell}^* + (1+\beta_k\gamma)\varepsilon_i^*}{(\beta_k + \gamma)\varepsilon_{shell}^* + (1-\gamma)\varepsilon_i^*} \quad (2.23)$$

$$\beta_k = \frac{1 - A_k}{A_k} \quad (2.24)$$

$$\gamma = \frac{(a_1 - d_{shell})(a_2 - d_{shell})(a_3 - d_{shell})}{a_1 a_2 a_3} \quad (2.25)$$

This reduces to Eq. 2.22 when $a_1 = a_2 = a_3 = r$ and $A_1 = A_2 = A_3 = 1/3$.

2.3.2 Equivalent circuit modelling

An equivalent circuit is a simplified circuit that retains the electrical characteristics of the original system. Equivalent circuit modelling (ECM) is a widely used way to describe the electrical properties of complex physical systems. The ECM provides a powerful way to discuss the electrical behaviour of a system without the complexity of the physical system. The equivalent circuit for a set of front-facing micro-electrodes is illustrated in figure 2.5 together with a sketch of the complex impedance response of such a circuit. The physical components modelled in the system are the electrolyte medium between the electrodes, the double layer impedance at the electrode surface and the parasitic capacitance.

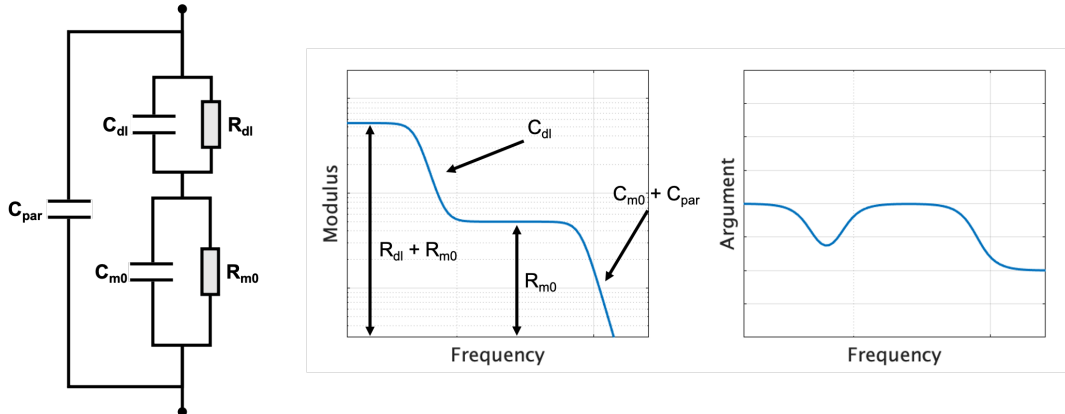


Figure 2.5: ECM of two front facing electrodes with medium in-between. ECM components are capacitance and resistance of the electrical double layer (C_{dl} & R_{dl}), the capacitance and the resistance of the medium (C_{m0} & R_{m0}), and the parasitic capacitance (C_{par}). An illustration of the frequency dependent modulus and argument with arrows indicating which components dominate at which frequencies.

Medium impedance

The medium between the electrodes is modelled as a capacitor (C_{m0}) and a resistor (R_{m0}) in parallel connection. The medium can be any liquid, but for biological applications a number of different saltwater solutions are used (e.g. phosphate buffered saline, Hanks Balanced Salt Solution, Ringer's solution, etc.). The capacitance of the medium arises from the strong polarity of the water molecules. The relative permittivity at room temperature is 80, however the exact relaxation mechanism of water is complex [53] and depends on temperature, frequency and confinement [54]. The conductivity of the medium depends on the ionic concentration and is considered to be linear at low voltages (at higher voltages the current is limited by mass transport of ions to the electrodes).

Double layer impedance at the electrode-medium interface

When a charged surface comes into contact with an electrolyte solution, an electrified layer forms at the interface between the two materials. While the electrical behaviour at this interface can be complicated to predict, the model developed by Stern through combinations of earlier models from Helmholtz and Gouy-Chapman, is considered to describe it adequately. As the electrode surface is covered in medium, a chemical reaction occurs where electrons are transferred between the electrode and the medium. When the reaction reaches its electrochemical equilibrium, a layered structure is formed in the electrolyte called the electrical double layer (EDL). The ECM can be divided into three sub-layers, the inner Helmholtz plane (IHP), the outer Helmholtz plane (OHP) and a diffuse ion layer or ion cloud. The IHP consists of a layer of oriented water molecules creating a hydration sheath at the electrode surface. The OHP is made up of hydrated ions, some of which adsorb to the electrode surface, breaking the IHP.

The capacitance associated with the IHP and OHP is called the Helmholtz capacitance (C_H) and is calculated using

$$C_H = \frac{\varepsilon_0 \varepsilon_r}{d_{OHP}} \quad (2.26)$$

where C_H is the capacitance per unit area (F/m^2), ε_0 is the vacuum permittivity, ε_r is the relative permittivity of the electrolyte and d_{OHP} is the distance from the electrode to the OHP. Due to the electrostatic restriction of the water molecules near the interface, the relative permittivity used to calculate the Helmholtz capacitance is significantly lower than the permittivity of water in bulk with studies finding the permittivity of confined water can be as low as 2. Typically, the distance from the electrode surface to the OHP is $\sim 5\text{\AA}$. The diffuse ion layer helps explain why the ECM depends on parameters such as temperature, applied potential and ionic strength of the medium. The characteristic thickness of the diffused layer is called the Debye length (λ_D) and is calculated using

$$\lambda_D = \sqrt{\frac{\varepsilon_0 \varepsilon_r V_t}{2nz^2q}} = \sqrt{\frac{\varepsilon_0 \varepsilon_r k_B T}{2N_A q^2 I}} \quad (2.27)$$

where V_t is the thermal voltage ($\frac{k_B T}{q}$), n is the bulk concentration of ions in the electrolyte (ions/l), z is the valence of the ions, q is the charge on an electron, T is the absolute temperature, N_A is Avogadro's number, and I is the ionic strength. The Debye length

depends on the bulk concentration of ions in the electrolyte and therefore also on the conductivity of the electrolyte. Table 2.1 shows typical Debye lengths in common buffer solutions [55] where it is seen that the Debye length for 1/10xPBS dilution starts being comparable to the thickness of a lipid cell membrane (5-10 nm).

Table 2.1: Debye lengths for dilutions of phosphate buffered saline (PBS) at a pH of 7.4. Values obtained from supplementary material of [55]

Solution	Ionic strength	Debye length (λ_D)
1xPBS	162.7 mM	0.76 nm
1/10xPBS	16.27 mM	2.41 nm
1/100xPBS	1.627 mM	7.61 nm

The capacitance created by the diffuse layer is also called the Gouy-Chapman capacitance and is calculated using

$$C_{GC} = \frac{\epsilon_0 \epsilon_r}{\lambda_D} \cosh\left(\frac{zV_0}{2V_t}\right) \quad (2.28)$$

where V_0 is the potential at the electrode surface. Since there is no confinement of the water molecules in the diffuse layer, the permittivity is considered to be equal to that of bulk water. By combining the Gouy-Chapman model (Eq. 2.28) with that of Helmholtz (Eq. 2.28), the total capacitance of the ECM (C_{DL}) can be found

$$\frac{1}{C_{DL}} = \frac{1}{C_H} + \frac{1}{C_{GC}} \quad (2.29)$$

Double layer resistance

A DC potential applied to the electrode may under certain conditions allow a current to flow caused by charge transfer through the double layer, diffusion of reactants to and from the electrode surface, chemical reactions at the electrode and exchange of metal atoms with corresponding ions in solution [56]. These effects leads to the addition in the ECM of a double layer resistance parallel with the double layer capacitance. These mechanisms are complex, not necessarily linear and will not be discussed in detail here.

Parasitic capacitance

The final component of the ECM is the stray capacitance that appears due to unwanted cross-connection between electrode vias and other interconnections (e.g spring-pins) in proximity to each other, either on the chip itself or in the connections between the chip and the electronics PCB.

Frequency dependent impedance response

As seen in figure 2.5 the impedance response of the ECM consists of four overall regions. At very low frequencies the impedance is very high, and current is only conducted through charge transfer in the gaps of the hydration sheath at the electrode surface. As the frequency is increase the ECM capacitance is short circuited. At some frequency, a plateau is reached where the medium resistance dominates. It is preferable to perform experimental measurements in this frequency range since it is free of influence from both the ECM

and the parasitic capacitance of the system. At even higher frequencies the parasitic capacitance and the capacitance of the medium dominates.

2.3.3 Model with bacteria

The simplest ECM representing a bacteria between two electrodes consists of the resistance of the medium in parallel with a capacitor representing the membrane of the bacteria and another resistor representing the cytoplasm in the core of the bacterium as shown in figure 2.6. Pure lipid membranes are considered very good insulators however bacteria membranes are not a pure lipid membranes. In fact, bacterial membranes and biomembranes in general are considered highly heterogeneous and dynamic structures, where lipids, proteins and other biomolecules interact dynamically. Even so, the electrical conductivity of a healthy and intact bacterial membrane is still considered to be very low. Since both the cytoplasm and medium contain electrolytes, the insulating membrane ends up acting like a capacitor (ie. an insulating layer separating two conducting solutions). To keep the model as simple as possible we omit the effects of the ECM at low frequencies and the effects of the parasitic capacitance at higher frequencies. These effects may influence the impedance response of the bacteria depending on the chosen frequencies. The impedance of Z (as shown in figure 2.6) is illustrated as being higher than Z_0 at low frequencies and drop to being lower than Z_0 when the membrane capacitance is short circuited. This is true if the resistance of the cytoplasm is lower than the corresponding volume of water that it replaces. Interestingly, while the differential modulus ($Z - Z_0$) appear similar to that of Z , the differential argument changes much more significantly compared to its non-differential counter-part.

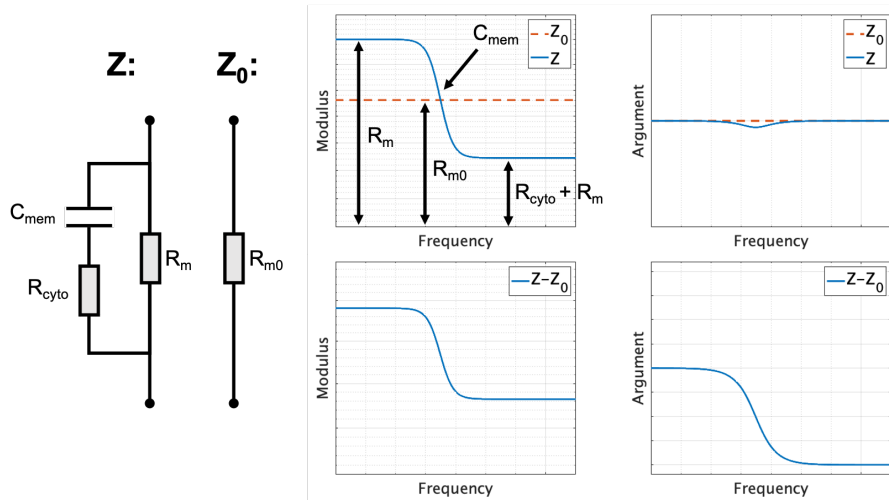


Figure 2.6: Simplest ECM of a cell suspended in medium between two electrodes (Z) and the corresponding electrode set without a cell (Z_0). Also shown is an illustration of the frequency dependent modulus and argument of the impedance of Z and the differential modulus and argument ($Z - Z_0$). The impedance of Z is illustrated as being higher than Z_0 at low frequencies and drop to being lower than Z_0 when the membrane capacitance is short circuited.

The cytoplasm consists of 80% water with various inorganic ions giving it conductivity, but also holds a number of different enzymes, nutrients, and the DNA of the bacterial

cell. The permittivity of these other biomolecules can affect the overall permittivity of the cytoplasm, and values of ~ 60 have been used for modelling [14, 36]. Bacteria can regulate the ionic content of the cytoplasm through e.g. osmoregulation [57] in response to external condition in order to survive which will lead to changes in the conductivity of the cytoplasm. This can happen slower over longer time as a response to changing growth conditions or very quickly if the environmental conditions rapidly change. Figure 2.7 illustrates how the impedance response of the ECM shown in figure 2.6 would change if the conductivity of the cytoplasm changes. It is especially interesting to notice the significant shift in differential argument when the impedance amplitude of Z crosses that of Z_0 and that the differential amplitude of $1 \times R_{cyto}$ and $20 \times R_{cyto}$ is very similar. This will become important later where we will use the differential argument to differentiate bacterial cells and particles based on their effective conductivity compared to the surrounding medium (ie. the relationship between the amplitude of Z and Z_0).

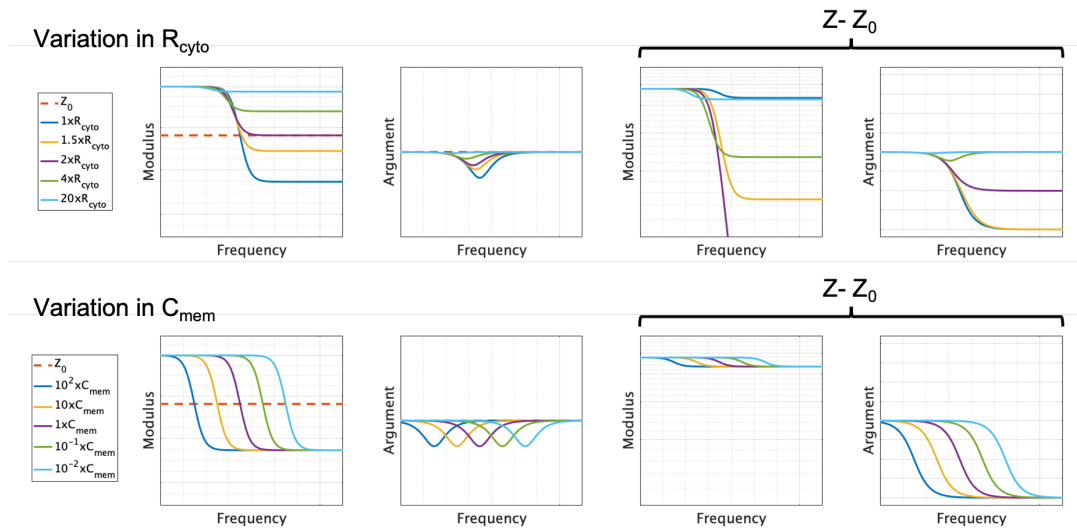


Figure 2.7: Impedance response of a single electrode set Z and the differential impedance $Z - Z_0$. The frequency dependent impedance response is plotted with variation in the cytoplasm resistance and membrane capacitance.

2.3.4 Model with bacteria with a perforated membrane

As previously discussed, the electrical resistance across an intact biological membrane is considered to be very high. However, perforation of the membrane (e.g. caused by inactivation agents like alcohol or antibiotics) will lower the membrane resistance as illustrated in figure 2.8. As the membrane resistance drops we see a change of both modulus and argument in the lower frequency range. Because the membrane capacitance is already short-circuited at higher frequencies it does not matter much in this frequency range when the membrane resistance drops. Again, it is interesting to note that the differential argument shifts significantly as the impedance of Z changes from being higher to lower than Z_0 .

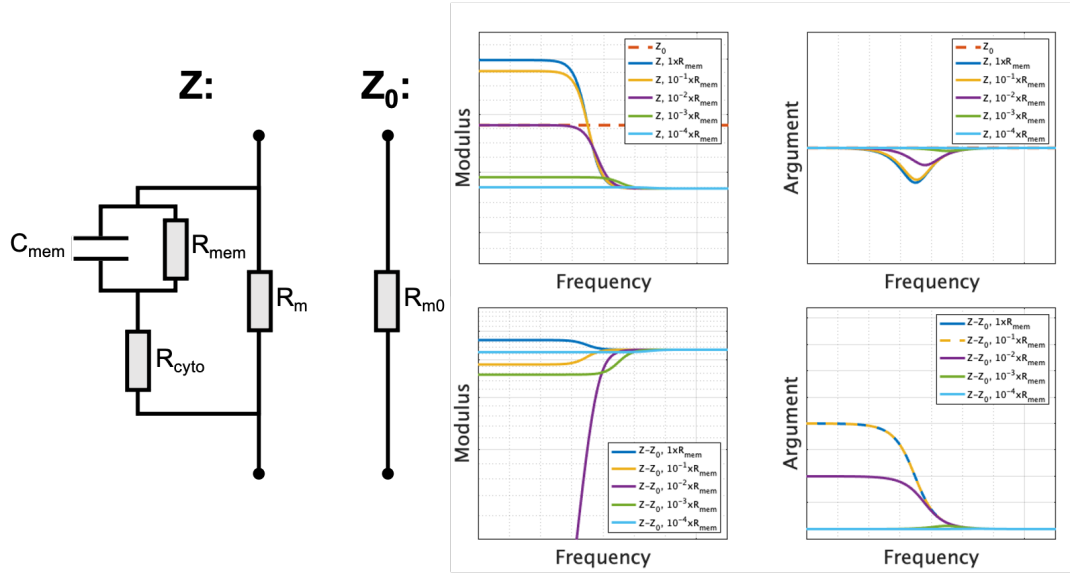


Figure 2.8: Impedance response as a function of membrane resistance for the single electrode set Z and the differential impedance $Z - Z_0$.

2.3.5 Quantitative evaluation of the ECM

While our discussion has focused more on the qualitative interpretation of various equivalent circuits, it is possible to use the equivalent circuits to make quantitative predictions of the impedance if the values or expressions for the individual components is known. For example, Morgan et al. [58] have derived equations based on Maxwell Mixture Theory for the resistance and capacitance of the medium and for the membrane capacitance and the cytoplasmic resistance. The model they use is a spherical cell with one membrane suspended between two electrodes.

$$R_m = \frac{1}{\sigma_m} \frac{1}{(1 - 3\Phi/2)} \frac{1}{l\kappa} \quad (2.30)$$

$$C_m = \epsilon_\infty l\kappa \quad (2.31)$$

$$C_{mem} = \frac{9\Phi R C_{mem,0}}{4} l\kappa \quad (2.32)$$

$$R_{cyto} = \frac{4 \left(\frac{1}{2\sigma_m} + \frac{1}{\sigma_{cyto}} \right)}{9\Phi} \frac{1}{l\kappa} \quad (2.33)$$

with

$$C_{mem0} = \frac{\epsilon_{mem}}{d} \quad (2.34)$$

$$\epsilon_{\infty} = \epsilon_m \frac{2\epsilon_m + \epsilon_{cyto} - 2\Phi(\epsilon_m + \epsilon_{cyto})}{2\epsilon_m + \epsilon_{cyto} + \Phi(\epsilon_m + \epsilon_{cyto})} \quad (2.35)$$

where C_{mem0} is the specific capacitance of the membrane, d is the thickness of the cell membrane and ϵ_{∞} is the permittivity at infinite frequency.

2.4 Chapter summary

In this chapter, the concepts of impedance has been introduced together with the material properties conductivity (σ) and permittivity (ϵ). We also introduced the frequency dependent complex permittivity and discussed how it can be used in effective medium approximations (such as Maxwell Mixture Theory) to calculate the impedance of a particle or bacteria suspended in an electrolyte medium between two electrodes.

The basic structure of bacteria was presented with particular focus on the differences between gram positive and gram negative bacteria. Gram negative bacteria has a three layered envelope structure with a thin peptidoglycan layer sandwiched between two lipid membranes, while gram positive have a thicker peptidoglycan layer encapsulating a single lipid membrane. This difference is particularly interesting since the electrically isolating lipid membranes play a crucial role in the impedance response of the bacteria.

This role was illustrated using a number of different equivalent circuit models where the bacteria envelope (including the membrane) was represented by a capacitor and the electrically conducting cytoplasm in the core of the bacterium was represented by a resistor. It was considered how the membrane capacitor shielded the cytoplasm at lower frequencies forcing the current to pass through the electrolyte around the bacterium, but as the frequency increased was bypassed and allowed probing of the cytoplasm. We saw how the differential impedance between an electrode set with a bacterium present and one with only electrolyte differed from that of just a single electrode set. This was especially apparent when the effective impedance of the bacterium changed from being higher than the surrounding medium to lower (or vice versa), for example when the frequency was increased and the membrane capacitor was short circuited, but also when the membrane resistance was lowered e.g. due to membrane perforation.

3 The impedance flow cytometer

This chapter will introduce the important parts and components of BactoBox together with the concepts and ideas needed to understand how they work.

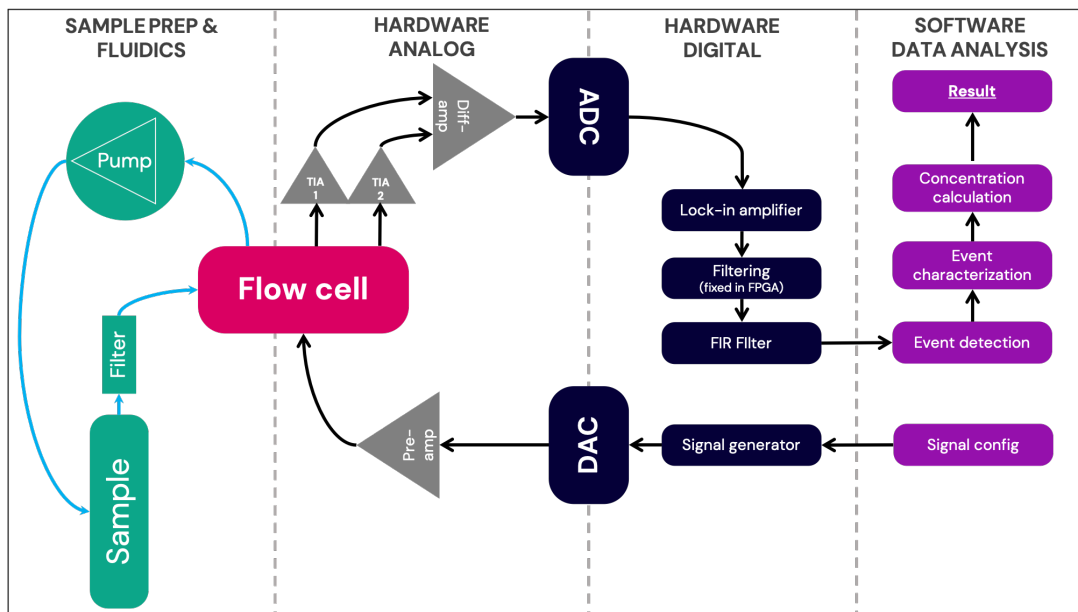


Figure 3.1: Flow diagram of the flow cytometer functionality

Figure 3.1 shows a functional diagram of the components of BactoBox divided into four areas (sample prep and fluidics, analog hardware, digital hardware and software) marked in different colours. Furthermore, the most important part of BactoBox, the flow cell or microfluidic chip, makes up the fifth area. The diagram in figure 3.1 only shows the primary functionality relevant to the measurement of bacteria and omits several auxiliary functions that are important to the actual operation of the device such as pump controls, display drivers, file management, etc. In the following sections we will go through the 5 areas and discuss the functionality and interface between them.

The sample prep and fluidics area is concerned with how the sample enters and exits the flow cell. The primary components are the sample vial, the pre-filter, the pump and the flow cell it self. The sample prep and fluidics area is discussed further in section 3.2.

The flow cell is the heart of the flow cytometer. It is a microfabricated microfluidic chip that contains the detection electrodes needed for impedance measurements of single bacteria. The flow cell interfaces with both the fluidic system and the analog electronics. The flow cell is discussed further in section 3.1.

The hardware (or electronics) is divided into two areas; analog and digital. The purpose of the analog electronics is primarily amplification of the detection signal before and after the flow cell. The digital hardware consists of a lock-in amplifier implemented on a field

programmable gate array (FPGA) where the detection undergoes several treatment steps. The electronics are discussed further in section 3.3.

Finally, the data analysis area is where the final data treatment happens. It is also here that the event detection is performed and here where the final concentration of bacteria is calculated. The data analysis is discussed further in section 3.4.

Before we go into more detail about each area of the device, let us take a look at BactoBox itself. During the span of this project BactoBox has been under constant development, which means that hardware and software has been continuously updated, however the basic functionality has been kept the same. One major hardware update has been done about halfway through the project (in late 2019), where the hardware components were unified on one PCB. Before this change the hardware was separated on several PCBs (e.g. the analog amplification circuit, i.e. TIA, was placed on a separate PCB). This pre-production version of BactoBox can be seen in figure 3.2. In Figure 3.2a, the outside of BactoBox is shown. Four buttons underneath the display control the basic functionality (measure, stop, empty and clean). The flow cell and flow cell cover are removed so that the fluidic and electrical interface between BactoBox and the flow cell can be seen. Figure 3.2b shows the inside of the pre-production BactoBox, including the peristaltic pump, the TIA, a Red Pitaya (an embedded device that combines a computer with ARM processor, an FPGA and a electronic board with ADCs and DACs) and connection boards. Later, in chapter 5, 6, 7 and 8, I will specify in the beginning of each chapter which BactoBox version has been used to collect the experimental data. The version before the hardware revision will be called v1 and the one after the revision will be referred to as v2.

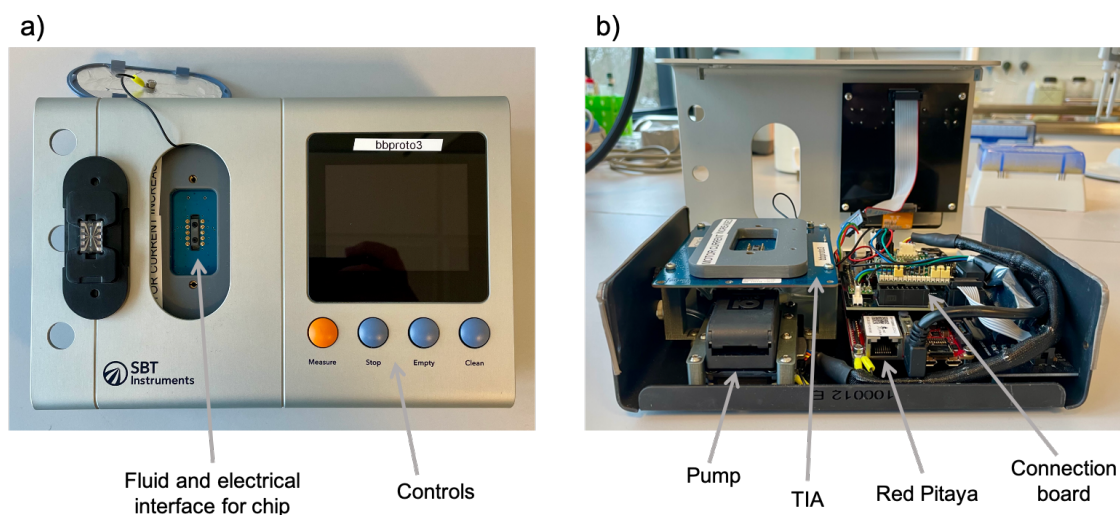


Figure 3.2: Image of Bactobox prototype v1. a) shows the outer shell with the user interface, buttons, fluidic and electronic connections for the flow cell. b) Inside of the v1 Bactobox.

Figure 3.3 shows Bactobox after the hardware unification. The outside remains essentially the same, but the inside is significantly cleaner. The Red Pitaya was replaced by a custom design (designed by TekPartner A/S, Herlev, Denmark) implementing the Zynq-

7000 SoC from Xilinx (San Jose, CA, USA) with software programmability and hardware programmability (in the form of an FPGA) very similar to the Red Pitaya. In figure 3.3a the external sample connections are also seen. A cap with tubing connected is secured at the top of a plastic vial placed in one of the three available sample notches.

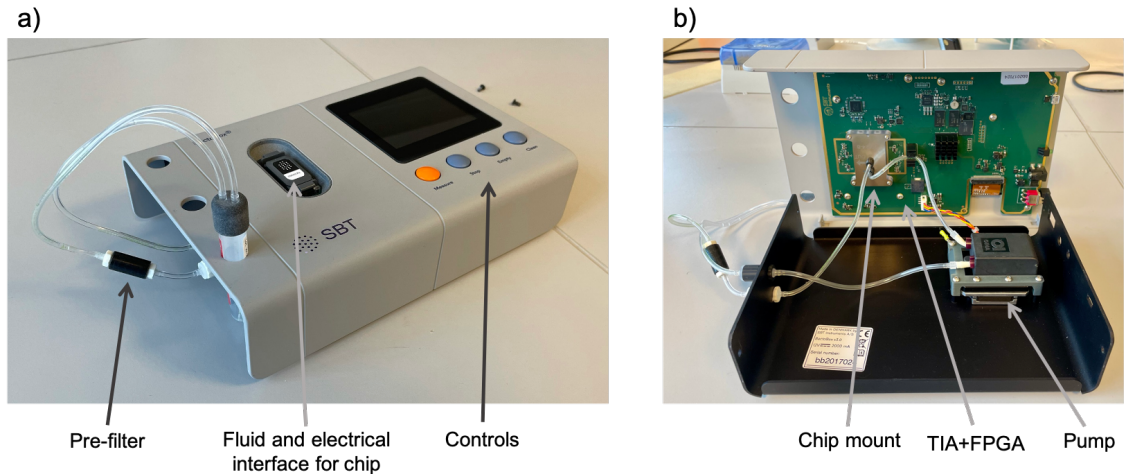


Figure 3.3: Image of Bactobox prototype v2. a) Outside of the device b) Inside of the v2 Bactobox.

3.1 Flow cell

The flow cell is the heart of the impedance flow cytometer. It is a microfabricated microfluidic chip and is therefore often referred to as the "microfluidic chip" or just the "chip". The reason it is also called the "flow cell", is to avoid confusion with electronic chips and microchips when discussing the device as a whole.

3.1.1 Electrode design

The majority of the literature available on design and fabrication of microfluidic chips for impedance flow cytometry focuses on the design of the micro-electrodes. The dimensions and configuration of the electrodes significantly influence the sensitivity.

Fundamentally, there are two ways to design the micro-electrodes: co-planar electrodes or frontfacing electrodes (illustrated in figure 3.4). In a co-planar electrode design all electrodes are fabricated on the same substrate (typically on the bottom of the detection channel). Usually the excitation voltage is applied to a centre electrode and the corresponding current is measured on two electrodes on either side of the input electrode. In a front-facing electrode design the electrodes are fabricated on both the top and bottom substrate. Different variations of input and output exist, but the most straight forward configuration is to apply the excitation voltage to the electrodes on the top of the channel and measure the corresponding current on the electrodes on the bottom. A significant challenge when fabricating front-facing electrodes is to align the top and bottom electrodes with each other. Co-planar electrodes, on the other hand, are easier to fabricate but suffer from larger variation in electric field across the measurement channel leading to lower sensitivity [25]. The chips used in this project all have a front-facing design.

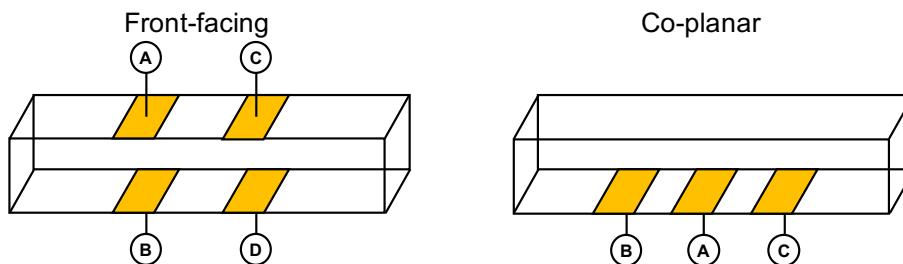


Figure 3.4: Illustration of front-facing and co-planar electrode designs. In the front-facing design, a voltage is applied to the top electrodes (A and C) and the resulting current measured on the bottom electrodes (B and D). For the co-planar design the voltage is applied to the center electrode (A) and measured on the adjacent electrodes (B and C).

3.1.2 Overall design

The microfluidic chips used in this project all have the same overall footprint. They are 10 mm x 15 mm x 1.4 mm, and made of two pyrex glass substrates bonded together by a 10 μm thick polymer spacer layer. The chip has two symmetrical detection sites on either side, each site has four detection electrodes (two on the top and two on the bottom) separated by the spacer layer in a front facing configuration. Each site is connected to 5 electrode pads near the edges of the chip for external connection (see figure 3.5). A large channel runs parallel to the length of the chip with an interchangeable inlet/outlet at either end. In some designs this channel is separated from the detection channel by a layer of polymer and in others they are in direct fluid connection with each other (more on that below). We will refer to the larger channel as the "bypass channel" since only a fraction of the liquid running through this channel pass between the detection electrodes. Practically this means, that the chip is less likely to clog, since larger particles and other debris can pass through the bypass channel instead of being forced through the much smaller detection channel. It also means that the pump used to inject fluid through the chip can run at much higher flow rates than what would otherwise be possible, which makes constructing the external fluidic connections much easier. A polymer structure in the middle of the bypass channel (often referred to as "the island") distributes the flow between the two measurement sites. The size of the island determines the relative volume of liquid running through the detection channel and bypass channel.

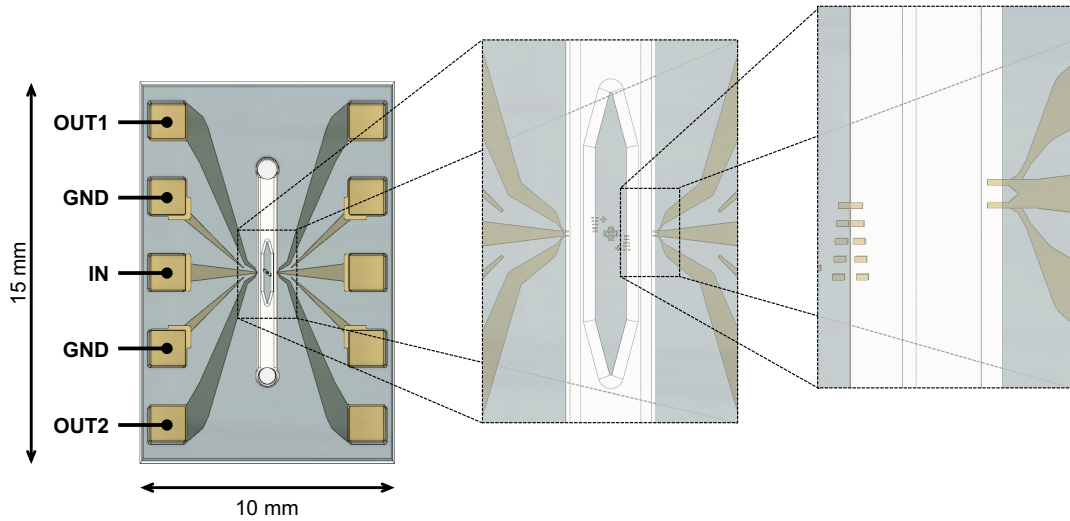


Figure 3.5: Top view of flowcell. The flow cell measures $10\text{ mm} \times 15\text{ mm}$ and has 2 mirrored sets of electrode connections on either side for signal input (IN), two for grounding (GND) and two signal outputs (OUT1 and OUT2). The electrode pads connect to electrode vias on the chip that ends up at the measuring sites on either side of the channel. The channel has an inlet and outlet at either end. In the center of the chip, a structure (referred to as the "island") splits the flow to the two measurement sites.

3.1.3 Specific designs used in this project

Two specific chip designs were used in this project; Design F and Design Q with dimensions as seen in figure 3.6. The two designs share the same electrode pad layout, inlet and outlet design and bypass channel design, but differ in how the detection electrodes and detection channel are designed.

Design F (figure 3.6c and 3.6d) has a detection channel that is physically separated from the bypass channel by a layer of SU8 extending in between the top and bottom wafers. All four channel boundaries are closed. The detection channel is $10\text{ }\mu\text{m} \times 10\text{ }\mu\text{m}$, with $10\text{ }\mu\text{m}$ long electrodes separated by $15\text{ }\mu\text{m}$ edge to edge.

In design Q (figure 3.6a and 3.6b) there is no physical boundary between the bypass channel and the detection channel, meaning that one of the four channel boundaries is open. The electrode width extends $25\text{ }\mu\text{m}$ into the detection channel and stops $10\text{ }\mu\text{m}$ from the edge of the bypass channel. The electrodes are separated by $29\text{ }\mu\text{m}$ edge to edge.

Figure 3.6e shows a microscope image of the cross sectional view of the bypass and detection channel of a chip that has been cut in half. The chip shown has an open boundary between the bypass and detection channel.

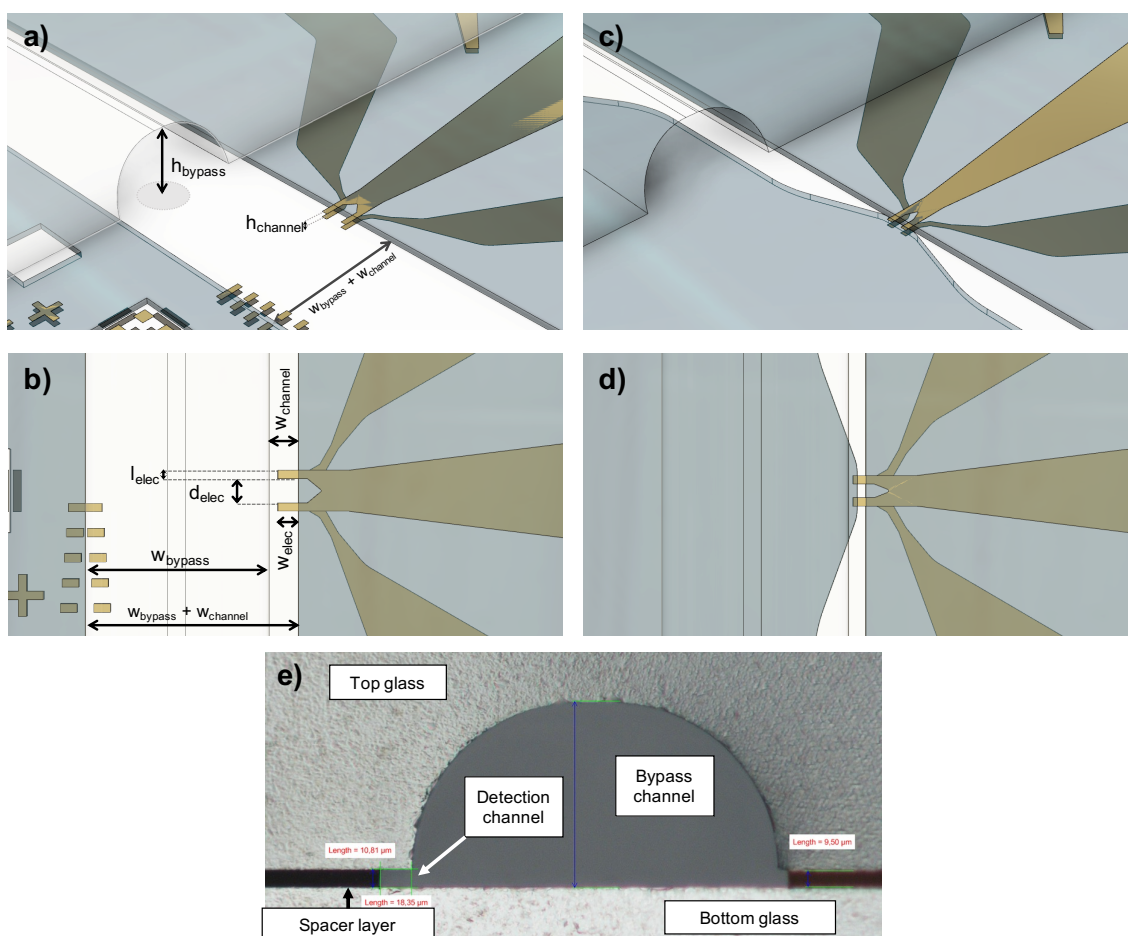


Figure 3.6: Two different chip designs were used for experiments, design Q, design F. a) Schematic of chip design Q with dimensions indicated. For visualization purposes the top substrate has been partially removed to increase clarity, in reality it extends the full length of the channel. b) top view of chip design Q with dimensions. c) schematic of chip design F. d) top view of chip design F. e) microscope image of the cross sectional view of the bypass and detection channel.

The dimensions of the microchannel and electrodes for the two designs can be seen in table 3.1.

The advantage of the open boundary design of design Q is that it limits the likelihood of channel clogging, since clusters of bacteria or other debris cannot get stuck as easily in the narrow entry of the channel. Furthermore, the wider electrodes in design Q allow for more liquid to flow between the electrodes, improving the detection statistics. The disadvantage of design Q is that the open boundary allows a decreasing gradient of electric field perpendicular to the flow direction, leading to a degree of positional dependence of the peak height on the boundary and higher variation in peak height from identical particles across the cross section. To illustrate this point, figure 3.7 shows the relative change in peak height (compared to the peak height in the middle of the channel, $z = 5\mu\text{m}$, and $5\mu\text{m}$ from the inner wall, $y = 5\mu\text{m}$) simulated using COMSOL for a $2\mu\text{m}$ polystyrene

2. Bypass flow: This region comprises the flow in the bypass channel. It is fluidically connected at both ends to the inlet/outlet and runs parallel to the detection flow. The dimensions and the flow velocity are both high. The Reynolds number in this region is in the transition region between laminar and turbulent flow.
3. Detection flow: The flow in this region carries the bacteria that will flow between the detection electrodes. This is the most microfluidic region of the chip. The flow is strictly laminar. The region is in contact with both the inlet/outlet region and the bypass region.

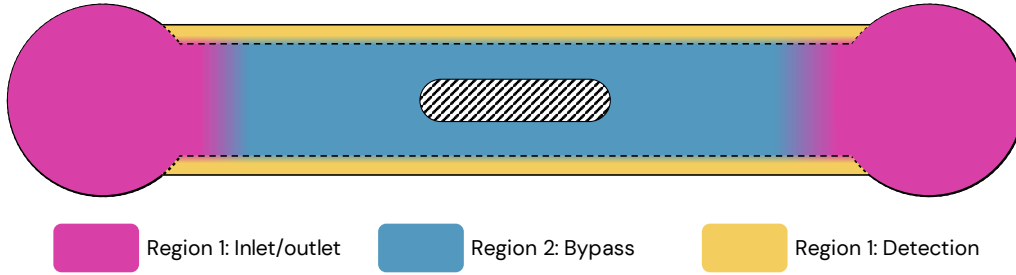


Figure 3.8: The flow on the microfluidic chip can be segmented into 3 regions as illustrated here.

Laminar flow and Reynolds number

In the limit of flow velocities the non-linear term of the Navier-Stokes equation can be neglected [59]. When this happens, the flow is can be described as "Stokes flow" and the value of the so-called Reynolds number (Re) is $\ll 1$. The Reynolds number is defined as

$$Re \equiv \frac{U \rho D_h}{\eta} \quad (3.1)$$

Where U is the characteristic fluid velocity, ρ is the fluid density, η is the dynamic viscosity of the fluid and D_h is the hydraulic diameter of the channel given as $\frac{4A}{P}$. When $Re \ll 1$, the viscous term of the Navier-Stokes equation dominates, whereas for $Re \gg 1$ the inertia term is the most important. Laminar flow is flow in which the fluid travels smoothly or in regular paths with little or no mixing. Laminar flow is contrasted with turbulent flow where the flow becomes chaotic and undergoes irregular fluctuations and mixing. Whether the flow is laminar or turbulent can be evaluated by examining the Reynolds number with laminar, turbulent and transition regimes defined as shown in table 3.2. It is important to note that Stokes flow implies laminar flow but not the other way around, meaning that inertia can play a role in laminar flow, for example during sudden changes in flow direction.

Table 3.2: Flow regimes based on Reynolds number [60]

Regime	Reynolds Number Range
Laminar	$Re < \sim 2000$
Transition	$\sim 2000 < Re < \sim 4000$
Turbulent	$Re > \sim 4000$

In a fluid containing a suspension of particles, the particles may be subjected to drag and lift forces, that scale with the fluid properties and dynamics. A particle Reynolds number (Re_p) exists based on the regular Reynolds number, that defines the relation between inertial and viscous interactions on particle behaviour [61]

$$Re_p = Re \frac{a^2}{D_h^2} = \frac{U \rho a^2}{\eta D_h} \quad (3.2)$$

where a is the particle diameter. When $Re_p \ll 1$ the viscous forces dominate. If Re_p is of the order of 1, the particles may experience inertial focusing. Inertial focusing means that a combination of lift and wall forces, focus the particles in the flow specific positions in the channel cross section [62]. For example, particles flowing in a circular channel will focus into a ring called the Segre-Silberberg annulus, while particles in a square channel will focus into four equilibrium positions near the walls of the channel. In both chip designs used in BactoBox, this can be problematic, especially if it occurs in the bypass channel and limits (or prevents) the entry of particles into the detection channel.

Table 3.3 shows the Reynolds numbers calculated for the detection region and bypass region for design Q and design F. The flow rates for the 2 regions are calculated using the relationship between hydraulic resistances discussed in the following section (see table 3.4), with a total flow rate of 1 ml/min through the entire flow cell.

Table 3.3: Calculated Reynolds numbers (eq. 3.1 and 3.2) for the detection channel and bypass channel with $a=1e-6$ m, $\rho=1000$ kg/m³ and $\eta=1e-3$ Ps. Channel dimensions from table 3.1 and a total flow rate of 1 ml/min separated into the bypass and detection channel using the ratios from table 3.4

		Detection	Bypass	Inlet/outlet
Design Q	Re	0.260	120.26	N/A
	Re_p	0.004	0.04	N/A
Design F	Re	0.086	120.30	N/A
	Re_p	0.034	0.04	N/A

We can see that the Reynolds number in the detection channel is <1 for both designs and we expect laminar flow in this region. In the bypass channel the Reynolds number is significantly higher, but still well below the transition region to turbulent flow. We therefore also expect the flow in the bypass channel to be laminar. We can also see that inertial focusing is not expected in either of the two regions, since the particle Reynolds number is <1 .

Hydraulic resistance

The "island" in the center of the chip distributes the flow between the two detection sites. The relation between the hydraulic resistance of the detection channel and the bypass channel determines how much of the volume passes between the detection electrodes. The relationship between the pressure drop (Δp) and the flow rate (Q) in a straight microfluidic channel is described by the Hagen-Poiseuille law

$$\Delta p = R_{hyd} \times Q \quad (3.3)$$

where R_{hyd} is the hydraulic resistance. Note the equivalence of pressure, flow rate and hydraulic resistance in the Hagen-Poiseuille law to voltage, current and resistance in Ohms law. The Hagen-Poiseuille is accurate when the flow is laminar flow and the channel is straight and can therefore be used to estimate the flow-rates in the bypass and detection channels.

Calculating the hydraulic resistance for the channels on the chips with design F (closed detection channel boundary) is fairly straight forward. The hydraulic resistance for the square detection channel (10 μm x 10 μm) [59] is calculated using

$$R_{hyd,sq} = 28.4\eta L \frac{1}{h^4} \quad (3.4)$$

where η is the dynamic viscosity, L is the channel length, h is the height and w is the width of the channel. The hydraulic resistance of the half circular bypass channel is calculated using the more general expression

$$R_{hyd,bypass} = 2\eta L \frac{P^2}{A^3} \quad (3.5)$$

Where P is the circumference of the perimeter of the channel cross-section and A is the area of the channel cross-section found as

$$P_{bypass} = 2w + \pi h - 2h \quad (3.6)$$

$$A_{bypass} = (w - 2h)^2 + \frac{1}{2}\pi h^2 \quad (3.7)$$

For design Q, the definitions become a little less clear. The fact that there is no physical boundary between the detection and bypass channel complicates the evaluation, e.g. when does the bypass channel start and the detection channel end? Here we choose to act as if an ultra thin boundary exist on the edge of the electrodes and approximate the hydraulic resistance as that of a rectangular channel given by

$$R_{hyd,sq} = \frac{12\eta L}{1 - 0.63(h/w)} \frac{1}{h^3 w} \quad (3.8)$$

Table 3.4 summarizes the relationship between the hydraulic resistances of the bypass and detection channels of the two flow cell designs. It is seen that at a flow rate of 5 ml/min the expected flow rate in the detection channel is around 0.25 $\mu\text{l}/\text{min}$ and 1.1 $\mu\text{l}/\text{min}$ for design F and Q respectively.

Table 3.4: Hydraulic resistances of the bypass and detection channel of design F, calculated using Eq. 3.5 and 3.4, and for design Q, calculated using Eq. 3.5 and 3.8. The flow rate in the detection channel is calculated with the assumption of total flow rate through the flow cell of 5 ml/min.

Flow cell	Bypass resistance	Detection resistance	Fraction in detection channel	Flow rate in detection channel
Design F	1.47×10^{11}	2.84×10^{15}	$\sim \frac{1}{20000}$	$\sim 0.25 \text{ } \mu\text{l/min}$
Design Q	1.47×10^{11}	6.42×10^{14}	$\sim \frac{1}{4500}$	$\sim 1.1 \text{ } \mu\text{l/min}$

3.1.5 Fabrication and materials

The microfluidic chips are fabricated by Micronit Microtechnologies in their cleanroom facilities in Dortmund, Germany. They are fabricated based on a design and specification from SBT Instruments, but we are not directly involved in the fabrication. This section gives a brief overview of how the chips are fabricated and what materials are used, but will not go into process specific details.

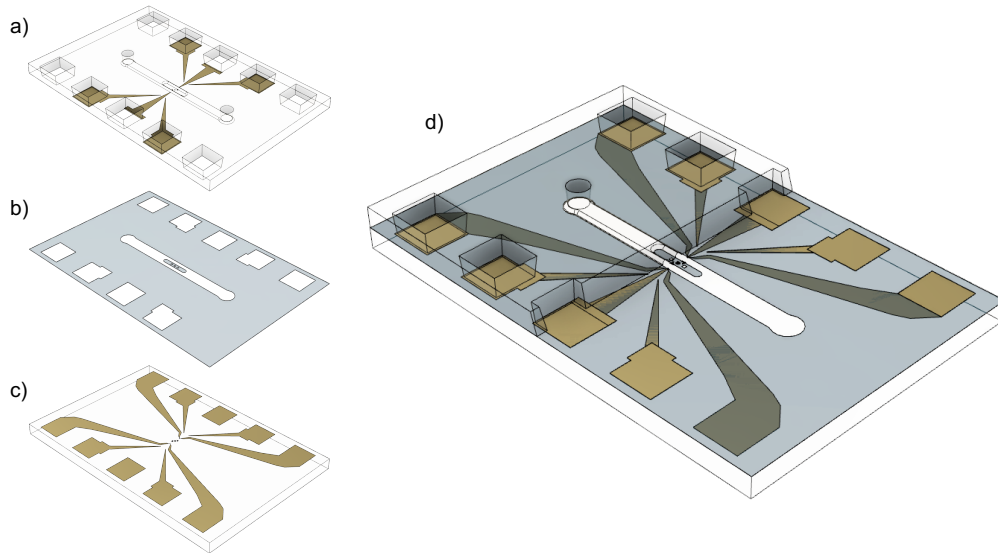


Figure 3.9: Exploded view of the flow cell substrates: a) top substrate, pyrex wafer with sand blasted through holes, fluidic channels etched with hydrofluoric acid and electrodes on the bottom side, b) spacer layer, 10 μm epoxy-based photosensitive polymer spin coated onto the bottom substrate and patterned using UV-lithography, c) bottom substrate, Pyrex wafer with electrodes.

The fabrication process can be split into three steps:

1. Fabrication of bottom substrate

The bottom substrate is a piece of pyrex glass (0.7 mm thick) with patterned electrodes on top as seen in figure 3.9c. The electrodes are patterned using a standard photolithography process with deposition of metal using e-beam evaporation and subsequent lift-off. The electrodes are made of 160 nm platinum with a 10 nm adhesion layer made of tantalum, chromium or titanium. Before metal deposition a recess of 170 nm is etched into the glass

so that the surface is planar and the electrodes do not protrude.

2. Fabrication of top substrate

The top substrate (figure 3.9a) is also a made of pyrex glass with a thickness of 0.7 mm. A 100 μm deep channel is etched into the substrate using an anisotropic hydrofluoric acid etch. Similar to on the bottom substrate, 10 nm Pt-electrodes are patterned on the pyrex with a 10 nm tantalum for adhesion. Because of the uneven topology created by the hydrofluoric acid etch, the photoresist used for the patterning is spray coated unto the substrate for better edge coverage. After electrode deposition and lift off, the back-side of the wafer is covered and holes for fluidic and electrode connections are sandblasted through the pyrex.

3. Bonding of top and bottom substrate

The top and bottom substrate are thermally bonded together with a 10 μm spacer layer (figure 3.9b) made of a photosensitive epoxy based polymer. The polymer is spin-coated onto the bottom substrate and openings for the channels are made using photolithography.

A critical step in the flow cell fabrication is proper alignment of the electrodes on the top and bottom substrate. Misalignment of the electrodes affect the cross sectional area of the channel where it is possible to detect particle transition and it can result in asymmetric transitions. But most of all it may cause an imbalance in the differential current, leading to clipping of the signal on the ADC. This will also be discussed later (section 3.3.1), but in short, the dynamic range of the ADC is -1.6 μA to 1.6 μA . Figure 3.10 shows the resulting changes in differential current due to misalignment and we can see that a misalignment of the top and bottom substrate along the channel of just 2 μm , will cause a differential current of close to 2 μA which is higher than the dynamic range of the ADC.

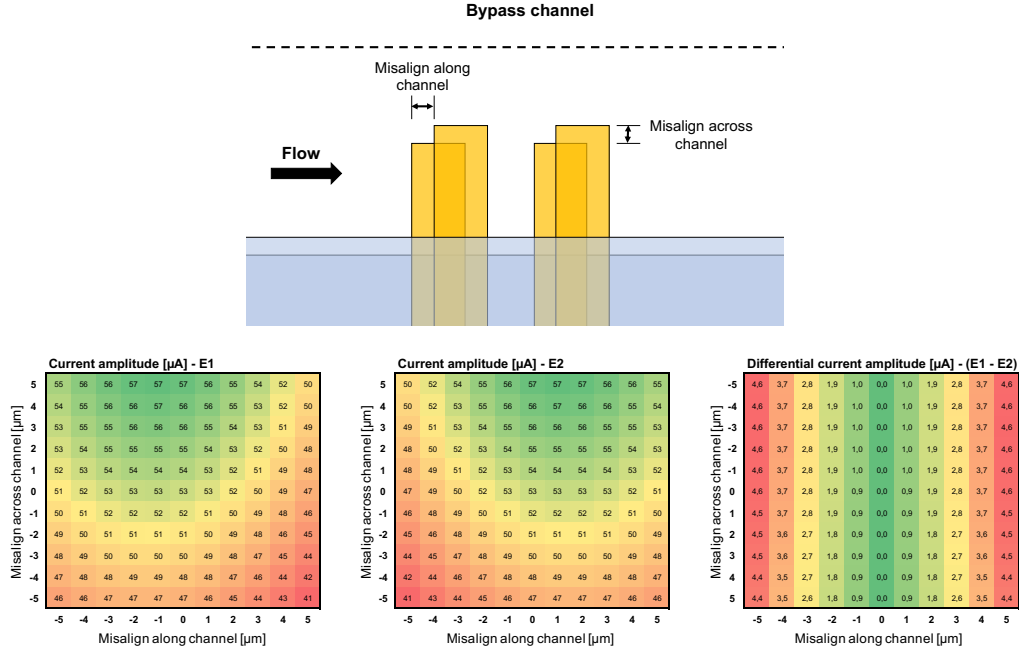


Figure 3.10: (Top) Sketch of the misalignment of the top and bottom substrates. (Bottom) COMSOL simulation showing the effects of misalignment of the top and bottom substrate during bonding. Simulated current amplitude at 366 kHz with misalignment along the channel and across the channel for the first (E1) and second (E2) electrode set and the differential current between the two (E1-E2).

3.1.6 Influence of DEP forces on the detected signal

As mentioned previously, a dielectric particle in a non-uniform electrical field experiences a dielectrophoretic (DEP) force that either repels or attracts the particle in the direction of increasing electric field. The magnitude and direction of the force depends on the medium and particles' electrical properties.

This is also true for particles and bacteria transitioning between the detection electrodes, meaning that the bacteria position and velocity may change during a transition and subsequently affect the detected double gaussian event. The bacteria also experience a strong drag force in the direction of the flow, which under normal flow conditions satisfies the conditions for Stokes drag, and therefore can be described for a sphere by

$$F_{d,sphere} = 6\pi\eta RU \quad (3.9)$$

and for a prolate ellipsoid moving lengthways with the flow by

$$F_{d,ellipsoid} = \frac{8\pi\eta R_1 U}{2 \ln \left(\frac{2R_1}{R_2} \right) - 1} \quad (3.10)$$

where η is the dynamic viscosity and U is the flow velocity relative to the bacteria. The drag force is considerably bigger than the DEP force along the channel, but because of the

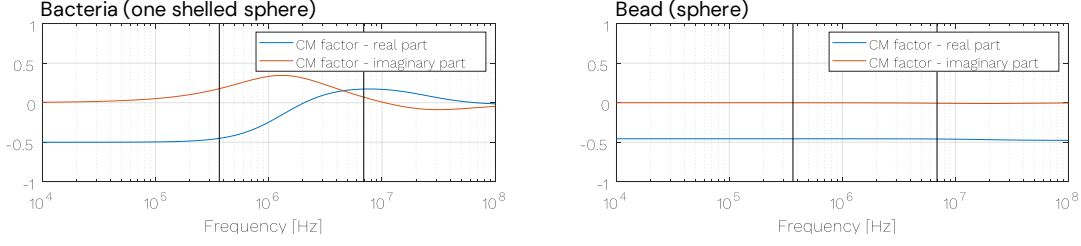


Figure 3.11: Calculated real and imaginary parts of the CM-factor for a one-shelled sphere and homogeneous sphere as a function of frequency.

parabolic flow profile caused by the no slip boundary effect, even small shifts in position across the channel can change the velocity of the bacteria. This is particularly true for flow cells with open boundary detection channels (i.e. design Q), where DEP forces may not only change the vertical position of the bacteria, but also push it from side to side during transitions near the open boundary. Figure 3.11 shows the real and imaginary part of the Clausius-Mossotti factor calculated for a homogeneous sphere (representing a polystyrene bead) and a one shelled sphere (representing a bacterial cell).

The vertical lines in the plot indicate the experimental frequencies of BactoBox (366 kHz and 6.9 MHz) and we see that the DEP force will be negative at both frequencies for the bead and negative at the low frequency but positive at the high frequency for the bacteria. In a case such as this with multifrequency DEP it has been shown that an effective frequency dependent Clausius-Mossotti factor (CM_{eff}) can be defined that determines the resulting DEP force on the bacteria [63]. Besides the frequency this factor also depends on the relative amplitudes of the AC signals. For the case of dual frequencies (f_1 and f_2) and a single pair of electrodes the effective Clausius-Mossotti factor can be calculated as

$$CM_{eff} = \frac{CM_{f_1} \times |E_{f_1}|^2 + CM_{f_2} \times |E_{f_2}|^2}{|E_{f_1}|^2 + |E_{f_2}|^2} \quad (3.11)$$

If we also assume that the fields have equal amplitude, it further reduces to

$$CM_{eff} = \frac{CM_{f_1} + CM_{f_2}}{2} \quad (3.12)$$

A particle tracing simulation is set up in COMSOL (COMSOL Multiphysics) in order to investigate the influence DEP forces will have on particle transitions through the flow cell. The particles are released from one end of a rectangular channel with two sets of electrodes on the top and bottom of the channel resembling the electrodes from flow cell design Q. The particles are released from one end in a grid as shown in figure 3.12 and are affected by a drag force (built in COMSOL force defined using Stokes law) and a multifrequency DEP force defined using Eq. 2.16 and Eq. 3.12. The drag force arises from a velocity field through the channel with no-slip boundaries on the top, bottom and inner wall (on the electrode side). The wall opposite the electrodes has a slip boundary to mimic the open boundary of the detection channel in flow cell design Q. Two DEP forces

are defined, one for a homogeneous sphere with the electrical properties of polystyrene beads and one calculated for a sphere with one shell and the electrical properties of a cell membrane and cytoplasm meant to mimic a bacteria. Figure 3.12 shows the particle position in the beginning of the simulation and the position at the end of the simulation for both beads and bacteria. The effect of the DEP forces is larger on the beads since they experience negative DEP at both the low and high frequency. The bacteria still experience net negative DEP (negative DEP at the low frequency but positive DEP at the high frequency), but to a smaller degree than the beads. The path of beads and particles in the center of the channel is unchanged, while especially particles transitioning on the edge of the electrodes experience large displacements.

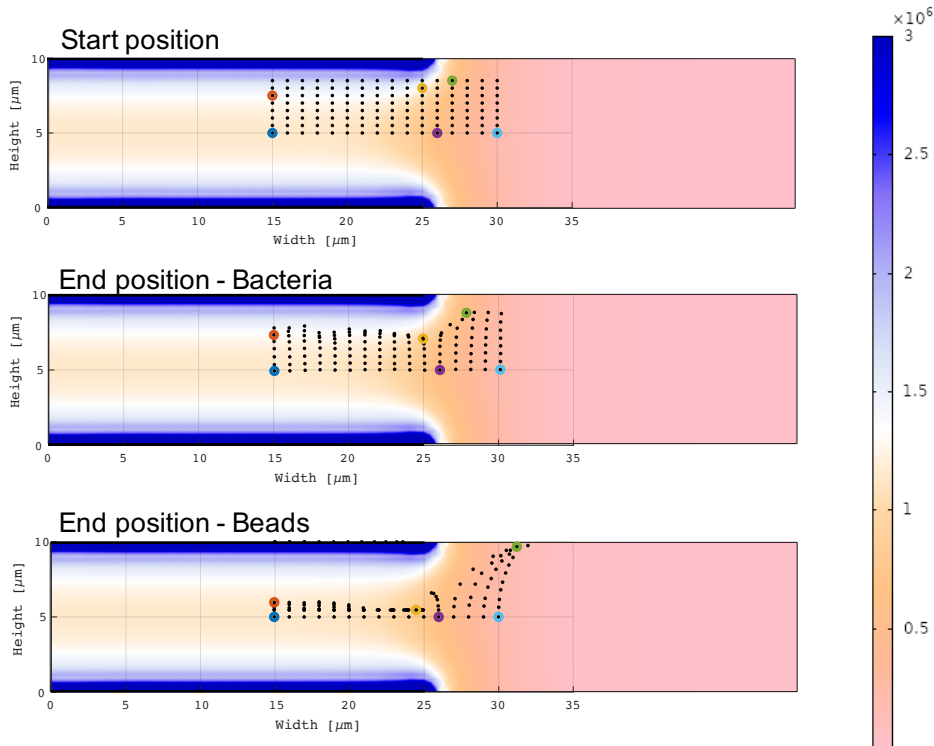


Figure 3.12: COMSOL simulation showing the effect of DEP forces on particle positions. Particles are released from a 8×16 grid. The color gradient indicate the strength of the electric field normal to a cross-sectional plane perpendicular to the flow direction on the edge of the electrode. Six particle positions are marked with colours (red, blue, purple, yellow, green, teal). The transition profiles of these events are shown in figure 3.14.

In order to investigate the influence of the displacement caused by DEP, an electrical simulation was set up in COMSOL where a sphere with the dielectric properties of a polystyrene bead was sequentially moved along the particle path predicted by the particle tracing simulation both with the DEP active and with it deactivated in the simulation. A potential of 16 Vpp with a frequency of 366 kHz was applied to the electrodes on the top of the channel and the differential current between the two electrodes on the bottom of the channel was evaluated for each particle position. It is expected that the displacement

of the particles will cause changes to the peak height during a transition as the particle is pushed away from the path with high electric field, but also in the time it takes a particle to transition from one electrode set to the next (the transition time) for example when particles are pushed into the higher velocity flow in the center of the channel. In figure 3.13, the simulated responses for particles with 6 different cross sectional starting positions are shown.

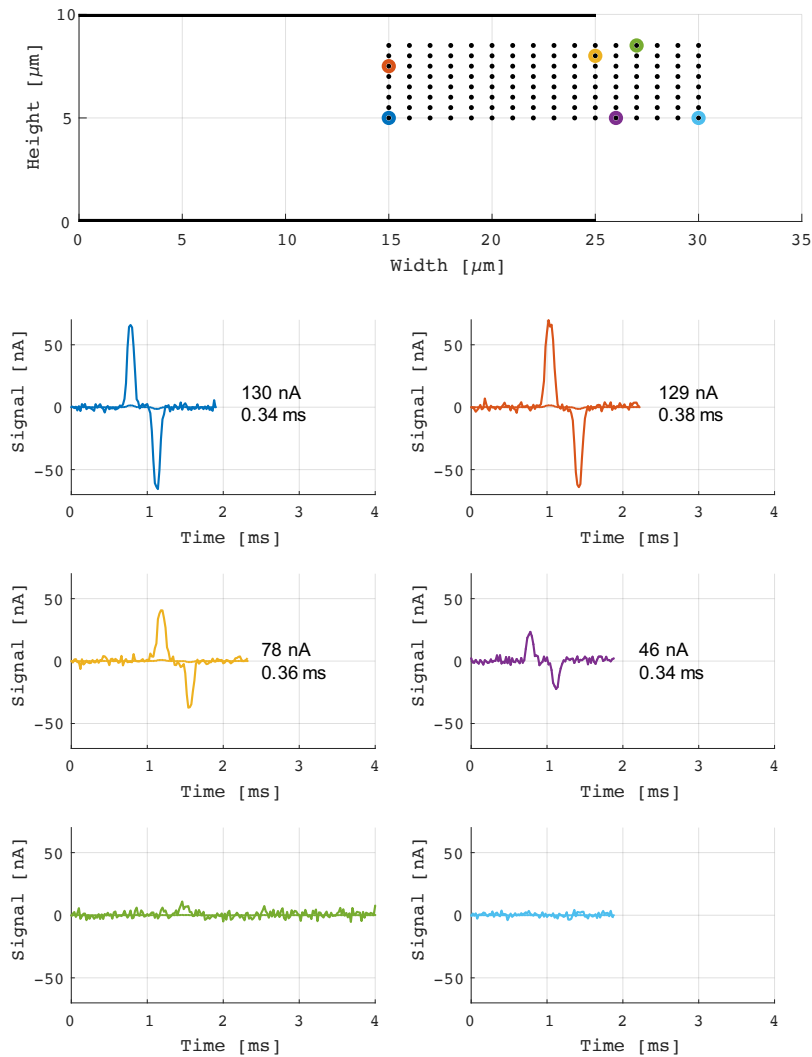


Figure 3.13: COMSOL simulation of transition of particles with different cross sectional positions. 6 transitions indicated by colors (blue, orange, yellow, purple, green, turquoise) with start positions also indicated by color. The thick line is the real part of the signal and the thin line is imaginary part. Note that none of the event have an observable response in the imaginary part of the signal.

Figure 3.14 shows the real part of the differential current for 3 of the particle transitions,

with and without active DEP forces. It is seen that particle in the center of the channel and away from the electrode edge (blue start position) does not experience any displacement and no change in either peak height or transition time. However, for particles not in the center of the channel (such as the particle in the red starting position) we see a minor change in peak height of 3% but a significant change of 20% in transition time, as the DEP force pushes the particle down and into the high velocity flow in the center of the channel. The biggest change is seen for particles on the edge of the electrodes (such as the one in the yellow starting position) where a change in peak height of 29% is seen along with a change in transition time of 40%.

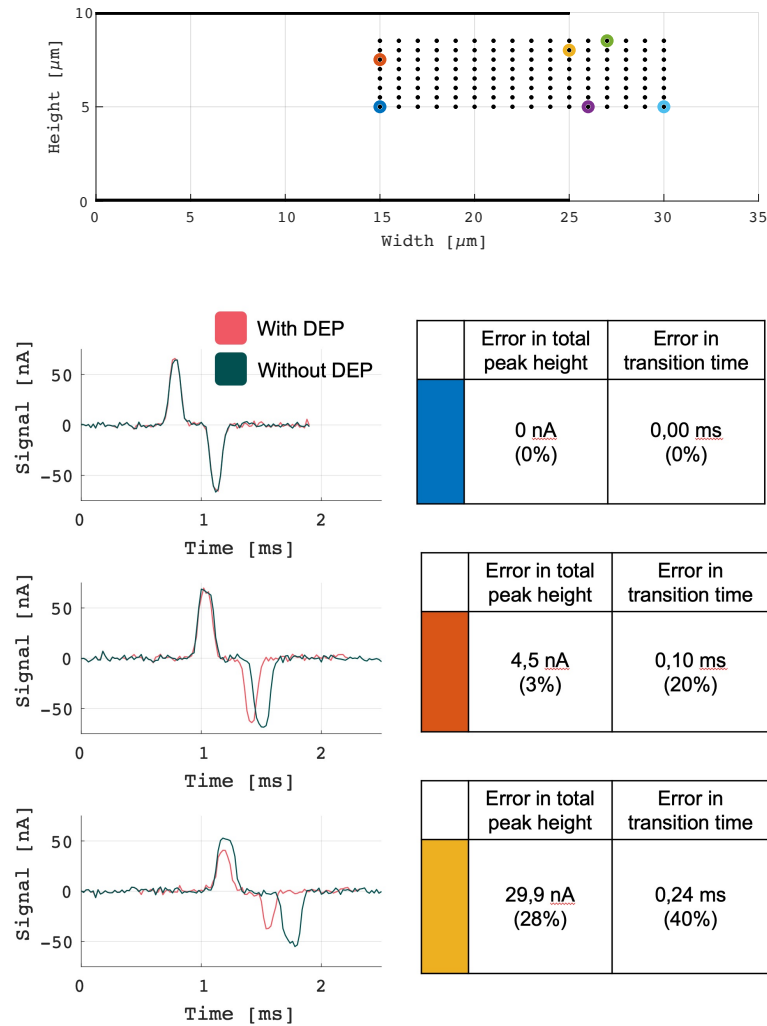


Figure 3.14: Comparison between particle transitions of 3 particles (blue, red and yellow) simulated with and without an applied DEP force. The table shows the difference in peak height and transition time with and without the DEP force applied to the particle.

In this section we have looked at the effects that DEP forces can have on the particle transitions in during measurements with BactoBox. We have seen that the DEP forces

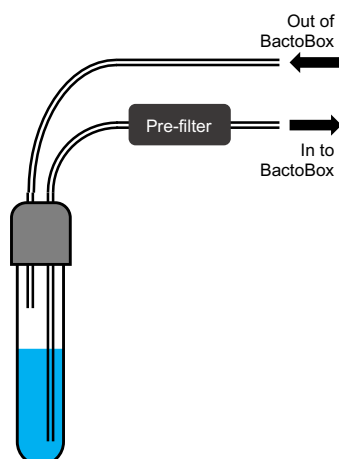


Figure 3.15: Flow diagram of the flow cytometer functionality

on bacteria are smaller than for e.g. polystyrene beads, since the bacteria experience a combination of positive and negative DEP forces at the two frequencies used that cancel each other out. Even so, the DEP forces will affect the cross sectional position of a transitioning particle or bacterium, especially if it is on the edge of the electrode. Simulations on polystyrene beads showed that, in a worst case scenario, the differences in peak height and transition time, with and without DEP force applied, was 29% and 40% respectively.

3.2 Sample and fluidics

The fluidics system brings the liquid from the sample vial through the microfluidic chip for analysis. The fluidics system consists of five parts: the microfluidic chip (as discussed in detail above in section 3.1), the sample vial, the tubing, the pre-filter and the pump. The flow cell is the interface between the electronics and the sample as seen in figure 3.1.

Sample vial

The sample vial is a clear, tubular, 6 ml plastic vial with a rounded bottom. Two pieces of tubing of unequal length are attached through the lid of the vial as shown in figure 3.15. One piece is long enough to reach the bottom of the vial, while the other sits about 1 cm into the vial.

To transfer the liquid into the tubing the pump creates a vacuum in the long piece of tubing which then sucks the liquid into the device, through the chip, and back out the short piece of tubing into the sample vial. To empty the fluidic system the pump changes the flow direction and air is sucked in through the short piece of tubing causing the liquid sample to be pumped back into the sample vial.

Pre-filter

As the sample leaves the sample vials it passes through a pre-filter that removes major debris and particles (clothes fibers, smalls hairs, etc.) from the sample flow. The pre-filter is a single layer mesh with a pore size of 38 μm . The pore size is smaller than the critical dimension on the chip ($\sim 100 \mu\text{m}$) and helps prevent clogging of the chip and other narrower parts of the flow path. When the measurement is done and the flow direction is reversed, debris and particles caught in the pre-filter is flushed back into the sample vial. Complete

or partial clogging of the pre-filter can occur with very dirty samples. In this case, the measurement results are invalid and the pre-filter needs to be cleaned or replaced.

Pump

The pump in BactoBox is a peristaltic pump. In a peristaltic pump a rotating set of rollers compress a flexible tubing, pushing the liquid in the tubing forward. A peristaltic pump has two main advantages as a pump in Bactobox. First of all the sample never leaves the tubing. This means that the chance of contamination is low and that sample wont come into contact with delicate valves that clog easily. Secondly, it is very easy to reverse the flow direction and as discussed above, this is essential for emptying the fluidic system of liquid. The disadvantages of the peristaltic pump is that it is physically large and that the rollers pushing liquid through the tubing creates a pulsating flow. This pulsation can be seen in the detection signal and creates an uneven base line for the detection of events. It can be mitigated by having softer tubing in the system absorbing the pulses or by filtering out the pulsation in the detection signal (see section 3.3.3).

3.3 Electronics

The electronics of the impedance flow cytometer, while not exactly considered "core technology", affect the functionality and measurement capability of BactoBox significantly. Without a basic understanding of the function of the electronics, it is easy to accidentally misinterpret the data output from the flow cytometer. Most of all, it is important to understand what changes in impedance are related to the sample of interest and which are artifacts (intentional or otherwise) from the electronics design. In this section we will first discuss the generation (in the digital domain) and amplification (in the analog domain) of the measured signal. Then we will discuss the function of the digital lock-in amplifier and the subsequent signal processing. This will not be a detailed technical walk-through of the implementation of the electronics (neither analog or digital) since that is outside the scope of this thesis, but more of a presentation and discussion of the function of the electronics parts.

3.3.1 Signal generation and analog amplification

The generalised signal path is shown in figure 3.16. A sine wave with two frequencies is generated and converted to an analog signal in the digital-analog-converter (DAC). Both the chosen frequencies and the amplitude of each frequency can be chosen in software. BactoBox currently has a limit of maximum 2 simultaneous frequencies. The amplitudes are chosen as a fraction of the total output with scaling values for each frequency (i.e. scale 0.5 is 50% amplitude of the max DAC output). The combined scale of the two frequencies cannot surpass 1.0.

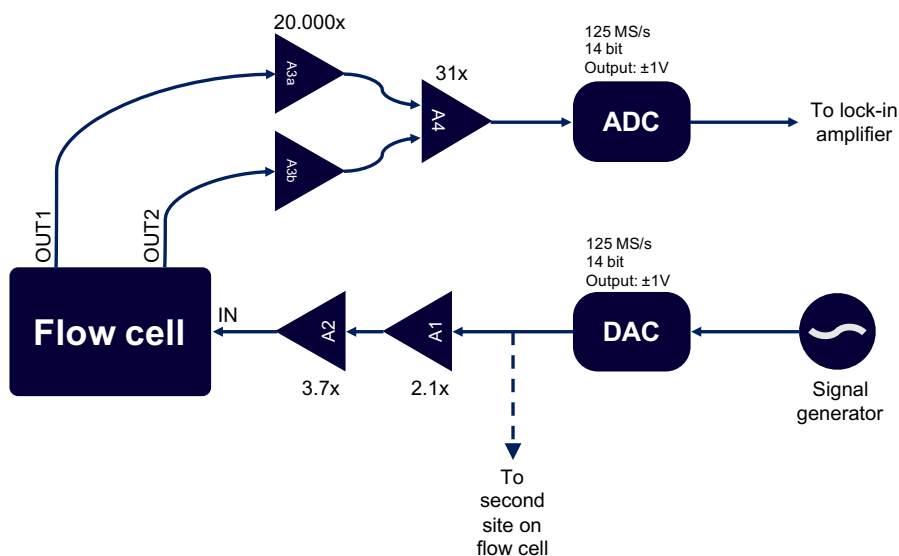


Figure 3.16: Flow diagram of the electronics functionality. The sine wave signal is generated and converted to an analog signal. The signal is amplified in two steps (A1 and A2) before entering the flow cell. The outputs from the two detection electrodes (A1 and A2) are amplified in two TIAs (A3a and A3b) and subsequently subtracted before being converted back into a digital signal. A duplicate signal path exists for both detection sites on the flow cell.

Before entering the flow cell, the signal is amplified through a series of 2 operational amplifiers (op amps). An op amp is basically a voltage amplifying device designed so that external components such as resistors and capacitors can be used to control the level of amplification. Here the signal goes through 2 amplification steps (A1 and A2 in figure 3.16) before it reaches the flow cell. Ideally, the total amplification after the two steps is 7.77x for a total peak-to-peak voltage of ~ 15.5 Vpp. However, while ideal op amps have infinite bandwidth (ie. uniform amplification at all frequencies) this is not the case in practice. To understand how this affects the signal in BactoBox, the voltage was measured at multiple frequencies (from 30 kHz to 25 MHz), one frequency at a time with the amplitude scaling of the output set to 1. The measured voltage as a function of frequency is shown in figure 3.17, and it is seen that the signal is attenuated when the frequency surpasses ~ 3 MHz. For experiments with BactoBox, frequencies of 366 kHz and 6.9 MHz are almost exclusively used and the peak-to-peak voltage is $\sim 30\%$ lower at 6.9 MHz compared to 366 kHz. If equal amplitudes of the 2 frequencies is desired, the scaling factors can be set so that the initial amplitude at 6.9 MHz is higher than for 366 kHz to compensate.

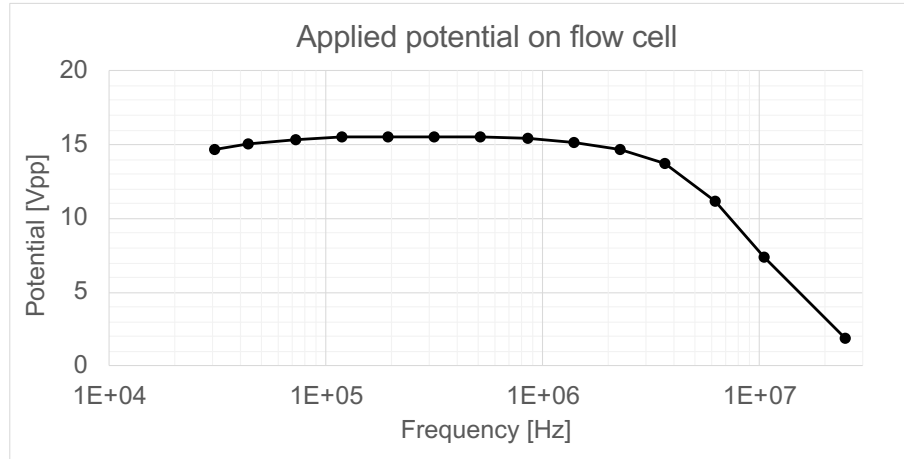


Figure 3.17: Measured potential applied to the flow cell after pre-amplification (after A2)

After exiting the chip, the signals from each of the two detection electrodes (OUT1 and OUT2 in figure 3.16) are again amplified, this time through a pair of transimpedance amplifiers with 20.000x amplification each. A transimpedance amplifier (or TIA) is a current to voltage converter and the amplification is high in order to amplify the small changes in current caused by the transitions of particle or bacteria in the flow cell.

After the TIA conversion, the signals from the two electrode sets are subtracted from each other and the differential signal is again amplified before it is converted back into a digital signal for further processing. The total signal amplification after the chip is 620.000x which means that the dynamic range of the DAC of $\pm 1V$ corresponds to a current difference between the electrode sets from the flow cell of $\pm 1.6 \mu A$. This is more than enough to handle the amplitude of a transitional event. The amplitude of a bacterial transition is usually on the order of 10 nA per frequency, which means that after amplification it will be ~ 6 mV.

However, if the differential current between the electrode sets exceeds the limit of the dynamic range it will lead to clipping of the signal, which in turn will ruin the proper and accurate detection of particles and bacteria. This becomes especially relevant if the top and bottom electrode are not aligned properly, as discussed in section 3.1.5.

3.3.2 Lock-in amplifier in FPGA

The lock-in amplifier [64] is extremely useful for detection of small signals in noisy environments at a defined frequency band. Lock-in amplifiers are very versatile and have been used as AC voltage and AC phase meters, noise measurement units, impedance spectrometers, network analysers and spectrum analysers.

Invented in the 1930's and subsequently commercialised in the mid 20th century, traditional lock-in amplifiers used analog frequency mixers and RC filters for the demodulation. However, modern instruments (including BactoBox) implement the functionality using fast digital signal processing e.g. on an FPGA.

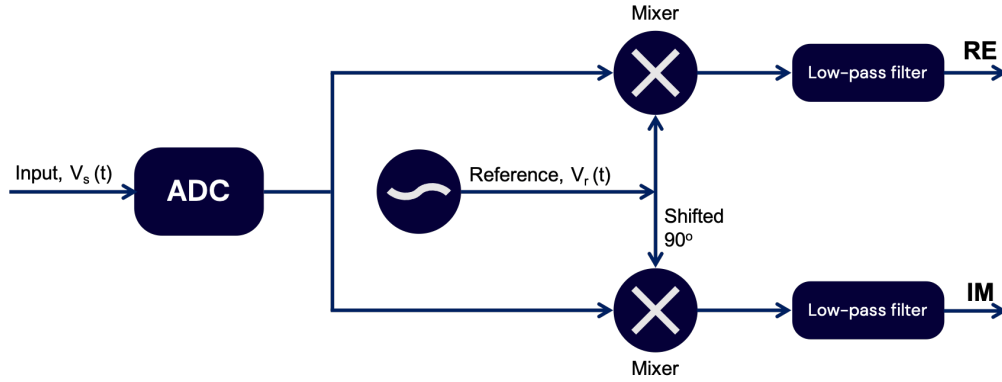


Figure 3.18: Block diagram of lock-in amplifier

The basic principle of the lock-in amplifier is sketched in figure 3.18. An input signal (V_{in}) is a mix of a signal of interest (V_s) with an amplitude (A_s) and a frequency (ω_s)

$$V_{in}(t) = V_s(t) + V_n(t) \quad (3.13)$$

$$V_s(t) = A_s \cos(\omega_s t) \quad (3.14)$$

A reference signal (V_r) is multiplied with the input signal in a frequency mixer giving a new mixed signal (V_{mix})

$$V_r(t) = A_r \cos(\omega_r t) \quad (3.15)$$

$$V_{mix}(t) = A_s A_r \cos(\omega_s t) \cos(\omega_r t) \quad (3.16)$$

Using a well known trigonometric identity

$$\cos(\omega_s t) \cos(\omega_r t) = \frac{1}{2} [\cos((\omega_s - \omega_r)t) + \cos((\omega_s + \omega_r)t)] \quad (3.17)$$

and tuning the reference signal so that ω_r is equal to the frequency of the signal of interest (ω_s), the mixed signal can be rewritten as

$$V_{mix}(t) = \frac{1}{2} A_s A_r [1 + \cos(2\omega_r t)] \quad (3.18)$$

By removing the $2\omega_r$ part of the mixed signal using a low-pass filter we end up with a frequency independent expression that is directly related to the amplitude of the signal of interest

$$V_{mix}(t) = \frac{1}{2}A_sA_r \quad (3.19)$$

The same expression can be derived using complex numbers, even if the reference signal and signal of interest are not in-phase

$$V_s(t) = A_s \cos(\omega_s t + \phi) = \frac{1}{2}A_s \left[e^{i\omega_s t + \phi} + e^{-i\omega_s t + \phi} \right] \quad (3.20)$$

With the complex reference signal

$$V_r(t) = A_r [\cos(\omega_r t) - i\sin(\omega_r t)] = A_r e^{-i\omega_r t} \quad (3.21)$$

Mixing the reference and signal of interest

$$V_{mix} = V_s(t)V_r(t) = \frac{1}{2}A_sA_r \left[e^{i((\omega_s - \omega_r)t + \phi)} + e^{-i((\omega_s + \omega_r)t + \phi)} \right] \quad (3.22)$$

$$V_{mix} = V_s(t)V_r(t) = \frac{1}{2}A_sA_r \left[e^{i\phi} + e^{-i(2\omega_s t + \phi)} \right] \quad (3.23)$$

And filtering out the frequency dependent part

$$V_{mix} = V_s(t)V_r(t) = \frac{1}{2}A_sA_r e^{i\phi} \quad (3.24)$$

From here it is trivial to find the real and imaginary parts of the signal. In practice the low-filtering in BactoBox consists of a moving average filter (MA), followed by a third order Cascaded-Integrator-Comb-filter (CIC). As the signal exits the lock-in-amplifier it has been down sampled to 366 kHz. The exact implementation and further detailing of the function of these filters is outside the scope of this thesis.

3.3.3 Signal filtering

Before the signal is delivered for processing in software it undergoes an additional series of filtration steps. First, a series of 4 half-band filters down samples the signal in order to lower the sample rate to make it more manageable for the CPU and to increase the effective bit range of the signal. Secondly (and since it is user configurable, more interestingly) a final FIR-filter is present for removing the remaining signal noise. In BactoBox, this filter has 141 coefficients and is currently designed using an implementation of a Wiener Filter [65]. Wiener filters are based on a statistical approach, while typical filters are designed based on a frequency response approach. For BactoBox this means that the filter design is based on empirically obtained distributions of variables related to the transitions, such as transition time, time between events, peak height and event width. It is a bandpass filter designed to remove high frequency ambient noise, as well as remove the low frequency pulsation introduced by the rollers on the peristaltic pump.

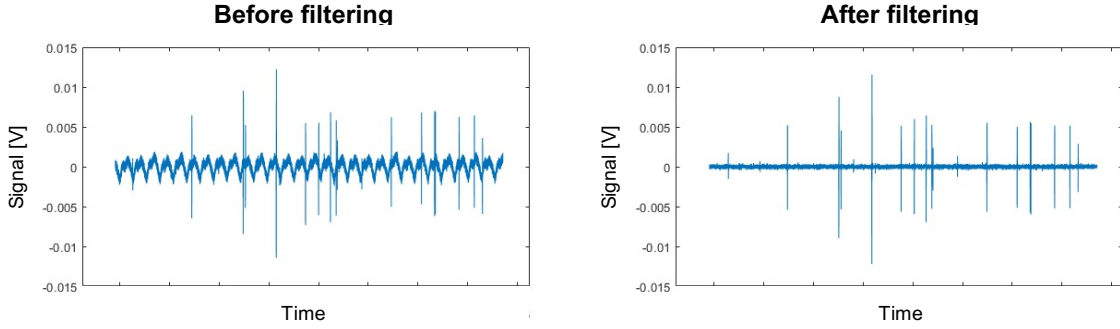


Figure 3.19: Data stream before and after the FIR-filter is applied

Again, it falls outside the scope of this thesis to discuss the design of this filter in detail, but I will stress that its presence is crucial for cleaning up the signal before event detection. Figure 3.19 shows a single data stream of recorded data with and without the final FIR filter applied. It is seen how the filter effectively removes noise and stabilizes the data stream for further analysis.

3.3.4 Frequency dependence compared to ZI impedance spectroscopy

When measuring the impedance response of bacteria samples with the BactoBox we want as little influence on the recorded signal as possible from sources that are not the bacteria themselves. For BactoBox, the measuring characteristics of the electronics, particularly the analog electronics, significantly affect the measured signal. In figure 3.20 the current measured during a frequency sweep of a flow cell with air and various dilutions of PBS performed using both BactoBox and using an impedance spectroscopy (HF2IS) from Swiss company Zurich Instruments is shown. The BactoBox used for the sweeps was modified so that only the output signal from one electrode was measured. To keep the signal amplitude within the dynamic range of the ADC, the amplitude was lowered to 2% of the usual amplitude. The measurements from the Zurich spectroscopy appear smoother because they are recorded after demodulation of the signal, while the BactoBox sweeps are read out directly from the input signal on the ADC. The measurements are performed on flow cells with design Q (see section 3.1).

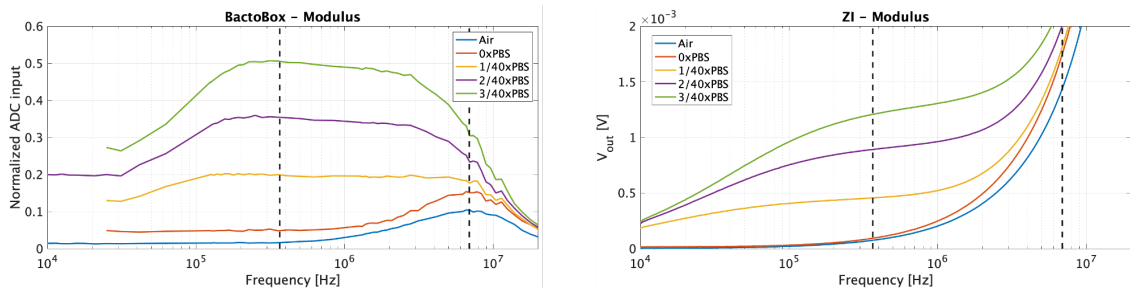


Figure 3.20: Frequency sweep with BB and ZI scope with air, 0xPBS, 1/40xPBS, 1/20xPBS and 3/40xPBS injected through the chip. Striped vertical lines indicate the two main measurement frequencies used for experiments with BactoBox (366 kHz and 6.9 MHz).

As discussed in section 2.3.2 we expect the current to increase (ie. the impedance to drop) as the frequency is increased and the electrical double layer on the electrode surface is bypassed. We then expect a flat region where the conductivity of the medium dominates the current. Finally we expect the current to increase further as the impedance drops when the parasitic and medium capacitance influence the signal. This is essentially what we observe when measuring the frequency dependent current using ZI impedance spectroscopy. We see an increase in current (in figure 3.20 shown as the voltage measured after the conversion in the TIAs) in the low frequency range, a flat region where samples with higher concentrations of PBS conducts more current, and another increase in current in the higher frequencies. For BactoBox, we also observe an increase in current in the low frequency followed by a flat region. However, we begin to see a drop in current amplitude at higher frequencies. In fact, we see that the signal is notably attenuated at the frequency used as the high frequency for experiments (6.9 MHz). This means that bacteria and other events detected in the high frequency will appear smaller than they actually are.

3.4 Software and signal analysis

In essence the analysis of the raw signal from the impedance flow cytometer is meant to do two things: to count and characterise events. In the BactoBox this is done with a set of algorithms designed and implemented at SBT Instruments. While optimization and tuning of these algorithms have not been a primary purpose of the PhD-project, it is still important to understand on a general level how the signal is analysed. In this section I will go through the data treatment from "raw" input data (ie. data stream output from the lock-in amplifier) to refined output data (such as concentrations or event information). Details of the implementation of the algorithm in terms of programming will not be described here. Instead a high level explanation of the analysis path will be given.

3.4.1 Event detection

The signal delivered to the algorithm (as seen in figure 3.19) is often referred to as the "raw" data stream (or signal), since it is what is recorded and saved when performing the impedance measurements. In reality we now know that this data has already undergone significant processing. Since we are only interested in the part of the signal during a transition of a particle or bacteria, the raw signal is analysed using a set of algorithms developed at SBT Instruments. Here I will provide an overall description of the algorithm functionality. For customers of BactoBox the algorithm is running live during a measurement, but for experiments performed in this PhD project the entire raw signal is saved and analyzed after the measurements are done. This means that the raw signal can be reanalyzed if needed at a later stage. This subsequent analysis is done using a combination of a custom program running the detection algorithm and various MATLAB scripts used for processing of the data. In order for the algorithm to also work on live data, the raw signal is cut into chunks of data (500 ms in length) before processing. Each chunk of data is then analysed individually and at the end of the analysis a check for duplicate events at the beginning or end of the chunk is performed. Peaks in the signal are identified using a peak detection algorithm developed by Eli Billauer [66]. The peak detection algorithm requires an initial estimate of the noise in the signal and here the interquartile mean of the entire chunk of data is used. This way of estimating noise (even though the interquartile mean is fairly robust) does depend on the height and number of events in the chunk, meaning that

at high concentrations of particles the algorithm has a tendency to overestimate the noise. In turn this may cause the algorithm to miss smaller events in the data stream. However, overall this has not been found to be a major problem. Some of the peaks found in the raw signal, may not be from actual event transitions, but rather noise (either random or from an external source) in the signal. To mitigate this we take advantage of the fact that we have more than one data stream. By comparing the peaks found in all four data streams (low and high frequency, real and imaginary parts) we can sort out peaks that are only present in one data stream. In BactoBox, the specific requirement is the the peak must be detected in at least two data streams. Furthermore, the peaks are also paired so that a peak is only accepted as a true peak if it has a neighboring peak with the opposite direction within a given time range in either direction of the data stream. If a peak has been correctly paired and identified in two or more data streams the location of the peak can be superimposed on the remaining peak less data streams (as illustrated in figure 3.21) and we call the collective information across all four data streams an 'event'. The orientation (or sign) of the peaks of an event (ie. up-down or down-up) is very important since it holds vital information about dielectric properties of the transitioning particle or bacteria. The orientation depends on the order of the subtraction of the signals from the two detection electrode sets in the analog electronics and on the direction of the flow through the chip. Here we have chosen to define the orientation via the sign of the first peak of the transition.

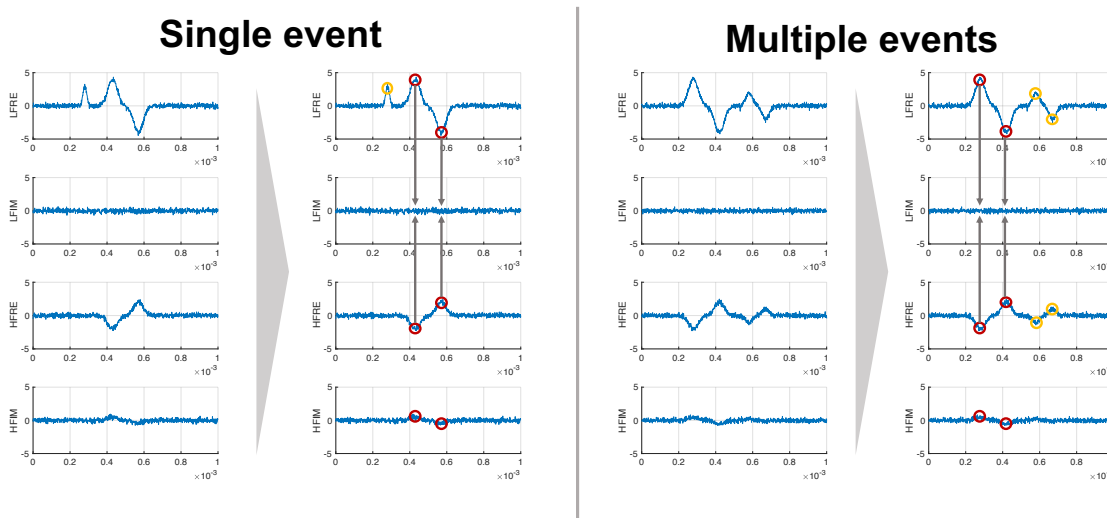


Figure 3.21: Illustration of the choosing and pairing of peaks in the data stream. Single event: the peak in the data are detected in all four data streams. If a peak occurs (shown with red circles) in two or more data streams in the same location and have a pairing partner with opposite orientation within a given time, it is considered a true peak and the pair is classified as an event. In this way false peaks that are not part of a transitions event (yellow circle) is rejected. Events are superimposed on data streams where no peaks where found. Multiple events: If multiple peaks are found in more than two data streams the algorithm employs a winner take all strategy based on parameters such as peak height, symmetry and offset of the peaks. The algorithm only choose an event (here shown with red circles) if it is clearly better than the other (here shown with yellow circles).

If more than two peaks occur close together (either due to noise, but more likely due to multiple transitions between the detection electrodes occurring in close succession) the algorithm can have a hard time deciding which peaks to pair. In the multi-event example given in figure 3.21, there are four potential peaks in the data stream made up of two events close together. It is crucial that the algorithm does not choose to pair the second and third peaks, since this would end up appearing as a single transition with the opposite orientation of the original two. To avoid this, a "clear winner" strategy is chosen, where the algorithm evaluates the possible pairing combinations based on a number of different parameter (peak height, symmetry, offset, etc.) and chooses the best event. In example in figure 3.21 the event comprised of the pairing of the first two peaks would be chosen since it has a higher peak height than the other possible combinations. This also means that the second event will be discarded. If no clear winner can be chosen all of the peaks are discarded. This will lead to an underestimation of events, especially if the concentration of bacteria is high. This is a choice made for BactoBox, since it is better to underestimate the concentration than mischaracterize an event. Based on numerical evaluations performed at SBT Instruments using generated test data where the concentration is known, the detection algorithm starts to under estimate the number of events when the concentration goes above $\sim 3.000.000/\text{ml}$.

Gaps in the argument due to noise

Because the signal is noisy the detected peak height will never actually be zero (see for example the LFIM signal in figure 3.21). This can lead to artifacts in the presentation of measurement data, especially when looking at the argument of the data.

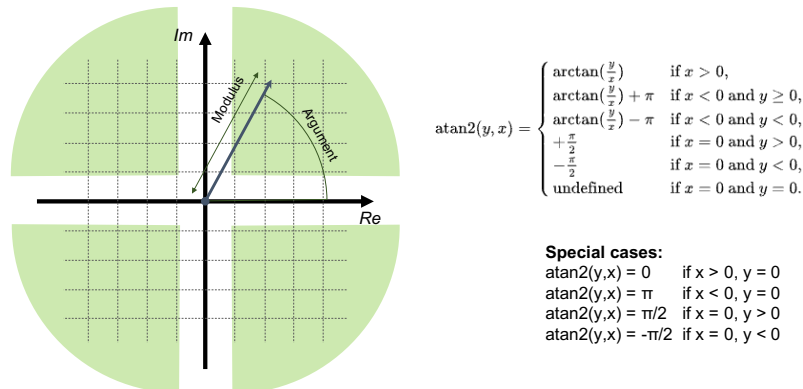


Figure 3.22: Illustration of the "gap" in argument due to noise. Due to noise in the signal the argument can only attain certain values (here shown in green). This is because the real and imaginary parts (x and y) can never be zero due to noise.

An illustration of why this is the case is shown in figure 3.22. In order for the argument to reach values of $0, \pi/2, -\pi/2$ and π , either the real or imaginary part must be 0. This is not possible due to the noise in the signal, and the argument is therefore excluded from attaining certain values. This is especially true when the peak-to-noise ratio is low and means that when plotting the measured impedance data in a scatterplot showing the argument (which we will do a lot), a population of events crossing over $0, \pi/2, -\pi/2$ or π may artificially appear as two separate populations. As such, there is nothing to do about this with the current software implementation, but future versions could include a grading

of the peak values when they approach the noise level to balance this out.

3.4.2 Concentration calculations

A key function of the BactoBox is that it is able to determine the concentration of particles or cells in a sample. In principle this appears straight forward and can be calculated using

$$C = \frac{N}{V} \quad (3.25)$$

where C is the concentration, N is the number of events counted and V is the volume of liquid passed between the detection electrodes during the measurement. The number of counted events is given directly from the event detection. Due to the design of the microfluidic chip and the fact that the exact flow rate from the peristaltic pump is unknown, we cannot directly calculate the volume that has passed between the electrodes. Instead, the average transition time of the events that have passed between the detection electrodes is used to estimate the volume of liquid

$$V = \frac{A \times d_{event} \times T}{k \langle t_{event} \rangle} \quad (3.26)$$

Where A is the cross section of the detection area perpendicular to the direction of the flow (width of the electrode multiplied by the height of the channel), d_{event} is the distance between the peaks of the event, T is the total measurement time, $\langle t_{event} \rangle$ is the inter-quartile average of the transition times of the events, and k is a parameter that compensates $\langle t_{event} \rangle$ due to the parabolic flow in the channel.

The average transition time ($\langle t_{event} \rangle$) can be estimated in a number of different ways (arithmetic mean, median, etc.) depending on the distribution of times. In BactoBox, the inter-quartile mean works well for sorting away outliers and is therefore used.

Compensation for parabolic flow

Since the flow profile in the microfluidic channel is parabolic (due to no slip boundaries) using the inter-quartile average transition time directly for flow rate estimation leads to an over estimation of the actual flow rate. Consider the example shown in figure 3.23. Here a very simple 2D stepwise velocity profile is shown (obviously the real flow does not look like this but it helps to prove the point). To make the example even simpler we assume that the concentration of particles are so that we see exactly 1 particle per second when the flow velocity is 1 m/s (and 2 particles per second when the flow velocity is 2 m/s and so on).

The average flow velocity in this example is 1.29 m/s but the average velocity of the particles is 2.11 m/s.

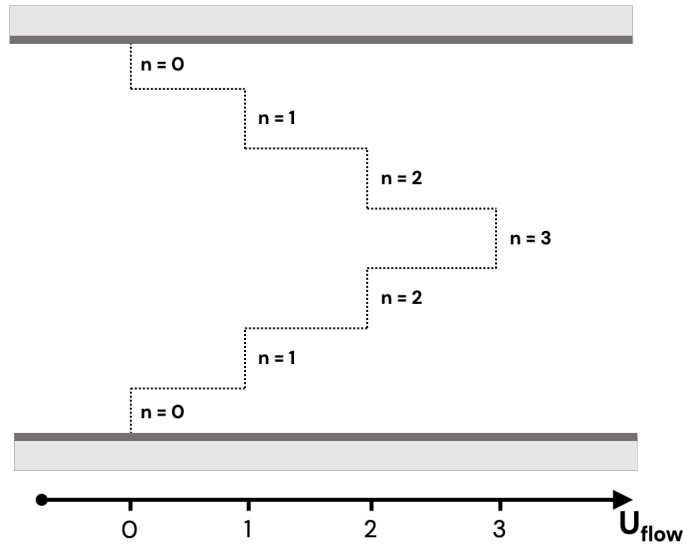


Figure 3.23: Simple example of 2D step wise flow profile with no. of particles (n) per time for each flow rate.

To compensate for this difference we introduce the parameter k

$$\langle U_{flow} \rangle = \frac{1}{k} \langle U_{event} \rangle = \frac{d_{event}}{k \langle t_{event} \rangle} \quad (3.27)$$

$$k = \frac{\langle U_{event} \rangle}{\langle U_{flow} \rangle} \quad (3.28)$$

The example from figure 3.23 can be expanded to the full parabolic flow profile for different channel designs (see figure 3.24) and k can be numerically evaluated. Table 3.5 shows the k -values for chip design F and chip design Q evaluated using MATLAB for compensating using either mean, median or interquartile mean.

Table 3.5: k values for chip design F and chip design Q numerically evaluated in MATLAB using the distributions seen in figure 3.24. The k -values are calculated as the average value of 50.000 events with x and y positions weighted by the distribution and the simple mean of the distribution itself

Flow cell design	k , mean	k , median	k , interquartile mean
Design F - closed boundary, 10x10	1.440	1.526	1.508
Design Q - open boundary, 10x25	1.249	1.373	1.348

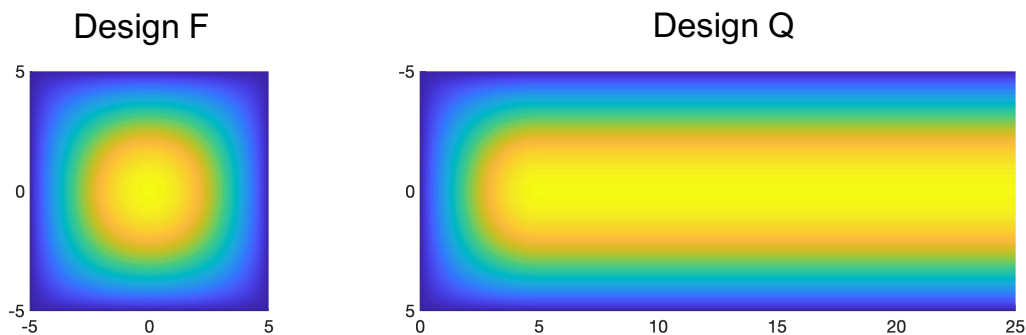


Figure 3.24: Distributions used for flow cell design F and Q to numerically evaluate the flow compensation parameter, k , using MATLAB. Since the particles follow the the distribution is used both for the velocity profile and particle distribution.

3.5 Chapter summary

In this section, the important parts of the impedance flow cytometer developed by SBT Instruments called BactoBox was introduced. First we focused on the flow cell (or microfluidic chip) at the heart of BactoBox. The flow cell is a microfluidic chip made of two pyrex substrates (top and bottom) held together by a 10 μm thick spacer layer made of epoxy polymer. The two flow cell designs used during the PhD project were presented. The two designs share most of their features, a large bypass channel etched into the top substrate with a symmetrical inlet and outlet at either end and 5 electrode connections on either side of the chip. The two designs differ in the design of the detection channel. The first flow cell design (design F) has a 10x10 μm detection channel with closed boundaries on every side, while the second flow cell design (design Q) has an open boundary on one side in direct fluid connection to the bypass channel. This reduces the likelihood of clogging, but also introduces uniformity challenges in the electric field on the edge of the electrode in the cross sectional dimension of the channel.

We briefly discussed the fluidic system employed in BactoBox. A peristaltic pump placed on the back side of the flow cell sucks sample liquid from a sample vial through a pre-filter (38 μm) and through the flow cell.

The electronics used in BactoBox was presented, starting with a discussion of the analog amplification of the detection signal with special focus on the bandwidth of pre-amplification circuits. It was seen that the pre-amplification circuit causes attenuation of the voltage applied to the detection electrodes at frequencies >3 MHz. We also saw that this effect could be observed directly on the signal after post-amplification (ie. after the output from the flow cell has been amplified further) and that the attenuation is specifically related to the circuits used in BactoBox when compared to measurements with an alternative system made by Zurich Instruments.

Finally the signal analysis done in software was discussed. The peak detection and pairing was presented and the compromises of the "winner takes all" strategy were discussed, mainly that it leads to under estimation of events, especially at high concentrations. We discussed the fact that the measured differential argument would never be able to reach values of 0, $\pi/2$, $-\pi/2$ and π , since the noise in the signal prevents any of the data streams

from being exactly zero. This leads to artificial gaps when the argument is plotted, e.g. in a scatter plot. Finally the way the concentration is calculated was presented. We discussed that the volume needed to calculate the concentration was estimated using the average transition time of the events and the cross sectional area of the detection channel. To estimate the volume using this method, it is important to compensate for the error made due to the parabolic profile of the flow in the detection channel caused by no slip boundaries at the channel walls. A compensation factor calculated numerically using MATLAB was then presented.

4 Data analysis and visualisation

4.1 Plotting the impedance results

Each event has 4 peaks from the real and imaginary data streams in low and high frequency (ie. LFRE, LFIM, HFRE, HFIM). For BactoBox, the low and high frequency is set at 366 kHz and 6.9 MHz, respectively, and these are the frequencies that will be used in the following.

The peak values can be plotted in different ways to visualise various characteristics of the data. Usually, the population of events from the same measurement is plotted together in the same plot together with data from other measurements for easier comparison. Figure 4.1 show the results from 2 impedance measurements on *E. coli* and polystyrene beads (2 μm diameter) plotted in various ways.

The most straight forward way to visualize the data is direct plotting of the obtained peak values for each event in a scatterplot. Low frequency (LFRE and LFIM) and high frequency (HFRE and HFIM) are split into two different plots as shown in figure 4.1a and figure 4.1b.

A scatterplot with the low frequency modulus ($|\text{LF}|$) on the x-axis and high frequency modulus ($|\text{HF}|$) on the y-axis as shown in figure 4.1c. The moduli are calculated from peak values using

$$|\text{LF}| = \sqrt{\text{LFRE}^2 + \text{LFIM}^2} \quad (4.1)$$

$$|\text{HF}| = \sqrt{\text{HFRE}^2 + \text{HFIM}^2} \quad (4.2)$$

Under the right circumstances the modulus will correlate with particle diameter (for example as seen in figure 4.2) and this kind of plot can also be made with the cubic root of the modulus to get a more direct relationship to particle radius. Technically the modulus always depends on the volume of the particle or bacteria, but especially when measuring on non-conductive particles this correlation is strong. As discussed before, bacteria and other cells are effectively nonconducting at frequencies where the cell membrane remains opaque (ie. lower frequencies). Here the current is forced around the bacteria and the impedance change is directly related to the volume of the cell. However, if the frequency is high enough so that the membrane is bypassed or if the membrane is not intact, the modulus current now depends on multiple factors such as degree of membrane integrity and cytoplasm conductivity. The "slope" of the population therefore also illustrates the opacity of the events (see more about opacity below).

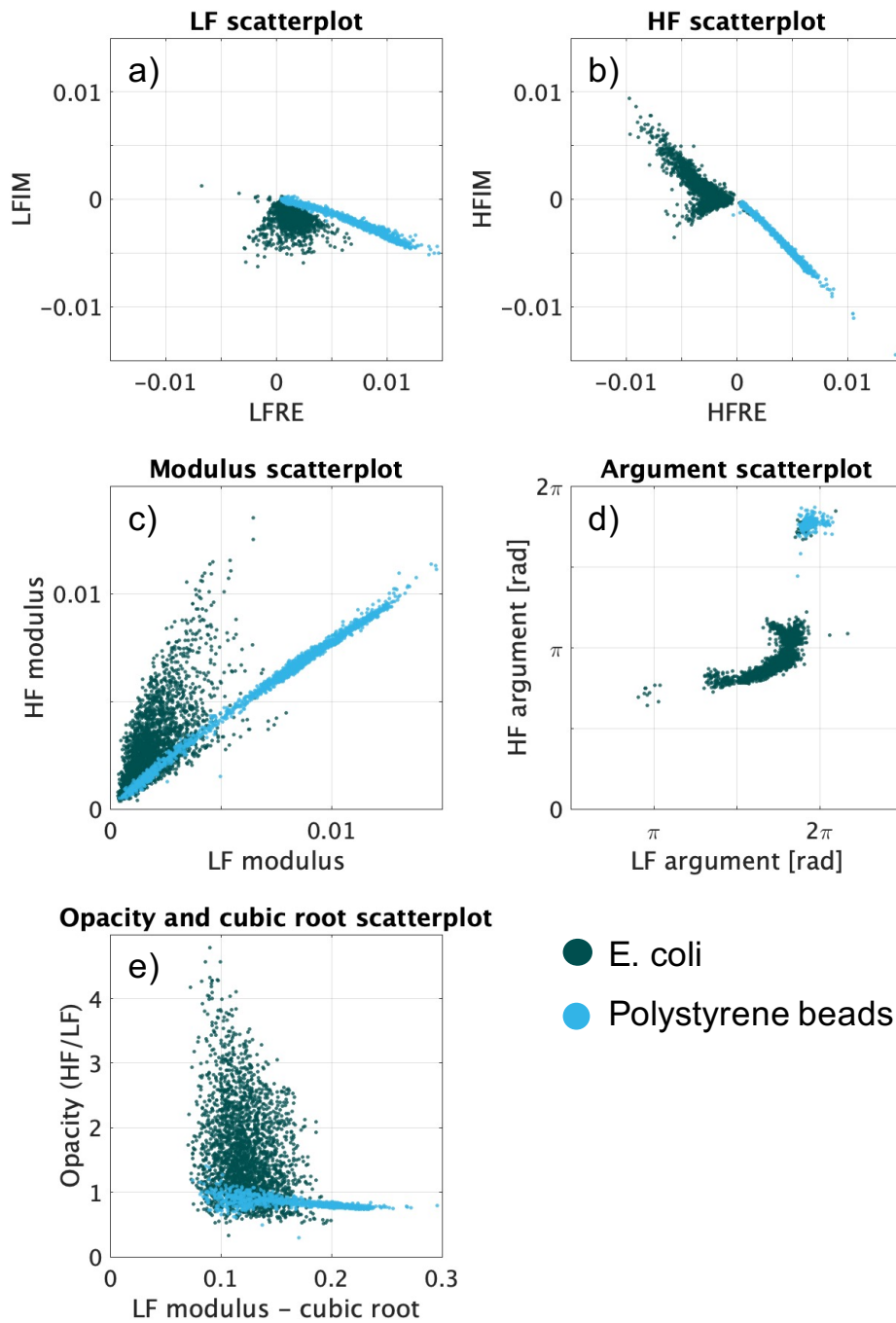


Figure 4.1: Scatter plots visualizing impedance data for 2 μm polystyrene beads and *E. coli*. a) shows the scatterplot plotted using the real and imaginary peak values at the low frequency, b) the the real and imaginary parts of the peaks acquired at the high frequency, c) the modulus calculated from the the low and high frequency peaks, d) the argument calculated from the low and high frequency peaks, e) opacity and cubed.

A scatterplot with the low and high frequency argument on the axis, calculated from the real and imaginary peak values, as shown in figure 4.1d. The argument (or phase) is

calculated using *arctan*, but modified so that it covers the range from $-\pi$ to π (ie. four quadrant inverse tangent). In most programming languages this is done using the function *atan2* (or *arctan2*) defined in the following way

$$\text{atan2}(y, x) = \begin{cases} \arctan\left(\frac{y}{x}\right) & \text{if } x > 0, \\ \arctan\left(\frac{y}{x}\right) + \pi & \text{if } x < 0 \text{ and } y \geq 0, \\ \arctan\left(\frac{y}{x}\right) - \pi & \text{if } x < 0 \text{ and } y < 0, \\ +\frac{\pi}{2} & \text{if } x = 0 \text{ and } y > 0, \\ -\frac{\pi}{2} & \text{if } x = 0 \text{ and } y < 0, \\ \text{undefined} & \text{if } x = 0 \text{ and } y = 0 \end{cases} \quad (4.3)$$

So that the argument for the low and high frequency is calculated from the peak values in the following way

$$\arg(\text{LF}) = \text{atan2}(\text{LFIM}, \text{LFRE}) \quad (4.4)$$

$$\arg(\text{HF}) = \text{atan2}(\text{HFIM}, \text{HFRE}) \quad (4.5)$$

For a given complex number, a complete rotation of the argument (ie. 2π radians) leaves the complex number unchanged ($\arg(Z) = \arg(Z) + 2\pi n$) and all of the events can be plotted in any range spanning 2π (e.g., 0 to 2π or $-\pi$ to π). The axis limits for the argument can preferably be chosen so that the population is shown within the boundaries of the plot. The argument is calculated from the ratio between the real and imaginary peak values and is therefore less affected by signal attenuation (as long as the signal to noise ratio is adequate). Figure 4.2 show histogram plots of the the cubed modulus and argument from measurements on 3 sizes of polystyrene beads with diameter of 1 μm , 1.5 μm and 2 μm . It is seen that the cubed modulus decrease as the bead size decreases. The increase in variation in the argument as the bead size decrease is due to a decrease in signal to noise (SNR) ratio. As the bead size decreases, the overall peak height also decreases while the noise stays the same resulting in a higher relative variation from peak to peak.

Opacity is the ratio of the high frequency modulus and the low frequency modulus and is a widely used parameter for comparing results from impedance flow cytometry. In figure 4.1e it is plotted on the y-axis with the cubed low frequency modulus on the x-axis.

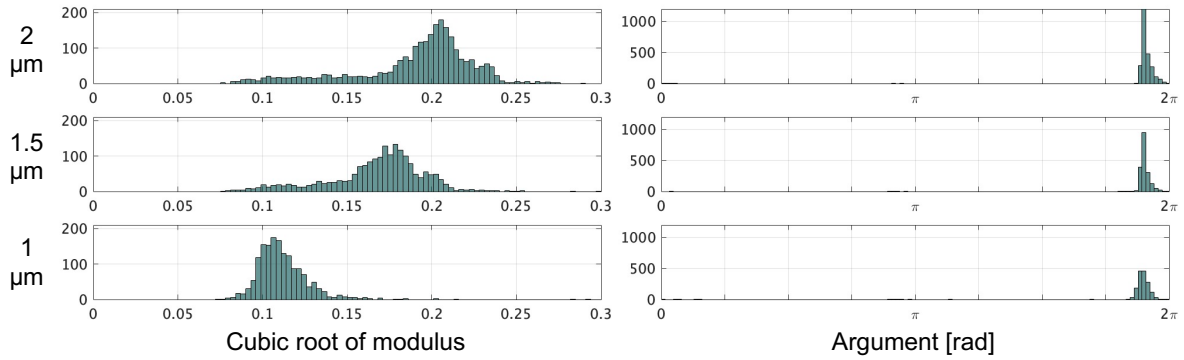


Figure 4.2: Histograms showing the cubed modulus and argument of polystyrene beads with 3 diameters: 1 μm , 1.5 μm and 2 μm , measured at a frequency of 366 kHz.

4.1.1 Visualizing population density

Sometimes it is more advantageous to visualize the data from the IFC experiments in density plots instead of scatter plots. Scatterplots are very useful for comparing two or more populations directly, but do not convey where the density of events very well. To visualize the density of events we can instead use a density plot (also called a heat map). Figure 4.3 demonstrate two different ways to do this: a direct density plot and the kernel density plot. To plot the direct density plot, the data space is divided in a fixed number of fields and the density is based directly on the number of events inside each field. To create the kernel density plot (also known as kernel density estimation or KDE [67, 68]) each event in the scatter plot is replaced by a kernel with a specified shape and width. The kernel can have many shapes but normally a gaussian shape is used. The sum of the kernels make up the kernel density map and create a smoothed out version of the direct density plot as shown in figure 4.3c.

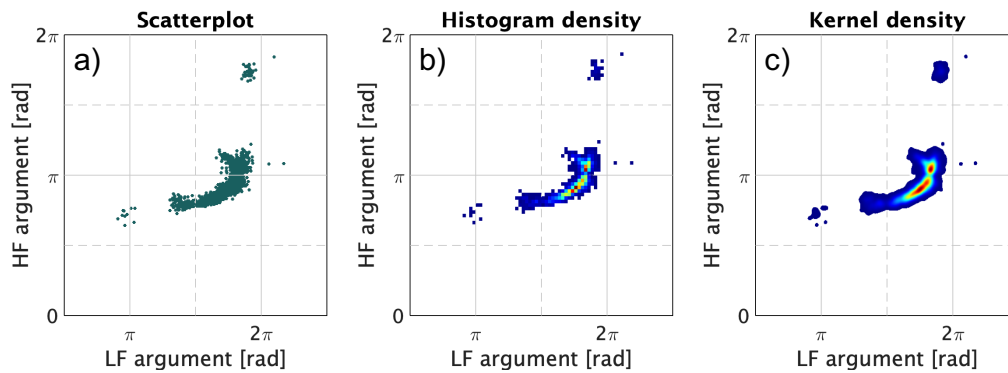


Figure 4.3: Comparison between (a) scatter plot, (b) heat map, and (c) kernel density map for a plot of low and high frequency argument from an IFC measurement of *E. coli*.

Plotting heat maps using the kernel density can create very nice and clear plots, but as with any estimation based method the parameters must be chosen with care in order to not lose vital information. Figure 4.4 shows the same data as before plotted for 3 different kernel bandwidth (ie. the width of the kernel). We can see that is the kernel bandwidth

is chosen too small (such as in figure 4.4a), the edges of the population becomes jagged and we lose the clarity achieved by the smoothing compared to the direct density plot. On the other hand, if the kernel bandwidth is too large (such as in 4.4c) the details of the data is lost and we risk misinterpreting the results.

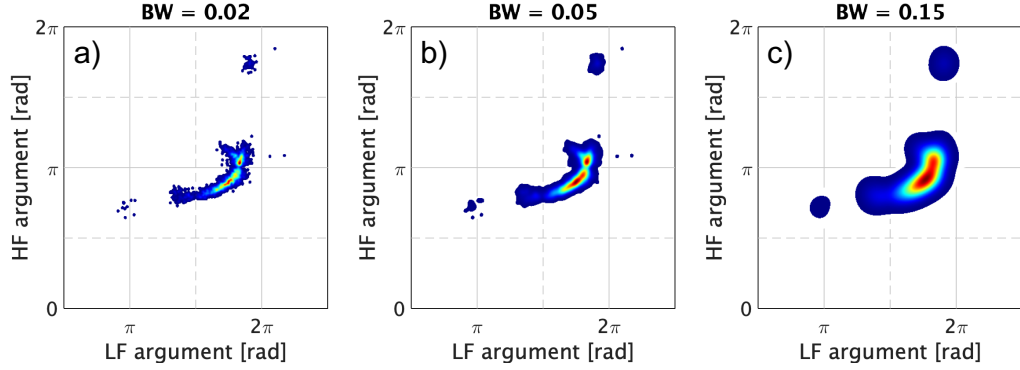


Figure 4.4: Comparison between 3 kernel density plots with bandwidths of (a) 0.02, (b) 0.05, and (c) 0.15 for a plot of low and high frequency argument from an IFC measurement of *E. coli*.

4.2 Comparing measurements

When simple visualization is not enough we need other methods to compare and analyse the IFC data. In the following sections 3 approaches to comparison of data from IFC is presented: classification with receiver operator characteristics, traditional statistical comparisons using means and medians, and a contour based method closely inspired by other IFC work [15]. These are of course only a few of the many ways the data can be analysed. For example, large IFC datasets are ideal for analysis using sophisticated multivariate methods or with machine learning, however, these methods are outside the scope of this work.

4.2.1 Receiver operating characteristic (ROC) curves

ROC curves are a way to visualise the diagnostic ability of a binary classifier when varying the classification threshold. A simple illustration of the idea is found in figure 4.5. Three artificial data sets (group A, group B, and group C), each containing height measurements from 6 people, is visualized as marks on a height scale (black, blue and yellow marks for each group). The origin of the groups are not that important in this example, but could be e.g. gender or nationality. The red vertical striped lines represents different values of the classification threshold. Also shown in figure 4.5 is a sketch of the ROC curve obtained from classification between group A and B, and group A and C. The axis of the ROC curve shows the false positive rate (FPR) and true positive rate (TPR) for any given threshold. The FPR is the number of events wrongly characterized as positive (FP) divided by the total number of actually negative events (TN+FP).

$$\text{FPR} = \frac{\text{FP}}{\text{TN} + \text{FP}} = 1 - \text{selectivity} \quad (4.6)$$

The FPR is equivalent to '1 - selectivity' and can also be described as "the probability of a false alarm".

The TPR is number of events correctly identified as positive divided by the total number of actually positive events (FN+TP).

$$\text{TPR} = \frac{\text{TP}}{\text{FN} + \text{TP}} = \text{sensitivity} \quad (4.7)$$

TPR is equivalent to the sensitivity.

Going back to the example in figure 4.5, if we compare group A and group B, and state that every events under threshold number 1 belongs to group A, we will have 6 true positives out of 6 actual positives in group A and 6 false positives out of 6 actual negatives in group B. We therefore start the ROC curve in the top right corner at a FPR of 100% and a TPR 100%. When the threshold moves down to threshold number 2, we still have 6 out of 6 true positives, but now we only have 3 false positive of 6 actually negative events, which places us at a TPR of 100% and a FPR of 50%. As the threshold moves down, the TPR and FPR change until they both reach 0% at threshold number 5. Doing the same for group A and group C yields a ROC curve (as shown in figure 4.5) that gets closer to the top left corner of the plot because the two groups have better separation in height and therefore are easier to classify correctly. For two equivalent population the ROC curve would follow the diagonal of the plot. An important parameter for ROC curves is the 'area under the curve' or AUC, with higher AUC indicating better classification. It is also clear from the example given in figure 4.5 that it matter how the threshold is defined. In the example we defined everything under the threshold as belonging to group A, but if we instead define that everything above the threshold belongs to group A, our ROC curve would hug the bottom right corner of the plot. Going forward we will always try to define the thresholds so that the ROC moves toward the upper left corner so that the AUC is higher than 0.5.

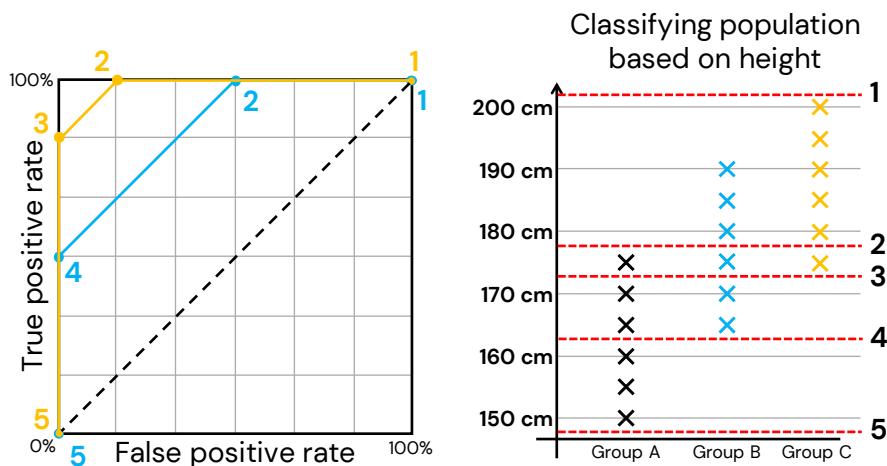


Figure 4.5: Simple illustration of how a ROC curve is generated for classification comparison based on height for three groups (A, B, C).

In principle any given threshold can be used to differentiate between two populations but depending on the dataset and the impact of the classification results it may be beneficial to choose a specific threshold. For example, if you are testing a population for a highly contagious virus it might be preferable to reduce the number of false negatives to limit spread of the virus at the cost of a higher false positives count.

To illustrate the function of the ROC curves with a real world dataset we re-use the impedance data for polystyrene beads and *E. coli* shown in figure 4.1 and create a ROC curve for each of the axis found in that figure as shown in figure 4.6 together with a table of the AUC values for each axis. It is seen that HFRE direct peaks, high frequency argument, and HFIM direct peaks gives the highest AUC and the best classification between the 2 μm polystyrene beads and the *E. coli*.

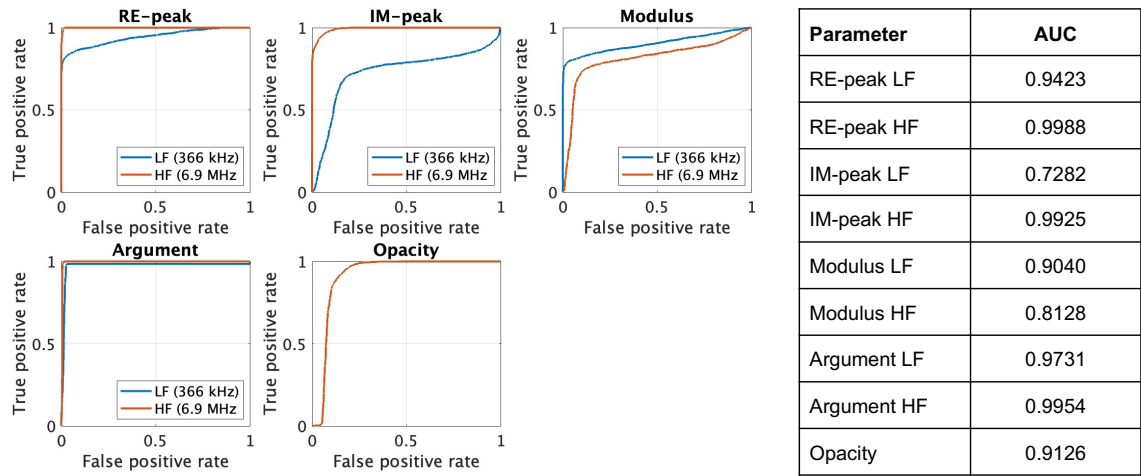


Figure 4.6: ROC curves and AUC values for data representation found in figure 4.1 for measurements of polystyrene beads and *E. coli*

4.2.2 Medians and means

Another, more traditional way to compare populations is to compare different kinds of population "averages" such as the mean or medians values either visually or statistically. The arithmetic mean (\bar{x}) is perhaps the most obvious parameter to use for population comparison and is calculated as the sum of measured values (e.g. low frequency arguments) divided by the total number of values (n).

$$\bar{x} = \frac{1}{n} \sum_{i=1}^n x_i \quad (4.8)$$

The mean is not a particularly robust parameter and is very susceptible to outliers in the population. To compensate for this, more robust parameters can be used such as the interquartile mean or, more suitably, the median. The median is the number in the "middle" of the list when the measured values are sorted in order from smallest to largest and is therefore much less susceptible to outliers at either end of the sorted list. An easy way to graphically compare the median (and other quartiles) of a population is to make

'box plots' from the event data. Figure 4.7 shows an example of boxplots create with MATLABs boxplot function for HF argument and opacity of polystyrene beads and *E. coli* (the same data plotted in scatter plots in figure 4.1d+e). The boxplot has a red line in the middle representing the median value with the edges of the blue box representing the quartiles of the population. The whiskers of the boxplot extend to the most extreme data points not considering outliers, and the outliers are plotted individually using a red '+' symbol.

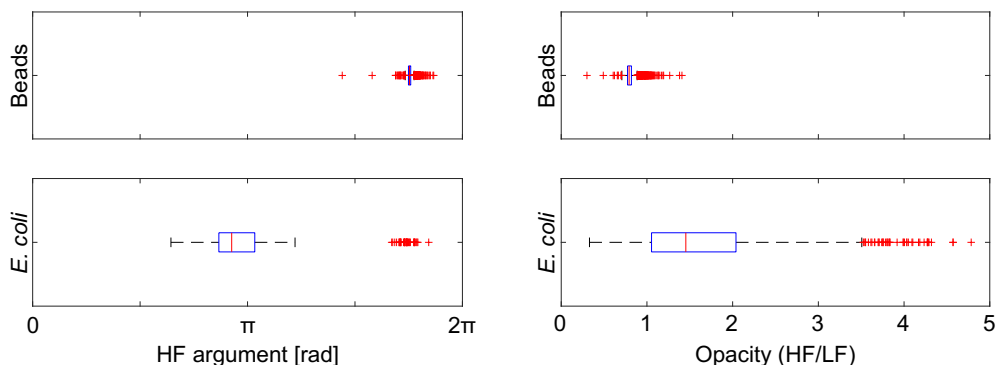


Figure 4.7: Boxplots showing comparisons between polystyrene beads and *E. coli* compared by their HF argument and opacity. Each boxplot has a red line in the middle representing the median value with the edges of the blue box representing the quartiles of the population. The whiskers of the boxplot extend to the most extreme data points not considering outliers, and the outliers are plotted individually using a red '+' symbol.

It is seen how the separation between the beads and *E. coli* populations is more absolute in the HF argument compared to opacity, similar to what was concluded from the the ROC curves discussed in the previous section.

Numerous methods exist for comparison of the statistical significant difference between the mean or median of two populations, for example a t-test for comparison of means or Mann-Whitney test for comparison of medians.

4.2.3 Contour comparison

While differences in mean and median can be quantified (tested statistically) it is harder to quantitatively compare two population based on the shape of the population and two different looking shapes can have the same mean. Spencer et al. [15] has in 2020 published their work on their impedance-based Fast Antimicrobial Susceptibility Test (iFAST). To evaluate shifts in populations they use a gate based method where a contour is defined around a population of cells so that 50% of the cell population is inside the contour. The same contour is then drawn onto cell populations from measurements where the cells have been exposed to antibiotics and the percentage of cells inside the contour is calculated. A decrease in cell concentration or or a change in the biophysical properties cells (causing a shift in the population) will leave fewer cells inside the original contour. The effectiveness of the antibiotic can thus be evaluated based on how many cells remain inside the contour. The term control gate is also used to describe the original contour. Spencer et al. uses a contour line that surrounds 50% of the data but in principle any contour line can be used.

$$\text{Fraction of cells in control gate} = \frac{\text{Number of cells in gate}}{\text{Number of cells originally in gate}} \quad (4.9)$$

This method works very well when evaluating measurements with a clear starting point (such as measuring the same sample 1 multiple times with a fixed time interval between each measurement). However, when comparing more independent samples it may be more advantageous to compare the number cells in the control gate to the total number of cells in the specific sample

$$\text{Fraction of cells in control gate} = \frac{\text{Number of cells in gate}}{\text{Number of total cells}} \quad (4.10)$$

If the contour gate is made so that 50% of the cells in one population is inside the gate, a similar population will also have close to 50% inside of the gate. If the difference in cells inside the gate is different compared to the original population, the populations are most likely not similar. The absolute difference in cell percentage inside the contour and the expected cell percentage thus gives an indication of the similarity of the populations

$$\text{Difference in cell fraction} = |\text{Target fraction} - \text{Fraction of cells in control gate}| \quad (4.11)$$

To illustrate this method, a simple experiment with BactoBox was performed to test the variation between different detection flow cells when measuring on *E. coli* bacteria. The bacteria was grown over night and samples with 3 ml of diluted phosphate buffered saline (PBS) were prepared. 3 μl of the overnight culture was pipetted directly into each 3 ml sample causing a dilution of broth and cell concentration of 1000x (overnight concentration for *E. coli* is roughly $10^9/\text{ml}$). 3 flow cells where used for measurements (Chip1, Chip2, Chip3) and measurements where performed on 3 samples for each flow cell. Furthermore, each flow cell has two measurement sites (site0, site1) for a total of 18 measurements. The flow cell are identical, except for site0 Chip1 which is known to be broken. This leads to an imbalance in current on Chip1 sit0 (ie. too high current on the ADC) and cutting of the signal.

Figure 4.8 shows the data from the first of the measurements from each site of all 3 flow cells with the outline of the control gate belonging to that measurement containing 90% of the cell population. Measurements from all 3 repetitions can be found in Appendix A.1.

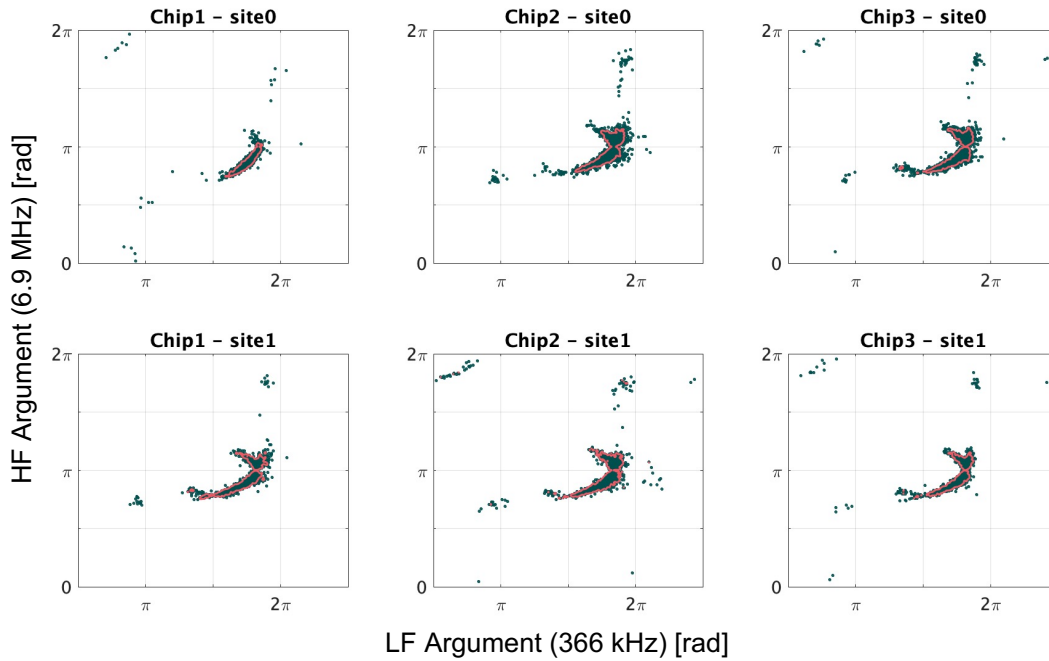


Figure 4.8: Scatterplots showing the low and high frequency argument with contours surrounding 90% of the cell population in each individual measurement. The data are obtained from measurements on *E. coli* bacteria in 3 different flow cells (Chip1, Chip2, Chip3), each with 2 measurements sites (site0 and site1).

In figure 4.9, the difference in cell fraction inside the contour using the contours and data from all 18 samples is visualised, calculated using Eq. 4.11. It is seen that variation between chips is relatively low except for the broken site on Chip1. However, some fluctuation between supposedly identical measurements do occur (e.g Chip3 site1, measurement 1).

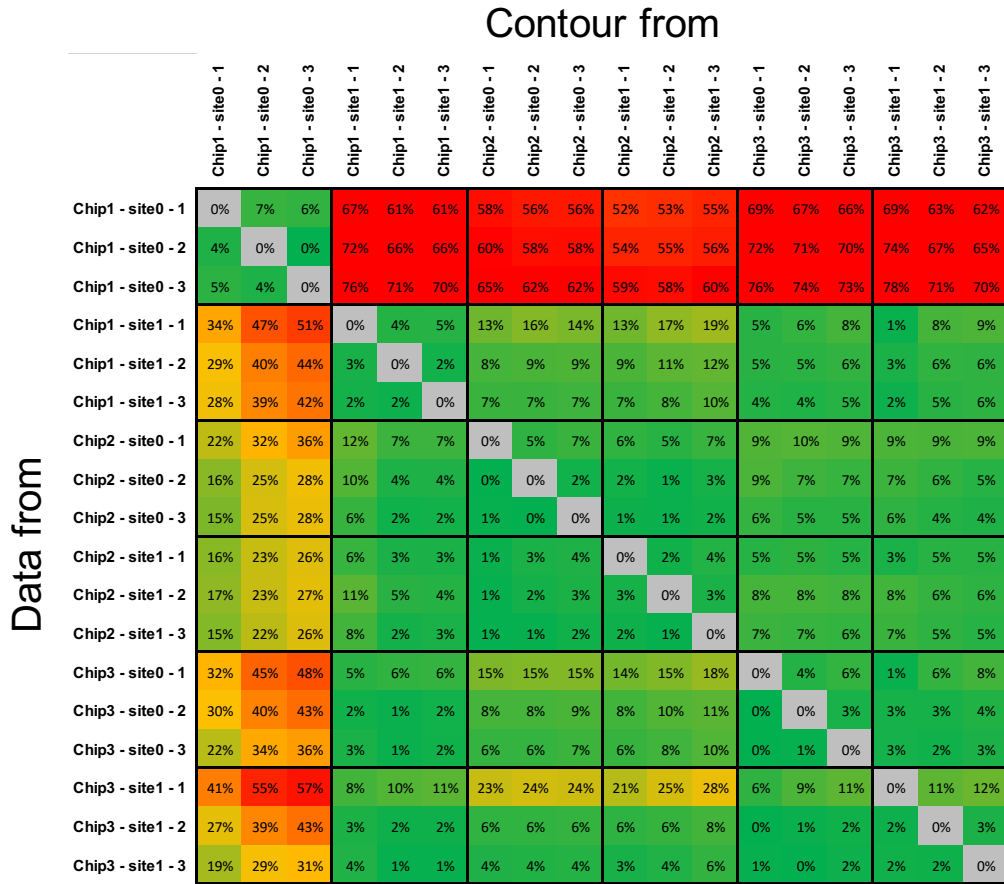


Figure 4.9: Contour comparison of 18 measurements on *E. coli* performed with 3 different flow cells. Data is set up in a grid with the data points from each measurement on the y-axis and the 90% contour from each measurement on the x-axis. Numbers in each grid point show the absolute difference in cell fraction from 90% when looking at the data from the measurement indicated on the x-axis inside the 90% contour from the measurement indicated on the y-axis. Color grading is based on the fraction difference and goes from green (0%) to yellow (30%) to red (>60%).

4.3 Chapter summary

In this chapter we have looked at the various ways the data from the IFC measurements can be visualized and analysed. We looked at the different ways the complex data can be visualised in scatterplots and discussed the advantages and disadvantages of scatterplots and density plots.

We then looked at using ROC curves to compare and classify events from different measurements. We introduced the area-under-curve (AUC) value from the ROC curves and used it to evaluate which data representation is best at differentiating between polystyrene beads and *E. coli*. At a low frequency of 366 kHz and a high frequency of 6.9MHz, we found that the high frequency argument, HFRE peaks and HFIM peaks provided strong classification performance.

We also looked at visualizing the data in box plots. Finally, we looked at an adapted method based on gating. We used this method to look at the variation between different measurement chips and found that the variation between working detection electrodes was relatively low, but that outliers with higher technical variation than expected can occur.

Part II

5 Bacteria characterisation and counting

From the very beginning of the PhD project it was known that we could differentiate between *E. coli* bacteria and polystyrene beads. One of the first activities during the project was to confirm and formalize this which led to the following paper:

- Clausen, C. H., Dimaki, M., Bertelsen, C. V., Skands, G. E., Rodriguez-Trujillo, R., Thomsen, J. D., & Svendsen, W. E. (2018). Bacteria detection and differentiation using impedance flow cytometry. *Sensors*, 18(10), 3496.

In the paper we look at detection of bacteria with a special focus on differentiation between species and on enumeration. We investigate the ability of the IFC system to accurately determine the concentration of *E. coli* in a sample by measuring on multiple samples with varying concentrations and comparing the results to standard plate counts. We find a strong linear correlation ($R^2 > 0.99$) between the two methods, but with a fixed offset in the measured concentration. We also compare the impedance signals from *E. coli* and *Staphylococcus aureus* and find that we can separate the two species based on their phase angle when measuring at 8 MHz. We theorise that the differentiation is possible because of the difference in the structure of the cell membrane between the gram-negative *E. coli* and the gram-positive *Staphylococcus aureus*.

This chapter starts with a reprint of the manuscript described above. It then moves on to discuss the reason for the clear distinction between beads and bacteria seen in the differential argument, especially in the high frequency, and demonstrates this point with some results from measurements on particles with different conductivities. Next, a simple experiment showing how the growth rate of *E. coli* can be tracked using BactoBox, and finally a presentation of measurements on 6 different bacteria strains is given.

The measurements from the paper are made with custom lab setup as described in the paper and is the only experimental data presented in this thesis not made with BactoBox (a pre-pre-prototype version of the BactoBox). The rest of the experimental data presented in this chapter is obtained using BactoBox v2 and flow cells with design Q.

5.1 Manuscript



Article

Bacteria Detection and Differentiation Using Impedance Flow Cytometry

Casper Hyttel Clausen ¹, Maria Dimaki ^{2,*}, Christian Vinther Bertelsen ^{1,2}, Gustav Erik Skands ¹, Romen Rodriguez-Trujillo ^{3,4}, Joachim Dahl Thomsen ² and Winnie E. Svendsen ²

¹ SBT Instruments ApS, Diplomvej 381, 2800 Kgs. Lyngby, Denmark; chc@sbtinstruments.com (C.H.C.); cvb@sbtinstruments.com (C.V.B.); ges@sbtinstruments.com (G.E.S.)

² Technical University of Denmark, Department of Micro- and Nanotechnology, Oersteds Plads 345 East, DK-2800 Kgs. Lyngby, Denmark; jdth@nanotech.dtu.dk (J.D.T.); wisv@nanotech.dtu.dk (W.E.S.)

³ Department of Electronics and Biomedical Engineering, University of Barcelona. C/Martí i Franquès 1, 08028 Barcelona, Spain; romen.rodriguez@ub.edu

⁴ Institute for Bioengineering of Catalonia (IBEC), the Barcelona Institute for Science and Technology (BIST), C/Baldiri i Reixac 10-12, 08028 Barcelona, Spain

* Correspondence: madi@nanotech.dtu.dk; Tel.: +45-45-256-402

Received: 20 September 2018; Accepted: 15 October 2018; Published: 17 October 2018



Abstract: Monitoring of bacteria concentrations is of great importance in drinking water management. Continuous real-time monitoring enables better microbiological control of the water and helps prevent contaminated water from reaching the households. We have developed a microfluidic sensor with the potential to accurately assess bacteria levels in drinking water in real-time. Multi frequency electrical impedance spectroscopy is used to monitor a liquid sample, while it is continuously passed through the sensor. We investigate three aspects of this sensor: First we show that the sensor is able to differentiate *Escherichia coli* (Gram-negative) bacteria from solid particles (polystyrene beads) based on an electrical response in the high frequency phase and individually enumerate the two samples. Next, we demonstrate the sensor's ability to measure the bacteria concentration by comparing the results to those obtained by the traditional CFU counting method. Last, we show the sensor's potential to distinguish between different bacteria types by detecting different signatures for *S. aureus* and *E. coli* mixed in the same sample. Our investigations show that the sensor has the potential to be extremely effective at detecting sudden bacterial contaminations found in drinking water, and eventually also identify them.

Keywords: electrical impedance spectroscopy; bacteria detection; bacteria differentiation; water quality; bacteria counting

1. Introduction

One of the most common ways to determine if bacteria are present in a given sample, e.g., food, urine, blood etc. is to plate the sample on an agar plate and culture it for 1–3 days inside an incubator. This method is extremely easy and precise, but also very time consuming, because you need to wait for the growth to occur before you know the concentration of your sample and can react accordingly.

This problem is of particular importance in drinking water systems [1,2], because the contaminated water can quickly affect a large population. The slow analysis time of a traditional plate count means that the water utilities cannot alert the population that a contamination is present before the potentially dangerous water is consumed. Due to the size of the piping system, it can also be difficult for the utilities to identify the source and location of the contamination and the drinking water can stay polluted for many days.

Effective enumeration of bacteria in liquid samples without the need for a time consuming culture step has been an issue for several years [3] and a number of methods already exist that address this problem. Some of the most prominent of these are fluorescence flow cytometry [4], electrical impedance spectroscopy [5] and image analysis methods [6]. However, fluorescence flow cytometry requires the use of either stains or labels in order to enumerate bacteria, which complicates the process [7]. Imaging techniques require the development of identification algorithms and are difficult to perform in real time.

Characterizing biological samples by detecting dielectric changes using electrical impedance is a technique that has been used in several forms, including Coulter counters and impedance flow cytometers. Electrical impedance spectroscopy (EIS) [8–11] has been used to investigate different biological samples in suspension and is able to characterize biological sample properties in a label free manner. In EIS, a microfluidic channel is used to direct a sample of particles dispersed in a liquid towards a set of electrodes with an applied AC electrical field [10]. Changes in the electric field during particle transitions depend on the dielectric and structural properties (size, composition) of the particles, which can therefore be determined through interpretation of the measured electrical current.

Different properties of the particles are probed at different frequencies, e.g., the particle size is probed at low frequencies in the kHz range while the particle composition is probed at higher frequencies in the low MHz range. Therefore, modern EIS devices apply a mixed multi-frequency signal in order to simultaneously probe the particle properties. Integration of EIS into microsystems is a relatively new development, which has been demonstrated to have various applications within characterization of biological samples [8,9]. The advantages of this integration are better control and higher sensitivity of the system.

The technique has been widely used for analysis of biological material; from differentiation of red blood cells extracted from fish and human leukocytes [12] to detection of DNA in droplets [13]. Gawad et al. [8] presented the first single cell EIS differential microfluidic cell analysis system. They reported the capability of EIS to differentiate erythrocytes and erythrocyte ghost cells, as well as solid particle size separation in continuous flow. Furthermore, the technology has been applied to a broad number of different micro-sized samples; it has been used to distinguish between different yeast cells [14] and human blood cells of different kinds [9,15–17]. EIS has also been used to measure the effect of electrical lysis on yeast cells [18]. Additionally, several reports exist on the modeling of the signal response and how to elucidate how the different properties of the sample influence the recorded signal [14,19]. Further applications include differentiating bacteria from polystyrene beads [20] and distinguishing heat treated bacteria samples from un-treated samples [11].

Millions of bacteria species exist, many with unique structural and pathogenic properties. Traditionally, bacteria are divided into two classes, gram negative and gram positive, depending on the ability of their cell wall to retain crystal violet dye. Gram positive bacteria have an outer membrane layer (see Figure 1), which is not present for gram negative bacteria. The presence of the extra membrane is therefore a potential target for differentiation between gram positive and gram negative bacteria by EIS.

In this paper we will present how we can detect and enumerate bacteria in water samples using EIS. We will show that it is possible to detect bacteria not only in artificial buffers (e.g., diluted PBS), but also in tap water. Furthermore, we will show that it is possible to differentiate between gram positive and gram negative bacteria, by using our method to distinguish between two of the most commonly found bacteria. The novelty of the paper lies in the real time continuous detection of bacteria in water samples using impedance, as opposed to publications detecting bacteria in a static environment.

2. Materials and Methods

2.1. Sample Composition

The bacteria used in this work are *Escherichia coli* (*E. coli*) and *Staphylococcus aureus* (*S. aureus*). *E. coli* is a rod shaped Gram negative bacterium with a length of 2–3 μm [21] and a diameter of 0.5 μm . It is a common cause for bacterial infections in humans and animals [22]. The cytoplasm of *E. coli*, which is considered to be electrically conductive, is surrounded by an electrically isolating lipid inner membrane (10 nm [23]), a conductive periplasmic space containing the peptidoglycan wall (20 nm [24]) and another isolating lipid outer membrane (13 nm), see Figure 1B.

S. aureus is a spherical Gram positive bacterium with a diameter of approximately 1 μm [25]. It has a conducting cytoplasm in the center surrounded by a lipid membrane and a peptidoglycan cell wall, characteristic of gram-positive bacteria. The lipid membrane has a thickness of 10 nm and is normally assumed to be non-conducting, while the cell wall has a thickness of 60 nm and is assumed to be electrically conducting [24], see Figure 1A.

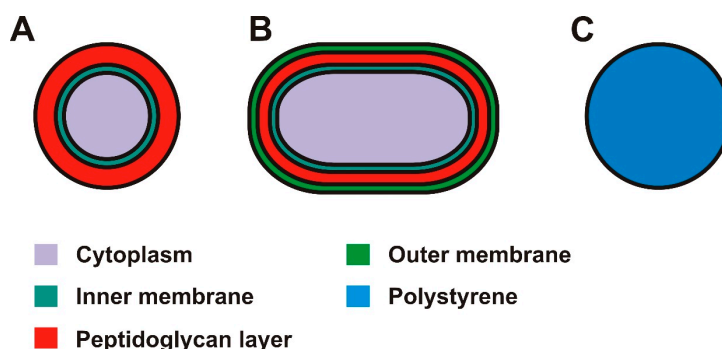


Figure 1. Schematic drawings of the bacteria and particles used in this report (A) Gram-positive *S. Aureus* (B) Gram-negative *E. coli*. (C) Polystyrene beads.

The bacteria (*Escherichia coli* strain INV- α from Invitrogen, Nærum Denmark, methicillin-susceptible *Staphylococcus aureus* from Statens Serum Institut, Copenhagen, Denmark), were cultured on appropriate pre-prepared agar plates (LB agar, L5542-10EA, Sigma Aldrich Denmark A/S, Copenhagen, Denmark; blood agar, A600, VWR, Copenhagen, Denmark, respectively). The bacteria were spread on the agar plates, dried (10–15 min), and incubated at 37 °C for 24 h. Before the experiments a small amount of *E. coli* was transferred from the agar plate into individual incubation tubes containing 5 mL of LB broth and incubated at 37 °C for 24 h with rotation (215 rpm). After the 24 h incubation 1 mL LB broth containing bacteria was centrifuged, the broth was removed, and the bacteria were re-suspended in either diluted PBS (1/20 \times PBS, D8537, Sigma Aldrich) or tap water at appropriate concentrations. Polystyrene beads, illustrated in Figure 1C, with diameters of 1 μm and 2 μm were used as non-biological reference particles. The polystyrene beads are dielectric homogenous spheres which conduct current primarily on their surface [26]. The polystyrene beads were acquired from Polysciences, Inc. (Warrington, PA, USA).

2.2. Detection Principle

Figure 2A illustrates the detection principle as well as the electrode configuration on the microfluidic chip. At low frequencies (100–1000 kHz) (Figure 2A, 1 and 2) it is expected that the electrical field will not be able penetrate the beads or the bacteria due to the isolating nature of their bulk and membrane, respectively. The current will only move in the liquid medium and the measured signal will depend on the volume displacement due to the particles or bacteria investigated,

i.e., the signal depends on particle/bacteria size. At higher frequencies (1 MHz–10 MHz), the electric field is still not able to penetrate the bulk of the polystyrene beads (Figure 2A, 3). However, it is capable of partially penetrating the membrane of the bacteria and thus probe the membrane and cytoplasm composition (Figure 2A, 4) [19].

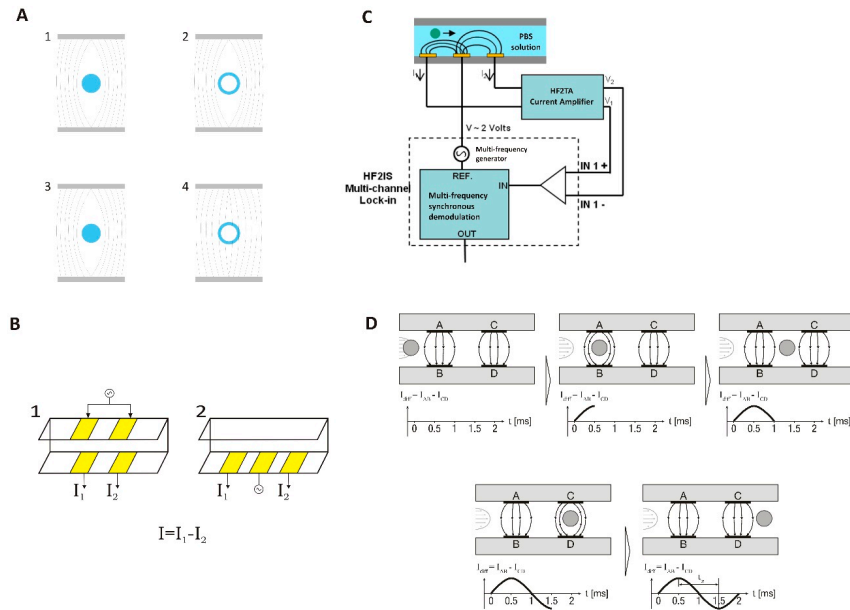


Figure 2. (A) Electric fields generated by two electrodes at low frequencies (1 and 2) and high frequencies (3 and 4) on beads (1 and 3) and bacteria (2 and 4). (B) Schematic of the measuring principle using front facing (1) or coplanar (2) electrodes. A differential signal between the two measuring electrodes is recorded for further analysis. (C) Schematic drawing of the measurement setup, in the case of coplanar electrodes. The sample is injected into the system by a syringe pump. A multi-frequency lock-in amplifier is used to generate and detect the signal. The signal from the measuring electrodes is passed through a current preamplifier before it is returned to the lock-in amplifier. (D) Schematic showing the detection principle. When the particle is not influencing the electric field generated by the electrodes, the differential signal is zero. As the particle travels in the channel it will only disturb the field of one set of electrodes at a time, which gives rise to a differential signal. When the particle leaves the electrodes area a transition looking like a sinusoidal signal will have been recorded, indicating the transition of one particle.

2.3. Chip Fabrication

Two types of chips were fabricated and used in this work: chips with coplanar electrodes and chips with front facing electrodes (Figure 2B). The fabrication process is similar for the two chip types: Gold electrodes were defined on 4-inch Pyrex wafers by photolithography, e-beam vapor deposition and lift-off, using titanium as an adhesive layer. On top of the electrodes the channels were formed in SU-8 2005 (MicroChem, Berlin, Germany) by negative photolithography as described by Demierre et al. [27,28]. The channels were sealed using a second Pyrex wafer (lid wafer) with openings for electrode access and fluidic inlet and outlet defined using powder blasting. The lid wafer used for the front facing electrodes had additionally gold electrodes fabricated as those of the bottom wafer. The lid wafer was then thermally bonded to the bottom wafer as described by Serra et al. [29]. The microchannels were 10 μm wide and 10 μm high. The front facing electrodes exposed to the

channel are 10 μm long and 10 μm wide with a pitch of 16 μm . The dimensions and pitch are the same for the coplanar electrodes.

2.4. Measurement Setup

The setup used in this work uses a layout as shown in Figure 2B. An AC excitation signal is applied to either the top electrodes (Figure 2B 1, front facing) or the middle electrode (Figure 2B 2, coplanar), and the current is measured at the two remaining electrodes. In order to normalize the detected signal a differential measurement is carried out between the two sets of electrodes, giving a measured current of $I = I_1 - I_2$, as shown in Figure 2B.

The measurement setup consists of a custom-built aluminum chip holder containing the necessary electrical and fluidic connections (fittings from Upchurch Scientific[®], IDEX Health and Science, Oak Harbor, WA, USA) for the microfluidic chip. O-rings were used to seal the fluid connections of the chip to the holder. Differential EIS measurements were performed with a HF2IS Impedance Spectroscopy (Zurich Instruments, Zurich, Switzerland). The peak differential current during a transition was used as the characterizing parameter of the particle. The signal was amplified by a HF2TA trans-impedance amplifier (Zurich Instruments). A schematic drawing of the setup is shown in Figure 2C. The applied signal was 3 V (amplitude) with the attenuation of the low pass filter of the lock-in set to 24 dB with a bandwidth of 502 Hz. The sample rate was 28,800 Sa/s. The preamplifier trans-impedance gain was set to 10 kV/A.

The sample liquid was driven through the chip using a Nexus 3000 syringe pump (Chemyx Inc., Stafford, TX, USA) at a rate of 0.01 $\mu\text{L}/\text{min}$. The measurements were carried out at two frequencies simultaneously; a low frequency of 200 kHz and a high frequency of 7 MHz. These frequencies were selected based on experimentally recorded spectra at frequencies between 200 kHz and 10 MHz on samples containing different bacteria (*E. coli*, *S. aureus* and *L. anisa*—data shown in Supplementary Figure S1).

2.5. Samples

The experiments were generally performed in a low conductivity saline solution (PBS diluted to 1/20 with Milli-Q water) in order to better control the conductivity of the medium and to ensure that the medium was particle free before introducing *E. coli* and polystyrene beads. The conductivity of the prepared saline solution was measured to be 85 mS/m with a CDM210 conductivity meter (Radiometer Analytical, Lyon, France).

Additionally, experiments in tap water were carried out. The samples were prepared in tap water to demonstrate the capabilities of the biosensor in its envisioned operational environment, considering that solid particles often exist in tap water supply and hence should be distinguishable from bacteria contamination.

The concentration of bacteria (*E. coli* and/or *S. aureus*) and beads of 1 and 2 μm diameter in the two sample buffers was always $2.5 \times 10^6 \text{ mL}^{-1}$ for each particle type. The beads were used in order to test the system's ability to discriminate solid particles in the 1 μm to 2 μm range from bacteria (which have approximately the same size) in tap water.

For the experiments investigating the sample concentration, the bacteria (*E. coli*) concentration was varied while the concentration of 2 μm beads was kept constant at 2×10^6 beads/mL.

2.6. Data Acquisition and Analysis

The raw data was recorded by a computer and analyzed using a custom MATLAB script (MathWorks Inc., Natick, MA, USA), which identifies the differential peak current (Figure 2D) during a particle transition. The program identifies the height and width of the peaks from the transitions for the signal at both frequencies. The concentration of particles (C) is calculated using the transition time (t_{trans}) (i.e., the time it takes a particle to pass from one measurement electrode to the next) and

the volume (V) between the electrodes together with the number of events (N) during the time of a measurement (t_m):

$$C = (Nt_m)/(Vt_{trans}) = (N \times t_{trans})/(V \times t_m) \quad (1)$$

In this way, the calculated concentration is independent of the flowrate of the sample.

3. Results and Discussion

3.1. Separation of Biological and Non-Biological Samples in Diluted PBS and Tap Water

Samples in tap water containing *E. coli*, 1 μm and 2 μm beads were driven through the chip. Figure 3A,B show a correlation plot of the peak differential current measured at 200 kHz versus the opacity ((high frequency peak differential current)/(low frequency peak differential current)) versus the phase angle response measured at 7 MHz, respectively. We observe a clear separation in the measured current response at 200 kHz for 1 μm and 2 μm beads. *E. coli* and 1 μm beads have roughly the same volume, and thus provide the same current response at the low frequency. As seen in Figure 3A, a plot of the opacity versus current is not able to differentiate between bacteria and beads of the same volume. However, a clear separation between 1 μm beads and bacteria can be seen in the phase angle measurements at 7 MHz. It is also observed that the 1 μm and 2 μm beads share the same phase angle response due to their similar bulk composition. It is reasonable to assume that the membrane structure of *E. coli* introduces a phase response at 7 MHz, which is different from the signal from the polystyrene beads, which do not have a membrane. This makes the phase angle a potentially useful parameter for differentiating microorganisms from other particles in tap water.

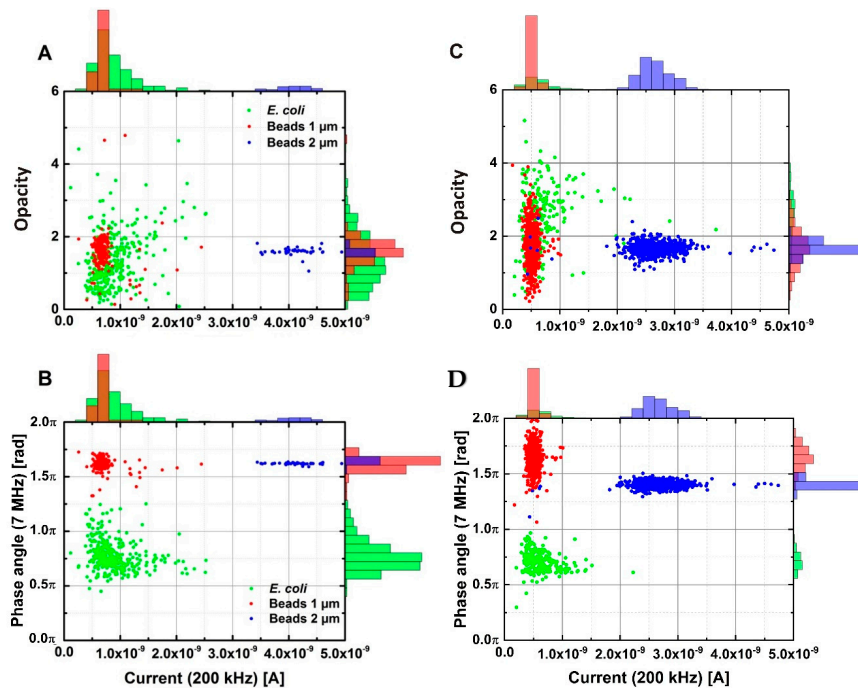


Figure 3. (A) Opacity plotted against the low frequency signal of *E. coli* and polystyrene beads in drinking water. (B) Phase shift at 7 MHz plotted against the low frequency signal of *E. coli* and polystyrene beads in drinking water. (C,D) Same as (A,B), but with the bacteria and beads dispersed in $1/20 \times$ PBS.

Tap water can be a difficult buffer to work with as its composition and electrical properties vary depending on the time of day and the source. In order to have a well-controlled buffer with a conductivity in the same range as tap water we used PBS diluted 20 times with milli-Q water ($1/20\times$ PBS), which has a conductivity of 0.085 S/m. *E. coli*, 1 μm and 2 μm beads were added to the buffer and the impedance response was measured with the sensor. The results are shown in Figure 3C,D. It is evident that the two buffers behave similarly, with the correlation plot of the current at 200 kHz versus the phase angle at 7 MHz still showing a clear separation between bacteria and beads. The small differences in the phase of the 1 and 2 μm beads in Figure 3D can most likely be attributed to the function of the filters in the measurement setup and variations in the data analysis algorithm.

Figure 3 confirms that $1/20\times$ PBS is a good substitute to tap water when one wants to control the properties of the liquid better, considering that tap water comes in a variety of conductivities and composition. We note here that the ionic strength (and effectively the conductivity) of the solution has an effect on the recorded high frequency phase. Tap water comes in a range of different conductivities, but it should preferably be between 0 and 150 mS/m to be suitable for human consumption. In this range of conductivities the phase signal from the bacteria is stable, as is shown in Figure S2 (Supplementary Data), and we can therefore conclude that local variations in drinking water conductivity will not have an effect on the sensor. However, we note that at higher conductivities the phase signal will change, e.g., if PBS is used as the solution, in which case the bacteria can no longer be distinguished from polystyrene beads (Figure S3 in Supplementary Data).

3.2. Determination of Bacteria Concentration

It is not essential to know the exact bacteria concentration when detecting sudden contamination events, however, it is very important to be able to detect a change in the bacteria concentration, as it is this change in concentration, which is used to determine if the water supply has been suddenly contaminated. As a result, any bacteria detection system should be capable of rapidly determining any increase in bacteria concentration.

To demonstrate the sensor's ability to accurately measure changes in concentration five samples with varying *E. coli* concentration and a fixed concentration of 2 μm beads were prepared (see Table 1). The concentration was then determined with the sensor with a measurement time of 25–30 min per sample. The samples were also plated and the colonies were counted after 24 h. The calculated concentrations by the EIS system (Equation (1)) and the plate count are shown in Table 1.

Table 1. Details of the concentration determination experiments, along with the measured transitions and the calculated concentrations by EIS and plating.

Sample	Measurement Time (s)	Beads (#)	Beads (/mL)	<i>E. coli</i> (#)	<i>E. coli</i> (/mL)	Plate Count (/mL)
A	1551.46	377	191,202	7	6221	3000
B	1554.65	426	201,612	92	48,181	154,000
C	1551.71	398	192,603	224	118,006	326,000
D	1551.9	366	185,596	483	274,769	643,000
E	1861.85	445	186,478	843	396,767	1.00×10^6

The plots shown in Figure 4 depict the measured data of the bacteria concentration as detected by the system and by CFU counting. The bacteria count of the system is not identical to the results obtained with the CFU method, but there is a proportional relation between the measured values by EIS and the values obtained by CFU. This indicates that the difference between the two counting methods is caused by the way the concentration is estimated (see Section 2.6), for example due to variations in the detection volume that arise from fabrication. The result could also be influenced by smaller bacteria, which are missed due to a lack of sensitivity in the system. The 2 μm beads are all counted successfully as the signal from these is at least 8 times larger than that for the bacteria. Even though the system is not able to accurately determine the exact concentration of bacteria in a sample, its ability to precisely determine a change in concentration makes it a candidate for monitoring bacteria contaminations

in liquid samples. Moreover, since the relationship between the actual (by CFU) concentration and measured concentration is linear, then the actual concentration can be accurately estimated after a system calibration.

We note that the discrepancy observed in sample A, where the concentration calculated by EIS is larger than the one found by CFU which arises due to statistical variations in low concentration samples along with the in-built errors in the data processing. Indeed, we note that in the 25 min of the experiment only seven transitions were registered as opposed to about 100 and over in samples B to E. As the data analysis software can erroneously detect up to five transition events in a clean sample, it is likely that the EIS calculated concentration for sample A is overestimated. From Table 1 and using samples B to E we can also estimate our detection limit as the concentration required for detecting a single transition event as 522 ± 40 bacteria/mL.

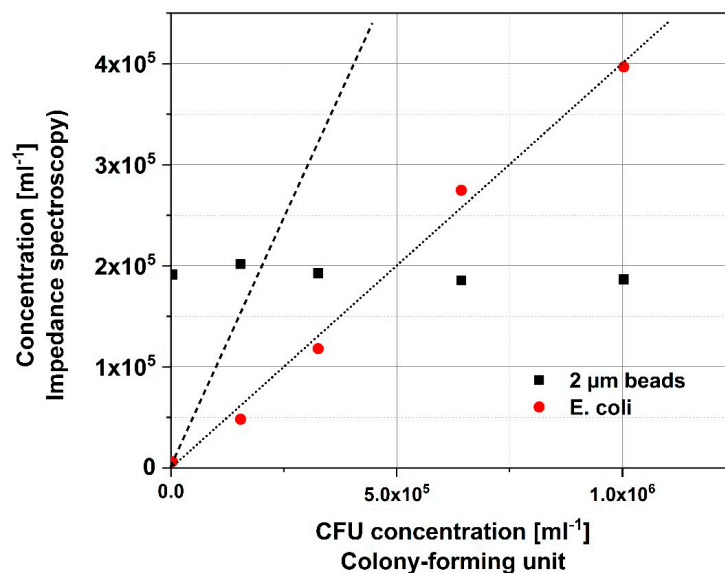


Figure 4. Bacteria concentration measured with the system (impedance spectroscopy) and colony-forming unit counting. The beads were only counted using the system and their concentration was kept constant at 2×10^5 mL⁻¹. The dashed line represents the 1:1 relation between the two methods. The dotted trend line for the *E. coli* data has an R^2 value of 0.9937.

3.3. Differentiation between Gram-Positive and Gram-Negative Bacteria

The structural differences between the membranes of Gram-positive and Gram-negative bacteria make it probable that a difference will appear on the high frequency phase signal. This is indeed the case, as can be shown in Figure 5. Figure 5A shows the correlation plot for three samples, one containing *E. coli* mixed with polystyrene beads, one containing *S. aureus* (MSSA) and one containing a mixed population of *E. coli*, MSSA and beads. In Figure 5A we can see that distinct populations appear around 2, 3 and 5 rad, with the population at 5 rad visible in all the samples, suggesting that this population comes from the polystyrene beads that were present in two of the samples. As the MSSA sample did not contain beads, it is plausible that there is some bead contamination in the system, giving rise to the bead signal in the MSSA sample.

By plotting the number of points appearing at the different phase angles in Figure 5B, we can see that *E. coli* and MSSA indeed present two distinct populations at 2 and 3 rad, respectively. Fitting the data using normal distributions we find that the mean phase value for the *E. coli* is 2.22 rad with a

standard deviation of 0.55 rad ($n = 325$), while the mean phase value for MSSA is 3.09 rad with a standard deviation of 0.26 rad ($n = 241$). The two means are statistically significantly different as the p -value is of the order of 10^{-90} . However, we note that the tails for the two distributions overlap at approximately the mean $+1 \times$ standard deviation for *E. coli* and the mean $-1 \times$ standard deviation for MSSA. Assuming a Gaussian distribution for the two populations, this means that we can correctly identify and categorize 84% of the bacteria in the sample.

Whether or not the differentiation method can be generalized to a larger number of different bacteria is still under investigation. Theoretically, different bacteria types have different membrane and cytoplasm structures and should therefore have different dielectric properties, though admittedly the differences are small. However, increasing the system sensitivity can be achieved by changing the channel geometry (e.g., in [30]), using a different set of frequencies or combining EIS with other dielectric based methods, such as DEP.

3.4. General Discussion

In the above we have presented how our device can detect and differentiate *E. coli* and *S. aureus* in water samples, however, the limit of detection (LOD) is far from what is required for such a sensor. The acceptable limit is 1 coliform per 100 mL water which is much lower than the ca. 500 bacteria/mL that our device can measure. Although *E. coli* and *S. aureus* were used as test bacteria in order to validate our method against the standard plate count, the purpose of this device is not to reach this type of sensitivity for a single bacteria species but to provide the total bacteria count in a water sample and detect changes to this number. Indeed, there are four main indicators used for water quality [31]: (a) Heterotrophic plate count (HPC), which refers to the number of culturable bacteria in a water sample, (b) Total coliform, (c) Fecal coliform and (d) *E. coli*. The presented sensor aims to address the first indicator, HPC [32]. Significant changes in HPC serve as an alert for possible deterioration of water quality, triggering further investigation. However, HPC only measures culturable bacteria, with the total number of bacteria being 1000 to 10,000 times higher [33]. The presented device can measure all bacteria in water, culturable or not, and therefore provides a fast and accurate measurement of the total bacteria count, that does not involve time-consuming culturing steps. The Danish limits for HPC are 5 bacteria per mL at 37 °C, which means a total of 5000 to 50,000 bacteria per mL, which is easily achievable with the presented device.

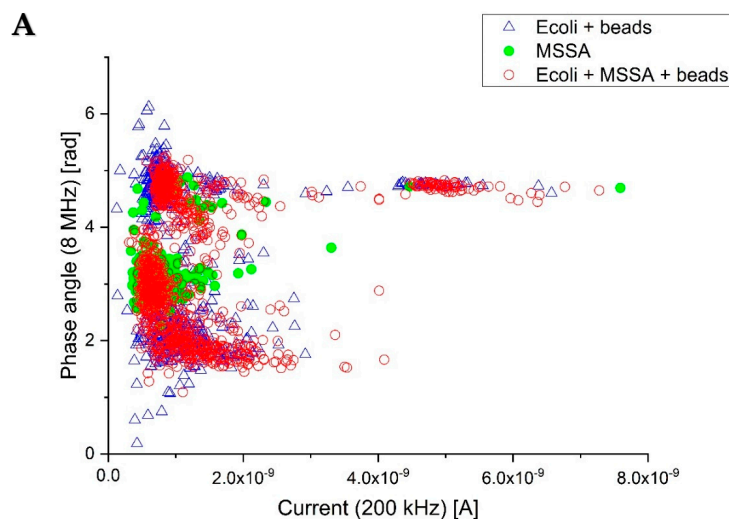


Figure 5. Cont.

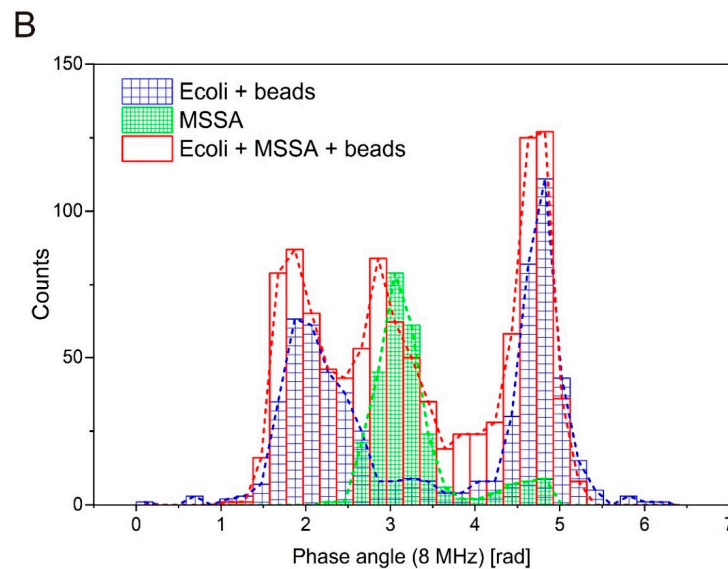


Figure 5. (A) Phase shift at 8 MHz plotted against the low frequency signal of the bacteria *E. coli* and *S. aureus* and polystyrene beads in diluted PBS (B) Histogram of the high frequency phase angle, clearly showing the two populations of bacteria.

The maximum continuous and flawless operation time for this device installed in a water pipe was 14 days, which is not adequate for a real life application. Future work will focus on improving the stability of the system and on establishing the functionality in real-world samples.

4. Conclusions

In conclusion, a microfluidic chip was fabricated and used to distinguish *E. coli* from solid particles represented by polystyrene beads in both tap water as well as a diluted saline solution using multi-frequency impedance spectroscopy. Using the phase angle response at a frequency of 7 or 8 MHz, *E. coli* bacteria could be separated from polystyrene beads on a single transition basis. Moreover, we were able to distinguish between gram-positive and gram-negative bacteria using this method. Together with the system's ability to detect bacteria concentrations with an LOD of 522 mL^{-1} and its ability to accurately determine a change in bacteria concentration, the system has been demonstrated to be an interesting candidate for further operational testing. All measurements were obtained with the label free technique of electrical impedance flow cytometry, and the results show great promise for using electrical impedance flow cytometry as the detection principle of the next generation of online and real-time water quality control sensors.

Supplementary Materials: The following are available online at <http://www.mdpi.com/1424-8220/18/10/3496/s1>.

Author Contributions: Conceptualization, C.V.B., G.E.S., R.R.-T. and J.D.T.; Data curation, C.H.C., M.D., C.V.B., G.E.S. and J.D.T.; Formal analysis, M.D. and C.V.B.; Funding acquisition, W.E.S.; Investigation, C.H.C., C.V.B. and G.E.S.; Project administration, W.E.S.; Supervision, R.R.-T. and W.E.S.; Validation, C.V.B.; Writing—original draft, C.H.C. and M.D.; Writing—review & editing, M.D., C.V.B., J.D.T. and W.E.S.

Funding: The research was supported by the Carlsberg Foundation (grant no. 2012_01_0191) and the Novo Nordisk foundation (grant no. 9659).

Conflicts of Interest: The authors declare no conflict of interest. The funders had no role in the design of the study; in the collection, analyses, or interpretation of data; in the writing of the manuscript, or in the decision to publish the results.

References

- Højris, B.; Christensen, S.C.; Albrechtsen, H.J.; Smith, C.; Dahlqvist, M. A novel, optical, on-line bacteria sensor for monitoring drinking water quality. *Sci. Rep.* **2016**, *6*, 23935. [[CrossRef](#)] [[PubMed](#)]
- Lopez-Roldan, R.; Tusell, P.; Cortina, J.L.; Courtois, S. On-line bacteriological detection in water. *TrAC Trends Anal. Chem.* **2013**, *44*, 46–57. [[CrossRef](#)]
- Hargeshimer, E.E.; Conio, O.; Popovicova, J.; Proaqua, C. *Online Monitoring for Drinking Water Utilities*; American Water Works Association: Denver, CO, USA, 2002.
- Hammes, F.; Egli, T. Cytometric methods for measuring bacteria in water: Advantages, pitfalls and applications. *Anal. Bioanal. Chem.* **2010**, *397*, 1083–1095. [[CrossRef](#)] [[PubMed](#)]
- Gawad, S.; Cheung, K.; Seger, U.; Bertsch, A.; Renaud, P. Dielectric spectroscopy in a micromachined flow cytometer: Theoretical and practical considerations. *Lab Chip* **2004**, *4*, 241–251. [[CrossRef](#)] [[PubMed](#)]
- Olesen, T.; Valvik, M.C.; Larsen, N.A.; Sandberg, R.H.; Unisensor, A.S. Optical Sectioning of a Sample and Detection of Particles in a Sample. U.S. Patent 8,780,181, 15 July 2014.
- Díaz, M.; Herrero, M.; García, L.A.; Quirós, C. Application of flow cytometry to industrial microbial bioprocesses. *Biochem. Eng. J.* **2010**, *48*, 385–407. [[CrossRef](#)]
- Gawad, S.; Schild, L.; Renaud, P.H. Micromachined impedance spectroscopy flow cytometer for cell analysis and particle sizing. *Lab Chip* **2001**, *1*, 76–82. [[CrossRef](#)] [[PubMed](#)]
- Holmes, D.; Pettigrew, D.; Reccius, C.H.; Gwyer, J.D.; van Berkel, C.; Holloway, J.; Davies, D.E.; Morgan, H. Leukocyte analysis and differentiation using high speed microfluidic single cell impedance cytometry. *Lab Chip* **2009**, *9*, 2881–2889. [[CrossRef](#)] [[PubMed](#)]
- Sun, T.; Morgan, H. Single-cell microfluidic impedance cytometry: A review. *Microfluid. Nanofluid.* **2010**, *8*, 423–443. [[CrossRef](#)]
- David, F.; Hebeisen, M.; Schade, G.; Franco-Lara, E.; Di Berardino, M. Viability and membrane potential analysis of *Bacillus megaterium* cells by impedance flow cytometry. *Biotechnol. Bioeng.* **2012**, *109*, 483–492. [[CrossRef](#)] [[PubMed](#)]
- Ayliffe, H.E.; Frazier, A.B.; Rabbitt, R.D. Electric impedance spectroscopy using microchannels with integrated metal electrodes. *J. Microelectromec. Syst.* **1999**, *8*, 50–57. [[CrossRef](#)]
- Lin, R.; Simon, M.G.; Lee, A.P.; Lopez-Prieto, J. Label-free detection of DNA amplification in droplets using electrical impedance. In Proceedings of the 15th International Conference on Miniaturized Systems for Chemistry and Life Sciences, Seattle, WA, USA, 2–6 October 2011; Volume 3, pp. 1683–1685.
- Haandbæk, N.; Bürgel, S.C.; Heer, F.; Hierlemann, A. Characterization of subcellular morphology of single yeast cells using high frequency microfluidic impedance cytometer. *Lab Chip* **2014**, *14*, 369–377. [[CrossRef](#)] [[PubMed](#)]
- Holmes, D.; Morgan, H. Single Cell Impedance Cytometry for Identification and Counting of CD4 T-Cells in Human Blood Using Impedance Labels. *Anal. Chem.* **2010**, *82*, 1455–1461. [[CrossRef](#)] [[PubMed](#)]
- Evander, M.; Ricco, A.J.; Morser, J.; Kovacs, G.T.; Leung, L.L.; Giovangrandi, L. Microfluidic impedance cytometer for platelet analysis. *Lab Chip* **2013**, *13*, 722–729. [[CrossRef](#)] [[PubMed](#)]
- Kirkegaard, J.; Clausen, C.H.; Rodriguez-Trujillo, R.; Svendsen, W.E. Study of Paclitaxel-Treated HeLa Cells by Differential Electrical Impedance Flow Cytometry. *Biosensors* **2014**, *4*, 257–272. [[CrossRef](#)] [[PubMed](#)]
- Mernier, G.; Hasenkamp, W.; Piacentini, N.; Renaud, P. Multiple-frequency impedance measurements in continuous flow for automated evaluation of yeast cell lysis. *Sens. Actuators B Chem.* **2012**, *170*, 2–6. [[CrossRef](#)]
- Morgan, H.; Sun, T.; Holmes, D.; Gawad, S.; Green, N.G. Single cell dielectric spectroscopy. *J. Phys. D Appl. Phys.* **2007**, *40*, 61–70. [[CrossRef](#)]
- Haandbæk, N.; Bürgel, S.C.; Heer, F.; Hierlemann, A. Resonance-enhanced microfluidic impedance cytometer for detection of single bacteria. *Lab Chip* **2014**, *14*, 3313–3324. [[CrossRef](#)] [[PubMed](#)]
- Grossman, N.; Ron, E.Z.; Woldringh, C.L. Changes in cell dimensions during amino acid starvation of *Escherichia coli*. *J. Bacteriol.* **1982**, *152*, 35–41. [[PubMed](#)]
- Freeman, J.T.; Anderson, D.J.; Sexton, D.J. Seasonal peaks in *Escherichia coli* infections: Possible explanations and implications. *Clin. Microbiol. Infect.* **2009**, *15*, 951–953. [[CrossRef](#)] [[PubMed](#)]

23. Mitra, K.; Ubarretxena-Belandia, I.; Taguchi, T.; Warren, G.; Engelman, D.M. Modulation of the bilayer thickness of exocytic pathway membranes by membrane proteins rather than cholesterol. *Proc. Natl. Acad. Sci. USA* **2004**, *101*, 4083–4088. [[CrossRef](#)] [[PubMed](#)]
24. Sanchis, A.; Brown, A.P.; Sancho, M.; Martinez, G.; Sebastian, J.L.; Munoz, S.; Miranda, J.M. Dielectric characterization of bacterial cells using dielectrophoresis. *Bioelectromagnetics* **2007**, *28*, 393–401. [[CrossRef](#)] [[PubMed](#)]
25. Wyatt, P.J. Cell Wall Thickness, Size Distribution, Refractive Index Ratio and Dry Weight Content of Living Bacteria (*Staphylococcus aureus*). *Nature* **1970**, *226*, 277–279. [[CrossRef](#)] [[PubMed](#)]
26. Park, S.; Zhang, Y.; Wang, T.H.; Yang, S. Continuous dielectrophoretic bacterial separation and concentration from physiological media of high conductivity. *Lab Chip* **2011**, *11*, 2893–2900. [[CrossRef](#)] [[PubMed](#)]
27. Demierre, N.; Braschler, T.; Linderholm, P.; Seger, U.; van Lintel, H.; Renaud, P. Characterization and optimization of liquid electrodes for lateral dielectrophoresis. *Lab Chip* **2007**, *7*, 355–365. [[CrossRef](#)] [[PubMed](#)]
28. Moresco, J.; Clausen, C.H.; Svendsen, W. Improved anti-stiction coating of SU-8 molds. *Sens. Actuators B Chem.* **2010**, *145*, 698–701. [[CrossRef](#)]
29. Serra, S.; Schneider, A.; Malecki, K. A simple bonding process of SU-8 to glass to seal a microfluidic device. In Proceedings of the Multi-Material Micro Manufacture, Borovets, Bulgaria, 3–5 October 2007; pp. 43–46.
30. Clausen, C.H.; Skands, G.E.; Bertelsen, C.V.; Svendsen, W.E. Coplanar Electrode Layout Optimized for Increased Sensitivity for Electrical Impedance Spectroscopy. *Micromachines* **2015**, *6*, 110–120. [[CrossRef](#)]
31. Verhille, S. Understanding Microbial Indicators for Drinking Water Assessment: Interpretation of Test Results and Public Health Significance. National Collaborating Center for Environmental Health. Available online: http://www.nceeh.ca/sites/default/files/Microbial_Indicators_Jan_2013_0.pdf (accessed on 16 October 2018).
32. World Health Organisation (WHO). *Guidelines for Drinking-Water Quality Incorporating First Addendum*, 3rd ed.; WHO: Geneva, Switzerland, 2006; Volume 1, p. 285.
33. Staley, J.T. Measurement of in situ activities of nonphotosynthetic microorganisms in aquatic and terrestrial habitats. *Ann. Rev. Microbiol.* **1985**, *39*, 321–346. [[CrossRef](#)] [[PubMed](#)]



© 2018 by the authors. Licensee MDPI, Basel, Switzerland. This article is an open access article distributed under the terms and conditions of the Creative Commons Attribution (CC BY) license (<http://creativecommons.org/licenses/by/4.0/>).

5.2 Influence of effective conductivity relative to the medium

When going through the theory of the impedance response of bacteria in chapter 2, we noted how the differential argument of the impedance between two electrode sets ($\arg(Z - Z_0)$) would shift significantly even when the argument from a single set (Z) would only change a little. In chapter 4 we also saw how the differential argument (at low and especially at high frequencies) was one of the best parameters to choose to differentiate between *E. coli* and polystyrene beads (figure 4.6). Before we go through more experimental data, we should discuss why this is in more detail.

Consider the phasor diagram shown in figure 5.1a. Two phase vectors, A and B1, are shown, and the modulus of phasor A is larger than the modulus of phasor B1. Similarly, two phasors are shown in figure 5.1b, but here the modulus of B2 is larger than the modulus of A. Finally, 5.1c shows the differential phasor (A-B1 and A-B2), and we see that the two differential phasors are out of phase (ie. they have a difference in argument of π) even though all three of the original phasors were completely in-phase. This example may seem trivial, but it can be related directly to our model of the differential impedance between two electrode sets during the transition of a bacteria or particle. As a bacteria passes between the first electrode set it will either increase or decrease the impedance compared to the situation when nothing but electrolyte is present between the electrodes. Since we always measure the difference in impedance, the argument (or phase) of the differential argument is directly dependent on whether the passing bacteria increases or decreases the impedance (ie. whether the modulus of the phasor is smaller or larger). If the impedance from both electrode sets are in-phase this means that the differential argument shifts with π -radians, but even if the two original phasors are not perfectly in-phase, the differential argument will still shift.

The same example, illustrated using the signal waveforms instead of phasors, is presented in the draft for the paper manuscript "The influence of exposure time in classification of heat-treated *E. coli* using impedance flow cytometry", presented in chapter 7.

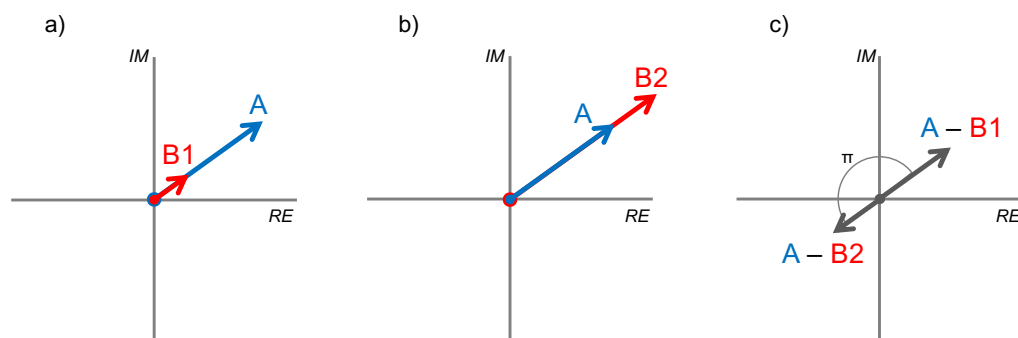


Figure 5.1: Phasor diagram illustrating the shift in differential argument as the modulus of two subtracted vectors changes. a) Modulus of A is larger than B1, b) Modulus of A is smaller than B2, c) the difference in argument between A-B1 and A-B2 will be π .

Whether the impedance is decreased or increased will depend on the effective conductivity of the bacteria compared to the surrounding electrolyte. For example, an intact bacteria

measured at a frequency low enough that the impedance across the membrane capacitor is very high will increase the impedance, but when the frequency is increased and the impedance across the capacitor drops it will appear more conductive than the surrounding medium if the medium conductivity is lower than that of the cytoplasm in the interior of the cell.

This idea can be generalized so that when the differential argument is plotted, e.g. in a scatter plot with low and high frequency differential argument on axis, the event populations will move between 3 primary positions each separated by roughly π -radians:

1. Events are effectively *less* conducting than the surrounding medium at both low and high frequency
2. Events are effectively *less* conducting than the surrounding medium at the low frequency, but *more* conducting in the high frequency
3. Events are effectively *more* conducting than the surrounding medium at both low and high frequency

In principle a fourth position exists where events that are more conducting in the low frequency compared to the high frequency would be placed, but it is not obvious what kind of real world particles would have this property. Perhaps, coiled nanotubes or similar structures would have inductor like properties, but this is pure speculation. For now we will stick to the 3 primary positions as shown in figure 5.2.

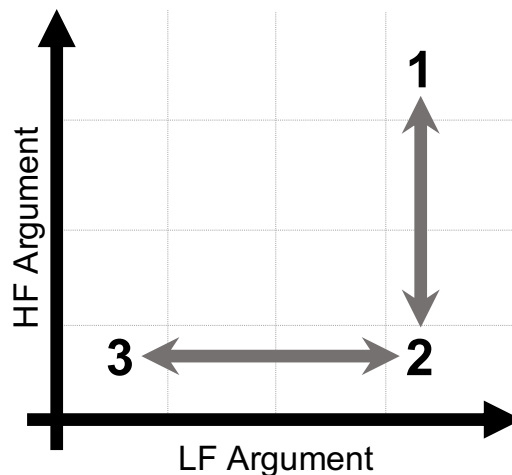


Figure 5.2: Sketch showing the 3 primary populations events will take in an differential argument scatterplot.

The placement of events among the 3 populations depends on the chosen frequency and the conductivity of the medium. In BactoBox the measurement frequencies (366 kHz and 6.9 MHz) are chosen so that the membrane shields the interior of the bacteria at the low frequency but the cytoplasm is probed at the high frequency. Similarly it is crucial to choose a medium conductivity below the expected cytoplasm conductivity in order to see the π -shift. The standard medium conductivity used for BactoBox measurements is

80 mS/m, which is below the cytoplasm conductivity found in the majority of bacteria. Under these conditions, we can say something about what kind of cells and particles we expect to see in the 3 positions:

- **Position 1:** Homogeneous non-conducting beads such as polymer beads (e.g. polystyrene), glass beads or ceramic beads. Also cells and cell like structures (e.g. vesicles or liposomes) where either the interior medium has a conductivity that is lower than that of the surrounding medium or where the membrane is too thick to be properly penetrated by the electric field even at the high frequency.
- **Position 2:** Intact cells and bacteria where the membrane shields the cytoplasm at the low frequency but is bypassed at the high frequency, so that the higher conductivity cytoplasm is probed.
- **Position 3:** Homogeneous conducting beads such as metal beads. Bacteria with perforated membranes that allow the cytoplasm to be probed even at low frequencies. Particles with conducting outer layers where current can run in the shell of the particle without having to first bypass a conducting membrane.

In order to illustrate the 3 positions experimentally, a simple experiment using polystyrene beads (2 μm from Polysciences, USA, non-conducting at both frequencies), *E. coli* (ATCC 8739, non conducting in the low frequency but conducting in the high frequency) and silver coated silica beads (85 nm silver coating on a 2 μm silica bead from Cospheric, USA, conducting at both frequencies). The measured differential arguments are shown in figure 5.3 and we see that the polystyrene beads are placed in location 1, the intact *E. coli* cells in position 2, and the conducting silver coated beads in position 3. The events showing up in position 1 for beads and bacteria are considered background particles present in every measurement. Generally there is always a few particles detected even when the the sample have been pre-filtered (e.g. sterile filtration through a 0.22 μm filter). The background can be particles left over in the system or debris e.g. from the tubing of the peristaltic pump. The frequencies used for measurements was 366 kHz and 6.9 MHz. All three samples were suspended in 1/20xPBS diluted with ultra pure water.

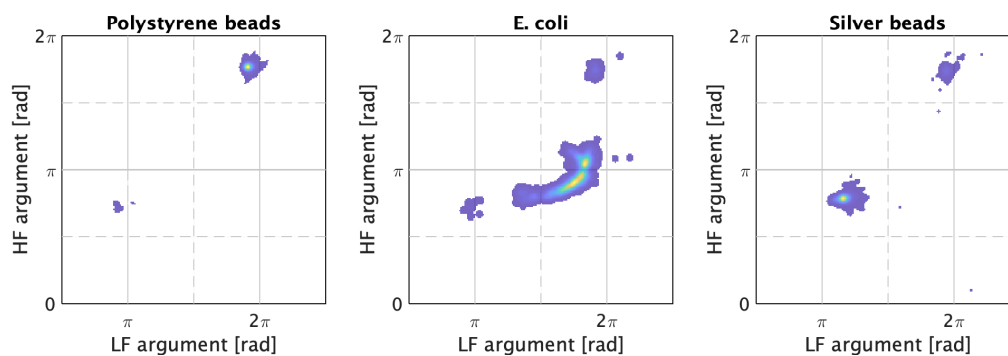


Figure 5.3: Differential argument measured on (a) polystyrene beads, (b) *E. coli* and (c) silver coated beads illustrating the 3 dominating positions in the argument plot. The frequencies used for measurements was 366 kHz and 6.9 MHz. All three samples were suspended in 1/20xPBS diluted with ultra pure water.

5.3 Growth tracking of *E. coli*

Most of the experimental work that is presented in this thesis focuses on the characterization of bacteria and not on the quantification. However, here I would like to present the results from a simple experiment where I am using BactoBox to track the growth of an *E. coli* culture by progressively measuring the concentration of cells and comparing it to concentration measurements using drop plating [69] on agar plates. The tracking of cell culture is an interesting commercial application for BactoBox, e.g. in fermentation processes.

The strain of *E. coli* used for this experiment is again ATCC 8739. It is grown overnight (ON) at 37°C in tryptic soy broth (TSB) after which 100 µl is reinoculated into 10 ml TSB. The concentration in the ON culture is roughly 10⁹/ml and we therefore expect a starting concentration of 10⁶. This means that we are not starting the cultures in the very early exponential phase and expect to be able to see the concentration increase fairly quickly. Every 2 hours 150 µl culture is extracted for experiments so that the final culture volume after 12 hours is 8.95 ml. 3 sample for BactoBox measurements are prepared by pipetting 3 µl from the extracted culture into 3 ml of 1/20xPBS (150 µl 1xPBS + 2.85 ml ultra pure water). 3 samples are prepared for each extraction time and measured with BactoBox. The measurement time for each sample is 180 seconds. Concentrations for each sample is calculated using the equations presented in section 3.4.2 (taking the 100x dilution into account) after which the mean and standard deviation is calculated for each extraction time. 10-fold dilution of the extracted culture is also made and plated on tryptic soy agar plates (TSA) using the drop plate technique (3 drops for each dilution). After 24 hours the CFU are counted and the original concentration is calculated based on the specific dilution.

The resulting concentrations from BactoBox measurements and plate counts can be seen in figure 5.4 and we see very good correlation between the obtained concentrations.

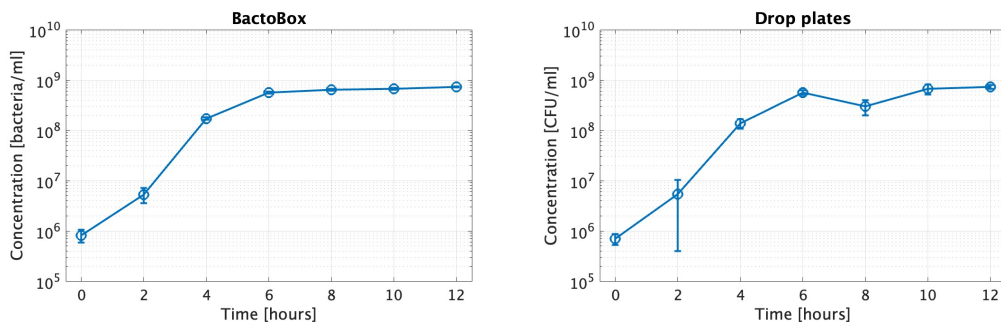


Figure 5.4: Growth tracking of *E. coli*. Concentration measurements of a growing culture of *E. coli* using BactoBox (left) and drop plates counts (right). Standard deviation based on 3 measurements are shown for each time point.

5.4 Different bacteria species

Bacteria are one of the most diverse organisms on earth with variation in both genotype and phenotype. In order to understand how (or if) this diversity influences measurements with IFC, 6 bacteria species (shown in table 5.1) were chosen, 3 gram-positive and 3 gram-

negative. 5 out of 6 of the species are rod shaped (the last is spherical), but even between the rod shaped species the diversity can be significant. For example, *B. subtilis* can grow to be ~ 20 μm in length depending on growth conditions, while *Acinetobacter baumannii* is much shorter and almost spherical. In this section, the impedance measurements of the 6 strains are presented and compared using an analysis based on ROC characteristics (see section 4.2.1). Specifically, we will test if it is possible to tell the species apart based on their shape and gram-type (ie. due to differences in cell envelope - see section 2.2).

Table 5.1: Overview of the 6 species used for experiments

Name	Strain	Gram	Shape	Other characteristics
<i>Escherichia coli</i>	ATCC 8739	neg	Rod	1-3 μm by 0.5 μm [70]
<i>Klebsiella aerogenes</i>	ATCC 13048	neg	Rod	Approximately 1-3 μm in length
<i>Acinetobacter baumannii</i>	NCIMB 12457	neg	Rod	Typically 1.0–1.5 μm by 1.5–2.5 μm , more coccoid like in the stationary phase [71]
<i>Listeria innocua</i>	ATCC 33090	pos	Rod	Short rod with rounded ends that occurs singly, in parallel, or in V shapes [72]. On the order of 0.5–2 μm in length [73]
<i>Bacillus subtilis</i> subsp. <i>spizizenii</i>	ATCC 6633	pos	Rod	Large and spore-forming cells with a sizes of 0.3-22 μm \times 1.2-7.0 μm [74]
<i>Staphylococcus epidermidis</i>	ATCC 12228	pos	Spherical	1 μm in diameter [75], found on skin and in mucous membranes [76], grows in cluster or as diplococci

Experiments were carried out with BactoBox v2 and flow cell design Q. All bacteria were grown in 10 ml tryptic soy broth (TSB) at 37°C with shaking at 200 rpm. All 6 species were grown under these conditions to simplify the experimental workflow, however some of the species will grow faster under other conditions. For example, it is recommended that *B. subtilis* is grown at 30°C, not 37°C. This difference in growth condition could affect the cell morphology and subsequently the impedance results. These results should therefore only be seen as an indication of how impedance can be used to sense morphological and electrical differences between species at these specific conditions, and not the final answer to what the impedance response of the specific species is. 3 μl from an over night (ON) culture of each species was reinoculated in TSB. For BactoBox measurements, 3 μl from each sample was extracted and diluted into 3 ml 1/20xPBS (phosphate buffered saline

diluted with ultra pure water). This was done after 3, 4, 5, 6, 7, 17, 19, 21 and 23 hours. Furthermore, the cultures were left in the incubator and samples were extracted after 7 and 14 days. BactoBox measurements were carried out at 366 kHz and 6.9 MHz as always. Measurements on polystyrene beads samples were performed before each time step to ensure that the impedance measurements were consistent.

In figure 5.5 and 5.6, kernel density plots of the resulting argument is shown for each species (and the polystyrene beads) from the measurements after 21 hours and after 7 days. The results from the remaining time steps can be found in Appendix B.1.

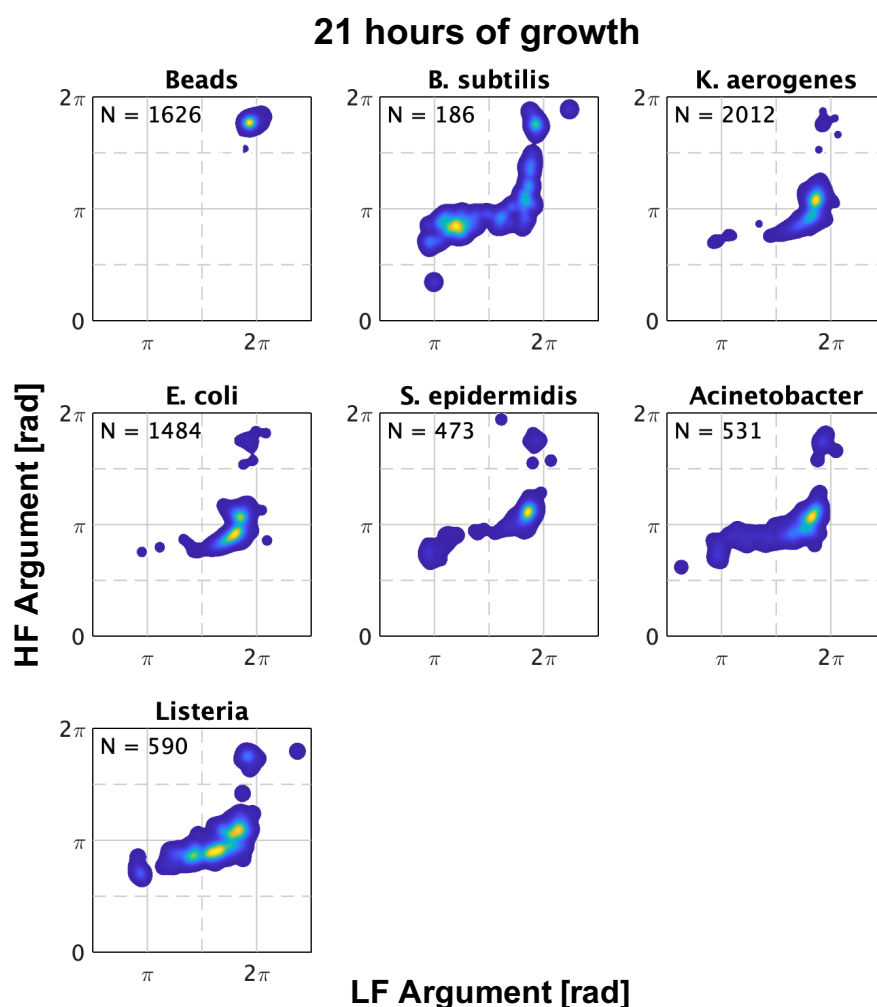


Figure 5.5: Kernel density plot of the low (366 kHz) and high (6.9 MHz) frequency differential argument from measurements of 6 species after 21 hours of growth. Number in the corner of each plot indicates the number of events that the kernel density plot is based on.

After 21 hours (figure 5.5) all 6 species have grown, but it is clear from the number of

events that they do not grow at the same rate. Especially the *B. subtilis* grow slow and based on the number of events we have 10x more *E. coli* than *B. subtilis* after 21 hours. The cell populations from all 6 species are placed at or in between the 3 primary positions discussed in the previous section. Except for *B. subtilis*, every species seems to have the majority of the events around position 2 as expected. However, it is also clear that, while the populations appear in the same general area, they are not identical. This is encouraging since it means that different species of bacteria do have different impedance response and that the difference can be visualized by the differential argument. It is not simple to determine the exact cell property that causes this difference from the density plots alone. For example, it appears that the highest density point of the *S. epidermidis* population is closer to position 1 (non-conductive) than e.g. the high point of the *E. coli* population. This could be because the membrane of the *S. epidermidis* is thicker than that of *E. coli* and therefore less transparent, but this can not be concluded directly from the density plots. The most distinct species population is that of *B. subtilis*, whose events are smeared across the range between the 3 primary positions. The highest density of cells are found close to position 3, indicating that the cells are more conducting than the medium around them, even in the low frequency. We will look at this in more detail in the coming section, but from just the density plots it is not apparent that the observed variation relates to the gram-type of the species. The populations of the gram-negative *E. coli* and *K. aerogenes* do appear similar in shape and location, but the 3 gram-positive species (*B. subtilis*, *S. epidermidis*, *Listeria*) do not.

After 7 days of growth (figure 5.6), we can see that the positions of the cell populations have changed. The *E. coli* and *K. aerogenes* populations remain largely in the same place, but both populations are less confined than they were after 21 hours. The *B. subtilis* population is also more confined than before and we now see the majority of the cells located at position 3. The same can almost be said for the *Acinetobacter* populations, where the majority of the cells are also located at position 3, but with a tail reaching across into position 2 and 1. The *Listeria* and *S. epidermidis* populations have split into 2 (maybe even 3 for *Listeria*) placed at position 2 and 3. After 7 days of growth, the cell cultures have undergone several cycles of perpetual cell growth and cell death. It is possible that the cells found at position 1 and 3 are dead or non-viable cells still present in the culture. It is however not obvious why these cells would be significantly more apparent in e.g. *S. epidermidis* compared to *E. coli*. The influence and characterization of non-viable cells will be discussed further in chapter 7.

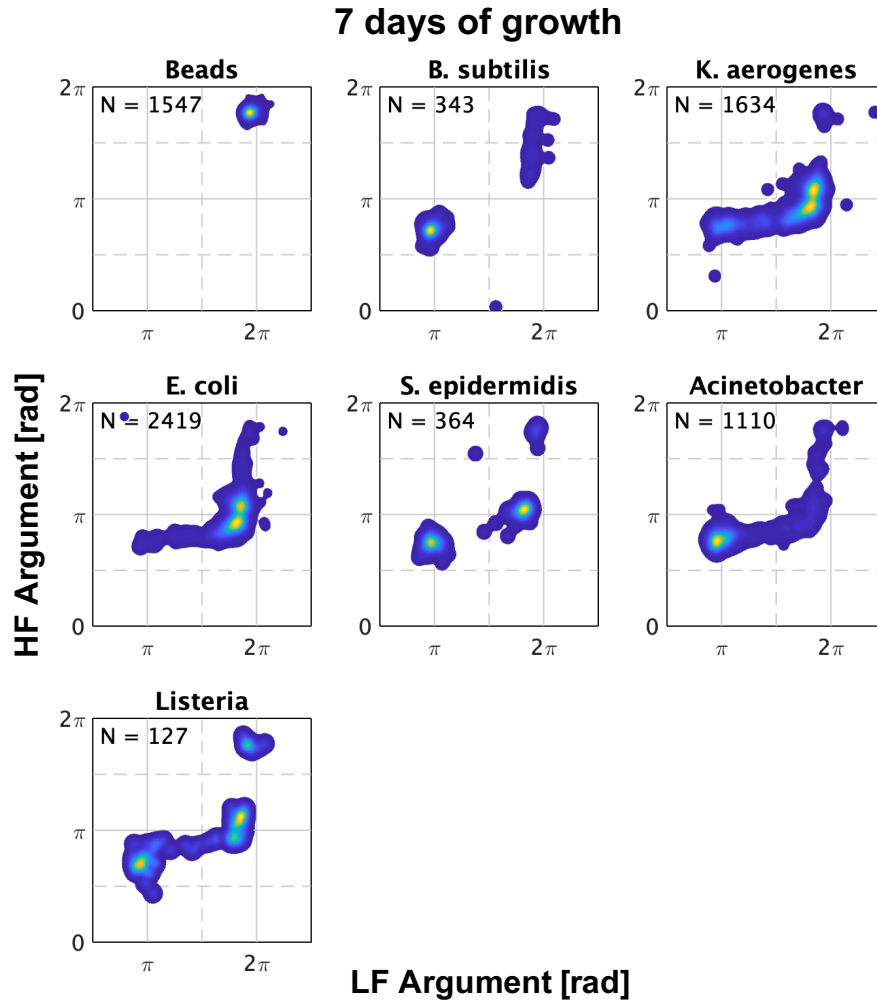


Figure 5.6: Kernel density plot of the low (366 kHz) and high (6.9 MHz) frequency differential argument from measurements of 6 species after 7 days of growth. Number in the corner of each plot indicates the number of events that the kernel density plot is based on.

Comparing gram-positive and gram-negative species

For a more quantitative comparison of the 3 gram-positive and 3 gram-negative species we group the populations together based on their gram-type and evaluate if it is possible to classify the two groups based on the differential argument. Figure 5.7 shows the calculated ROC curves comparing the grouped populations of gram-positive and gram-negative species, classified based on the differential argument in both low and high frequency, for the data obtained after 21h and 7 days of growth. Remember that for ROC curves, the classification is better the closer the curve gets to the top left corner of the plot (100% TPR and 0% FPR). We define our threshold and ROC curve so that a true positive event corresponds to a gram-positive bacteria correctly identified as gram-positive. Subsequently, a false positive event is a gram-negative bacteria wrongly classified as gram-positive.

We can see that the classification between gram-positive and gram-negative cells based on the differential argument is quite poor at both frequencies. After 21 hours of growth it is practically impossible to differentiate gram-positive and gram-negative cells, however for LF argument it is possible to achieve a TPR of 90% unfortunately at the cost of a FPR of 60%. This means that when 90% of the gram-positive bacteria are correctly identified only 40% of the gram negative will be. The ROC curve analysis has also been carried out using the moduli of the measured data. The results of that analyses also did not reveal a great difference between the gram-types (see ROC curves in Appendix B.2). In practice this level of classification is not very useful, and the conclusion from the considerations of the density plots remains the same: based on the data obtained in this experiment, it is not possible to generally differentiate gram-positive and gram-negative bacteria based on their impedance response.

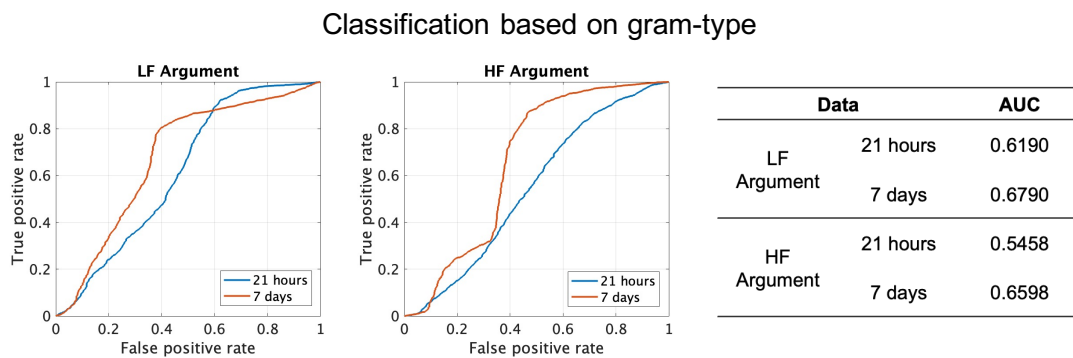


Figure 5.7: ROC curves comparing the differential argument of the data from 6 bacteria species seen in figure 5.5 and 5.6 grouped based on the gram-type of the species (ie. gram-positive: *B. subtilis*, *S. epidermidis*, *Listeria* and gram-negative: *E. coli*, *K. aerogenes*, *Acinetobacter*). The ROC curves are calculated for low and high frequency argument (366 kHz and 6.9 MHz) from measurements made after both 21 hours and 7 days. Also shown is a table with the values for the area under the curve (AUC) for the 4 ROC curves.

It is important to note that the data has not been balanced in any way. Normally, it is not necessary to balance the data for ROC analysis since the positive and negative events are independent of each other. However, here we mix multiple populations into one to create the datasets and these populations are not balanced. A balanced dataset could provide slightly better AUC values (e.g., since the *B. subtilis* would be weighted higher), but it wouldn't change the overall conclusion, that a general difference between gram-positive and gram-negative bacteria is there.

Comparing *Staph ep.* to the rod-shaped species

The only non rod-shaped species that has been investigated is *Staphylococcus epidermidis*, although some of the rod-shaped species are quite short mainly *Acinetobacter* and *Listeria*. To investigate how well the coccoid shaped *S. epidermidis* can be differentiated from the remaining 5 species, the AUC is calculated when comparing *S. epidermidis* individually to each of the rod-shaped species as well as to the polystyrene beads. The resulting AUCs can be seen in table 5.2.

Based on the calculated AUC values it is not possible to say that the coccoid *S. epidermidis*

Table 5.2: Area under curve for ROC curves based on the low and high frequency argument from impedance measurements of gram-positive *Staphylococcus epidermidis* individually compared to each of the 5 gram-negative strains. An AUC is closer to 1 means better classification (separation) between two cell populations. An AUC of 0.5 means the population cannot be differentiated.

Name	Threshold in LF Argument		Threshold in HF Argument	
	21 hours	7 days	21 hours	7 days
<i>Polystyrene beads</i>	0.95	0.95	0.99	0.99
<i>Escherichia coli</i>	0.67	0.73	0.82	0.63
<i>Klebsiella aerogenes</i>	0.51	0.64	0.71	0.57
<i>Acinetobacter baumannii</i>	0.72	0.68	0.73	0.62
<i>Listeria innocua</i>	0.78	0.54	0.77	0.53
<i>Bacillus subtilis subsp. spizizenii</i>	0.73	0.70	0.71	0.74

can be differentiated from the rod-shaped cells, especially not when compared to the polystyrene beads.

The conclusion based on the data and analysis presented in this section must be that, while there are definitely differences in the impedance response of the different bacteria species, it is not obvious that these differences are related to the gram-type or the shape of the bacteria. In my opinion, the phenotypical expression (e.g. based on growth conditions) and the state of the bacteria (e.g. dormant or dead), affects the bacteria morphology and consequently the impedance response to a similar degree. To investigate this in greater detail, a powerful method for cell bacteria morphology would be a great help. Here electron microscopy comes to mind, since it has been used before to visualize the cell structure of bacterial cells [77, 78]. The preparation of the cells could pose a potential challenge. Traditionally, cells are prepared through a drying and fixing process using ethanol, HMDS and glutaraldehyde [79] that can affect the cell morphology.

5.5 Chapter summary

In this chapter we have looked at impedance results from various experiments meant to show how or if, IFC (and more specifically BactoBox) can be used to count and characterize bacteria and other particles. First, a manuscript of a reprint of a paper made in the very beginning of the PhD project was presented. It showed that it is possible to detect *E. coli* and *Staphylococcus* bacteria and differentiate them from polystyrene beads.

We then went on to discuss how changes in the relative effective conductivity between the electrolyte medium and the transitioning particle or bacteria causes an obvious shift in differential argument. This means that when plotting the differential argument data

(e.g. in a scatter plot), the event populations will generally be placed in three primary positions and this point is illustrated by experimental data for polystyrene beads, bacteria and silver coated silica beads.

To demonstrate the counting ability of BactoBox, a simple growth tracking experiment with *E. coli* was presented. We showed that the concentrations measured on a growing culture with BactoBox corresponded very well with what was found using plate counting on agar plates.

Finally, the impedance response of 6 different bacteria species was investigated. We found that the response was not identical for the 6 species, but were not able to correlate the impedance response to gram-type or bacteria shape.

6 Liposomes

The experiments that form the basis of the results presented in this chapter were carried out during a research stay at the University of Barcelona from November 2019 to February 2020. The work was carried out in the laboratories at the Department of Electronics and Biomedical Engineering with advice and assistance from assistant professor Romén Rodríguez Trujillo and PhD student Martina Di Muzio. The work resulted in a manuscript that, at the time of writing this, is being revised for resubmission:

- Bertelsen, C. V., Skands, G. E., Trujillo, R. R., Muzio, M. D., Gomila, G., Dimaki, M., & Svendsen, W. E. (2021). Advancing impedance flow cytometry using custom-synthesized liposome samples as a model for cellular studies. *is being revised for resubmission*

This chapter contains a short introduction and a print out of that manuscript.

All the experimental data presented in this chapter is obtained with a BactoBox v2 and flow cell design Q.

6.1 Introduction

Liposomes are vesicles that come in many sizes and consists of one or more lipid membranes around an aqueous core, as seen in figure 6.1. The reason liposomes are interesting in regards to detection with IFC, is that liposomes can be synthesized so that the properties that matter to the IFC measurements will be known. As we have discussed previously, bacteria are diverse and their electrical properties can be complex to predict. By replacing the bacteria with the much simpler liposomes, we hope to gain a better understanding of what properties can and cannot be probed with IFC in general, and also specifically with BactoBox.

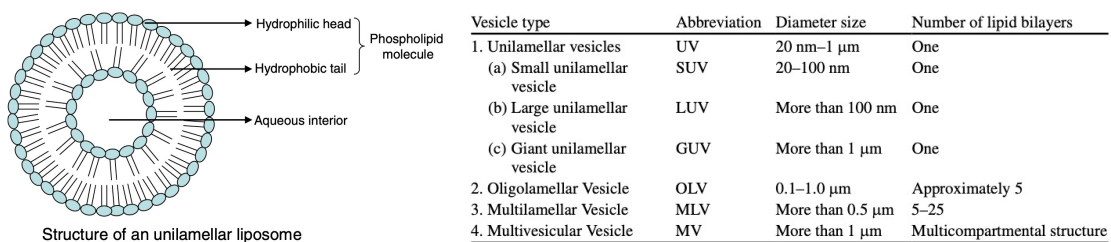


Figure 6.1: Illustration of a liposome and table of liposomes characterisation according to size and lamellarity, both adapted from [80].

The synthesis process is fairly simple. In the manuscript draft printed in the next section, we describe our work with liposomes synthesised using two different phospholipids, Dioleoylphosphatidylcholine (DOPC) and Dipalmitoylphosphatidylcholine (DPPC). The phospholipids are bought from Avanti Polar Lipids (Alabama, USA) and are suspended in chloroform. The processes for liposome synthesis is very similar for the two lipids. First,

the lipids are placed in a glass tube and the chloroform is gently evaporated so that a layer of dried lipids cover the inside wall of the glass tube. Then, an aqueous medium is added to the dried lipids. Since the lipids are amphiphilic they will spontaneously form vesicles with bi-layer membranes that encapsulates part of the aqueous medium in which they are suspended. By choosing the conductivity of the suspension medium (in our case, by suspending in a PBS dilution) the conductivity of the interior medium of the liposome can be controlled. To homogenise the liposome size, the suspension is injected back and forth through a filter with a specified pore size (e.g., 1 μm filter). As the liposomes squeeze through the filter, they break and form smaller vesicles that conform to the pore size. Finally, we can now control the conductivity of the medium outside the liposomes by e.g. diluting with ultra-pure water to lower the conductivity or add PBS to raise it. Through this synthesis process the membrane composition, medium inside the liposomes, and medium outside the liposomes can be controlled.

In the following section, a draft for a short manuscript describing our work with IFC detection and characterization of liposomes is printed.

6.2 Manuscript

ADVANCING IMPEDANCE FLOW CYTOMETRY USING CUSTOM-SYNTHESIZED LIPOSOME SAMPLES AS A MODEL FOR CELLULAR STUDIES

Christian Vinther Bertelsen^{1,2}, Gustav Erik Skands², Romén Rodríguez Trujillo^{3,4}, Martina Di Muzio⁴, Gabriel Gomila^{3,4}, Maria Dimaki¹, Winnie Edith Svendsen¹

¹Technical University of Denmark, DTU Bioengineering, Kgs. Lyngby, Denmark

²SBT Instruments A/S, Herlev, Denmark

³University of Barcelona, Department of Electronics and Biomedical Engineering, Barcelona, Spain

⁴Institute for Bioengineering of Catalonia (IBEC), The Barcelona Institute of Science and Technology (BIST), Barcelona, Spain

ABSTRACT

Electrical modeling of biological cells and particles in impedance flow cytometry systems is challenging due to the complex nature of the samples. In this paper we propose to advance the fundamental understanding of impedance measurements of individual cells or particles by synthesizing liposomes with specific dielectric properties such as size, membrane composition and core conductivity. We measure the impedance response of the liposomes and successfully correlate it to theoretical predictions, showcasing the valuable insight this type of manufactured sample can have in the advancement of the technology.

KEYWORDS

Impedance Flow Cytometry, Liposomes, Single Particle Detection, Sensors, Microfluidics

INTRODUCTION

Impedance flow cytometry (IFC) relies on the analysis of the dielectric properties of individual cells or particles based on the changes in differential current as the cells pass inbetween a set of microelectrodes as illustrated in Figure 1a. Characterization of electrical impedance at different frequencies provides insight into the properties of the cells/particles and the suspending medium, making it an effective tool for single cell analysis [1]–[3]. IFC has found applications for single cell analysis of many different cell types and has enjoyed many technical improvements and developments in the last decades [4]–[6]. Cells and especially cell membranes are complex systems with considerable variation in composition. For example, the cell envelope of bacteria differs based on both genotype and phenotype even within the same strain or species [7]. This diversity creates significant challenges when attempting to link particular impedance behaviours to specific cell characteristics.

Because of this complexity, the advancement of IFC requires a comprehensive understanding of precisely which cell properties can be probed and under which circumstances. One way to tackle this problem of complexity is to develop more sophisticated and specialized theoretical models, however such models can easily become too closely tied to specific use-cases to be of general use. We propose a different approach. Instead of tailoring the models to fit the biological samples, we want to tailor the samples to fit a more general model.

In this paper we present our initial efforts at advancing the fundamental understanding of the capabilities of IFC.

Our goal is to establish if custom-synthesized liposomes with specific properties (e.g. size, membrane composition, core content, etc.) can be used to gain deeper insight into the IFC's capacity to probe specific cell properties.

Liposomes are small vesicles with an amphiphatic membrane composed of phospholipids (illustrated in Figure 1b). They are spherical, typically ranging from 10 nm to a few μm in diameter and consist of an aqueous core surrounded by one or more lipid bilayers. Liposomes can be synthesized with exact control of properties like size, membrane structure, core contents and lipid composition. They are formed when phospholipids spontaneously arrange to form closed spheres once hydrated. Liposomes have found widespread popularity as nanocarriers for drug delivery and a quick method for characterization of their properties would be a useful tool in fields like pharmaceutical production or biotech R&D. Furthermore, liposomes are also used as models for cell systems, making them promising candidates for advancing IFC.

The general electrical properties of a single membrane liposome can be expressed using a simple equivalent circuit model as shown in Figure 1c. Due to the insulating nature of the lipid membrane it behaves as a capacitor (C_{mem}). At low frequencies, this forces the current around the liposome and through the exterior medium (represented by R_{ext} in the equivalent circuit). At higher frequencies, the impedance of the membrane capacitor decreases and the current can now flow through the liposome core (R_{core}).

The liposomes used for experiments were synthesized with diameters of 1 μm using two different lipids, Dioleoylphosphatidylcholine (DOPC) and Dipalmitoylphosphatidylcholine (DPPC). DOPC & DPPC are compositionally similar lipids with some key differences in e.g. the phase transition temperatures [8]. Furthermore, the lipids were synthesized with different core content in order to control the core conductivity. One sample of liposomes was synthesized with ultra pure water (UPW) in the core and another with phosphate buffered saline (1xPBS) in the core. The impedance response of the synthesized liposomes was measured using IFC at two frequencies and successfully correlated to predictions made using Maxwell Mixture Theory [9].

To our knowledge this is the first time that the dielectric properties of single liposomes have been measured in this way. We also believe that with increased understanding, IFC could become a valuable technique for fast characterization of liposomes in the future and accelerate the use of liposomes in pharmaceutical R&D

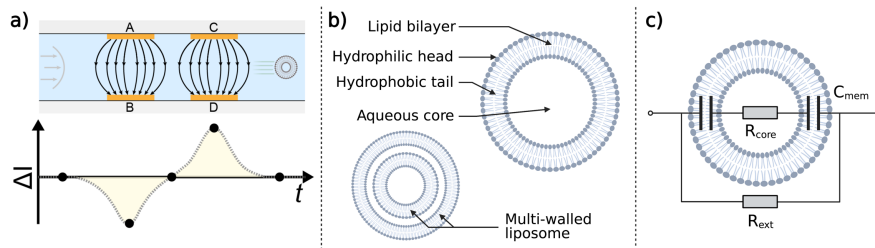


Figure 1: a) Illustration showing the basic principle behind impedance flow cytometry. A particle (e.g., a liposome) transitions between two sets of electrodes sequentially (A-B then C-D) disturbing the electric field between them leading to a characteristic Gaussian double peak in the time-dependent differential current. b) Liposome sketch showing the basic structure of a liposome. c) Simple equivalent circuit illustrating the expected electrical behavior of a liposome.

and production processes.

METHODS

Theoretical modelling

We use Maxwell Mixture theory and the Maxwell-Garnett mixing equation [10] to calculate the complex impedance between a set of front facing microelectrodes with dimensions $10 \times 10 \times 25 \mu\text{m}$ (height \times width \times length). We calculate the impedance with a shelled-sphere (to represent the liposome) present between the electrodes and without a particle present and find the differential current (ie. the reciprocal impedance).

Table 1: Parameters (mean and standard deviation) used for theoretical calculations

Parameter	Mean	SD	Ref
Low frequency	366 kHz	-	-
High frequency	6.94 MHz	-	-
Media conductivity	90 mS/m	-	-
Media permittivity	80	-	-
Bead diameter	2 μm	0.2 μm	
Bead conductivity	4.8 mS/m	-	[11]
Bead permittivity	2.55	-	[12]
Liposome diameter	1 μm	0.2 μm	-
Liposome interior conductivities	5e-6 mS/m 1600 mS/m	-	-
Liposome interior permittivity	80	-	-
Liposome membrane conductivity	1e-7 mS/m	-	[13]
Liposome membrane permittivity	3.2	0.1	[14]
Liposome membrane thickness	5 nm	0.5 nm	[14]

To introduce variation to the theoretical model, a MATLAB-function calculating the impedance of a single event is set up in a for-loop. The specific parameters used to calculate the impedance of each event in the loop are drawn from a normal distribution with the mean and standard deviation found in Table 1. The impedance of 1000 events are calculated for each desired sample type (beads, liposomes with 1 membrane, liposomes with 2 membranes, etc.), with each event having slightly varying

parameters. In this way, we generate a population of events with simulated variation.

The results are plotted as kernel density maps using MATLAB's `ksdensity` function (with normal kernel smoothers and a bandwidth of $0.02 \times \pi$) to simulate the noise of the experimental measurements (e.g., white noise). For easier comparison, the argument is shifted so that the theoretical result calculated for the polystyrene beads lines up with the experimentally obtained argument for the polystyrene beads. This means that the theoretical argument is shifted $0.9 \times \pi$ radians in the LF argument and $0.65 \times \pi$ radian in the HF argument. The difference in argument between the experimental and theoretical argument is caused by a frequency dependent phase shift in the electronics of the prototype impedance flow cytometer.

Liposome synthesis

The lipids used for liposome synthesis were DOPC and DPPC both suspended in chloroform and acquired from Avanti Polar Lipids, Alabama, USA (product no. 850375C and 850355C, respectively). Liposomes were synthesized according to the manufacturers instructions [15]. 40 μl stock solution was pipetted into a glass vial and the chloroform was gently evaporated from the solution using a nitrogen gun. 1 ml of either UPW (Ultra pure water, Milli-Q®, Merck Millipore, Darmstadt, Germany) or 1xPBS (Phosphate Buffered Saline 1x, Sigma-Aldrich) was added to synthesize the liposomes with the desired core conductivity. The concentration of lipids in the suspension was $\sim 1\text{mM}$. Liposomes were then synthesized by extrusion using a mini-extruder (Avanti 610000 - Extruder set with holder/heating block) and a polycarbonate membrane with a 1.0 μm pore size (Avanti 610010 - PC membranes 1.0 μm). For samples with DOPC the resuspension and extrusion were done at room temperature ($\sim 25^\circ\text{C}$) while for the samples with DPPC both resuspension and extrusion were done at 60°C in order to be above the phase transition temperature of the lipids. At the end of the liposome synthesis we end up with 4 samples: DOPC liposomes with UPW inside, DOPC liposomes with 1xPBS inside, DPPC liposomes with UPW water inside and DPPC liposomes with 1xPBS inside.

Preparation of samples for IFC

To prepare the samples for IFC measurements it was

necessary to reduce the concentration of the liposomes and to match the conductivity of the exterior medium (outside of the liposomes) across all samples. The target conductivity of the exterior medium was ~ 90 mS/m. This was achieved by diluting the solutions of synthesized liposomes with 1xPBS and UPW. For the samples with UPW inside, 30 μ l of liposome solution was mixed with 150 μ l 1xPBS and 2.82 ml UPW. For the sample with PBS inside, 30 μ l of liposome solution was mixed with 120 μ l 1xPBS and 2.85 ml UPW. The final conductivities were measured (PRIMO5, Hanna Instruments, UK) to be 89 mS/m and 88 mS/m for the UPW-filled liposomes and the PBS-filled liposomes samples respectively.

IFC measurements

Impedance measurements were performed using an impedance flow cytometer prototype from SBT Instruments A/S (Herlev, Denmark). The prototype allows for using two simultaneous frequencies; in this work we used 366 kHz as the low frequency (LF) and 6.9 MHz as the high frequency (HF). In addition to measurements on liposomes, control measurements were performed on 2 μ m polystyrene beads (Polysciences Inc., PA, USA), also suspended in 1/20xPBS (~ 90 mS/m conductivity) and diluted to a concentration of $\sim 1e6$ /ml from the stock concentration.

Data treatment and visualization

The output from the impedance flow cytometer prototype consists of four data streams containing the recorded I/Q signal from the two frequencies (ie. a real and imaginary part for each of the two frequencies). These data

streams are run through a custom software program developed by SBT Instruments that identifies transition peaks (seen in Figure 1c) in the recorded data and exports the peak values to a CSV-file. The argument for each peak value is calculated using MATLAB and the results are plotted in density maps.

RESULTS & DISCUSSION

Figure 2 shows the obtained differential currents from both the theoretical and experimental investigations. We see the polystyrene beads (Figure 2a and 2f) in a closely confined population and the liposomes with UPW in the core placed in close vicinity (Figure 2b and 2c). This is expected, since even at higher frequencies when the current penetrates the lipid membrane the UPW core is still not electrically conducting. However, when the conductivity in the core of the liposomes is increased (Figure 2g and 2h) we begin to see a dispersion of the population along the HF axis, because the HF current penetrates the membrane and travels through the high conductivity PBS in the core of the liposome decreasing the impedance.

While the measurements of liposomes synthesized with DOPC and DPPC (Figure 2b, 2c, 2g and 2h) are not identical, no obvious difference is seen between the two populations. This may be due to variation in other liposome properties (such as size or number of membranes) obscuring a minor difference caused by the difference between the lipids. In fact, comparison between the experimental (Figure 2g and 2h) and theoretical (Figure 2i) results suggests that it is unlikely that the synthesized liposomes are strictly single-walled. The theoretical prediction for single-walled liposomes is different from the

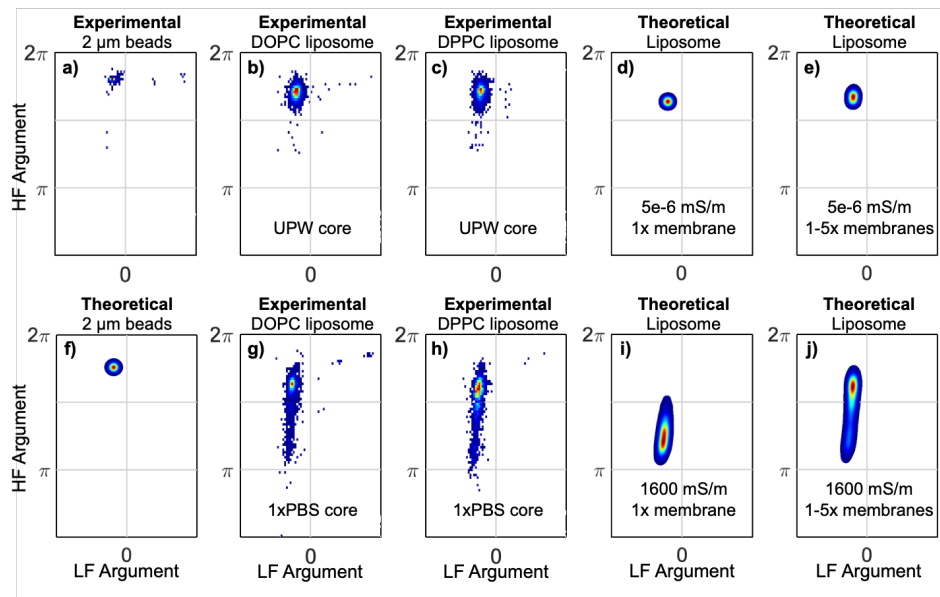


Figure 2: Density plots showing the differential argument found for the low frequency (366 kHz) and high frequency (6.9 MHz). The results are shown for experimental investigations (a, b, c, g, h) and theoretical calculations (d, e, f, i, j) for the various samples of beads and liposomes.

observed experimental results, however when extending the theoretical model to include liposomes with extra membranes (Figure 2j) the resulting differential argument is much more in line with the experimental results.

We see several ways to mitigate this effect. Improvements to the sensitivity of the IFC system could allow for detection of smaller liposomes with a higher chance of being single walled. Furthermore, increasing the high frequency would allow for short-circuiting of multiple membranes and thus improve the separation of the response between liposomes with different core conductivities, but limitations in the electronics implementation of the flow cytometer prototype makes testing this at frequencies above 8 MHz impossible at the moment. On the other hand, extrusion is not the only method for liposome synthesis. For example, methods for synthesizing giant unilamellar vesicles [16] could presumably be adapted to produce liposomes with single membranes and diameters above 1 μm .

CONCLUSION

We have presented the first ever IFC measurements of single liposomes purposefully synthesized to have specific dielectric properties. We have shown that liposomes synthesized with a diameter of 1 μm can be detected using IFC and that, at the given frequencies, the difference in core conductivity of the liposomes can be probed. We have also shown that through careful control of the synthesis of the liposomes, it is possible to successfully predict the response using a theoretical model with the assumption that the liposomes have multiple membranes.

These initial investigations pave the way for a more comprehensive understanding of naturally complex biological entities and systems through characterization with IFC and demonstrate the potential of IFC as a valuable tool for single liposome characterization.

ACKNOWLEDGEMENTS

Figure 1 is created with BioRender.com

REFERENCES

- [1] C. V. Bertelsen, J. C. Franco, G. E. Skands, M. Dimaki, and W. E. Svendsen, 'Investigating the Use of Impedance Flow Cytometry for Classifying the Viability State of E. coli', *Sensors*, vol. 20, no. 21, p. 6339, Nov. 2020, doi: 10.3390/s20216339.
- [2] C. H. Clausen *et al.*, 'Bacteria detection and differentiation using impedance flow cytometry', *Sensors (Switzerland)*, vol. 18, no. 10, p. 3496, 2018, doi: 10.3390/s18103496.
- [3] H. Morgan, T. Sun, D. Holmes, S. Gawad, and N. G. Green, 'Single cell dielectric spectroscopy', *Journal of Physics D: Applied Physics*, vol. 40, no. 1, pp. 61–70, 2007, doi: 10.1088/0022-3727/40/1/S10.
- [4] T. Sun and H. Morgan, 'Single-cell microfluidic Impedance cytometry: A review', *Microfluidics and Nanofluidics*, vol. 8, no. 4, pp. 423–443, 2010, doi: 10.1007/s10404-010-0580-9.
- [5] J. Chen, C. Xue, Y. Zhao, D. Chen, M. H. Wu, and J. Wang, 'Microfluidic impedance flow cytometry enabling high-throughput single-cell electrical property characterization', *International Journal of Molecular Sciences*, vol. 16, no. 5, pp. 9804–9830, 2015, doi: 10.3390/ijms16059804.
- [6] R. J. Yang, L. M. Fu, and H. H. Hou, 'Review and perspectives on microfluidic flow cytometers', *Sensors and Actuators, B: Chemical*, vol. 266, pp. 26–45, 2018, doi: 10.1016/j.snb.2018.03.091.
- [7] T. J. Silhavy, D. Kahne, and S. Walker, 'The Bacterial Cell Envelope', *Cold Spring Harbor Perspectives in Biology*, vol. 2, no. 5, pp. a000414–a000414, May 2010, doi: 10.1101/cshperspect.a000414.
- [8] S. Attwood, Y. Choi, and Z. Leonenko, 'Preparation of DOPC and DPPC Supported Planar Lipid Bilayers for Atomic Force Microscopy and Atomic Force Spectroscopy', *IJMS*, vol. 14, no. 2, pp. 3514–3539, Feb. 2013, doi: 10.3390/ijms14023514.
- [9] T. Sun, S. Gawad, N. G. Green, and H. Morgan, 'Dielectric spectroscopy of single cells: Time domain analysis using Maxwell's mixture equation', *Journal of Physics D: Applied Physics*, vol. 40, no. 1, pp. 1–8, 2007, doi: 10.1088/0022-3727/40/1/S01.
- [10] J. Cottet, O. Fabregue, C. Berger, F. Buret, P. Renaud, and M. Fréna-Robin, 'MyDEP: A New Computational Tool for Dielectric Modeling of Particles and Cells', *Biophysical Journal*, vol. 116, no. 1, pp. 12–18, 2019, doi: 10.1016/j.bpj.2018.11.021.
- [11] T. Sun, D. Holmes, S. Gawad, N. G. Green, and H. Morgan, 'High speed multi-frequency impedance analysis of single particles in a microfluidic cytometer using maximum length sequences', *Lab Chip*, vol. 7, no. 8, p. 1034, 2007, doi: 10.1039/b703546b.
- [12] S. Park, Y. Zhang, T. H. Wang, and S. Yang, 'Continuous dielectrophoretic bacterial separation and concentration from physiological media of high conductivity', *Lab on a Chip*, vol. 11, no. 17, pp. 2893–2900, 2011, doi: 10.1039/c1lc20307j.
- [13] G. Wiegand, N. Arribas-Layton, H. Hillebrandt, E. Sackmann, and P. Wagner, 'Electrical Properties of Supported Lipid Bilayer Membranes', *J. Phys. Chem. B*, vol. 106, no. 16, pp. 4245–4254, Apr. 2002, doi: 10.1021/jp014337e.
- [14] G. Gramse, A. Dols-Perez, M. A. Edwards, L. Fumagalli, and G. Gomila, 'Nanoscale Measurement of the Dielectric Constant of Supported Lipid Bilayers in Aqueous Solutions with Electrostatic Force Microscopy', *Biophysical Journal*, vol. 104, no. 6, pp. 1257–1262, Mar. 2013, doi: 10.1016/j.bpj.2013.02.011.
- [15] N. J. Alves, W. Cusick, J. F. Stefanick, J. D. Ashley, M. W. Handlogten, and B. Bilgicer, 'Functionalized liposome purification via Liposome Extruder Purification (LEP)', *Analyst*, vol. 138, no. 17, p. 4746, 2013, doi: 10.1039/c3an00680h.
- [16] H. Stein, S. Spindler, N. Bonakdar, C. Wang, and V. Sandoghdar, 'Production of Isolated Giant Unilamellar Vesicles under High Salt Concentrations', *Front. Physiol.*, vol. 8, Feb. 2017, doi: 10.3389/fphys.2017.00063.

CONTACT

*C. V. Bertelsen, tel: +45 28573339; cvbe@dtu.dk

6.3 Chapter summary

In this chapter, a short presentation of the work with liposomes made from two different lipids has been given. Multiple liposome samples were synthesized with different medium conductivities inside and outside of the lipid membrane and the impedance response of each sample was measured. There was no obvious difference in the impedance response of liposomes synthesised with different lipids, but there was a detectable difference in liposomes with ultra pure water inside, compared to liposomes with phosphate buffered saline inside. By comparing the experimental results to theoretical calculations of the expected impedance, we speculate that the liposomes are not unilamellar but instead multilamellar. The presence of the additional membranes shields the interior of the liposomes from being probed effectively with IFC. Since multilamellar liposomes is a known artifact from extrusion synthesis of liposomes, a different technique could be employed in the future to control the number of membranes (e.g., microfluidic jetting).

7 Viability Classification

The work presented in this chapter has resulted in two manuscripts (one published and one submitted) that will be reprinted here in their full length after a short introduction to the importance topic of viability classification with IFC.

The two paper presented are:

- Bertelsen, C. V., Franco, J. C., Skands, G. E., Dimaki, M., & Svendsen, W. E. (2020). Investigating the Use of Impedance Flow Cytometry for Classifying the Viability State of *E. coli*. *Sensors*, 20(21), 6339. Reproduced under open access Creative Commons CC BY 4.0 license
- Bertelsen, C. V., Skands, G. E., Dimaki, M., & Svendsen, W. E. (2021). The influence of exposure time in classification of heat-treated *E. coli* using impedance flow cytometry. *Submitted to ACS Sensors, May 2021*. Reproduced with permission from ACS Sensors, submitted for publication. Unpublished work copyright 2021, American Chemical Society.

The experimental data in this chapter is obtained with both BactoBox v1 and v2, and with flow cell designs F and Q. All data for the first paper presented ("Investigating the Use of Impedance Flow Cytometry for Classifying the Viability State of *E. coli*") is obtained with BactoBox v1 and flow cell design F. This is also true for the extra experiments with inactivation of *Staphylococcus* presented in section 7.4. The experiments with prolonged heat exposure are carried out with BactoBox v2 and flow cell design Q. It was not a deliberate choice to change the flow cell design and BactoBox, but rather a practical necessity.

7.1 Introduction

Cell viability is obviously very important for risk analysis in production environments such as in food production or pharmaceutical production. As discussed in section 2.2.3, viability does not have a straight forward definition but is generally considered to be when a bacteria loses its ability to duplicate and grow into larger colonies. In the following we will use the term "inactivated" to cells that have been shown not to grow on the surface of appropriate nutritional medium under appropriate conditions. This definition can be misleading in an actual production environment where some or even most of the bacteria found could be dormant or otherwise viable but nonculturable. However, for the purposes of the experiments on reference strains presented in this chapter, the definition is useful. Traditional growth based quantification will by this definition only be able to identify viable (ie. non-activated) bacteria. This means that even cells that retain some structure but has undergone critical deterioration of key cell structures (mainly perforation of the membrane) will not grow and will therefore not be counted using growth based methods. However, in IFC even bacteria such as these will be counted if they retain enough structure to give rise to a change in impedance during a transition. It is therefore crucial to be able to understand if IFC, and specifically the implementation of IFC found in BactoBox, is able to accurately distinguish a viable cell from an inactivated one.

In order to investigate this, we have performed inactivation experiments of *E. coli* using heat, ethanol and autoclavation and measured the subsequent impedance response. We have then compared that to the response of viable *E. coli* to determine if it is possible to classify between them. This work forms the basis of the paper titled "Investigating the Use of Impedance Flow Cytometry for Classifying the Viability State of *E. coli*" presented in the following pages. Furthermore, we have looked further into the heat inactivation of *E. coli* and our findings are presented in the paper manuscript titled "The influence of exposure time in classification of heat-treated *E. coli* using impedance flow cytometry". This paper has not yet been published (May 2021), but has been submitted for review in the journal ACS Sensors.

One important thing to be aware of is that the experimental results presented in the two manuscripts were made with 2 different versions of the BactoBox (as discussed in the beginning of chapter 3). The two versions are functionally the same, but many of the components have been changed. This means that the differential argument has shifted for all events. Fortunately, the relative position of the bacteria populations have not changed in the plot.

7.2 Manuscript - paper 1



Article

Investigating the Use of Impedance Flow Cytometry for Classifying the Viability State of *E. coli*

Christian Vinther Bertelsen ^{1,2,*} , Julio César Franco ¹, Gustav Erik Skands ², Maria Dimaki ¹
and Winnie Edith Svendsen ¹

¹ DTU Bioengineering, Technical University of Denmark, Søtofts Plads 221, 2800 Kgs. Lyngby, Denmark; jucesarfranco@gmail.com (J.C.F.); madi@dtu.dk (M.D.); wisv@dtu.dk (W.E.S.)

² SBT Instruments A/S, Symfonivej 37, 2730 Herlev, Denmark; ges@sbtinstruments.com

* Correspondence: cvbe@dtu.dk

Received: 7 October 2020; Accepted: 3 November 2020; Published: 6 November 2020



Abstract: Bacteria detection, counting and analysis is of great importance in several fields. When viability plays a major role in decision making, the counting of colony-forming units grown on agar plates remains the gold standard. However, because plate counts depend on the growth of the bacteria, it is a slow procedure and only works with culturable species. Impedance flow cytometry (IFC) is a promising technology for particle detection, counting and characterization. It relies on the perturbation of an electric field by particles flowing through a microfluidic channel. The perturbation is directly related to the electrical properties of the particles, and therefore provides information about their composition and structure. In this work we investigate whether IFC can be used to differentiate viable cells from inactivated cells. Our findings demonstrate that the specific viability state of the bacteria has to be considered, but that with proper characterization thresholds, IFC can be used to classify bacterial viability states. By using three different inactivation methods—ethanol, heat and autoclavation—we have been able to show that the impedance response of *Escherichia coli* depends on its viability state, but that the specific response depends on the inactivation method. With these findings we expect to be able to optimize IFC for more reliable bacteria detection and counting in the future.

Keywords: impedance spectroscopy; impedance flow cytometry; bacteria detection; bacteria characterization; bacteria inactivation; lab-on-a-chip

1. Introduction

There is an increasing need for fast and accurate quantification of bacteria concentrations in multiple fields such as environmental monitoring and hazard analysis in multiple industries, particularly the food industry. The purpose of the quantification is to ensure that the total bacteria concentrations in the production adhere to the regulations and guidelines set by national and international authorities and to ensure safe and high-quality products. Monitoring happens by collecting samples of cleaning water (e.g., CIP-water (clean-in-place) from production equipment) or by collecting samples from production surfaces [1] (e.g., using a moist swab) and resuspending the collected bacteria in an appropriate buffer liquid. The bacterial concentrations in the collected samples are then analyzed using plate counting [2]. This method is well established and reliable, but is notoriously slow and only shows the presence of culturable bacteria [3]. Consequently, a need exists for a fast and reliable method for the quantification of bacteria concentrations in samples that can complement or replace traditional plate counting.

In recent years, a number of alternative technologies for the quantification of bacteria concentrations has emerged to overcome the limitations of traditional plate counting. Some examples are polymerase chain reaction-based (such as real-time PCR or qPCR) or fluorescence-based techniques (such as

fluorescent-assisted cell sorting). However these methods are labor-intensive and require complicated sample processing with expensive reagents [4]. Impedance Flow Cytometry (IFC) is an emerging technology for single-cell analysis and particle enumeration [5]. This technology has shown its potential for single-cell analysis in samples containing a wide range of cell types. It has been used to characterize the electrical properties of Red Blood Cells (RBCs) [6], to analyze plant spores [7], to identify the differentiation state of Mesenchymal Stem Cells (MSCs) [8], to characterize and classify tumor cells [9], to study the effect of chemotherapy treatment on the cell membrane of HeLa cells [10], to monitor the viability of yeast cells [11] and to analyze pollen samples [12]. Due to their small size, it can be difficult to achieve sufficient signal-to-noise when measuring bacteria using IFC. Several suggestions have been given on how to improve this [13–15]. The spectral response of *E. coli* has previously been studied using impedance spectroscopy techniques [16,17], and while some research has gone into specifically investigating the use of IFC to detect bacteria [18,19], assess the viability of *Bacillus megaterium* [20] and to classify bacteria based on their species [21], a general characterization of bacteria using IFC remains an underdeveloped research area.

In this paper we take a more general approach to the analysis of bacteria viability with IFC by including general inactivation methods such as ethanol and autoclaving. To our knowledge this is also the first time IFC has been used to study the viability of *E. coli*.

IFC has a number of advantages over competing methods for bacteria analysis, mainly that it is label-free, non-invasive, sensitive and fast. A traditional plate count will underestimate the true number of viable bacteria in non-laboratory cultures and environmental samples since it is not able to detect the presence of unculturable species or bacteria that are intact and metabolically active but unable to divide under ordinary conditions (viable but non-culturable bacteria) [22–25]. In IFC, every particle or cell in the samples is counted and characterized no matter what the species is or what viability state the bacteria is in. Consequently, IFC has the potential to provide a more accurate measurement of the total bacteria count by including cells which would previously have been unseen.

However, using IFC as a replacement for traditional plate counting may also introduce new technical challenges. When a bacterium is inactivated it loses its ability to divide and subsequently will not generate a visible colony (colony-forming unit, CFU) on an agar plate. In this case, the cell could retain enough of its cellular structure to still be counted using IFC and lead to a false positive detection of inactivated cells. It is therefore imperative that the change in dielectric response of inactivated bacteria is investigated and characterized, if IFC is going to emerge as a useful and reliable alternative to plate counting.

Despite being frequently used, the term bacteria viability does not have a straightforward definition [26]. A comprehensive definition of viability considers cell component integrity, metabolic activity and ability to proliferate. However, in this article we will use viability (i.e., “a viable cell”) to mean either a cell that shows an intact cellular structure (specifically the cell membrane) or is able to give progeny on an appropriate agar and generate visible colonies. Similarly, we will use the term “inactivated cell” to mean a cell that has undergone an inactivation process so that it no longer fulfills the viability conditions described above. The inactivation agents used in this study are ethanol, heat (at 90 °C) and autoclaving. These methods are expected to act with rapid and nearly simultaneous oxidation or denaturation of multiple targets, including the cytoplasmic membrane, proteins, ribosomes, and/or DNA [26].

In this paper we use a prototype multi-frequency impedance flow cytometer developed by the Danish company SBT Instruments A/S (Herlev, Denmark) to test the impedance response of *Escherichia coli* (*E. coli*). We inactivate the *E. coli* cells using three different methods (ethanol, 90 °C heat or autoclaving) and compare it to the impedance response of untreated *E. coli* cells. We also discuss the expected impact of the inactivation on the electrical properties of the bacteria. Furthermore, we compare the experimental impedance measurements with CFU counts and fluorescence imaging to determine whether the change in impedance response can be correlated to the cells’ ability to grow and

the membrane integrity of the cells, respectively. Finally, we evaluate the sensitivity and specificity of IFC as a tool for characterizing inactivated and viable cells.

2. Materials and Methods

2.1. Impedance Flow Cytometry

The working principle of impedance flow cytometry (which has also been described in detail elsewhere [27–29]) is illustrated in Figure 1. An electrolyte with suspended particles and/or microorganisms was injected through a microfluidic channel by a pump. A set of 4 microelectrodes were located on the top and bottom (2 on the top and 2 on the bottom) of the microfluidic channel facing each other. A multi-frequency alternating current (AC) voltage was applied to the two electrodes on the top of the channel, giving rise to a current perpendicular to the direction of the flow, which was measured on the two electrodes on the bottom of the channel. In our case, we used two frequencies—a low frequency of 366 kHz and a high frequency of 6.9 MHz. When a particle or a bacterium passes between the electrodes, it changes the dielectric properties of the space between the top and bottom electrodes and causes a change in current. The difference in current between the two electrodes on the bottom of the channel was measured giving rise to a characteristic double gaussian event as shown in Figure 1. Each event was detected and analyzed in order to characterize the properties of each passing particle or bacterium.

A more detailed description of the impedance flow cytometer and the event detection used in this work can be found in the Section 1.1 of Supplementary Materials.

In order to understand the interaction between bacteria and the current flowing between the electrodes, it is common to represent the electrical properties of cells as electrical components in an equivalent circuit model (ECM) where the cell is modelled as a simple single-shelled particle [30] as seen in Figure 2a. An equivalent circuit is a simplified circuit which retains the electrical characteristics of the original physical system. The assumption in the ECM is that the complex permittivity and conductivity of a physical system can be replaced by equivalent electrical components [31].

A simple ECM of a bacteria suspended in a liquid between two electrodes has components representing the resistance and capacitance of the electrolyte (R_m, C_m), the resistance and capacitance of the cell membrane (R_{mem}, C_{mem}) and the resistance of the cell interior (i.e., cytoplasm) (R_{cyto}) [32]. Electrolyte resistance and capacitance are material properties that depend on the ionic strength of the electrolyte, but also on the temperature of the solution.

Figure 2b shows the expected electric field penetration in polystyrene beads as well as in treated and untreated bacteria. Polystyrene beads are often used as reference samples in IFC experiments and are expected to be electrically isolating at both low and high frequencies [21]. For a viable bacterium, electrical conductivity across the membrane is considered to be very low (i.e., high membrane resistance) [33]. Combined with a noticeably high membrane capacitance this means that the membrane offers a significant barrier to current flow even at relatively high frequencies in the range of 100–500 kHz. At higher frequencies, the membrane capacitance is effectively short-circuited allowing the electric field to probe the interior of the cell as illustrated in Figure 2b.

In this work we investigate how changes in membrane structure due to inactivation affects the electrical properties of the membrane and cell interior. During inactivation with either heat or ethanol it is expected that the membrane properties will change significantly, which in turn will affect both the effective membrane resistance and capacitance. Primarily, we expect that a disrupted membrane will have a significantly lower resistance allowing current to flow through the cell at lower frequencies as illustrated in Figure 2b.

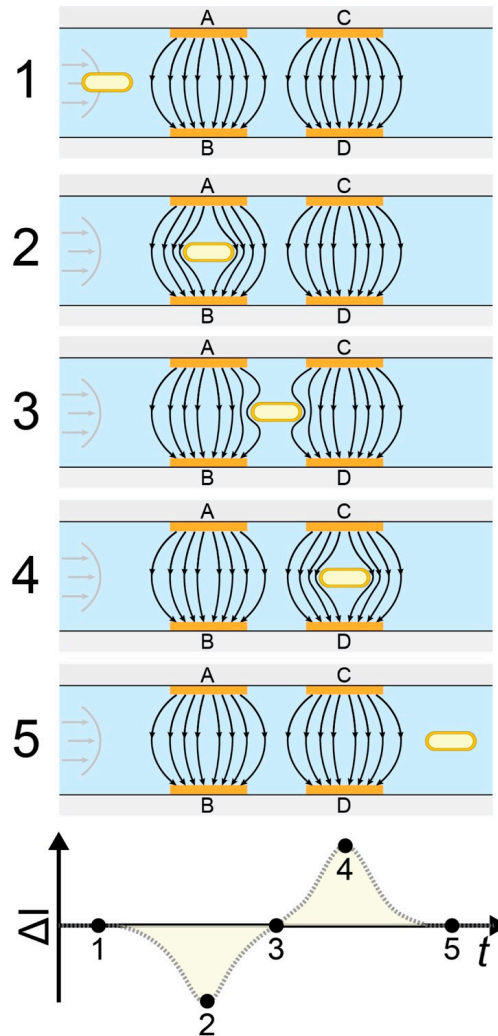


Figure 1. Detection principle. Schematic of 5 positions of a transitioning bacteria (1, 2, 3, 4, and 5) and the corresponding differential current ($\Delta I = I_{AB} - I_{CD}$). When a bacterium enters the detection area (position 1), the current between the two electrode sets is identical ($I_{AB} = I_{CD}$), resulting in a differential current of zero. When the bacterium moves between electrodes A and B (position 2), the electric field is perturbed resulting in a non-zero differential current. When the bacterium is exactly between the electrode sets (position 3) the differential current is again zero. As the bacterium transitions between electrodes C and D and further out of the detection area, the electric field is again perturbed giving rise to a differential current (position 4). At position 5, the differential current is again zero as the bacterium exits the detection area.

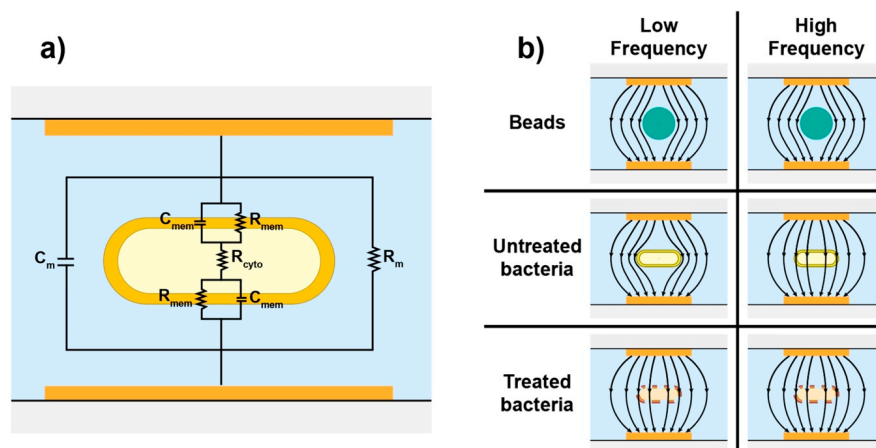


Figure 2. (a) Simplified equivalent circuit model of *E. coli* bacteria. The model is composed of components representing the electrolyte resistance and capacitance (R_m , C_m), the resistance and capacitance of the cell membrane (R_{mem} , C_{mem}) and the resistance of the cell interior (R_{cyto}). (b) Electric field penetration in polystyrene beads and in bacteria with different viability states at low and high frequencies.

2.2. Experimental Procedure

We grew *Escherichia coli* cells in tryptic soy broth and inactivated them using ethanol, heat and autoclaving in three separate experiments. In each experiment, we performed IFC measurements, plate counts and fluorescent microscopy on the inactivated sample as well as on an untreated control sample. A flow diagram of the sample preparation can be found in the Section 1.2 of the Supplementary Materials.

2.2.1. Preparing Bacteria Samples

Escherichia coli (Migula) Castellani and Chalmers ATCC 8739 (Microbiologics®, Saint Paul, MN, USA) was inoculated on tryptic soy agar (TSA, Sigma Aldrich, St. Louis, MO, USA) plates using a resuspended lyophilized pellet following the manufacturer's instructions. The plates were incubated overnight at 37 °C and stored in the fridge.

For each experiment, a pre-culture was prepared by inoculating 10 mL of tryptic soy broth (TSB, Sigma Aldrich) with a single colony picked from the TSA plate. The pre-culture was incubated overnight in a shaking incubator at 37 °C and 200 RPM. The experimental culture was prepared by inoculating 40 mL of fresh TSB with 40 μ L from the pre-culture (1:1000 dilution) and incubated again in a shaking incubator at 37 °C and 200 RPM until they reached the exponential growth phase (approximately 4 h for a final concentration of $\sim 10^8$ CFU/mL). We used cells in the exponential phase to avoid a high degree of natural cell death which could occur in the later stages of growth.

2.2.2. Bacteria Inactivation

For the ethanol inactivation, 40 mL of experimental culture was split into two vials (2×20 mL) one for inactivation and one for control. The bacteria were harvested from each vial by centrifugation at 10,000 rpm for 5 min (Multifuge X3, Thermofisher). The sample for inactivation was resuspended in 20 mL of a 70% ethanol solution (70% *v/v*, TechniSolv, VWR chemicals). After 5 min of exposure to ethanol, the bacteria suspension was centrifuged at 10,000 rpm for 5 min and resuspended in fresh PBS (Dulbecco's Phosphate Buffered Saline, Sigma-Aldrich). To ensure no ethanol was remaining in the solution, the bacteria suspension was centrifuged again at 10,000 RPM for 5 min and resuspended in PBS. The control sample was resuspended in PBS instead of ethanol but was otherwise taken through the same steps.

For the heat inactivation, bacteria were harvested from the 40 mL exponentially growing experimental culture by centrifugation at 10,000 rpm for 5 min and were subsequently resuspended in 40 mL fresh PBS. After that, 3 mL of resuspended bacteria were transferred to a glass vial. A block of aluminum with drilled holes for sample vials was placed on a hot plate at 90 °C. When the aluminum block reached 90 °C the sample vial was placed inside the block for 5 min and subsequently placed on ice for 5 min to cool down. The viable control sample was placed on ice for 5 min after being transferred to the glass vial and then kept at room temperature until further analysis.

For the autoclave inactivation, bacteria were harvested from the 40 mL exponentially growing experimental culture by centrifugation at 10,000 rpm for 5 min and subsequently resuspended in 40-mL fresh PBS. After this, 3 mL of resuspended bacteria were transferred to a 50 mL glass bottle. The bottle was placed in the autoclave and a standard cycle of 25 min was run (125 °C at 20 PSI). The control samples were kept in the fridge for the duration of the inactivation process.

2.2.3. Impedance Protocol

Bacteria for the IFC measurements were harvested from the 40 mL exponentially growing experimental culture by centrifugation at 10,000 rpm for 5 min and subsequently resuspended in 40-mL fresh PBS. Subsequently, 30 µL of the bacteria sample were pipetted into a tube containing 3 mL of 1/20-diluted PBS (diluted with Milli-Q water), for a total reduction in concentration of 1/100.

The impedance measurements were carried out using a prototype impedance flow cytometer from SBT Instruments A/S (Herlev, Denmark). All measurements were performed using two simultaneous frequencies: 366 kHz and 6.9 MHz. Frequencies in this range have previously been shown to effectively characterize bacteria and non-bacteria [21]. The AC voltage applied to the electrodes was 15.8 V_{pp}. The total measuring time per sample was 5 min. The current response was recorded with a sample rate of 23 kSa/s. An individual data stream was recorded simultaneously for the real and imaginary parts of the complex current for both the low and the high frequency. When the measurements were finished the data were transferred to a PC for further analysis.

A separate reference sample of polystyrene beads (1.5 µm, Polysciences, Inc., Warrington, USA) was analyzed during each inactivation experiment. The beads were prepared by diluting the stock solution of beads in 1/20-diluted PBS for a final concentration of $\sim 1 \times 10^6$ beads/mL.

The concentration of cells (C) was calculated using the average transition time of the events (t_{event}), the dimensions of the detection volume on the microfluidic chip (w —width of the channel, h —height of the channel, and l —distance from electrode edge to electrode edge), the total number of events during a measurement (N) and the total measurement time (T). The following equation was used to calculate the concentration:

$$C = \frac{Nk\langle t_{event} \rangle}{whlT}, \quad (1)$$

with k being a dimensionless constant calculated numerically that compensates for the parabolic flow profile in the microchannel.

A schematic overview of the experimental setup including the impedance flow cytometer can be found in the Section 1.1 of the Supplementary Materials together with a short description of the fabrication of the microfluidic chip and the event detection algorithms.

2.2.4. ROC Curves and Classification

In order to test the classification capabilities of the impedance flow cytometer we plotted receiver operating characteristic curves (ROC curves) showing the false positive rate (FPR, equal to 1-selectivity) and the true positive rate (TPR, equal to sensitivity) for varying thresholds. The sensitivity is defined as the ratio between the number of true positive events and the number of total positive events, and the selectivity is defined as the ratio between true negative events and the number of total negative events. In this work we define positive events as describing an intact cell. The sensitivity is therefore understood to be the ratio between the number of events characterized as viable bacteria in the untreated sample

(true positives) and the total number of events in the untreated sample (total positives). Similarly, the selectivity is understood to be the ratio between the number of events characterized as not viable cells and the total number of events in the inactivated samples (or bead samples).

The curves were plotted using MATLAB. The threshold varied in steps from one extreme (100% FPR and 100% TPR) to the other (0% FPR and 0% TPR) and the corresponding FPR and TPR were calculated for each step. In our case, we chose the classification of a viable untreated bacterium as a positive classification.

2.2.5. CFU Counting

After the inactivation procedure, the inactivated samples were diluted 10 times by transferring 100 μL of the bacterial suspension into a microcentrifuge tube containing 900 μL of PBS. The control samples were further diluted by repeatedly vortexing and transferring 100 μL to the next tube until reaching a 10^{-6} dilution. The undiluted and last dilutions from each sample (both inactivated and control) were plated individually on separate TSA plates using an automatic pipette (Eppendorf Xplorer, Eppendorf). In total, five evenly spaced droplets of 20 μL from each sample were dispensed per plate [34]. After the drops on the agar dried, the plates were sealed with parafilm and incubated at 37 $^{\circ}\text{C}$ overnight. Colonies were manually counted in droplets with 6 to 60 colonies. The five drops for each dilution were considered to calculate the CFUs and the standard deviation for each initial sample.

2.2.6. Fluorescent Imaging

Undiluted bacteria suspensions were stained after the inactivation process using the LIVE/DEAD[®] BacLight[™] Bacterial Viability Kit (Thermo Fischer Scientific, Waltham, MA, USA). The principle of the staining mix is based on the differential exclusion of the dyes according to membrane integrity. Bacteria with intact membranes show only green fluorescence while bacteria with compromised or disrupted membranes show green and red fluorescence.

A solution containing a 1:1 mixture of SYTO9 at 3.34 mM and propidium iodide at 20 mM was prepared and 3 μL were added to 1 mL of bacteria suspension. After 15 min of incubation in complete darkness, 5 μL of bacteria suspensions were deposited on top of a poly-L-Lysine-coated glass slide and covered with a $1 \times 1 \text{ cm}^2$ cover slide. The fluorescent samples were observed under the epifluorescence microscope (Heat and Ethanol: Axioplan 2, Zeiss; Autoclave: Olympus U-TV1X-2 + U-LH100HG) using two filters—FITC for the visualization of green fluorescence and a TRITC for the visualization of red fluorescence. Pictures were taken with the coupled camera (Heat and Ethanol: CoolSNAP-Proof Color, Media Cybernetics; Autoclave: XC30, Olympus) and image processing was performed using Fiji ImageJ [35] (see Section 1.3 of Supplementary Materials for further details). A different microscope was used to capture images of the autoclaved sample due to repeated problems with a low intensity in that particular sample.

3. Results

Three different inactivation experiments were carried out using inactivation treatments with ethanol, heat and autoclavation, respectively. Shortly after each inactivation was completed, the untreated and treated samples were analyzed using the impedance flow cytometer and the concentration and electrical responses were obtained from the recorded data. The same samples were also analyzed using plate counting to investigate viability and fluorescent microscopy in order to investigate membrane integrity.

3.1. Concentrations of Bacteria Samples

Bacteria concentrations were studied after the inactivation treatment using drop plating and IFC in parallel. The concentrations measured with drop plating and IFC for the untreated and treated samples from the three inactivation experiments can be found in Table 1. The concentration of bacteria in the untreated samples was roughly 10^8 CFU/mL in all three experiments. No standardization of the

concentration (e.g., using optical density) was performed with the different untreated samples, which could reduce the variation in future experiments. When compared to the counts per milliliter provided by IFC, we see that IFC consistently measures lower concentrations. This difference is attributed to a lack of calibration in the prototype impedance flow cytometer and has been observed before [21]. However, the standard deviation is significantly lower using IFC compared to the plate counts.

Table 1. Bacteria concentration (mL^{-1}) for the treated and untreated samples calculated from drop plating and impedance measurements.

	Drop Plates (CFU/mL $\times 10^6$)	IFC (counts/mL $\times 10^6$)
Ethanol Experiment		
<i>Untreated</i>	520 \pm 165	243 \pm 47
<i>Treated</i>	0 \pm 0	72 \pm 8
Heat Experiment		
<i>Untreated</i>	590 \pm 110	384 \pm 12
<i>Treated</i>	0 \pm 0	68 \pm 3
Autoclave Experiment		
<i>Untreated</i>	860 \pm 152	434 \pm 23
<i>Treated</i>	0 \pm 0	36 \pm 10

No growth was detected in the inactivated samples on the agar plates (inactivation efficiency of 100%). However, with IFC it was still possible to detect events after inactivation for all three inactivation methods. This suggests that some of the inactivated cells retain enough cell integrity after inactivation to be detected by the impedance system. In general, the lower concentration in the treated samples can be attributed to complete cell disintegration during the inactivation. Such a process is more likely to happen in *E. coli* when heat is applied, especially for a prolonged time, compared to cells exposed to ethanol [36], which corresponds well with the reduction in cell counts that we see for the three methods.

3.2. Characterization by Impedance

The measured argument and modulus of detected bacteria from each of the three inactivation experiments are shown in Figure 3, together with the measured response of a reference sample of polystyrene beads. It is evident that the beads and untreated bacteria populations, individually, appear in the same position for each of the three experiments, demonstrating that the observed changes in impedance response of the treated cells is related to the inactivation process and not the general sample handling.

Figure 3 shows the differentiation of 1.5 μm beads, untreated *E. coli* and treated *E. coli* based on the low- and high-frequency arguments. For the ethanol and autoclave inactivation experiment we observed a significant shift between untreated and treated bacteria, except in different directions. However, no such shift was observed in the heat inactivation experiment.

The measured argument from the ethanol inactivation experiment (Figure 3a), allows us to distinguish a population for each sample with only minor overlap. The untreated bacteria and the beads show a separation between sample populations experiencing the high frequency due to the short-circuiting of the membrane capacitance, while the responses in the low-frequency condition are more similar. The untreated population of cells shows a greater variation compared to the beads as can be expected in biological samples. Comparing the ethanol-treated population to the untreated population, we observe a shift primarily in the low-frequency argument. This corresponds well with the expected response, where disruptions of the membrane lower the effective membrane resistivity and allow the electric field to penetrate the cells even at lower frequencies.

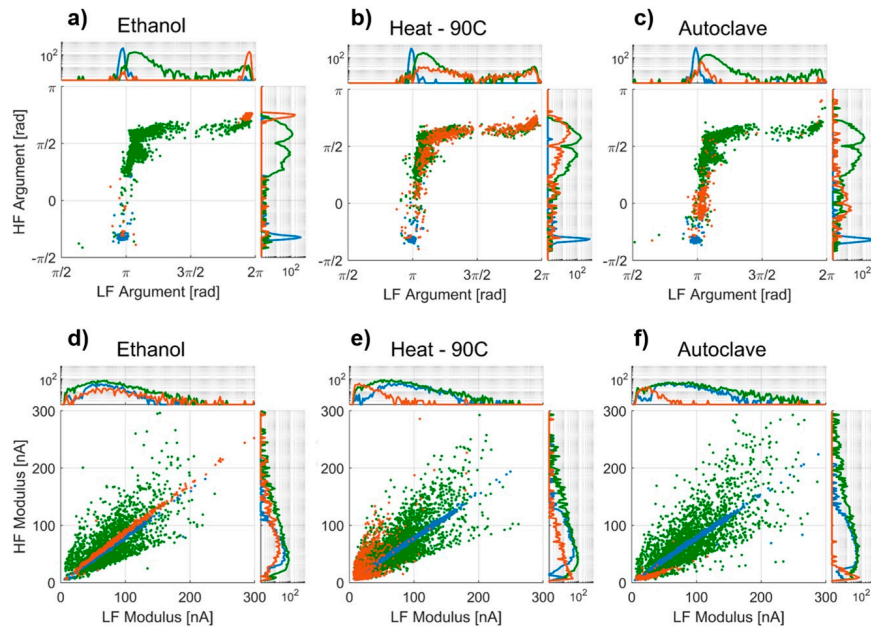


Figure 3. Low-frequency argument vs. high-frequency argument from the impedance measurements from the (a) ethanol, (b) heat and (c) autoclave experiments. Low-frequency modulus vs. high-frequency modulus from the impedance measurements from the (d) ethanol, (e) heat and (f) autoclave experiments. Each dot represents an event (bacteria or bead passing between the detection electrodes) with: 1.5- μm beads colored blue (\bullet), untreated *E. coli* colored green (\bullet), and treated *E. coli* colored orange (\bullet). A log-scaled population density is plotted on the edges of each plot.

Unexpectedly, it is not possible to differentiate bacteria treated at 90 °C for 5 min from untreated bacteria (Figure 3b) in either the low- or high-frequency argument. This suggests that the treated bacteria have similar electrical properties to untreated bacteria and still retain a high degree of membrane integrity.

The population from the autoclaved sample shows a shift towards the beads in both the high-frequency and low-frequency argument, differentiating the majority of the autoclaved bacteria from the untreated bacteria (Figure 3c). Due to the high pressure and temperature of the autoclave, it is likely that the bacteria shattered and that we observed cells with highly damaged cell walls. If the cell wall is damaged to a degree in which the majority of the cytoplasm has been replaced by electrolyte, the electrical response would be similar to what we observed.

The modulus of the differential current is different for the three treated samples. The population of ethanol-treated bacteria (Figure 3d) is narrow with low variation and a slope close to 1, aligning well with the idea of a disrupted membrane, where current can flow through equally well in both low and high frequencies.

The heat-treated sample (Figure 3e) shows a variation in modulus similar to that of the untreated bacteria but with a smaller magnitude overall.

Similar to the heat-treated sample, the modulus for the autoclaved population (Figure 3f) is smaller compared to the untreated sample. However, for this sample we see a relatively small high frequency (HF) modulus compared to the low frequency (LF) modulus. This could support the idea that the majority of the cytoplasm has been replaced by electrolyte. At low frequencies, the disrupted membrane lets the current flow through the cell, but the intact part of the membrane still provides some

resistance to the current flow. However, at higher frequencies the capacitance of the lipid membrane is short-circuited leading to cell walls that are more “transparent” and, due to the exchange of cytoplasm, a smaller differential current.

3.3. Fluorescence Imaging

To check whether it is indeed a loss of membrane integrity that causes the changes in impedance response, we investigated the bacteria using fluorescent staining.

Images of untreated and treated fluorescent bacteria and their corresponding membrane integrity percentages are shown in Figure 4. As expected, untreated samples showed a high degree of membrane integrity across all three experiments: 92.3% for ethanol, 98.7% for heat and 94.8% for autoclave. The deviation from a 100% membrane integrity is expected to be due to a small percentage of fast-growing cells with compromised membranes [37] or bacteria that were structurally damaged during sample preparation.

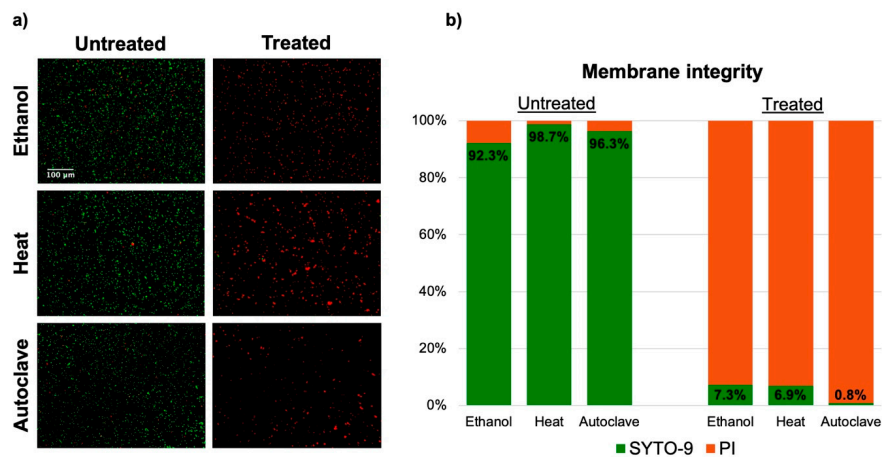


Figure 4. Results from the fluorescence imaging. (a) Images of untreated and treated bacteria from all three inactivation experiments showing green (SYTO-9) and red (PI) fluorescence. As expected, most of the untreated bacteria appear as green, while the treated bacteria appear as red. (b) Membrane integrity percentage for each sample (n = 3 for ethanol and heat, n = 4 for autoclave).

The bacteria in all three treated samples exhibited low membrane integrity percentages: 7.3% for ethanol, 6.9% for heat and 1.7% for autoclave. However, these percentages are still higher than we would expect considering the plate counts (0% viability for all treatments). This could mean that a small population of bacteria keep membrane integrity but are unable to divide, or that there is an unknown intrinsic error related to the staining protocol.

These results show that all three inactivation methods used in this study—ethanol, heat and autoclave—disrupt the membrane of the bacteria. It is worth mentioning that the total number of bacteria was substantially lower in the treated samples with respect to the untreated samples. This evidence aligns with the results obtained from the plate counts for each experiment.

3.4. Characterization of Treated and Untreated Bacteria

So far, the measured current response has been investigated and correlated to the biological state of the samples. However, in order to use IFC as an alternative to plate counts (e.g., as a risk assessment tool in the food industry) it is also important to consider the effectiveness of the viability classification of the technology—i.e., investigate how well the technology can characterize viable cells as viable and

how well it can characterize inactivated cells as inactivated. We therefore investigated the classification of untreated and treated bacteria for each of the three inactivation methods and determined the optimal classification threshold for each of them. We achieved this by using ROC curves as seen in Figure 5. Based on the individual thresholds for each of the inactivation methods, we found two thresholds that together return the best classification between untreated and treated bacteria across all samples. The thresholds were set in the high-frequency argument since this yielded the overall best sensitivity and selectivity. A similar analysis for the low-frequency argument can be found in the Section 2.1 of the Supplementary Materials.

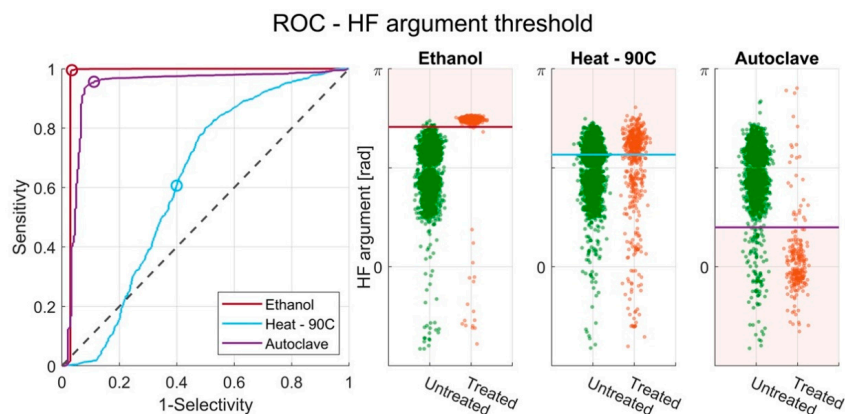


Figure 5. Receiver operating characteristic (ROC) curves showing the performance of the classification based on a threshold in the HF argument of treated and untreated *E. coli* for the ethanol, heat and autoclave experiments. The circles indicate thresholds of 2.22, 1.78 and 0.63 for the three experiments, respectively. The same thresholds are visualized in a categorical scatter plot showing the distribution of events in the HF argument for the untreated and treated *E. coli* for each of the three inactivation experiments.

3.4.1. ROC with Single HF Argument Threshold

Figure 5 shows the ROC curves obtained for the HF argument from the three inactivation experiments. Optimal threshold values that classify untreated and treated *E. coli* were identified as 2.22, 1.78 and 0.63 for the ethanol, heat, and autoclaving inactivation experiments, respectively. The optimal thresholds were chosen in order to maximize sensitivity and selectivity.

The classification of untreated bacteria and bacteria treated with either ethanol or autoclaving is strong, with a sensitivity of 99.5% and 95.5%, and a selectivity of 96.7% and 88.8%, respectively. The area under the curve (AUC) values calculated for each ROC curve can be found in Table 2 and show an AUC of 0.97 and 0.93 for the ethanol experiment and autoclave experiment. However, for the heat-treated cells, the classification is quite poor with an AUC of 0.62, a sensitivity of 60.7% and a selectivity of 60.0%. This corresponds well with the observed differences in dielectric responses seen for the three experiments (Figure 3).

Included in the figure are three categorical scatter plots including the used thresholds for the HF argument. The categorical scatter plots show that the identified thresholds work well for separating untreated and treated cells in the ethanol and autoclaving experiments but not in the heat experiment.

A summary of the AUC, sensitivity and selectivity found for each optimal threshold can be found in Table 2.

Table 2. AUC (Area under the curve), sensitivity and selectivity found using the optimal thresholds for each of the inactivation experiments. AUC is a quality measure of the classification in general, with 1 indicating perfect classification and 0.5 indicating random classification (poor quality). The sensitivity indicates the methods ability to identify *E. coli* in the untreated sample as viable. The selectivity indicates the methods ability to identify *E. coli* in the treated samples as not viable.

	AUC	Threshold	Sensitivity	Selectivity
Ethanol	0.97	2.22	99.5%	96.7%
Heat	0.62	1.78	60.7%	60.0%
Autoclave	0.93	0.63	95.6%	88.8%

In the Section 2.2 of the supplementary materials, three additional repetitions of the ethanol inactivation experiment are shown. The additional experiments displayed good repeatability of the results with sensitivities of 99.1%, 98.3% and 99.1%, and selectivities of 97.0%, 86.5% and 98.8%.

3.4.2. ROC with Multiple HF Argument Thresholds

We have identified two thresholds (one from the ethanol inactivation experiment and one from the autoclaving experiment) that work well for classifying untreated bacteria from ethanol-treated and autoclaved bacteria, respectively. In a real-world situation, we cannot be sure how the bacteria are inactivated and therefore want to establish a general threshold that is as effective as possible for most situations. We therefore combine the two thresholds and classify every event between the thresholds as untreated bacteria and every event outside the thresholds as non-bacteria.

The thresholds are illustrated in Figure 6a and the sensitivity and selectivity for each of the three treated samples are summarized in Figure 6b. We see that the combined thresholds are generally good at classifying untreated cells, ethanol-treated cells and autoclaved cells with sensitivities and selectivities >90%. Similarly, the selectivity of the system towards polystyrene beads was >99.7% in all three experiments. However, the combined threshold is still very poor at classifying the heat-treated cells with a selectivity of only 18%.

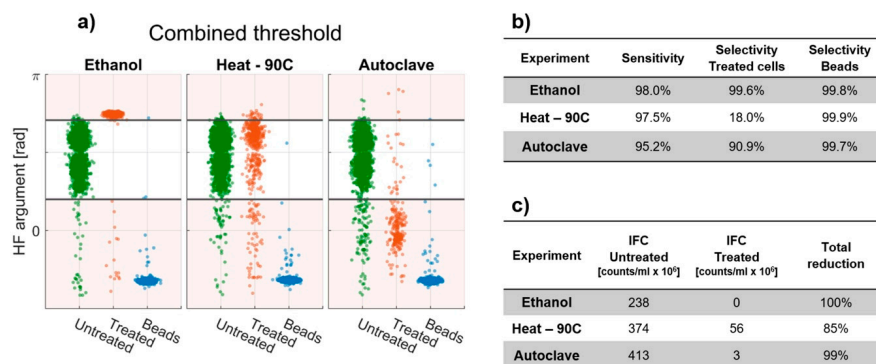


Figure 6. (a) Categorical scatter plot showing the HF argument for the untreated samples and the treated samples from the ethanol, heat and autoclave experiments. The horizontal black lines indicate the upper and lower threshold (2.22 and 0.68, respectively) used to classify viable and non-viable cells. (b) Sensitivity and selectivity found using the dual thresholds for each of the inactivation experiments. (c) Viable bacteria counts detected with Impedance Flow Cytometry (IFC) using the combined thresholds to characterize the cells for the treated and untreated samples together with the total reduction in cell count after inactivation.

Even so, if the reduction in cell count from cell disruption during inactivation is combined with the improved threshold limits from the ROC analysis ($Reduction = 1 - \left(\frac{C_{treated}}{C_{untreated}}\right)$), the total reduction in detected viable bacteria was found to be 100% after ethanol treatment, 85% after heat treatment and 99% after autoclavation (see Figure 6c).

Future experiments should focus on investigating the impedance response of the inactivated bacteria at additional frequencies in order to optimize the sensitivity and selectivity of the system. The full spectral sweep could be obtained by measurements using a chip with interdigitated electrodes similar to what is carried out in [16] and determining the frequencies with the highest differentiation between intact and inactivated cells. This is, of course, of particular interest when investigating the heat-inactivated samples, where improved sensitivity is crucial for the application of the technology. Special focus should be put on trying to understand why the impedance response of a heat-treated bacteria appears similar to untreated cells, even though they do not grow. It would be interesting to understand whether the number and/or size of the disruptions in the membrane play a role in this. Additionally, it would be interesting to monitor the cellular degradation of the cells over time (1–24 h) after inactivation with all three methods.

4. Discussion and Conclusions

In this paper we have shown how an impedance flow cytometer prototype can be used to detect and characterize *E. coli* bacteria that have been inactivated with ethanol, heat and autoclaving.

We compared the bacteria counts from IFC with those obtained from plate counts for treated and untreated bacteria and saw that the inactivation processes yielded zero CFU counts, but that the impedance flow cytometer still detected cells regardless of the viability state showcasing the increased sensitivity of the technology.

We have shown that the impedance response of bacteria changes significantly upon ethanol inactivation. This observation reinforces the belief that ethanol inactivates without necessarily dissolving the entire cell but strongly affecting the integrity of the membrane. By analyzing the impedance response of the ethanol-treated cells we were able to classify the treated cells from untreated cells with a selectivity of 99.6%.

Similarly, the impedance response of bacteria that remained after autoclaving also changed, although differently from the ethanol-inactivated cells. Here the impedance change indicates a broken cell membrane in combination with a replacement of cytoplasm with the surrounding electrolyte. By analyzing the impedance response of the autoclaved treated cells, we were able to classify the treated cells from untreated cells with a selectivity of 90.6%.

However, no significant differences were observed in the impedance response of heat-inactivated cells. This suggests that no measurable changes occurred in the cell bacteria properties, or that the system we used is not fully optimized to detect those changes. The selectivity towards treated cells was only 18.0%.

Nevertheless, investigations with fluorescent dyes showed that the cell membrane was indeed disrupted after inactivation with all three methods, proving that the structure of the cell membrane changes during inactivation. These results demonstrate that IFC can be used to detect and characterize the membrane integrity of *E. coli* bacteria, but with the current flow cytometer it is not possible for all inactivation methods. However, further investigation using different frequencies could improve this.

The need for a fast and accurate quantification of bacteria concentrations in the food industry, and other fields, is still commercially unfulfilled. This work has shown that IFC could be a promising candidate to fulfil this need, as the technology shows potential in differentiating between bacteria samples that are treated and untreated using a number of different inactivation methods.

Supplementary Materials: The following are available online at <http://www.mdpi.com/1424-8220/20/21/6339/s1>, Figure S1: (a) Schematic drawing of the impedance flow cytometer setup. A peristaltic pump continuously pumps liquid from a sample tube through the detection flow cell. The multifrequency excitation signal is pre-amplified before entering the flow cell. The measured current is differentially amplified in a trans-impedance amplifier (TIA)

and the complex amplitudes from each frequency are isolated using a digital lock-in amplifier. All components are integrated in the impedance flow cytometer. A PC is used to visualize and download the recorded data. (b) Image of the impedance flow cytometer with a connected laptop. Insert shows the flow cell with the microfluidic chip mounted in a plastic casing, Figure S2: Illustration showing the bacteria preparation. A single colony from an agar plate is transferred to 40-mL tryptic soy broth (TSB) and incubated overnight in a shaking incubator at 37 °C and 200 RPM. To prepare the experimental culture, 40 µL is transferred to a fresh vial of 40-ml TSB and further incubated for ~4 h, Figure S3: Illustration showing the sample preparation for the inactivation experiment with ethanol, Figure S4: Illustration showing the sample preparation for the inactivation experiment with heat or autoclave, Figure S5: ROC curves showing the performance of the classification based on a threshold in the LF argument of treated and untreated *E. coli* for the ethanol, heat and autoclave experiments. The circles indicate thresholds of 5.98, 3.65 and 3.32 for the three experiments, respectively. The same thresholds are visualized in a categorical scatter plot showing the distribution of events in the LF argument for the untreated and treated *E. coli* for each of the three inactivation experiments, Figure S6: ROC curves showing the performance of the classification based on a threshold in the HF argument for three repetitions of the ethanol inactivation experiment. The circles mark a threshold of 2.22 corresponding to the optimal threshold for classification of untreated and ethanol-treated *E. coli*. The same threshold is also visualized in three categorical scatter plots showing the distribution of events in the HF argument for the three repetitions of the ethanol inactivation experiment, Table S1: AUC (Area under curve), Sensitivity (TPR) and Selectivity (1-FPR) found using the optimal thresholds for each of the inactivation experiments. AUC is a quality measure of the classification in general with 1 indicating perfect classification and 0.5 indicating random classification (poor quality). The sensitivity indicates the methods ability to identify *E. coli* in the untreated sample as viable. The selectivity indicates the methods ability to identify *E. coli* in the treated samples as not viable, Table S2: Area under curve (AUC), sensitivity (TPR) and selectivity (1-FPR) found using the optimal threshold for classification of untreated and ethanol-treated *E. coli* for each of the repetitions of the ethanol inactivation experiments.

Author Contributions: Conceptualization, C.V.B., J.C.F., G.E.S. and W.E.S.; methodology, C.V.B., J.C.F., G.E.S., M.D. and W.E.S.; software, C.V.B.; validation, C.V.B. and J.C.F.; formal analysis, C.V.B. and J.C.F.; investigation, C.V.B. and J.C.F.; resources, C.V.B. and G.E.S.; data curation, C.V.B. and J.C.F.; writing—original draft preparation, C.V.B. and J.C.F.; writing—review and editing, C.V.B., J.C.F., G.E.S., M.D. and W.E.S.; visualization, C.V.B. and J.C.F.; supervision, G.E.S., M.D. and W.E.S.; project administration, C.V.B.; funding acquisition, C.V.B., G.E.S. and W.E.S. All authors have read and agreed to the published version of the manuscript.

Funding: This work was supported by Innovation Fund Denmark (grant no. 7038-00185B).

Conflicts of Interest: The funders had no role in the design of the study; in the collection, analyses, or interpretation of data; in the writing of the manuscript, or in the decision to publish the results. Christian V. Bertelsen and Gustav E. Skands are co-founders of SBT Instruments A/S and both own shares in the company.

References

1. Ismaïl, R.; Aviat, F.; Michel, V.; Le Bayon, I.; Gay-Perret, P.; Kutnik, M.; Federighi, M. Methods for Recovering Microorganisms from Solid Surfaces Used in the Food Industry: A Review of the Literature. *Int. J. Environ. Res. Public Health* **2013**, *10*, 6169–6183. [[CrossRef](#)] [[PubMed](#)]
2. Gracias, K.S.; McKillip, J.L. A review of conventional detection and enumeration methods for pathogenic bacteria in food. *Can. J. Microbiol.* **2004**, *50*, 883–890. [[CrossRef](#)]
3. Jasson, V.; Jacxsens, L.; Luning, P.; Rajkovic, A.; Uyttendaele, M. Alternative microbial methods: An overview and selection criteria. *Food Microbiol.* **2010**, *27*, 710–730. [[CrossRef](#)]
4. Kant, K.; Shahbazi, M.-A.; Dave, V.P.; Ngo, T.A.; Chidambara, V.A.; Than, L.Q.; Bang, D.D.; Wolff, A. Microfluidic devices for sample preparation and rapid detection of foodborne pathogens. *Biotechnol. Adv.* **2018**, *36*, 1003–1024. [[CrossRef](#)]
5. Gawad, S.; Schild, L.; Renaud, P. Micromachined impedance spectroscopy flow cytometer for cell analysis and particle sizing. *Lab Chip* **2001**, *1*, 76–82. [[CrossRef](#)]
6. Zheng, Y.; Shojaei-Baghini, E.; Azad, A.; Wang, C.; Sun, Y. High-throughput biophysical measurement of human red blood cells. *Lab Chip* **2012**, *12*, 2560–2567. [[CrossRef](#)]
7. Canonge, J.; Philippot, M.; Leblanc, C.; Potin, P.; Bodin, M. Impedance flow cytometry allows the early prediction of embryo yields in wheat (*Triticum aestivum* L.) microspore cultures. *Plant Sci.* **2020**, *300*, 110586. [[CrossRef](#)]
8. Song, H.; Rosano, J.M.; Wang, Y.; Garson, C.J.; Prabhakarandian, B.; Pant, K.; Klarmann, G.J.; Perantoni, A.; Alvarez, L.M.; Lai, E. Identification of mesenchymal stem cell differentiation state using dual-micropore microfluidic impedance flow cytometry. *Anal. Methods* **2016**, *8*, 7437–7444. [[CrossRef](#)]

9. Zhao, Y.; Zhao, X.; Chen, D.; Luo, Y.; Jiang, M.; Wei, C.; Long, R.; Yue, W.; Wang, J.; Chen, J. Tumor cell characterization and classification based on cellular specific membrane capacitance and cytoplasm conductivity. *Biosens. Bioelectron.* **2014**, *57*, 245–253. [\[CrossRef\]](#)
10. Kirkegaard, J.; Clausen, C.H.; Rodriguez-Trujillo, R.; Svendsen, W.E. Study of Paclitaxel-Treated HeLa Cells by Differential Electrical Impedance Flow Cytometry. *Biosensors* **2014**, *4*, 257–272. [\[CrossRef\]](#)
11. Opitz, C.; Schade, G.; Kaufmann, S.; Di Berardino, M.; Ottiger, M.; Grzesiek, S. Rapid determination of general cell status, cell viability, and optimal harvest time in eukaryotic cell cultures by impedance flow cytometry. *Appl. Microbiol. Biotechnol.* **2019**, *103*, 8619–8629. [\[CrossRef\]](#)
12. Heidmann, I.; Schade-Kampmann, G.; Lambalk, J.; Ottiger, M.; Di Berardino, M. Impedance Flow Cytometry: A Novel Technique in Pollen Analysis. *PLoS ONE* **2016**, *11*, e0165531. [\[CrossRef\]](#)
13. Farooq, A.; Butt, N.Z.; Hassan, U. Exceedingly Sensitive Restructured Electrodes Design for Pathogen Morphology Detection using Impedance Flow Cytometry. In Proceedings of the 2020 42nd Annual International Conference of the IEEE Engineering in Medicine & Biology Society (EMBC), Montreal, QC, Canada, 20–24 July 2020; pp. 2500–2503.
14. Clausen, C.H.; Skands, G.E.; Bertelsen, C.V.; Svendsen, W.E. Coplanar Electrode Layout Optimized for Increased Sensitivity for Electrical Impedance Spectroscopy. *Micromachines* **2014**, *6*, 110–120. [\[CrossRef\]](#)
15. Zhang, Z.; Gong, M.; Xie, X.; Du, Y.; Cheng, Z.; Zhou, W. The Buffer Conductivity Optimization for Single Bacteria Detection Based on Electrical Impedance Flow Cytometry. In Proceedings of the Fourth International Conference on Biological Information and Biomedical Engineering, Chengdu, China, 21–23 July 2020; pp. 1–5.
16. Mallén-Alberdi, M.; Vigués, N.; Mas, J.; Fernández-Sánchez, C.; Baldi, A. Impedance spectral fingerprint of *E. coli* cells on interdigitated electrodes: A new approach for label free and selective detection. *Sens. Bio-Sens. Res.* **2016**, *7*, 100–106. [\[CrossRef\]](#)
17. Mejri, M.B.; Baccar, H.; Ktari, T.; Aouni, M.; AbdelGhani, A. Detection of E.Coli Bacteria Using Impedance Spectroscopy and Surface Plasmon Resonance Imaging Based Biosensor. *Sens. Lett.* **2011**, *9*, 2130–2132. [\[CrossRef\]](#)
18. Haandbæk, N.; With, O.; Bürgel, S.C.; Heer, F.; Hierlemann, A. Resonance-enhanced microfluidic impedance cytometer for detection of single bacteria. *Lab Chip* **2014**, *14*, 3313–3324. [\[CrossRef\]](#)
19. Bernabini, C.; Holmes, D.; Morgan, H. Micro-impedance cytometry for detection and analysis of micron-sized particles and bacteria. *Lab Chip* **2011**, *11*, 407–412. [\[CrossRef\]](#)
20. David, F.; Hebeisen, M.; Schade, G.; Franco-Lara, E.; Di Berardino, M. Viability and membrane potential analysis of *Bacillus megaterium* cells by impedance flow cytometry. *Biotechnol. Bioeng.* **2011**, *109*, 483–492. [\[CrossRef\]](#) [\[PubMed\]](#)
21. Clausen, C.H.; Dimaki, M.; Bertelsen, C.V.; Skands, G.E.; Rodriguez-Trujillo, R.; Thomsen, J.D.; Svendsen, W.E. Bacteria Detection and Differentiation Using Impedance Flow Cytometry. *Sensors* **2018**, *18*, 3496. [\[CrossRef\]](#) [\[PubMed\]](#)
22. Byrd, J.J.; Xu, H.S.; Colwell, R.R. Viable but nonculturable bacteria in drinking water. *Appl. Environ. Microbiol.* **1991**, *57*, 875–878. [\[CrossRef\]](#)
23. Kikkeri, K.; Breazeal, M.V.R.; Ren, X.; Pruden, A.; Agah, M. A Monolithic Dielectrophoresis Chip With Impedimetric Sensing for Assessment of Pathogen Viability. *J. Microelectromech. Syst.* **2018**, *27*, 810–817. [\[CrossRef\]](#)
24. Nyström, T. Not quite dead enough: On bacterial life, culturability, senescence, and death. *Arch. Microbiol.* **2001**, *176*, 159–164. [\[CrossRef\]](#)
25. Fakruddin; Bin Mannan, K.S.; Andrews, S. Viable but Nonculturable Bacteria: Food Safety and Public Health Perspective. *ISRN Microbiol.* **2013**, *2013*, 1–6. [\[CrossRef\]](#)
26. Cangelosi, G.A.; Meschke, J.S. Dead or Alive: Molecular Assessment of Microbial Viability. *Appl. Environ. Microbiol.* **2014**, *80*, 5884–5891. [\[CrossRef\]](#)
27. Cheung, K.; Gawad, S.; Renaud, P. Impedance spectroscopy flow cytometry: On-chip label-free cell differentiation. *Cytom. Part A* **2005**, *65*, 124–132. [\[CrossRef\]](#)
28. Xu, Y.; Xie, X.; Duan, Y.; Wang, L.; Cheng, Z.; Cheng, J. A review of impedance measurements of whole cells. *Biosens. Bioelectron.* **2016**, *77*, 824–836. [\[CrossRef\]](#)
29. Sun, T.; Morgan, H. Single-cell microfluidic impedance cytometry: A review. *Microfluid. Nanofluidics* **2010**, *8*, 423–443. [\[CrossRef\]](#)

30. Morgan, H.; Sun, T.; Holmes, D.; Gawad, S.; Green, N.G. Single cell dielectric spectroscopy. *J. Phys. D Appl. Phys.* **2006**, *40*, 61–70. [[CrossRef](#)]
31. Sun, T.; Bernabini, C.; Morgan, H. Single-Colloidal Particle Impedance Spectroscopy: Complete Equivalent Circuit Analysis of Polyelectrolyte Microcapsules. *Langmuir* **2010**, *26*, 3821–3828. [[CrossRef](#)]
32. Cheung, K.C.; Di Berardino, M.; Schade-Kampmann, G.; Hebeisen, M.; Pierzchalski, A.; Bocsi, J.; Mittag, A.; Tárnok, A. Microfluidic impedance-based flow cytometry. *Cytom. Part A* **2010**, *77*, 648–666. [[CrossRef](#)]
33. Bai, W.; Zhao, K.; Asami, K. Dielectric properties of *E. coli* cell as simulated by the three-shell spheroidal model. *Biophys. Chem.* **2006**, *122*, 136–142. [[CrossRef](#)]
34. Herigstad, B.; Hamilton, M.; Heersink, J. How to optimize the drop plate method for enumerating bacteria. *J. Microbiol. Methods* **2001**, *44*, 121–129. [[CrossRef](#)]
35. Schindelin, J.; Arganda-Carreras, I.; Frise, E.; Kaynig, V.; Longair, M.; Pietzsch, T.; Preibisch, S.; Rueden, C.; Saalfeld, S.; Schmid, B.; et al. Fiji: An open-source platform for biological-image analysis. *Nat. Methods* **2012**, *9*, 676–682. [[CrossRef](#)]
36. Taddese, R.; Belzer, C.; Aalvink, S.; De Jonge, M.I.; Nagtegaal, I.D.; Dutilh, B.E.; Boleij, A. Bacterial Zombies and Ghosts: Production of Inactivated Gram-Positive and Gram-Negative Species with Preserved Cellular Morphology and Cytoplasmic Content. *bioRxiv* **2018**, 458158. [[CrossRef](#)]
37. Shi, L.; Günther, S.; Hübschmann, T.; Wick, L.Y.; Harms, H.; Müller, S. Limits of propidium iodide as a cell viability indicator for environmental bacteria. *Cytom. Part A* **2007**, *71*, 592–598. [[CrossRef](#)]

Publisher’s Note: MDPI stays neutral with regard to jurisdictional claims in published maps and institutional affiliations.



© 2020 by the authors. Licensee MDPI, Basel, Switzerland. This article is an open access article distributed under the terms and conditions of the Creative Commons Attribution (CC BY) license (<http://creativecommons.org/licenses/by/4.0/>).

7.3 Manuscript - paper 2

The influence of exposure time in classification of heat-treated *E. coli* using impedance flow cytometry

Christian Vinther Bertelsen^{a,b,*}, Gustav Erik Skands^b, Marcos González Díaz^b, Maria Dimaki^a & Winnie Edith Svendsen^a

^aDTU Bioengineering, Technical University of Denmark, Søtofts Plads 221, 2800 Kgs. Lyngby, Denmark

^bSBT Instruments A/S, Symfonivej 37, 2730 Herlev, Denmark

KEYWORDS: *impedance spectroscopy, impedance flow cytometry, bacteria detection, bacteria characterization, bacteria inactivation, lab-on-a-chip*

ABSTRACT: An investigation into the effects of prolonged exposure to heat on the impedance response of *E. coli* bacteria is presented. Theoretical predictions show that perforation of the bacteria membrane during heat exposure will change the impedance of the bacterial cell from effectively less conducting than the suspension medium to effectively more conducting. Consequently, this results in a shift in the differential argument of the electrical current that can be measured with impedance flow cytometry. This shift is confirmed experimentally through measurements on samples with varying medium conductivity and heat exposure times. It was seen that increased exposure time and lower medium conductivity resulted in better classification between untreated and heat-treated *E. coli*. The best classification was achieved with a medium conductivity of 0.045 S/m after 30 minutes of heat exposure, demonstrating the potential of impedance flow cytometry as a fast method for differentiation between untreated and heat-treated bacterial cells.

INTRODUCTION

Impedance flow cytometry (IFC) has seen significant interest and investigation in the last 2 decades¹⁻³ due to its potential for label free characterization of biological cells and its simple process for fabrication of chips. In impedance flow cytometry, a liquid containing particles or cells is continuously injected flowing across a set of detection electrodes. The change in current during the passing of a particle is measured simultaneously at multiple frequencies and, as a result, different parts of the cell structure are probed.

The majority of IFC related work has focused on characterization of larger cells such as red blood cells, yeast and other eukaryotic cells⁴⁻⁹. Less work has gone into investigating bacteria and other smaller particles, likely because it is difficult to achieve sufficient signal-to-noise ratios for smaller cells. Multiple studies have tried to suggest changes to the design and fabrication of the detection electrodes meant to improve the sensitivity of the technology¹⁰⁻¹⁵. However, the bacteria studies that have been done have focused on simple detection and differentiation from non-biological particles¹⁶⁻¹⁸, and on the assessment of the viability of the bacteria¹⁹⁻²¹.

Previously, we have looked into the effect of three inactivation methods on the IFC characterization of *E. coli*²². To do that, we

inactivated the bacteria using ethanol, autoclaving and heat exposure (90°C). We then investigated the viability of the cells before and after inactivation using three methods: plate counts on agar plates, membrane integrity using a fluorescent viability kit and impedance flow cytometry (using a prototype impedance flow cytometer from the Danish company SBT Instruments A/S). The plate counts confirmed the inactivation (i.e., no growth) for all three inactivation methods and the investigation with the fluorescent viability kit showed that the membranes of the bacterial cells were perforated after inactivation. Surprisingly however, we found that the impedance response was different after inactivation for the three inactivation methods. While cells inactivated with either ethanol or with autoclaving could be classified as such with a selectivity of 99.6% and 90.9% compared to viable cells, cells inactivated by heat (90°C) could only be classified with a selectivity of 18.0% compared to untreated cells. This left a fascinating unanswered question about why heat inactivated bacteria, that show no growth on appropriate agar plates and have perforated membranes, do not exhibit a significant change in impedance response.

In this paper, we describe our latest investigations of the impedance response of bacterial cells after heat inactivation. We attempt to clarify how the duration of the heat exposure affects the IFC results. We investigate if prolonged exposure to heat (at 90°C) affects the ability of IFC to classify heat-treated cells

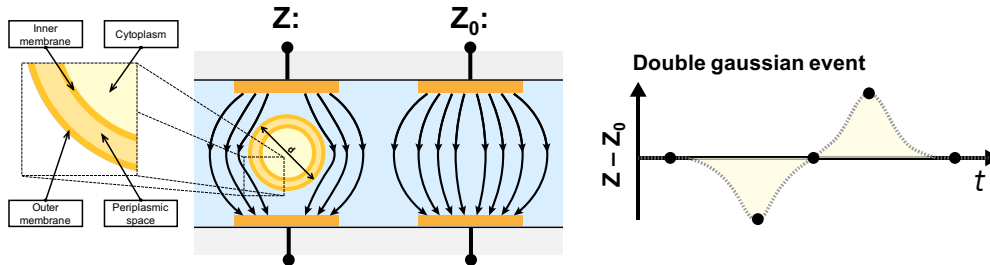


Figure 1: Dielectric bacteria modelling. a) Sketch showing a microfluidic channel with two sets of front-facing micro-electrodes. A bacterium represented as a sphere with diameter, d , and three concentric shells around it, is located between the first set of electrodes. The shells represent the outer membrane, periplasmic space and inner membrane of the cell. b) Characteristic double gaussian event that forms in the differential impedance ($Z - Z_0$) when the bacterium transitions sequentially between the two electrode sets.

from untreated cells, again using an impedance flow cytometry prototype from SBT Instruments. We also examine what role the conductivity of the suspension media plays in the effectiveness of the classification. We attempt to explain the observed behavior using an analytical model based on Maxwell mixture theory.

THEORY

Impedance measurements of cells has been used for almost a hundred years to study the viability of cells and cell cultures²³. The prevailing idea is that the inactivation method perforates the lipid membrane of the cell, leading to a break-down of metabolic activity and an inability of the cell to maintain structure^{24,25}.

This is especially true for eukaryotic cells, but also cells with more rigid envelope structures are considered non-viable when the lipid membrane is broken²⁴. For a healthy cell, an intact membrane acts as an insulating barrier surrounding the cytoplasm in the core of the cell. More specifically the insulating

membrane acts as a capacitor that electrically shields the cell interior at lower frequencies (typically $< 1\text{MHz}$) but is short circuited at higher frequencies ($> 1\text{MHz}$) making way for electrically probing of the membrane and cell interior²⁶. This idea is also the basis of several commercially available cell counters based on the coulter counter principle²⁷.

Bacteria are not homogenous particles but are often represented by more or less complex models of concentric shells (i.e., the cell envelope) around a homogeneous interior (i.e., the cytoplasm of the cell). Since we are performing the IFC experiments on samples with gram-negative *E. coli* bacteria, we have chosen to represent the bacteria as a spherical model with three shells representing the three layers found in the cell envelope structure of gram-negative bacteria: the outer membrane, the periplasmic space, and the inner membrane (or plasma membrane), as shown in the inset of Figure 1a. The impedance chips used for the experiments have two sets of front-facing micro-electrodes as illustrated in Figure 1a. As the bacteria transitions through the micro-channel and sequentially passes between the two sets of electrodes, the corresponding differential impedance forms a

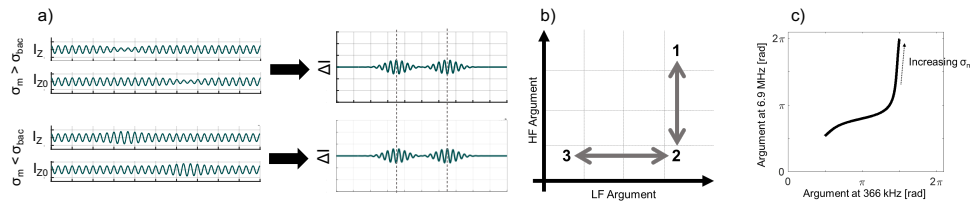


Figure 2: Influence of relative conductivity. a) Sketch of the time dependent AC current (one frequency) on two electrode sets during the passage of a particle/bacterium with a lower effective conductivity than the medium surrounding it ($\sigma_{bac} < \sigma_m$) and the reverse situation where the particle/bacterium has a higher effective conductivity compared to the medium ($\sigma_{bac} > \sigma_m$). b) Sketch of the 3 main proposed positions of particles/bacteria populations in a scatterplot with argument at low frequency on the x-axis and the argument of the high frequency on the y-axis. In position 1, the impedance of the particles/bacteria are effectively higher than that of the surrounding medium at both low and high frequency (e.g. homogenous non-conducting beads). In position 2, the impedance of the particles/bacteria in the high frequency is lower than that of the medium (e.g. bacteria cells with intact membranes if the high frequency is high enough to bypass the membrane capacitance). In position 3, the particles/bacteria are effectively more conducting than the medium at both frequencies (e.g. cells with broken membranes). c) Analytical calculation based on MMT that shows the behavior of a bacteria with fixed properties in a medium with increasing conductivity. The bacteria position follows the predicted positions as the media conductivity increases (i.e. as the bacteria moves from more conducting to less conducting than the medium).

characteristic double Gaussian shown in Figure 1b. The peak value of the transition corresponds to the situation where the cell is between one of the electrode sets. In the following, we will refer to the peak impedance between the first electrode set (with the bacterium) as Z , and the impedance of the second electrode (without the bacterium) set as Z_0 .

We use Maxwell mixture theory to predict the impedance behavior of inactivated cells (i.e., cells with perforated membranes). To do this, we will use the complex permittivity that depends on the relative permittivity (ϵ), the conductivity (σ) and the angular frequency (ω) in the following way

$$\epsilon^* = \epsilon - j \frac{\sigma}{\omega} \quad (1)$$

For a non-homogeneous shelled sphere like the one used to represent the gram-negative bacterium, an effective complex permittivity (ϵ_{eff}^*) can be calculated that takes the combined electrical properties of the interior of the cell (ϵ_i^*) and each of the shells into account. This complex permittivity can be calculated by first calculating the effective permittivity of the interior sphere with one shell and then continually adding additional shells starting from the innermost one.

$$\epsilon_{eff}^* = \frac{\left(\frac{d/2}{d/2 - d_{shell}}\right)^3 + 2 \left(\frac{\epsilon_i^* - \epsilon_{shell}^*}{\epsilon_i^* + 2\epsilon_{shell}^*}\right)}{\left(\frac{d/2}{d/2 - d_{shell}}\right)^3 - \left(\frac{\epsilon_i^* - \epsilon_{shell}^*}{\epsilon_i^* + 2\epsilon_{shell}^*}\right)} \quad (2)$$

The effective permittivity of the bacteria suspended in the electrolyte medium (ϵ_{mix}^*) is given by the Maxwell-Garnett mixing equation

$$\begin{aligned} \frac{\epsilon_{mix}^* - \epsilon_m^*}{\epsilon_{mix}^* + 2\epsilon_m^*} &= \phi \frac{\epsilon_{eff}^* - \epsilon_m^*}{\epsilon_{eff}^* + 2\epsilon_m^*} \Rightarrow \\ \epsilon_{mix}^* &= \epsilon_m^* \frac{1 + 2\phi \frac{\epsilon_{eff}^* - \epsilon_m^*}{\epsilon_{eff}^* + 2\epsilon_m^*}}{1 - \frac{\epsilon_{eff}^* - \epsilon_m^*}{\epsilon_{eff}^* + 2\epsilon_m^*}} \end{aligned} \quad (3)$$

Where ϕ is the volume fraction occupied by the bacterial cell and (ϵ_{mix}^*) is the complex permittivity of the medium.

The differential complex impedance of the entire system ($\Delta Z = Z - Z_0$) can then be calculated using equation (4) and (5)

$$Z = \frac{1}{j\omega \epsilon_{mix}^* l \kappa} \quad (4)$$

$$Z_0 = \frac{1}{j\omega \epsilon_m^* l \kappa} \quad (5)$$

With κ being a correction factor for the non-uniformity of the electric field at the electrode edges into account^{2,28} that depends on the width of the electrodes in the direction of the flow and the height of the detection channel, and l is the length of the electrode perpendicular to the flow. Using Ohms law, the current (I^*) and subsequently the differential current (ΔI^*) can be calculated

$$I^* = \frac{U}{Z^*} \quad (6)$$

$$\Delta I^* = I^* - I_0^* \quad (7)$$

The differential modulus and argument can then be calculated using

$$\text{mod}(\Delta I^*) = |\Delta I^*| = \sqrt{\text{re}(\Delta I^*)^2 + \text{im}(\Delta I^*)^2} \quad (8)$$

$$\text{arg}(\Delta I^*) = \text{atan2}(\text{re}(\Delta I^*), \text{im}(\Delta I^*)) \quad (9)$$

The cell properties of the bacteria depend on factors such as strain and growth conditions²⁹. For modelling we use electrode dimensions of 10 μm width and 25 μm in length and a channel height of 10 μm identical to the dimension of the chip used for experiments. The applied voltage (U) is 16 V_{pp} combined for both frequencies and the bacteria diameter is 1 μm with the dielectric properties of the shells and interior found in Table 1.

Usually, IFC experiments are carried out using medium with relatively high conductivity (e.g., 1xPBS at ~ 1.6 S/m) compared to the cells that are probed. This is overall a good strategy since it usually leads to higher current and better signal-to-noise ratio (i.e., peak-to-noise).

However, we conduct our experiments using phosphate buffered saline (PBS) diluted with ultrapure water (UPW) to lower the conductivity of the PBS. While this does affect the peak-to-noise ratio, it also leads to a situation where the differential argument of the current depends heavily on whether the bacterium

Table 1: Dielectric properties and thickness of the three shells (outer membrane, periplasmic space, inner membrane) and the interior core (cytoplasm) used for modeling of the bacterium. Dielectric properties from²⁸

	Outer membrane	Periplasmic space	Inner membrane	Cytoplasm	Media
Conductivity (σ) [mS/m]	1e-1	3200	1e-6	220	40 80 160 800
Permittivity (ϵ)	12.1	60	5.5	108	80
Thickness [nm]	8	15	4	N/A	N/A

increases or decreases the impedance of the system during a transition. More specifically, the differential current shifts out of phase if the cell changes from being effectively less conducting to effectively more conducting than the medium and vice versa. If the original signals that are subtracted are in phase, the resulting differential phase will shift from in-phase to out-of-phase when the amplitude of one of the signals changes from larger to smaller than the other signal. This idea is illustrated in Figure 2 for situations where the bacteria is less conducting than the medium and more conducting than the medium.

For bacteria measurements with IFC various conditions determine if this shift happens. For example, when changing the frequency from a low frequency where the membrane blocks the current and the impedance is high, to a higher frequency where the membrane is more transparent to the current, and the impedance is lowered (on the condition that the conductivity of the cell interior is higher than that of the media). Additionally, the phase shift will also occur at lower frequencies when the membrane of the cell is perforated, e.g., after inactivation. As the membrane perforates, the effective impedance of the membrane drops, and the cell interior is probed even at lower frequencies.

For cell measurements, the two subtracted signals are not necessarily completely in-phase due to the capacitance of the system (primarily from the lipid membrane). Even so, when plotting the differential argument, the detected events are expected to move between three general positions as indicated in Figure 2b:

- **Position 1:** The cells/particles are effectively less conducting than the medium at both low and high frequency ($|Z| > |Z_0|$). This could be e.g., polystyrene beads.
- **Position 2:** The cells/particles are effectively less conducting than the medium at the low frequency ($|Z| > |Z_0|$), but more conducting in the high frequency ($|Z| < |Z_0|$). This could be e.g., cells with intact cell membranes that are opaque at low frequencies but transparent at high frequencies
- **Position 3:** The cells/particles are effectively more conducting than the medium at both low and high frequency ($|Z| < |Z_0|$). This could be e.g., cells with broken membranes that allow current to run through the more conducting cell interior, even at low frequencies.

Whether the bacteria are more or less conducting compared to the surrounding media obviously depends on the conductivity of the medium. In Figure 2c, the differential argument calculated using the model properties found in Table 1 is plotted with increasing medium conductivity for the two frequencies used for experiments (366 kHz and 6.9 MHz). As the medium conductivity increases, it is seen that the predicted differential argument passes through the 3 positions as the cells go from being more conducting to less conducting than the medium.

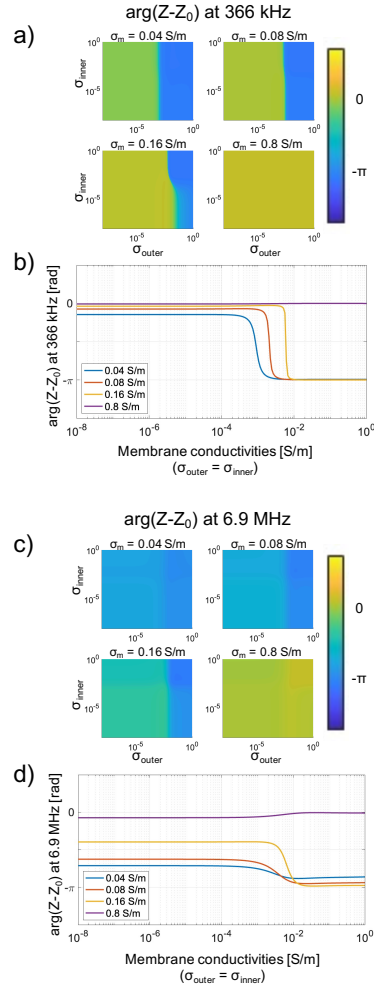


Figure 3: Differential argument as a function of membrane conductivity. Color gradient map of the calculated differential argument for increasing conductivity of the inner and outer membrane (σ_{inner} , σ_{outer}) at the experimental frequencies of (a) 366 kHz and (c) 6.9 MHz at 4 different medium conductivities (σ_m): 40 mS/m, 80 mS/m, 160 mS/m and 800 mS/m. b) and d) show the differential argument at the diagonal line ($\sigma_{inner} = \sigma_{outer}$) of the color gradient maps for each of the conductivities.

In Figure 3 the differential phase as a function of inner and outer membrane conductivity is plotted for the two experimental frequencies (366 kHz and 6.9 MHz) and changing medium conductivities (40 mS/m, 80 mS/m, 160 mS/m and 800 mS/m). We

see that the conductivity of both membranes can increase multiple orders of magnitude before the shift occurs and that the shift does not happen if the medium conductivity is higher than the cytoplasm conductivity (here 220 mS/m). This tells us that it is not just a matter of 'if' the membrane is perforated, but also the degree of perforation and that a perforated membrane in itself is not enough to differentiate inactivated cells from intact cells based on differential argument.

The analytical results lead to the following expectations for the experimental results:

- A shift in the argument means that the membrane is perforated enough, so that the effective conductivity of the cell is higher than that of the surrounding media.
- It is not necessary that both outer and inner membranes are perforated if the conductivity of the periplasm is high enough, so the cell becomes effectively more conducting than the media surrounding it.
- The shift in argument is expected to happen "sooner" (i.e., at lower membrane conductivities) when the media conductivity is lower
- If the argument does not shift, it means that the membrane is not sufficiently perforated or that the conductivity of the cell interior is lower than that of the surrounding media
- The shift in argument is expected to be more significant in the low frequency compared to the high frequency

METHODS

Testing the effects of prolonged heat exposure

Preparation of heat inactivated samples were performed in order to duplicate results from our previous work²². *E. coli* bacteria (ATCC8739) were grown overnight in TSB (tryptic soy broth, Sigma Aldrich) at 37°C and with 180 rpm shaking. 5 vials of 1 ml of the overnight culture were prepared in glass vials and 4 of them were placed inside an aluminum heat block on a hotplate. The hotplate was set to 90°C and the temperature of the block was monitored using a thermometer submerged in an ultrapure water (UPW) sample also placed in the heat block.

One bacteria sample was placed directly on ice, while the subsequent 4 samples were removed from the heat block after 5, 10, 20 and 30 minutes and then placed on ice.

Drop plating (3 drops of 10 µl on tryptic soy agar) was used to confirm the inactivation was successful, so that no cell growth was observed after 24 hours in any of the heat-treated samples.

For IFC measurements, 3 µl of bacteria sample was transferred into 3 ml (1/1000 dilution) of diluted PBS (Dulbecco's Phosphate Buffered Saline, Sigma Aldrich). This is done to reduce

both the concentration of cells in the sample and the conductivity contribution from the growth media. The PBS was diluted with UPW in the following ratios: 1/40, 1/20, 1/10 and 1/2. The UPW is deionized, and the conductivity of the sample is therefore dependent on the dilution of the PBS. The conductivity of the 4 samples was measured using a Primo5 conductivity meter (HannaNorden AB, Sweden) to be 45 mS/m, 85 mS/m, 175 mS/m and 860 mS/m, respectively.

IFC measurements

The IFC measurements were carried out using an impedance flow cytometer prototype from SBT Instruments A/S (Herlev, Denmark). Each sample was measured using the IFC prototype at two simultaneous frequencies of 366 kHz and 6.9 MHz. The voltage applied to the electrode was 15 V_{pp} for all samples except for the samples in 1/2xPBS where it was reduced to 1.5 V_{pp} to avoid clipping of the differential signal at the ADC. The clipping of the signal happens because of asymmetries in the detection electrode fabrication that causes the differential current between the electrode sets (Z and Z_0) to be different from 0. As the medium conductance is increased this non-zero current increases beyond the dynamic range of the ADC in the flow cytometer. To mitigate this the input voltage is reduced leading to a reduction in peak height of the events. Because the argument is calculated as the ratio of imaginary and real part of the signal, a reduction in peak height does not affect it, but obviously the moduli cannot be compared without some form of normalization.

The raw IFC measurements were analyzed using a custom software program created by SBT Instruments. The results were plotted as density plots (based on kernel density estimation) showing the differential argument for low and high frequency. Furthermore, ROC-curves were generated using MATLAB to show how well the heat inactivated cells can be differentiated from untreated cells.

RESULTS & DISCUSSION

No cell growth was seen on any of the heat exposed samples after 24 hours at 37°C, meaning that the *E. coli* are inactivated after 5 min of exposure to 90°C.

Impedance response of heat-treated *E. coli*

Figure 4 shows the measured differential argument of the impedance at 366 kHz and 6.9 MHz. The figure shows a grid of plots, each plot based on a measurement with a specific heat exposure time and medium conductivity. The exposure time increases with each row from leftmost (0 min, i.e., untreated) to rightmost (30 min). Similarly, measurements with low conductivity medium (1/40xPBS) are found in the top row, with increasing conductivity for the rows below, ending at 1/2xPBS at the bottom row.

The interplay between the exposure time, medium conductivity and the movement of the measured population between the three general positions is seen in Figure 4.

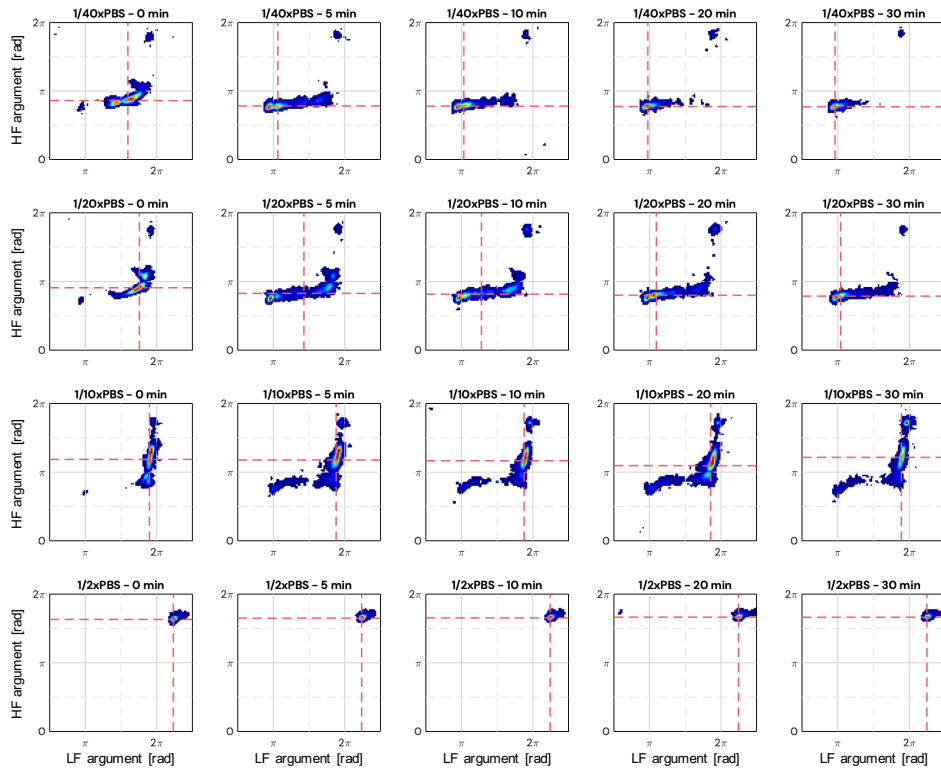


Figure 4: Density plots of experimental results. Density plots showing the results from individual measurements on samples with increasing heat exposure times (0 min to 30 min in columns left to right) and medium conductivity (1/40xPBS to 1/2xPBS in rows top to bottom). Striped, red lines indicate the median value of the LF and HF argument for each population.

When the surrounding media conductivity is low (i.e., 1/40xPBS and 1/20xPBS), the differential argument shifts when the heat exposure time increases and more of the cells shift from position 2 towards position 3. This supports the idea that prolonged exposure to heat, further breaks down the cell membrane and allows current to pass through the bacterium at the low frequency, effectively shifting the cell from being less conducting to more conducting than the medium surrounding it.

It also supports the prediction that simple perforation is not enough to shift the population, but that the effective conductivity of the membrane must change several orders of magnitude before the shift happens (e.g. longer exposure causes larger or additional ruptures in the membrane).

Remember that the bacteria cells in these sample do not grow, so it is not a question of whether the additional perforation in-

activates the cell. The important point is that the perforation becomes more apparent in the impedance signal as the population shifts more for increased exposure times.

As the media conductivity increases (1/10xPBS and 1/2xPBS), the shift in differential argument is not apparent. For the sample 1/10xPBS, we see that some cells shift when going from untreated cells to heat inactivated cells, but most of the cells stay in the same position. We only expect the relative impedance to change if the conductivity of the cell interior is higher than that of the medium and these results therefore indicate that the cytoplasm conductivity is at or below that of 1/10xPBS (~160 mS/m). This may be an underestimation, since exchange between cytoplasm and medium could occur as the membrane perforates artificially lowering the cytoplasm conductivity. However, if the cytoplasm was fully replaced by medium, we would not expect to see a shift in population at the lower medium conductivities.

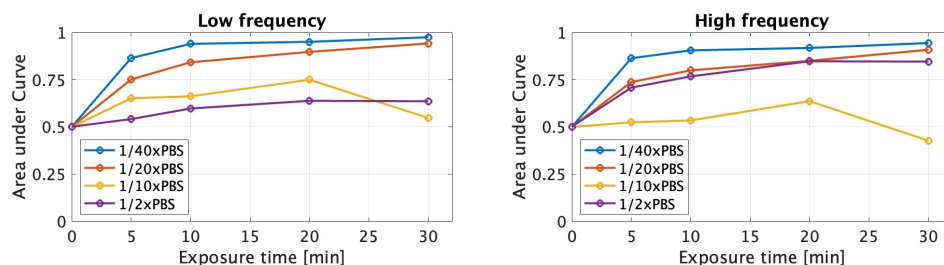


Figure 5: Area under curve. AUC values as a function of exposure time for low and high frequency (366 kHz and 6.9 MHz). For each exposure time the AUC for samples with conductivities of 1/40xPBS, 1/20xPBS, 1/10xPBS and 1/2xPBS is plotted. An AUC value of 0.5 indicates that classification is not possible, while an AUC of 1 means perfect classification.

Classification of viable and inactivated bacteria

Differentiation between untreated and heat-treated cells is done by generating ROC curves and calculating the area-under-curve (AUC). A higher AUC is an indication of better classification while an AUC of 0.5 means the classification is no better than random. The calculated AUC based on the low and high frequency argument as a function of exposure time can be seen in Figure 5. They show that the classification between heat-treated and untreated *E. coli* improves as the exposure time is extended, as well as for lower medium conductivities. The ROC curves themselves can be seen in the supplementary material (figure S1).

From Figure 5 we can see that the best classification between untreated and heat-treated bacteria is achieved when classifying based on the low frequency argument, for the bacteria that have been exposed to the heat for 30 minutes (although the improvement from 10 minutes to 30 minutes is not very large) and are suspended in the lowest conductivity medium (1/40xPBS). Under these conditions, a simultaneous sensitivity of 97.1% (ratio of untreated bacteria correctly classified as such) and a selectivity of 99.1% (ratio of heat-treated bacteria correctly classified as such) can be achieved. This is a noticeable improvement compared to our previous work, where the optimal threshold (found in the high frequency argument) only yielded a selectivity of 18.0%.

CONCLUSION

In this paper, we have presented our measurements on heat treated *E. coli* bacteria using impedance flow cytometry. We have shown that the bacteria can be classified based on whether they are heat-treated or not, but that the performance of the classification depends on the duration of the heat exposure and the conductivity of the medium. This is because the classification relies on a shift in the differential argument of the bacteria that occurs when the bacterial cell changes from being less conducting to more conducting than the medium surrounding it. We found the best differentiation between untreated and heat-treated *E. coli* when the sample was heat-treated for 30 minutes

and was suspended in a medium with a conductivity of 45 mS/m (1/40xPBS).

ASSOCIATED CONTENT

Supporting Information

The Supporting Information is available free of charge on the ACS Publications website.

1. Supplementary figure of ROC curves (S1)
2. Author contribution – Credit statement (PDF)

AUTHOR INFORMATION

Corresponding Author

* E-mail: cvbe@dtu.com

Author Contributions

Specification of author contributions can be found in the Credit statement in the supplementary information

Funding Sources

This research is partially funded by Innovation fond Denmark, grant no. 7038-00185B

Notes

Christian V. Bertelsen and Gustav E. Skands are co-founders of SBT Instruments A/S and both own shares in the company

ABBREVIATIONS

IFC – Impedance flow cytometry; ROC – receiver operating characteristic; AUC – area under curve; PBS – phosphate buffered saline

REFERENCES

1. Gawad, S., Schild, L. & Renaud, P. Micromachined impedance spectroscopy flow cytometer for cell analysis and particle sizing. *Lab on a Chip* **1**, 76–82 (2001).
2. Morgan, H., Sun, T., Holmes, D., Gawad, S. & Green, N. G. Single cell dielectric spectroscopy. *Journal of Physics D: Applied Physics* **40**, 61–70 (2007).
3. Xu, Y. *et al.* A review of impedance measurements of whole

7

- cells. *Biosensors and Bioelectronics* **77**, 824–836 (2016).
4. Spencer, D. & Morgan, H. High-Speed Single-Cell Dielectric Spectroscopy. *ACS Sens.* **5**, 423–430 (2020).
 5. Honrado, C., Ciuffreda, L., Spencer, D., Ranford-Cartwright, L. & Morgan, H. Dielectric characterization of Plasmodium falciparum-infected red blood cells using microfluidic impedance cytometry. *Journal of the Royal Society, Interface* **15**, 20180416 (2018).
 6. De Ninno, A. *et al.* Coplanar electrode microfluidic chip enabling accurate sheathless impedance cytometry. *Lab on a Chip* **17**, 1158–1166 (2017).
 7. De Ninno, A. *et al.* High-throughput label-free characterization of viable, necrotic and apoptotic human lymphoma cells in a coplanar-electrode microfluidic impedance chip. *Biosensors and Bioelectronics* **150**, 111887 (2020).
 8. Heidmann, I., Schade-Kampmann, G., Lambalk, J., Ottiger, M. & Di Berardino, M. Impedance Flow Cytometry: A Novel Technique in Pollen Analysis. *PLoS ONE* **11**, e0165531 (2016).
 9. Canonge, J., Philippot, M., Leblanc, C., Potin, P. & Bodin, M. Impedance flow cytometry allows the early prediction of embryo yields in wheat (*Triticum aestivum* L.) microspore cultures. *Plant Science* **300**, 110586 (2020).
 10. Clausen, C. H., Skands, G. E., Bertelsen, C. V. & Svendsen, W. E. Coplanar electrode layout optimized for increased sensitivity for electrical impedance spectroscopy. *Micromachines* **6**, 110–120 (2015).
 11. Cottet, J. *et al.* How to improve the sensitivity of coplanar electrodes and micro channel design in electrical impedance flow cytometry: a study. *Microfluidics and Nanofluidics* **23**, 11 (2019).
 12. Zhang, X. *et al.* The influence of the electrode dimension on the detection sensitivity of electric cell–substrate impedance sensing (ECIS) and its mathematical modeling. *Sensors and Actuators B: Chemical* **247**, 780–790 (2017).
 13. Winkler, T. E., Ben-Yoav, H. & Ghodssi, R. Hydrodynamic focusing for microfluidic impedance cytometry: a system integration study. *Microfluidics and Nanofluidics* **20**, 134 (2016).
 14. Grenvall, C., Antfolk, C., Bisgaard, C. Z. & Laurell, T. Two-dimensional acoustic particle focusing enables sheathless chip Coulter counter with planar electrode configuration. *Lab on a Chip* **14**, 4629–4637 (2014).
 15. Farooq, A., Butt, N. Z. & Hassan, U. Exceedingly Sensitive Restructured Electrodes Design for Pathogen Morphology Detection using Impedance Flow Cytometry. in *2020 42nd Annual International Conference of the IEEE Engineering in Medicine Biology Society (EMBC)* 2500–2503 (2020). doi:10.1109/EMBC44109.2020.9176444.
 16. Clausen, C. H. *et al.* Bacteria detection and differentiation using impedance flow cytometry. *Sensors (Switzerland)* **18**, 3496 (2018).
 17. Haandbæk, N., With, O., Bürgel, S. C., Heer, F. & Hierlemann, A. Resonance-enhanced microfluidic impedance cytometer for detection of single bacteria. *Lab on a Chip* **14**, 3313–3324 (2014).
 18. Bernabini, C., Holmes, D. & Morgan, H. Micro-impedance cytometry for detection and analysis of micron-sized particles and bacteria. *Lab on a Chip* **11**, 407–412 (2011).
 19. David, F., Hebeisen, M., Schade, G., Franco-Lara, E. & Di Berardino, M. Viability and membrane potential analysis of *Bacillus megaterium* cells by impedance flow cytometry. *Biotechnology and Bioengineering* **109**, 483–492 (2012).
 20. Di Berardino, M. *et al.* Impedance microflow cytometry for viability studies of microorganisms. *Imaging, Manipulation, and Analysis of Biomolecules, Cells, and Tissues IX* **7902**, 790212 (2011).
 21. Spencer, D. C. *et al.* A fast impedance-based antimicrobial susceptibility test. *Nat Commun* **11**, 5328 (2020).
 22. Bertelsen, C. V., Franco, J. C., Skands, G. E., Dimaki, M. & Svendsen, W. E. Investigating the Use of Impedance Flow Cytometry for Classifying the Viability State of *E. coli*. *Sensors* **20**, 6339 (2020).
 23. Green, R. G. & Larson, W. P. Conductivity of bacterial cells. *Journal of Infectious Diseases* **30**, 550–558 (1922).
 24. Cangelosi, G. A. & Meschke, J. S. Dead or alive: Molecular assessment of microbial viability. *Applied and Environmental Microbiology* **80**, (2014).
 25. Shehadul Islam, M., Aryasomayajula, A. & Selvaganapathy, P. R. A Review on Macroscale and Microscale Cell Lysis Methods. *Micromachines* **8**, 83 (2017).
 26. Mallén-Alberdi, M., Vigués, N., Mas, J., Fernández-Sánchez, C. & Baldi, A. Impedance spectral fingerprint of *E. coli* cells on interdigitated electrodes: A new approach for label free and selective detection. *Sensing and Bio-Sensing Research* **7**, 100–106 (2016).
 27. Rhyner, M. N. The Coulter Principle for Analysis of Subvisible Particles in Protein Formulations. *AAPS J* **13**, 54–58 (2010).
 28. Gawad, S., Cheung, K., Seger, U., Bertsch, A. & Renaud, P. Dielectric spectroscopy in a micromachined flow cytometer: Theoretical and practical considerations. *Lab on a Chip* **4**, 241–251 (2004).
 29. Nanninga, N. Morphogenesis of *Escherichia coli*. *Microbiol Mol Biol Rev* **62**, 110–129 (1998).

7.4 Additional experiments with *Staphylococcus*

An obvious question that arises after seeing the results from the inactivation experiments with *E. coli* is whether these results can be generalized for all bacteria. Unfortunately it has not been possible within the scope of this thesis to investigate the full extend of this questions, but a few simple experiments have been performed that may shed a some light on the matter.

The inactivation with ethanol and heat has been repeated on samples of *Staphylococcus epidermidis* and the resulting scatter plot of the differential argument can be seen in figure 7.1. The experimental parameter are the same as the ones used for *E. coli* inactivation here and we see that the behaviour during ethanol inactivation is very similar to what was seen with *E. coli*. However, we did not experience the same issues differentiating between viable and heat treated cells when using *S. epidermidis* instead of *E. coli*. This may simply be because the *S. epidermidis* are mote heat-sensitive than the *E. coli* and that the membrane perforates sufficiently for the shift in argument to happen after just 5 minutes of exposure. At any rate, further experimentation is needed in order to understand the dynamic relationship between membrane perforation and heat exposure for different bacteria species.

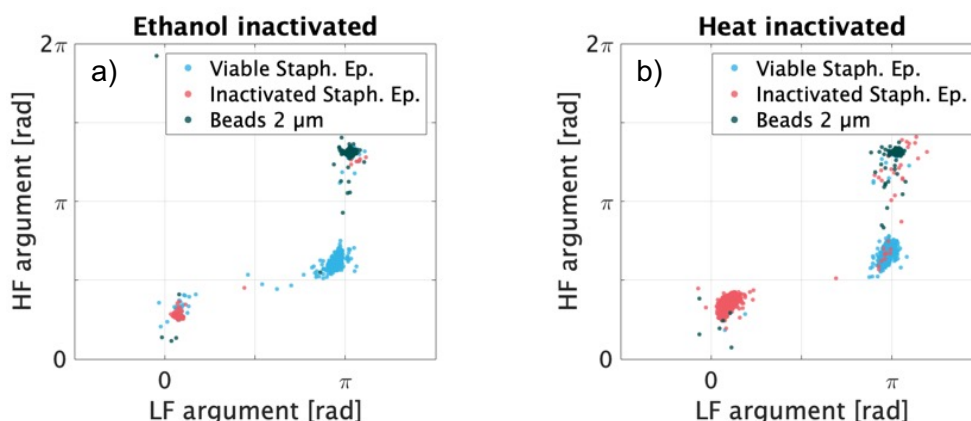


Figure 7.1: Differential argument measured on viable and inactivated *Staphylococcus epidermidis* together with polystyrene beads. a) Shows ethanol inactivated (5 min, 70% ethanol) and b) shows heat inactivated (5 min, 90°C).

7.5 Using spheres or ellipsoids for modelling

In chapter 2, equations for calculating the effective complex permittivity of shelled particles was presented for both spherical (Equation 2.22) and ellipsoidal (Equation 2.23) models. The *E. coli* used for inactivation experiments are rod-shaped and it is therefore relevant to consider the differences predicted by the two models. In this section we will compare the theoretical predictions of the three model configurations shown in figure 7.2, a spherical three-shell model, a rod-shaped three-shell model oriented parallel to the flow direction and a rod-shaped three-shell model with the main axis oriented perpendicular to the flow direction. Cell dimensions are chosen so that the sphere and the ellipsoid has approximately the same volume.

Figure 7.2 (bottom) show the predicted differential modulus and argument of the current for the three models. It is seen that the spherical model and the ellipsoid parallel with the flow have similar responses in the lower frequencies but differ slightly in the high frequency. However, as the ellipsoid is rotated so that it is perpendicular to the flow direction the current changes significantly across the entire frequency range, notably also in the differential argument. Intuitively, drag forces will orient the rod-shaped *E. coli* parallel to the flow and the majority of events are therefore expected to follow the model shown in figure 7.2b.

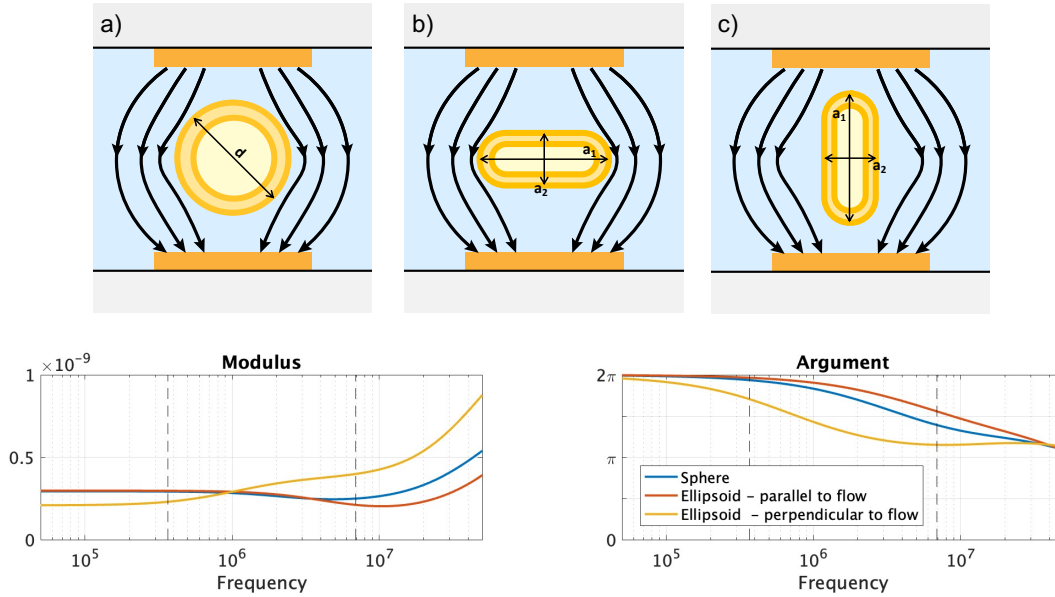


Figure 7.2: Illustration of (a) a spherical three shell model, (b) a rod-shaped three-shell model oriented parallel to the flow direction and (c) a rod-shaped three-shell model with the main axis oriented perpendicular to the flow direction. Underneath the differential modulus and argument calculated using either Equation 2.22 or Equation 2.23 is shown for each of the three models. Vertical striped lines are placed at the two frequencies used for experiments with BactoBox, 366 kHz and 6.9 MHz. The parameters used to calculate the differential argument are: $\sigma_m = 0.08$ S/m, $\varepsilon_m = 80$, $\sigma_i = 0.22$ S/m, $\varepsilon_i = 108$, $\sigma_{outer} = 1 \times 10^{-4}$ S/m, $\varepsilon_{outer} = 12.1$, $d_{outer} = 8$ nm, $\sigma_{peri} = 3.2$ S/m, $\varepsilon_{peri} = 60$, $d_{peri} = 15$ nm, $\sigma_{inner} = \times 10^{-9}$ S/m, $\varepsilon_{inner} = 5.5$, $d_{inner} = 4$ nm, $d_{sphere} = 0.8$ μ m, $a_1 = 2$ μ m, $a_2 = a_3 = 0.5$ μ m.

In figure 7.3, the differential argument as a function of membrane conductivity is shown. The results from the spherical model are the same that are presented in the manuscript of the second paper (Figure 3, section 7.3) with the two ellipsoidal models shown next to it. Again, the spherical and parallel ellipsoid model have similar predictions and it is worth noting that the shift in differential argument happens around the same membrane conductivity. When the ellipsoid is perpendicular to the flow direction, the shift is smaller and it happens roughly an order of magnitude lower in the membrane conductivity compared to the two other models. Therefore, if the flow cytometer was designed in a way that forces the bacteria to pass by the electrodes perpendicular to the flow direction it may improve the classification between untreated and heat-treated bacteria.

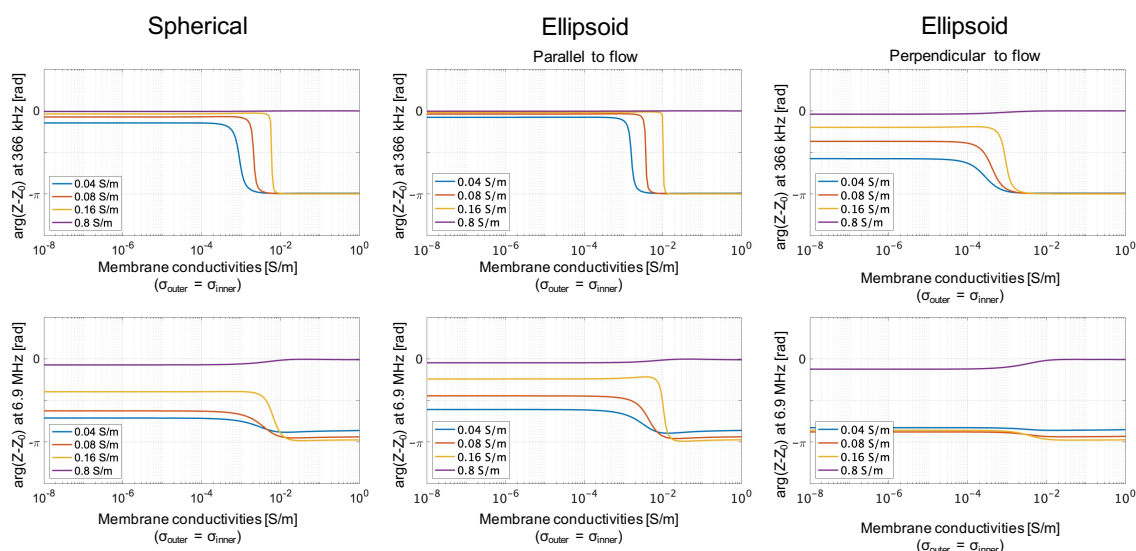


Figure 7.3: Comparison of the shift in differential argument as the membrane conductivity increases calculated for a spherical, ellipsoid oriented parallel to the flow and ellipsoid oriented perpendicular to the flow models. The same parameters as figure 7.2 are used, except $d_{sphere} = 1 \mu\text{m}$, $a_1 = 3 \mu\text{m}$, $a_2 = a_3 = 0.58 \mu\text{m}$.

Finally we will briefly consider the rotational effects caused by the induced polarization of the bacteria during a transition. As a rule of thumb, an ellipsoidal particle will orient itself with the direction of the electric field along the axis with the smallest Clausius-Mossotti factor (Equation 2.17) [81]. For the rod-shaped bacteria this means that the long axis will orient along the electric field. In practice, this means that while the bacteria may enter the detection area parallel to the flow, the influence of the electric field will induce a rotation of the cell towards a more perpendicular position (ie. the bacteria is rotating during the transition). This effect has not been investigated further during this project, but it would be a very interesting phenomena to investigate in future experiments to see if it is prominent at the flow rates and field strengths used in BactoBox.

7.6 Chapter summary

In this chapter we have looked at two papers that both investigate the influence of inactivation of *E. coli* using different methods. The first paper presented the results of experiments with 3 different inactivation methods, ethanol, autoclavation, and heat exposure at 90°C . After inactivation the cells were investigated using traditional plate counts, a fluorescent assay that probe the membrane integrity and with impedance flow cytometry. We saw that after inactivation with each of the three methods, the *E. coli* did not grow and the membrane was perforated. Even so, we saw 3 different impedance responses depending on which inactivation method was used. This led to the conclusion that it is not just a matter of if the bacteria are inactivated but also how, and it showed that impedance flow cytometry can reveal additional information about bacterial cells after inactivation compared to the two other methods. We also investigated whether the inactivated bacteria could be distinguished from untreated cells and found that cells inactivated with ethanol or with autoclaving could be classified as inactivated with a selectivity of 99.6% and 90.9%

compared to viable cells. However, cells inactivated with heat could only be classified with a selectivity of 18.0% compared to untreated cells. This led to the work presented in the draft for the second manuscript, where we investigate the heat-inactivation of *E. coli* further. Here we found that extended exposure to the heat resulted in better classification between untreated and heat-treated *E. coli* based on the differential argument. We also found that lowering the conductivity of the suspension medium improved the classification. This is because the differential shifts as the bacteria turn from being effectively less conducting than the medium surrounding it, to more effectively more conducting (i.e., as the membrane perforates more during the extended exposure to heat). This is the same idea that is presented in section 5.2. We then looked at two IFC measurements made for ethanol and heat inactivation of *Staphylococcus epidermidis* and we saw that the impedance behaviour for the ethanol inactivated was similar to that of *E. coli*, but for the heat inactivation it was not. These simple experiments show that the results obtained for *E. coli* can not necessarily be generalized for all bacteria species. Finally, the influence of the shape and orientation of the bacterial cells on the theoretical models was discussed.

8 Antibiotic susceptibility testing using IFC

The work presented here was conducted and carried out in collaboration with two students (Arshwinth Arulmurugananthavadivel & Savannah Rosa Bruun Frederiksen) as part of their bachelor projects. Arshwinth's project was titled "*Impedance flow cytometry for antibiotic susceptibility testing*" and carried out in the spring of 2020. Savannah's project was titled "*Probing the antibiotic susceptibility of Pseudomonas aeruginosa using impedance flow cytometry*" and carried out in the fall and winter of 2020.

All the experimental data presented in this chapter is obtained with a BactoBox v2 and flow cell design Q.

8.1 Introduction and motivation

In the last 50 years, Antimicrobial resistance (AMR) has grown as a global threat and today the World Health Organisation (WHO) acknowledges antimicrobial resistance as one of the biggest dangers to human health and development [82]. Resistance to common antibiotics has been observed in most major pathogens and by 2050 AMR is predicted to be responsible for 10 million deaths every year [83].

Since the discovery of penicillin in the late 1920s, antibiotics have proved to be an invaluable tool in treating many different bacterial infections. Unfortunately, unlike most other drugs, antibiotics lose their effectiveness over time as bacteria develop new resistance mechanisms meaning that the number of drugs available treatment of infections shrink every year. Furthermore, the increasing level of AMR means that physicians must administer increasingly higher doses in order to effectively combat infections. This, in turn, leads to overuse of antibiotics and eventually to even higher AMR levels in bacteria. Besides overuse and misuse of existing antibiotics, the antibiotic resistance crisis is accelerated by a lack of developments of new drugs [84].

One reason for the overuse of antibiotics and the lack of development of new, more effective, antibiotics is the lack of efficient tools for fast screening of the efficacy of specific antibiotics on specific infections. Antibiotic susceptibility testing (AST) primarily relies on tried and tested methods based on either genotypic test, such as screening for the presence of specific resistance genes, or phenotypic tests based on well-known growth-based methods such as broth dilutions and disk diffusion assays. Phenotypic tests are the most common, where the goal of the test is to establish the lowest concentration of an antibiotic capable of visibly inhibiting the growth of a particular bacteria. This concentration is called the minimum inhibitory concentration (MIC) and typically requires incubation time of 24 hours or more [85]. Another, less common parameter used to quantify antibiotic susceptibility is the minimum bactericidal concentration (MBC) which is the minimum concentration of an antibiotic necessary to inactivate the entire population of bacteria, not just inhibit the growth. The MBC is therefore by definition equal to or higher than the MIC.

Of particular concern are multidrug-resistant (MDR) and extremely drug-resistant (XDR) bacteria strains. *Pseudomonas aeruginosa* is a rod-shaped, gram-negative bacteria that causes infections multiple places in the human body, often in the respiratory system [86]. For example, *P. aeruginosa* is the key bacterial agent of cystic fibrosis, a life threatening disease with no known cure, where thick mucus clogs up the lungs causing severe damage to the respiratory system. *P. aeruginosa* is one of the first pathogens seen to exhibit both MDR and XDR and is therefore often used as a model organism when studying AMR. Until recently, it was believed that *P. aeruginosa* had developed resistance to all classes of anti-pseudomonal agents except polymyxins (also known by the commercial name Colistin) [87]. Colistin is a last-resort antibiotic that is effective against most gram-negative bacteria. It works by disrupting the bacterial cell membrane leading to cell death, a process that involves electrostatic attraction of the antibiotic to the outer membrane of the bacteria. It is only used as a last-resort treatment because of severe nephrotoxic and neurotoxic effects [88, 89]. Similar to other inactivation methods that disrupt the cell membrane in some way, the cell membrane disruption caused by Colistin is expected to be detectable using IFC. Recently, strains of *P. aeruginosa* with Colistin-resistance have been found [90] further complicating the treatment of infections. *P. aeruginosa*' resistance against colistin is related to a change in the surface charge of the bacteria [91, 92] and is therefore likely to affect the impedance response of the cell.

8.1.1 Purpose and goals

We are interested in experimentally investigating two situations where IFC could be used to improve the work flow of antimicrobial susceptibility testing. First of all, we want to test if inactivation of bacteria susceptible to colistin will change their impedance behaviour due to perforation of the cell membrane. Experimentally, we will investigate this for both *E. coli* and *P. aeruginosa*. We are also interested in exploring if a correlation exists between the impedance response, the concentration of the antibiotic and the AMR of the bacteria. If this is possible, it could reduce the time needed for AST of colistin from days to minutes. Secondly, we want to test if AMR caused by changes in the surface charge of *P. aeruginosa* can be probed with IFC *before* exposure to any antibiotics.

8.2 Theoretical modelling of surface charge

Colistin (also known as polymyxin E) is a polypeptide with antimicrobial properties. Colistin disrupts the outer membrane in gram-negative bacteria by binding electrostatically to the negatively charged lipopolysaccharides (LPS), specifically to lipid A. This binding replaces otherwise stabilizing cations in the membrane and allows colistin to enter the cell and perforate both the outer and inner membrane of the cell as illustrated in figure 8.1. Colistin is not effective against gram-positive bacteria species, since the thick outer peptidoglycan layer prevents colistin from interacting with the lipid membrane.

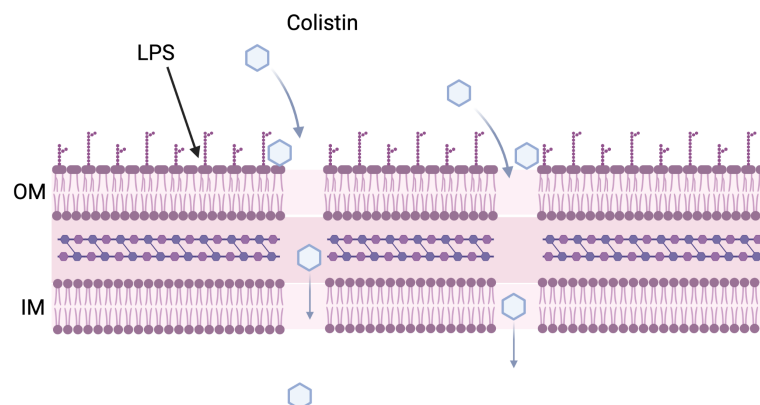


Figure 8.1: Illustration showing the antimicrobial mechanism of colistin. Colistin disrupts the outer and inner membrane in gram-negative bacteria leading to a perforated cell envelope. Created with Biorender.com.

The resistance mechanism of *P. aeruginosa* against colistin involves a change in the net charge of the outer membrane as illustrated in figure 8.2a. The change in charge is caused by a chromosomal mutation leading to either the loss of LPS or modification of the LPS through the addition of 4-amino-4-deoxy-L-arabinose (L-Ara4N) to the phosphate groups of the LPS lipid A region (figure 8.2b). The change in charge reduces the possibility of colistin attaching to the membrane and thus lowers its effectiveness as an antimicrobial agent.

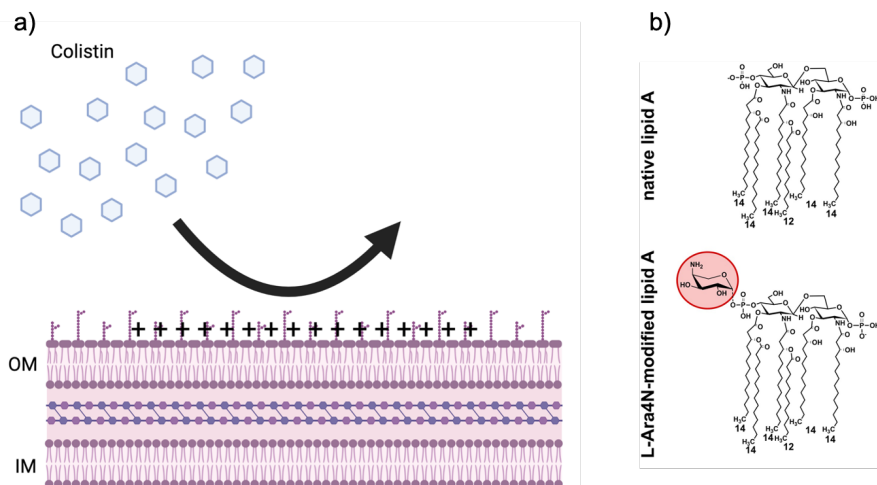


Figure 8.2: a) The change in the surface charge repels colistin molecules and increases the AMR of the cell. Created with Biorender.com. b) Illustration of the chemical structure of lipid A with and without L-Ara4N modification (adapted from [93]).

Experimentally we are interested in investigating two relevant scenarios. First of all, we want to test if we can detect the cell perforation caused by exposure to colistin. Secondly,

we want to see if we can detect changes in the surface charge of resistant bacteria before exposure to any antibiotic.

The impedance changes caused by the perforation of the membrane of bacteria without significant resistance is expected to be similar to other inactivation methods that disrupt the membrane (see chapter 7). Consider the ECM shown in figure 8.3a. As colistin perforates the membrane, the resistance across the membrane (R_{mem}) lowers and the current is able to run through the cytoplasm (R_{cyto}). The change in membrane resistance is dependent on the degree of perforation and therefore on the AMR of the bacteria and exposure conditions (time, concentration, etc.). Depending on experimental conditions, the cytoplasm may also mix with the external medium changing the resistance inside the cell (R_{cyto}).

It is not straight-forward how changes in the surface charge will affect the impedance response of a bacteria. Biological membranes are hugely complicated and well worth studying in detail, but to keep things relatively simple, we are going to limit our considerations to 2 effects:

1. How changes in the surface charge affect the intrinsic capacitance of the outer membrane?
2. How will the capacitance of the electric double layer surrounding the bacteria change if the surface charge changes?

Figure 8.3b shows how a bacteria with a changing surface charge could be modelled.

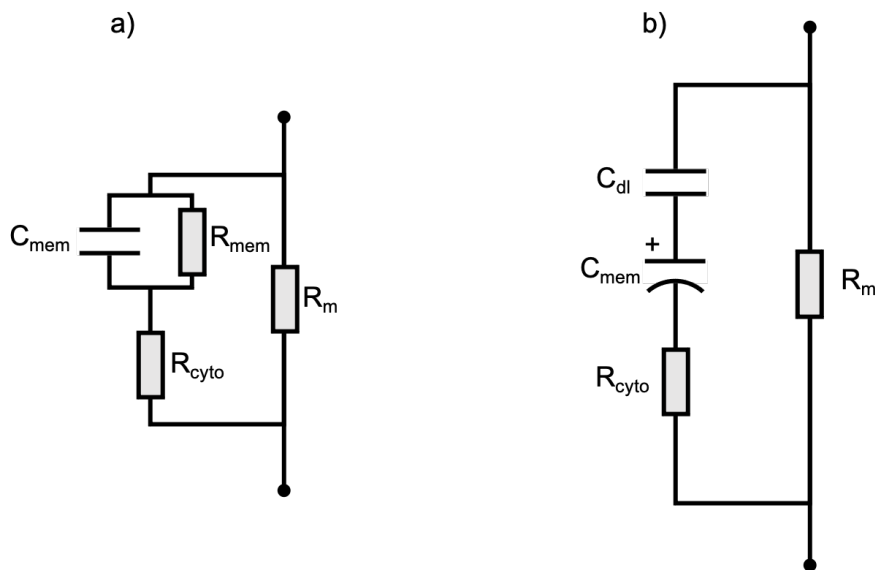


Figure 8.3: Equivalent circuit models used to evaluate changes in impedance due to colistin exposure. a) Circuit with media resistance (R_m) in parallel connection with a bacteria represented by a membrane (R_{mem} , C_{mem}) and cytoplasm (R_{cyto}). As the membrane perforates the resistance across the membrane is expected to drop. b) Circuit with media resistance (R_m) in parallel connection with a bacteria. Two separate capacitors in series represent the diffuse ion layer (C_{DL}) and polarised membrane capacitance (C_{mem}).

Changing the surface charge will change the capacitance (the ability to store charge) of the membrane (ie. its ability to store charge) by changing the natural polarisation of the membrane. As a result, the membrane capacitor will be charged even in the absence of an applied voltage. This is illustrated in the ECM in figure 8.3b as a polarised capacitor. In reality this may be a redundant addition to the ECM since most biological membranes are naturally polarised due to asymmetries in lipid composition or due to the curvature of the membrane creating differences in charge density on the inside and outside of the membrane. In fact, trans membrane potential is known to play an important role in fundamental cellular functions such as ATP synthesis [94]. Furthermore, depending on the phase state of the lipid membrane various degrees of electrostriction can occur, where the electrostatic attraction between the two surfaces of the membrane will compress the membrane [95]. Currently, I am not aware of a model that can predict the change in membrane capacitance based on the pre-polarisation of the membrane, and we will have to see if a difference can be detected experimentally.

Also added to the ECM in figure 8.3b is an additional capacitor on the outside of the membrane capacitor. This capacitor is meant to represent the capacitance created by the diffuse surface layer (DSL) of ions surrounding the bacteria. As previously discussed in relation to the detection electrodes (section 2.3.2), when a charged surface is submerged in an electrolyte an electrical double layer (EDL) will form at the interface. This phenomena also occurs on the surface of charged colloids in suspension and therefore also for bacteria with charged surfaces. For metal electrodes submerged in an electrolyte, the EDL can be modelled by three sub-layers, the inner Helmholtz plane, the outer Helmholtz plane and a diffuse layer of ions (see section 2.3.2). While the electrode-electrolyte interface is fairly well defined the same cannot be said for the interface between the outer membrane and the suspension medium. It is difficult to imagine how the formation of a heterogeneous inner and outer Helmholtz layers across the surface of the bacteria would occur and no clear consensus exists as to how these layers would look. The diffuse layer, however, will be present around the bacteria forming what we will refer to as the diffuse surface layer (DSL) and is what forms the basis of e.g. the electrophoretic mobility of bacteria. Figure 8.3b presents a suggestion for an ECM for a bacteria with a polarised membrane and an electric double layer capacitance on the outside of the membrane stemming from the surface charge.

A term often used in relation to the surface charge of bacteria is the zeta potential. Imagine a boundary inside the diffuse ion layer where the ions are connected tightly enough to the particle or bacteria, so that when the particle moves, the ions move with it. Outside the boundary the ions are left behind when the particle moves. The zeta-potential is the electrostatic potential at this imaginary "slipping plane" within the diffuse layer. It is easy to measure experimentally although care must be taken to control the experimental parameters when doing so [96]. While the zeta potential is not equal to the surface potential we will use it as an approximation of the surface potential and subsequently the surface charge. Soon et al. [97] measure the zeta potential of colistin-susceptible and colistin-resistant *Acinetobacter baumannii* and find that wild-type cells exhibit a greater negative charge (-60.5 to -26.2 mV) than the colistin-resistant cells (-49.2 to -19.1 mV). Meanwhile, Shepard et al. [98] report the zeta potential of *Pseudomonas aeruginosa* PAO1 to range from around -25 mV to +15 mV depending on the growth

conditions and growth medium. Lima et al. [99] have also measured the zeta potential for *Pseudomonas aeruginosa* and report values around -15 mV. The zeta potential for *E. coli* and *S. aureus* has been measured by Halder et al. [100] and were found to be -44.2 and -35.6 mV, respectively. They also observed a 50 % increase in zeta potential when treating the samples with polymyxin B.

8.2.1 Evaluation of the surface double layer capacitance

Using Eq. 2.27 and Eq. 2.28 from chapter 2 we can try to calculate the capacitance of the diffuse surface layer (DSL). Figure 8.4a shows the calculated capacitance of the DSL as a function of surface potential at different media conductivities. The ionic strength of the media affects the Debye length, which is shown in 8.4b (1xPBS has a ionic strength of ~160 mM [55]). We see that changing the surface potential from -100 mV to 0 mV in 1xPBS, changes the DSL capacitance from ~10 pF to ~3 pF (less than an order of magnitude). Similarly, for the other medium conductivity the relative change in DSL capacitance is low.

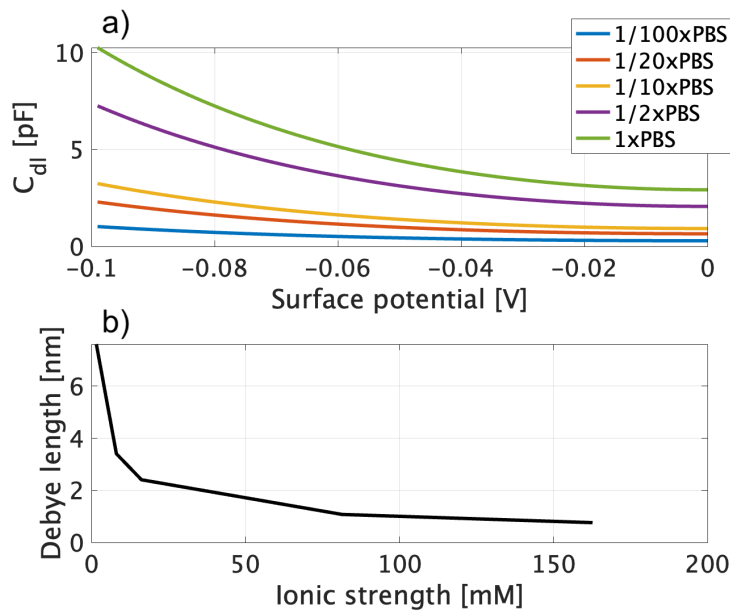


Figure 8.4: a) Diffuse surface layer capacitance as a function of surface potential calculated using Eq. 2.28 for media conductivities of 1/100xPBS, 1/20xPBS, 1/10xPBS, 1/2xPBS and 1xPBS. b) Debye length as a function of the ionic strength of the medium Eq. 2.27. The parameters used for the calculation can be found in table 8.1.

Figure 8.5 shows the differential impedance response as a function of DSL capacitance calculated based on the ECM shown in figure 8.3b and component values calculated using the equations derived by Morgan et al. (presented on page 35) using the parameters found in table 8.1. The plot shows the expected differential impedance at 366 kHz and 6.9 MHz (the values used for experimental measurements). At 366 kHz both the modulus and argument of the differential impedance only changes very slightly with the DSL capacitance. In the high frequency we see a significant shift in both modulus and argument when the DSL capacitance drops below approximately 10^{-15} (1 fF). This is however a couple of orders of

Table 8.1: Parameters used to calculate the differential impedance response of a microfluidic channel with a bacteria (represented as a sphere with one shell). Values from [101].

Parameter	Value
Temperature	298 K
Cell diameter	1 μm
Medium permittivity	80
Electrode width	10 μm
Electrode length	25 μm
Channel height	10 μm
Cytoplasm conductivity	0.5 S/m
Cytoplasm permittivity	50
Membrane thickness	10 nm
Membrane permittivity	8
Valence of ions in PBS	1

magnitude lower than the expected DSL capacitance and we can therefore not expect to see differences in the measured impedance from the predicted differences in surface charge shown in figure 8.4a.

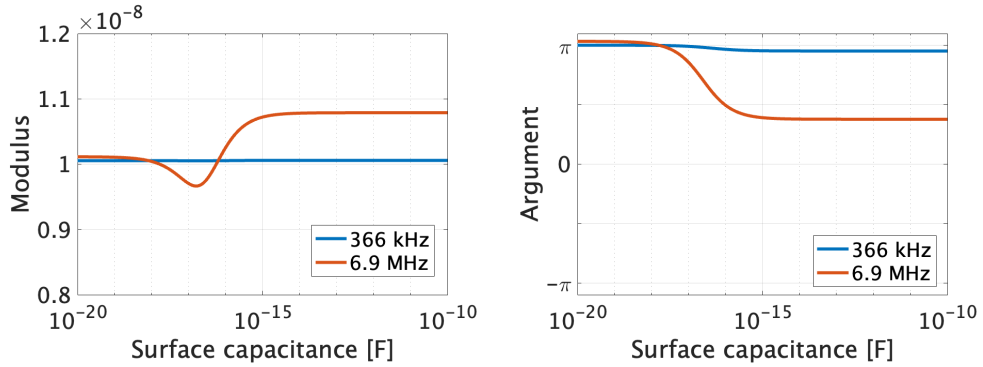


Figure 8.5: Calculated impedance response as a function of diffuse surface layer capacitance.

8.3 Experimental methods

8.3.1 Bacteria strains

For experiments, three bacteria strains were used: one *E. coli* strain and two *Pseudomonas aeruginosa* strains. The *E. coli* strain (*Escherichia coli* (Migula) Castellani and Chalmers ATCC8739) is colistin susceptible. The MIC of colistin for treatment of *E. coli* reported to be around 1 $\mu\text{g}/\text{ml}$ [102]. The two *P. aeruginosa* strains used were a wild-type strain susceptible to colistin designated PAO1 and a colistin resistant strain designated Q5. Q5 is PAO1 with five additional mutations introduced to the chromosome that add resistance to colistin. The resistance is provided through mutations in the genes *pmrB*, *opr86*, *lpxC*, *PA5194* and *PA5005* [90]. The reported MIC of colistin for the *P. aeruginosa* strains were 1 $\mu\text{g}/\text{ml}$ and 512 $\mu\text{g}/\text{ml}$ for PAO1 and Q5, respectively. Both *P. aeruginosa* strains were acquired from Copenhagen University, courtesy of postdoc Vinoth Wigneswaran.

8.3.2 Colistin treatment and IFC measurements of *E. coli*

Experiments with *E. coli* were carried out in the spring 2020. Due to COVID19 the labs at the university were closed and the experiments were instead carried out at SBT Instruments' labs. The choice of materials and methods are therefore different from what was later used for *P. aeruginosa* analysis.

E. coli bacteria (ATCC8739) was incubated overnight at 37°C on a tryptic soy agar (TSA) plate. On the day of the experiments, 5 colonies were collected from the plate using a culture loop and gently re-suspended in 20 ml of 1/20xPBS giving a concentration around 100e6/ml. To confirm the concentration, 30 µl of sample was diluted into 3 ml of 1/20xPBS (1/100 dilution) and measured with BactoBox with a target concentration of 1e6/ml. If the concentration was too low, an additional colony was collected from the plate and added to the sample. If it was too high, the sample was further diluted with 1/20xPBS. Colistin concentrations were prepared by dissolving colistin sulfate (Sigma Aldrich, C2700000) in ultra-pure water for a stock concentration of 1 mg/ml. A serial dilution of colistin from 80 µg/ml to 1.25 µg/ml with each step in the dilution halving the concentration was then prepared (total of 8 concentration including 0 µg/ml as seen in figure 8.6). 0.5 ml of bacteria sample (at ~100e6 cells/ml) was added to each colistin concentration (halving the colistin concentration in each vial) and the samples were left for 3 hours at room temperature. Then, 30 µl from each sample was transferred to 3 ml of 1/20xPBS and measured using BactoBox. The remaining 970 µl was plated on petrifilm (3M Petrifilm™) and left in an incubator at 37°C for 48 hours.

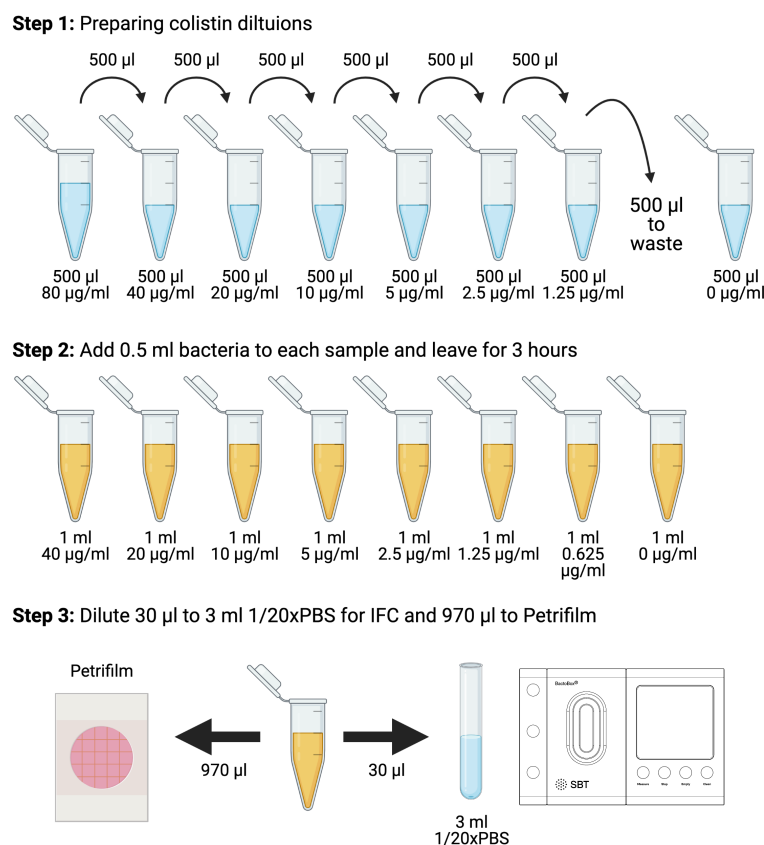


Figure 8.6: Schematic showing the treatment of *E. coli* with colistin at concentrations. First, samples of decreasing colistin concentrations are created via serial dilution, each step halves the concentration. Then 0.5 ml *E. coli* at $\sim 100 \times 10^6$ cells/ml, are added to each vial and left for 3 hours. Finally the treated *E. coli* samples are split for plating on Petrifilm and for IFC measurements. Created using Biorender.com.

Impedance measurements were carried out with BactoBox at two frequencies (366 kHz and 6.9 MHz) with a total measurement time for each sample of 60 seconds.

MIC determination of susceptible and resistant *P. aeruginosa* strains

MIC determination for *P. aeruginosa* was done via micro broth dilution (MBD) in microtiter plates for both the PAO1 strain (susceptible) and the Q5 strain (resistant). Wells were prepared with 50 µl of LB agar with concentrations of colistin ranging from 1048 to 1 in each together with a well for growth control and contamination control of 100 µl each. To prepare the bacteria, 100 µl of liquid overnight culture was reinoculated in 10 ml LB for both PAO1 and Q5 and left in the incubator for 4 hours. This was done in order to get bacteria in the exponential growth phase with as few non-viable cells as possible. After four hours, the bacterial concentration was measured with IFC and the culture was diluted to obtain $\sim 1 \times 10^6$ cells/ml. 50 µl of diluted culture was added to each well in the microtiter plate (except the contamination control). The microtiter plate was left overnight at 37°C and 180 rpm. The MIC value was determined as the lowest colistin concentration with no visible growth.

8.3.3 Colistin treatment and IFC measurements of *P. aeruginosa* strains

Colistin treatment and IFC measurements were performed in a similar way to how it was done with *E. coli*. 0.5 ml of the exponential culture was added to samples of 0.5 ml colistin with varying concentration (from 1028 µg/ml to 0 µg/ml) prepared via serial dilution. Note that efficacy of the antibiotic depends on the concentration of both bacteria and colistin concentration [103] (ie. if the colistin concentration is kept constant, a rise in bacterial concentration will lower the effectiveness of the colistin). The bacteria concentration needs to be relatively high (~500e6 cells/ml) to retain enough bacteria in the sample for IFC after the subsequent dilution step. The samples were left for 3 hours at room temperature, after which 6 µl from each sample was pipetted into 3 ml of 1/20xPBS. Impedance measurements were carried out with BactoBox at two frequencies (366 kHz and 6.9 MHz) with a total measurement time for each sample of 180 seconds.

8.4 Experimental results

8.4.1 Colistin treatment and IFC measurements of *E. coli*

Measurements with BactoBox revealed that the impedance response of *E. coli* changes when the cells are treated with colistin. Figure 8.7 shows the measured differential argument of the 8 samples of *E. coli* treated with increasing concentrations of antibiotic. At 0 µg/ml the bacteria population is placed in the by now well known "banana" shape (position 2 as discussion in section 5.2), although a significant portion of the population is placed in the bottom left corner of the banana (position 3). This could be because the bacteria are grown on the surface of an agar plate overnight and resuspended in 1/20xPBS just before the beginning of the experiment instead of from a liquid culture. Meaning that dead cells from the agar surface or cells with additional extracellular material compared to the cells from the liquid culture would be transferred to the sample. As the colistin concentration increases the cells shift right and up, closer to the position of beads and e.g. autoclaved cells (position 1). This indicates that the cells have a higher impedance than the surrounding medium in both low and high frequency, presumably because the cytoplasm has a lower conductivity than expected, either intrinsically or because of mixing with the surrounding media. However, it is evident from the Petrifilm (also figure 8.7) that the colistin is inactivating the cells. Since we are growing the cells on Petrifilm, the growth is a better indicator of MBC than MIC because all cells need to be dead to see no colonies. At 2.5 µg/ml of colistin, we see the first visual indication of the inactivation and at 10 µg/ml no colonies are seen. Both concentrations are higher than the expected MIC of ~1 µg/ml, which may be due to the high concentration of cells or because we are looking at the growth on plates instead of in liquid culture. Nevertheless, the shift in differential argument appears to happen in correspondence with the changes in CFU count on the Petrifilm.

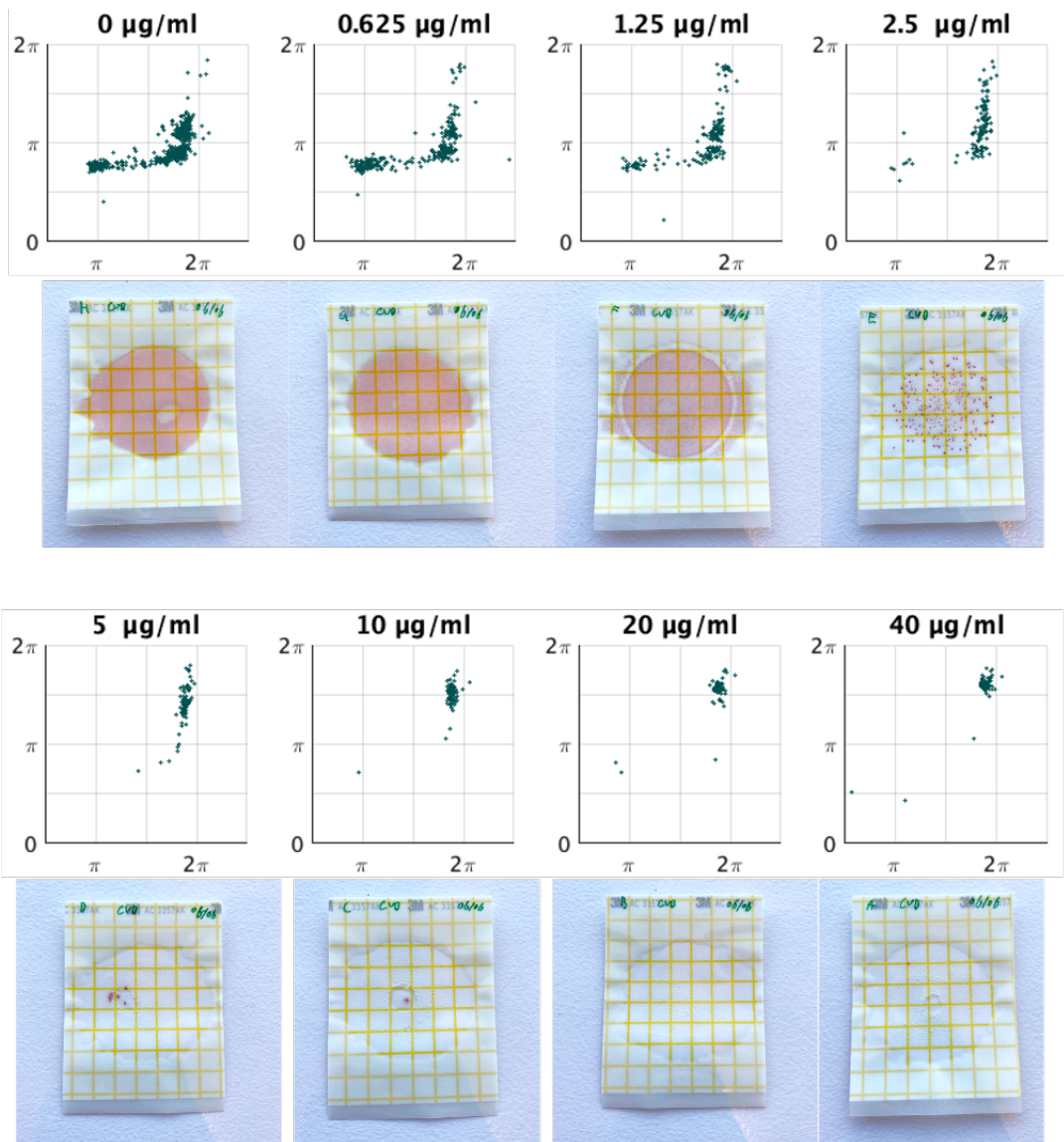


Figure 8.7: Scatter plots showing the differential argument for *E. coli* samples with increasing concentrations of colistin (from 0 $\mu\text{g/ml}$ to 40 $\mu\text{g/ml}$). Under each scatterplot the Petrifilm from the corresponding sample is shown after 48 hours growth at 37°C.

To better illustrate this, we can look at the box plots for the low and high frequency argument shown in figure 8.8. The box plots show the median (vertical red line), quartiles (top and bottom of the blue box), extremes (whiskers) and outliers (red plusses) of the population. In the low frequency we see that the median only changes slightly with increased colistin concentration, but that the number of outliers in the population reduces as we move up in colistin concentration. This is slightly surprising and again illustrates the point that the cell remains less conductive compared to the medium at the low frequency. If the cell membrane was disrupted we would expect a decrease in impedance as the current flows through the conductive cytoplasm. If we assume that the membrane is in fact disrupted (which the inactivation shown on the Petrifilm would suggest), then this

must mean that the conductivity of the cytoplasm is lower than expected (likely due to mixing with the surrounding medium) or that the cell has simply collapsed in on itself. Looking at the high frequency differential argument shown in figure 8.8 we see that it shift upwards (again supporting the idea of an exchange of cytoplasm). We also see that the shift starts at 2.5 $\mu\text{g}/\text{ml}$ and ends at 10 $\mu\text{g}/\text{ml}$, very similar to what we saw with the growth on the Petrifilm.

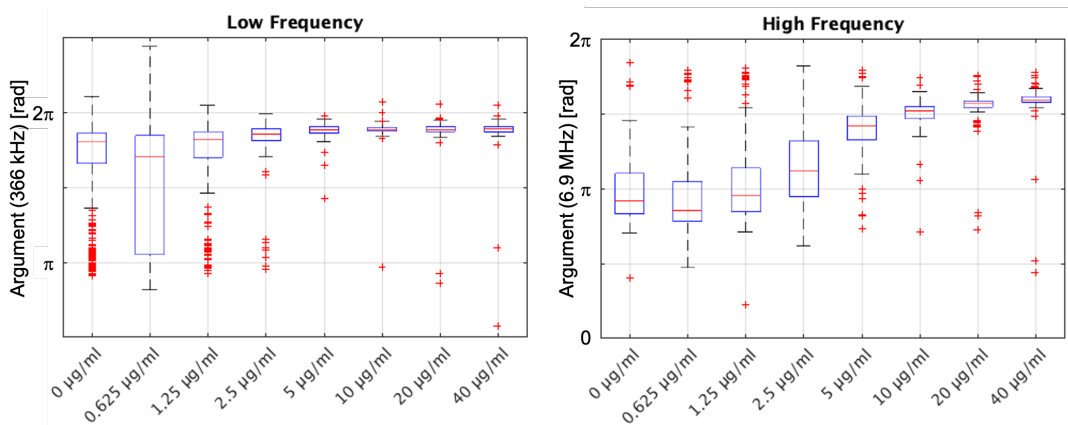


Figure 8.8: Boxplots comparing the shift in low and high frequency argument of *E. coli* at increasing concentrations of colistin. The central red line indicates the median, and the bottom and top edges of the box indicate the quartiles. The whiskers extend to the most extreme data points not considered outliers, and the outliers are plotted individually using red '+' symbols.

8.4.2 MIC determination and colistin treatment of *P. aeruginosa*

The MIC of *Pseudomonas aeruginosa* PAO1 and Q5 was determined using micro broth dilution (MBD) to be 1 and 8 $\mu\text{g}/\text{ml}$, respectively. This is as expected for PAO1, but much lower than expected 512 $\mu\text{g}/\text{ml}$ reported for Q5. The experiment was repeated multiple times with the MIC for the colistin resistant *P. aeruginosa* shifting between 8 and 16 $\mu\text{g}/\text{ml}$. It is currently unclear if the resistance is in fact weaker than expected or if the mismatch in results are related to the MBD procedure in some way. Nevertheless, Q5 does have higher resistance to colistin compared to PAO1. To illuminate this further, drop plating of the bacteria culture after 3 hours of exposure to colistin (similar to the procedure before IFC measurements) was done. The plating (see appendix C.1 for images) revealed that a much higher concentration of colistin was required to inactivate the bacteria with with 32 $\mu\text{g}/\text{ml}$ and 1024 $\mu\text{g}/\text{ml}$ needed for PAO1 and Q5, respectively. The increase in needed concentration is probably caused by the higher initial bacteria concentration.

Figure 8.9 shows the measured differential argument for PAO1 at increasing colistin concentrations. As with *E. coli* we see a shift in the differential argument as the colistin concentration increases, however unlike the *E. coli* the population shifts down and to the left, indicating that the cells become more conducting than medium around them.

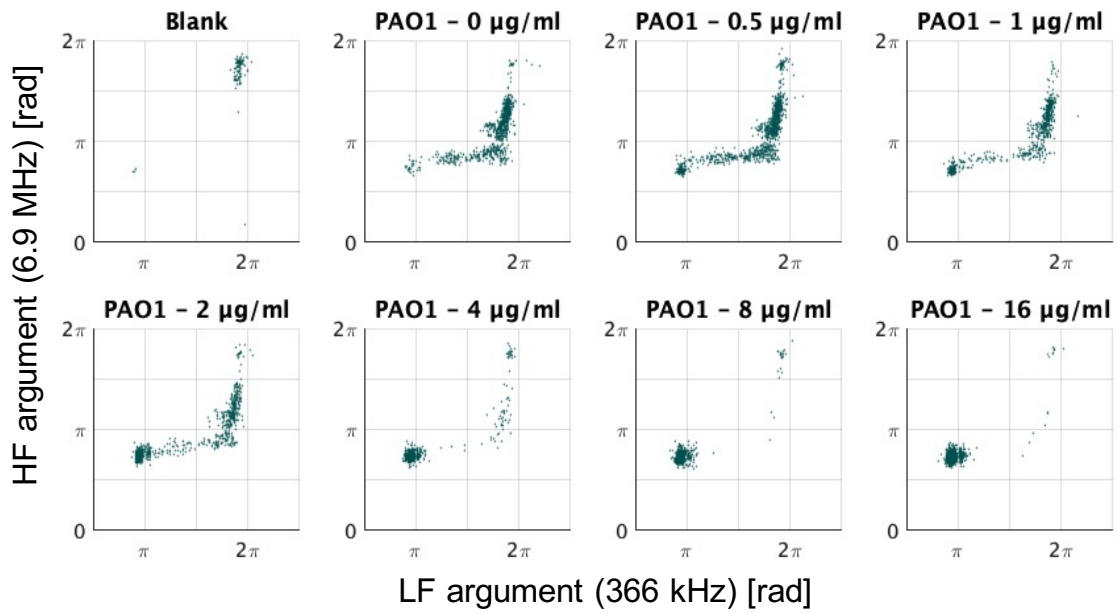


Figure 8.9: Scatterplots showing the shift in populations of colistin susceptible *P. aeruginosa* (PAO1) at increasing colistin concentrations. First a background measurement (Blank) is shown with no added bacteria. Then the results from samples with 0, 0.5, 1, 2, 4, 8 and 16 $\mu\text{g/ml}$.

The shift is even clearer when looking at the box plots in figure 8.10, especially in the low frequency. Here we see a shift of the median of almost 2π as the colistin concentration is increased from 1 $\mu\text{g/ml}$ to 4 $\mu\text{g/ml}$. Some outliers remain close to 2π , but we see from the extension of whiskers, that the majority of the population has shifted. The shift occurs at a slightly higher colistin concentration than the expected 1 $\mu\text{g/ml}$, probably due to the high bacteria concentration in the samples artificially increasing the MIC. The cells are changing from being less conductive than the medium to more conducting, as expected when the membrane is perforated and the current runs through conductive cytoplasm. The shift is also seen in the high frequency argument, but to a lesser extent, implying the the membrane was at least still partially opaque at the high frequency.

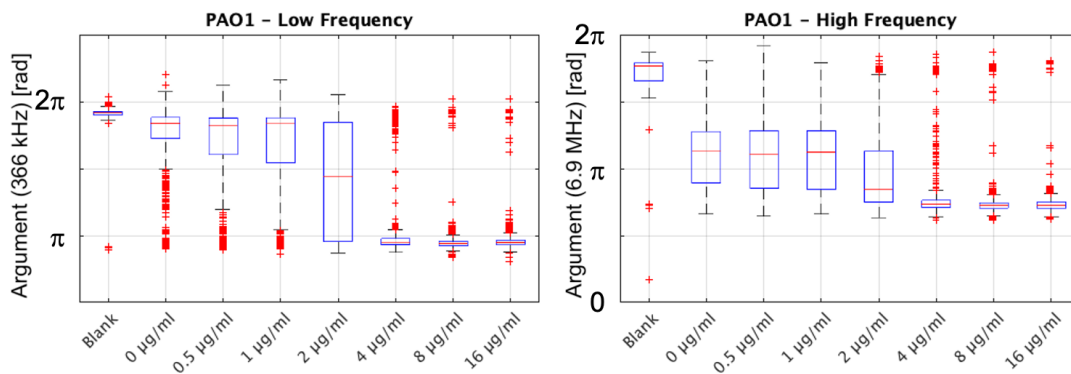


Figure 8.10: Boxplots comparing the shift in low and high frequency argument of colistin susceptible *P. aeruginosa* (PAO1) at increasing concentrations of colistin. The central red line indicates the median, and the bottom and top edges of the box indicate the quartiles. The whiskers extend to the most extreme data points not considered outliers, and the outliers are plotted individually using red '+' symbols.

Finally, the differential argument for Q5 at increasing colistin concentrations is shown in figure 8.11 with the corresponding box plots shown in figure 8.12. Note that the dilution range of colistin is different than the one shown for PAO1 in figure 8.9 and 8.10. Looking first at the low frequency differential argument, we again see a shift in median of approximately 2π , as the colistin concentration changes from $8 \mu\text{g/ml}$ to $32 \mu\text{g/ml}$ (the MIC determined using MBD was $8 \mu\text{g/ml}$). However, when the colistin concentration is increased even further we see a shift back to the original argument, except with fewer outliers, and the population ends up in a position similar to where we saw the colistin treated *E. coli*. As the colistin concentration increases the cells go from having a higher impedance compared to the medium, to having a lower impedance than the medium, and finally back to having a higher impedance at the highest colistin concentrations.

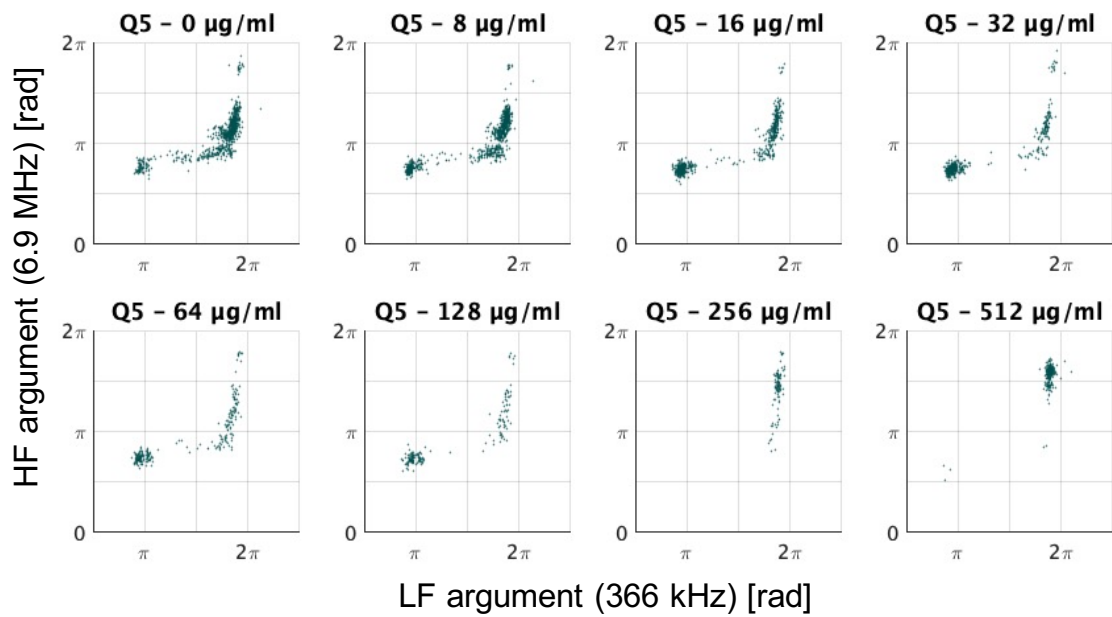


Figure 8.11: Scatterplots showing the shift in populations of colistin resistant *P. aeruginosa* (Q5) at increasing colistin concentrations.

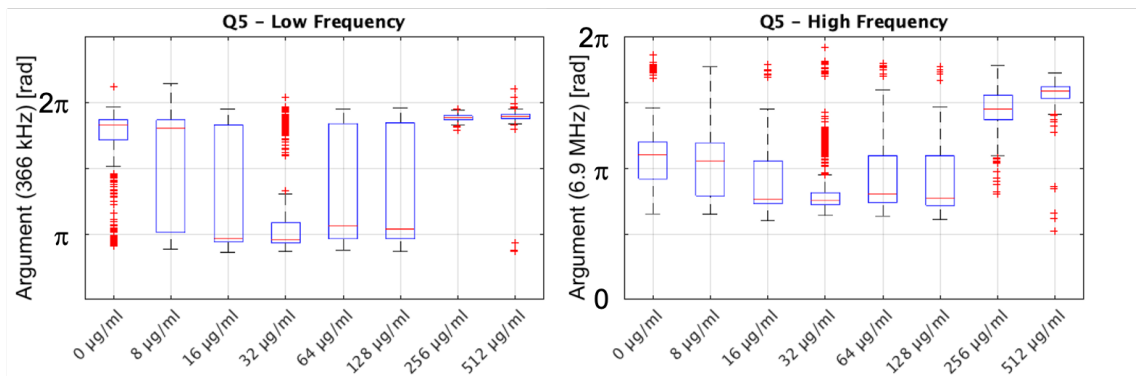


Figure 8.12: Boxplots comparing the shift in low and high frequency argument of colistin resistant *P. aeruginosa* (Q5) at increasing concentrations of colistin. The central red line indicates the median, and the bottom and top edges of the box indicate the quartiles. The whiskers extend to the most extreme data points not considered outliers, and the outliers are plotted individually using red '+' symbols.

The reasons for this behaviour are not obvious. Supposedly, the increased colistin concentration would cause to a higher degree of membrane perforation for the same bacteria concentration leading to easier exchange of cytoplasm and medium. However, this does not explain why the *E. coli* behaviour is different from *P. aeruginosa* at comparable concentrations of colistin. While both bacteria are gram negative some differences in both the outer [104] and inner [105] membrane have been reported. Furthermore, since the *E. coli* were grown on an agar plate and not in suspension like the *P. aeruginosa*, the additional extracellular material from the *E. coli* may help keep the cytoplasm from mixing with the

surroundings.

8.4.3 Comparison between untreated susceptible and resistant *Pseudomonas aeruginosa*

Lastly we compare the impedance response of untreated PAO1 and Q5 to see if the presumed differences in surface charge is detectable. Figure 8.13 shows box plots of the differential argument in the low and high frequency for repeated experiments with PAO1 and Q5. The measurements were performed on diluted (1/500 in 1/20xPBS) overnight cultures. For Q5 the experiment was performed twice with three repetitions each time. For PAO1 the experiment was performed 3 times, also with 3 repetitions.

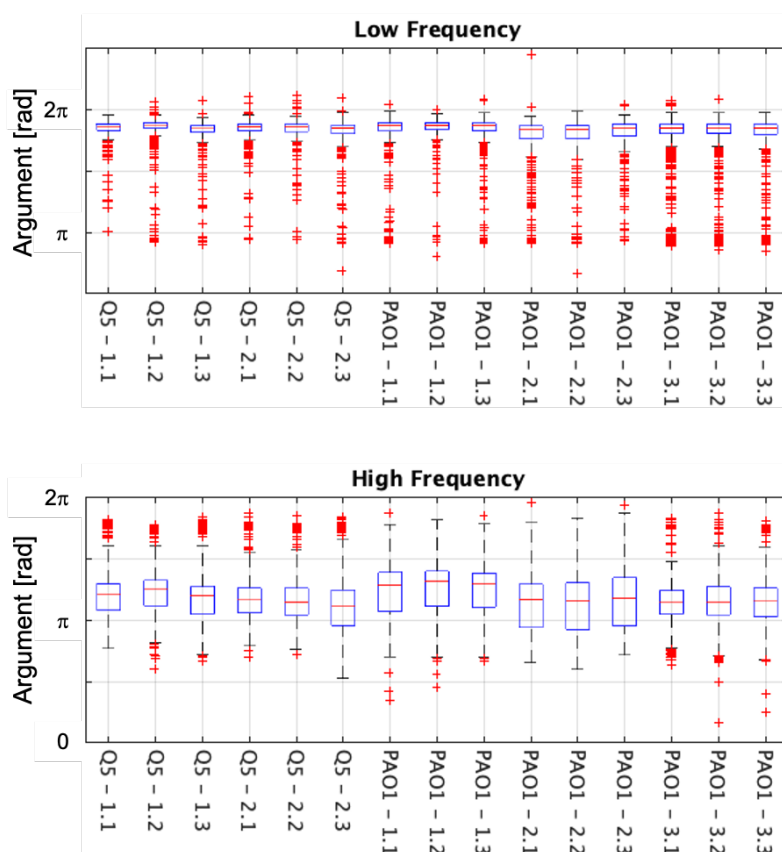


Figure 8.13: Boxplots comparing the measurements of colistin susceptible (PAO1) and resistant (Q5) *P. aeruginosa* with no exposure to colistin. The central red line indicates the median, and the bottom and top edges of the box indicate the quartiles. The whiskers extend to the most extreme data points not considered outliers, and the outliers are plotted individually using red '+' symbols.

It is seen in the boxplots shown in figure 8.13 that the impedance response of PAO1 and Q5 overlap significantly and that no obvious distinction between the two can be made. It is also clear that the variation between measurement (particularly between experiments) is too great. The variation is expected to arise from a mix of both biological variation and technical variation. For each experiment a new culture of *P. aeruginosa* is grown and the cells might develop differently from time to time. At the same time, the

impedance measurements may vary based on external factors such as temperature and medium composition (the technical variation is however fairly low, see section 4.2.3).

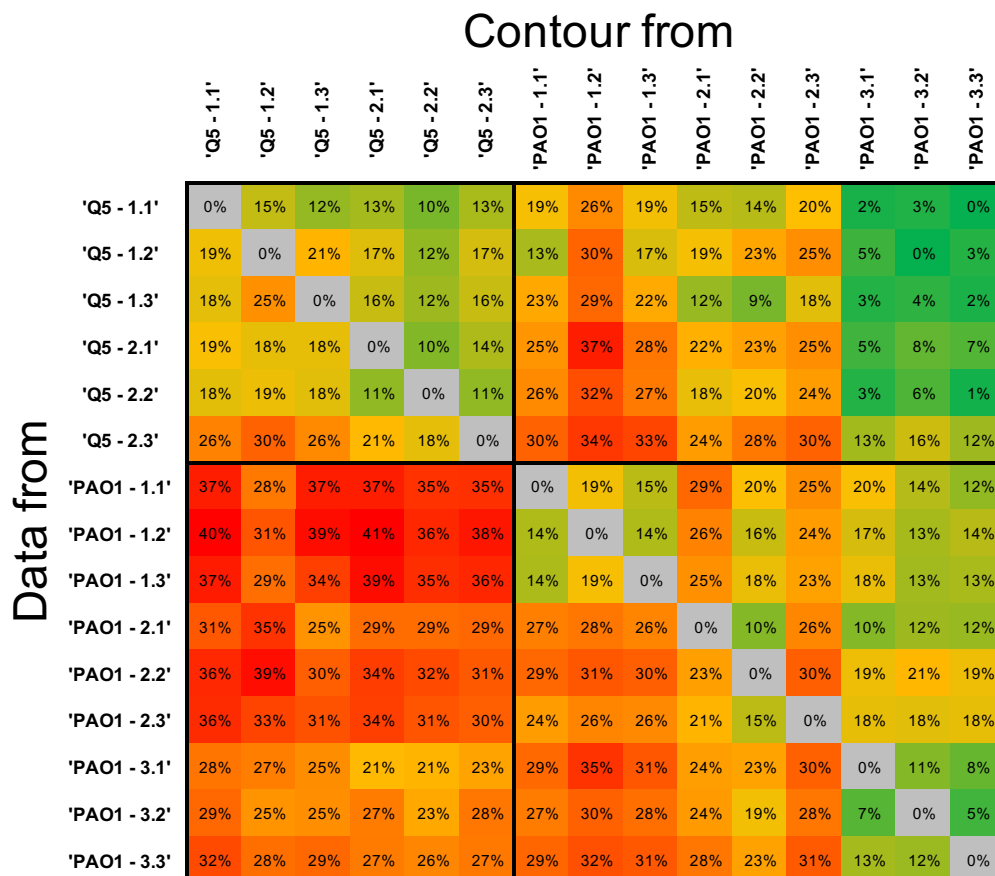


Figure 8.14: Contour comparison of 6 measurements on colistin resistant (Q5) and 9 measurements on colistin susceptible (PAO1) *P. aeruginosa*. Data is set up in a grid with the data points from each measurement on the y-axis and the 60% contour from each measurement on the x-axis. Numbers in each grid point show the absolute difference in cell fraction from 60% when looking at the data from the measurement indicated on the x-axis inside the 60% contour from the measurement indicated on the y-axis. Color grading is based on the fraction difference and goes from green (0%) to yellow (30%) to red (>60%).

In a final attempt at finding differences between PAO1 and Q5, the contour method presented in section 4.2.3 is used with a target cell fraction of 60%. The results are shown in figure 8.14. Four boxes are defined in the plot separating the measurement data and contours from the two strains from each other. If we look at the contours from the Q5 data (left side of the matrix), we see that they better represent the Q5 data compared to PAO1 (however, the last Q5 measurement, 2.3, does not fit this pattern). Looking instead at the contours from the PAO1 data, it seems as good at representing Q5 and PAO1. Thus, even though differences between the strains can be seen, the two strains can not be clearly differentiated from each other.

8.5 Chapter summary

Based on the results obtained and described in this chapter it is evident that IFC has the potential to play a role in antibiotic susceptibility testing, but that more work is required to mature the technology and understand the relationship between the MIC and the impedance measurements. The effect of the antibiotic colistin on the impedance response of *E. coli* and *P. aeruginosa* cells has been tested and a correlation between bacterial inactivation of the antibiotic and a shift in the differential argument of the impedance measurements was found. However, we encountered difficulty in obtaining a stable MIC value for the resistant *P. aeruginosa* strain and more experiments should be conducted before a more rigorous conclusion can be made. We also tested if it was possible to distinguish colistin susceptible *P. aeruginosa* from resistant *P. aeruginosa*, based on the idea that the antibiotic resistance arise due to changes in the surface charge of the cells causing changes in the membrane capacitance and the capacitance of the diffuse ion layer surrounding the bacteria. However, it was not possible to consistently differentiate the susceptible strain from the resistant strain.

9 Conclusion and outlook

A need exists for a new, fast and accurate method for characterization and quantification of bacterial samples. In this thesis, the impedance flow cytometer developed by SBT Instruments (i.e., BactoBox) has been presented and used for characterization of various bacterial samples.

First the theory behind dielectric measurements of bacterial cells was presented. Bacterial cells are one of the most diverse populations on earth and come in many shapes and sizes. This means that there is no single model that can describe the impedance response of every bacteria, however some common characteristics exist that can be generalized. For example, mixture theory can be used to calculate an effective complex permittivity that describes the bacterial cell suspended in a liquid electrolyte between two microelectrodes. The modelling of the cell can be more or less complex, taking into account multiple membranes and the shape of the cell as well as the geometry of the detection electrodes.

Next, a presentation of the five functional areas that make up BactoBox was given. The design of the flow cell at the heart of BactoBox involves a larger bypass channel in connection with a much smaller detection channel. This combination of channels is unique in IFC systems and enables BactoBox to have a much higher flow rate through the entire flow system compared to other systems. Two different designs were used for experiments. In the first design, the detection channel is separated from the bypass channel by a polymer wall. This improves the variation of the electric field and thus leads to less signal variation but is also more prone to clogging. The other design has an open boundary between the detection channel, which leads to less clogging but higher signal variation. A COMSOL simulation revealed that the variation in the field strength on the electrode edge caused to a loss of peak height of ~50%. The difference in size between the bypass and detection channel means that flow behavior for each region must be considered individually. We saw that while the Reynolds number was 500-1000x times larger in the bypass channel compared to the detection channel, it was still well below the threshold of turbulent flow (approximately 20x lower). This means that the flow in both channels is laminar and that the distribution of flow between them can be calculated using the Hagen-Poiseuille law to find the ratio between their hydraulic resistances. Additionally, the fluidic system, electronics and software analysis of BactoBox was discussed. It was particularly interesting, that the input voltage to the detection electrodes was attenuated significantly (~30%) at higher frequencies (>3MHz). If this attenuation is not taken into account, either through balancing the input magnitudes of the signal or through post processing of the data, it may lead to misinterpretation of the results. Finally, the importance of compensating the concentration calculation because of the parabolic flow profile in the detection channel was discussed. The flow rate is estimated based on the average time it takes a particle or bacteria to pass between the electrodes. Because of the parabolic flow profile the flow rate is overestimated since more particles pass the electrodes in the fast flow. This leads to an error when calculating the concentration. The error is corrected through a correction factor multiplied to the average transition time. This correction factor is calculated numerically using MATLAB and is found to be 1.44 and 1.25 for the two flow cell designs.

BactoBox was used to experimentally characterize bacteria and other particles under a number of different circumstances. The first important results were that particles and bacteria can be differentiated based on their effective conductivity compared to the liquid medium surrounding them. For example, if a bacterial cell is perforated during inactivation, it changes from being less conducting than the surrounding medium (the cell membrane electrically isolates the cell) to being more conducting (the membrane is broken, and the cytoplasm is probed), as long as the cell interior is more conducting than the medium. This change in conductivity is very apparent in the differential argument measured with IFC and forms the basis of the differentiation between bacteria and other particles in BactoBox. Because of this the conductivity of the media has been kept at low for all of the experimental work, by using phosphate buffered saline diluted with filtered and deionized water (typically in a ratio of 1/20).

BactoBox was used to measure the impedance response of 6 different bacteria strains. The strains were a mix of gram-positive and gram-negative bacteria, 5 of them were rod-shaped while the last was spherical. While impedance response populations differed between the species (although still with significant overlap), it was not possible to link the impedance response to the gram-type or shape of the species. This is partly because of complexity in the bacteria structure and morphology, with significant variation in size and membrane based on e.g. growth conditions even within the same species. In an attempt to remove some of this variation and get a better understanding of the probable properties of a bacterial cell, an experiment using custom-synthesized liposomes was set up. The liposomes were synthesized so that the conductivity both inside and outside the liposome, as well as the lipid composition in the membrane, was known. Measurements on the liposome sample showed that they could be differentiated based on their interior conductivity. However, comparisons with theoretical calculations revealed that the liposomes were not unilamellar but instead had multiple membranes. This made proper probing of the liposome interior impossible since it was shielded by the membranes. To truly use liposomes as a model particle for IFC measurements all properties should be known, including the number of membranes. This can be achieved either by changing the synthesis method to one where the control of the number of membranes is better (e.g. microfluidic jetting) or by having a control method that can evaluate the number of membranes (e.g. optical inspection of stained membranes)

An important aspect of BactoBox, when used to evaluate the risk of bacterial contamination in e.g., a production environment is that it can differentiate between viable and dead bacteria. To test this, *E. coli* bacteria were inactivated using 3 different inactivation methods (ethanol, autoclaving, and heat exposure) and then investigated using traditional plate counts, a fluorescent assay that probe the membrane integrity and with impedance flow cytometry. It was seen that after inactivation with each of the three methods, the *E. coli* did not grow, and the membrane was perforated. Surprisingly however, the impedance response was different for each of the inactivation methods. This led to the conclusion that it is not just a matter of if the bacteria are inactivated but also how, and it showed that impedance flow cytometry can reveal additional information about bacterial cells after inactivation compared to the two other methods. Also, surprisingly, it was found that while *E. coli* inactivated with ethanol and through autoclaving could be differentiated from untreated cell (with a specificity of 99.6% and 90.9%), the cells inactivated with

heat could not. This spurred additional experiments with heat exposure, and it was found that prolonged exposure to the heat led to better classification between untreated and heat-treated *E. coli* and that lowering the conductivity of the suspension medium also improved the classification. To truly understand the correlation between heat-exposure and impedance response an alternative method for direct inspection of the degradation of the membrane will be needed. Here electron microscopy seems like an obvious candidate, where scanning electron microscopy (SEM) could be used to evaluate the surface morphology and transmission electron microscopy (TEM) could be used to evaluate the cross section of the envelope structure.

Finally, the effects of treatment with the antibiotic colistin on *E. coli* and *Pseudomonas aeruginosa* bacteria was investigated. It was found that treatment with colistin also led to a shift in the differential argument which became more significant at higher concentrations of antibiotic. Additionally, the shift occurred at higher colistin concentrations when a *Pseudomonas aeruginosa* strain with known resistance to colistin was used, relating the shift in argument to the minimum concentration needed to inactivate the bacteria. This shows how impedance flow cytometry and BactoBox has the potential to play a role in antibiotic susceptibility testing in the future, if it is developed properly.

Seen together, these investigations provide a deeper insight into the workings of the technology employed in BactoBox and the consequences of some of the implementation choices made. The presentation of the theoretical background together with the walk-through of the functional parts of BactoBox can form the backbone of future product development activities, while the experimental work can provide insight into where to focus improvements of the product and core technology going forward and inspiration to future applications.

9.1 Future outlook

The work with understanding how the electrical properties of bacteria can be measured with IFC and how to interpret the obtained results is far from complete. If there is one thing I have learned during the course of this project, it is that impedance measurements of bacterial cells is a complex and highly multidisciplinary endeavor. In the following section I will give my perspective and suggestions for continuing the work in the future.

Further work with synthesis and measurements of liposomes needs to be done. Specifically, the synthesis method needs to be improved so that unilamellar liposomes can be produced. Sonication is the most extensively used method for liposome synthesis but small size and pollution from the sonication probe tip makes it an undesirable method for synthesis for our application [106]. Instead an injection based method could be used, preferably implemented in a microfluidic device [107, 108]. However, the amount of work required to synthesize liposome with desired properties may be overwhelming compared to the experimental pay off. Alternatively, a characterisation method that probes the number of membranes could be used to adapt the theoretical model to the experimental conditions. While several methods exist for size classification of liposomes (such as atomic force microscopy, nano particle tracing and dynamic light scattering), characterization methods for the lamellarity are less common. For this, techniques like small angle x-ray scattering and analysis of the changes in the fluorescent spectrum of labelled liposomes [109] should be explored. If these challenges can be solved, I believe characterisation of liposomes

can become a great tool for understanding how biological cells and particularly biological membranes are characterised using IFC.

During this project, the change in impedance due to inactivation of bacterial cells was investigated. The majority of this work was done with *E. coli*, with only a few experiments performed with other species. Future experiments should focus on investigating whether the results observed for *E. coli* can be generalized to more species. This means mapping of the impedance of the bacteria after inactivation, but also understanding the variation of untreated cells from species to species. An interesting approach to this, could be to find bacteria that are resistant to specific types of inactivation (e.g. a heat resistant strain). An experiment could be set up with the goal of identifying the resistant strain. This will be important since BactoBox will be used in many different environments all over the world each having a unique microbial environment.

However, to truly understand which of the many morphological and structural changes that occur in the bacteria during inactivation can be probed with IFC, an alternative method will be needed to compare and validate the obtained results with. For this I believe that correlation between electron microscopy images and the impedance results will be very insightful. Scanning electron microscopy (SEM) should be used to investigate the surface morphology of the the bacterial cells. It would be particularly interesting to use SEM to visualise the perforation or deterioration of the cell membrane after inactivation. As discussed in chapter 7, the impedance response is different based on the type of inactivation used and it would be very valuable to correlate this change to the the actual state of the cell membrane. Furthermore, transmission electron microscopy (TEM) could be used to measure the actual dimensions of the bacterial cell and particularly the thicknesses of the various layers in the cell envelope. In chapter 5 we discussed how different bacteria species provided slightly different impedance responses and it would be interesting to see if these difference could be related to actual differences in bacterial cell structure. Beside the fact that SEM and TEM are not easy techniques to master, I have two other concerns with using electron microscopy as a comparison technique. First of all, since both SEM and TEM images are taken in near vacuum, the cells must be dehydrated before they can be investigated. Great care must be taken that the dehydration process will not change the cell morphology beyond what has already happened during inactivation. Second, in IFC we observe populations of several hundred or thousands of cells, while electron microscopy look at only a few. This means that some of the inherent variation observed with IFC may be lost during an analysis using SEM or TEM. Alternatively, powerful techniques that provide both electrical characterisation and visual information about the bacteria properties at the same time such as scanning dielectric force volume microscopy [110] or electro-optical impedance microscopy [111] could be used.

For IFC and BactoBox to have an impact in the field of antibiotic susceptibility testing, the experimental work presented in this thesis should be expanded upon, by testing additional bacteria strains and antibiotics. While the work presented relies on the perforation that colistin causes in the bacterial membrane, it has been shown elsewhere that the strictly inhibitory effects of other antibiotics (e.g. β -lactams) can also can be detected with impedance [15]. Additional experiments should be performed to confirm if this is also the case with BactoBox and to show the value the instrument can have in more clinical settings. Comparisons with traditional AST will also help quantify the relationship be-

tween the change in impedance and the actual minimum inhibitory concentration. On a more fundamental level, it should be investigated if the surface charge of particles can be measured with IFC. A better understanding of the experimental conditions (e.g. frequencies, medium conductivity) required to probe the surface charge is needed. Potentially, liposomes could be synthesized with a controllable surface charge (through the choice of lipids) and used as a model for this work.

Finally, I would suggest that the way the differentiation/classification between different cells and particles is done should be explored in more depth. During this work, classification was only ever done based on one variable at a time (most of the time the differential argument). It should be explored if multivariate analysis would yield better classification and differentiation, for example between different species of bacteria. It would also be very beneficial to include more than two simultaneous frequencies for this kind of analysis, however adding additional frequencies will also add noise to the signal and may prevent detection of smaller cells. For this purpose, machine learning techniques could be utilized to find the particular variables that best differentiate cells with particular properties. The challenge here is to provide complete and accurate training datasets for the algorithms. For example, in the dataset for heat-inactivated *E. coli* (chapter 7), we can say with a relatively high certainty that the cells in the dataset are in fact inactivated (ie. they do not grow), but we can not necessarily guarantee that all of the cell in the untreated dataset are in fact viable. Uncertainties like this will affect the ability of a machine learning algorithm to find accurate parameters for differentiation.

Bibliography

- [1] C. V. Bertelsen, J. C. Franco, G. E. Skands, M. Dimaki, and W. E. Svendsen, “Investigating the Use of Impedance Flow Cytometry for Classifying the Viability State of *E. coli*,” *Sensors*, vol. 20, p. 6339, Nov. 2020.
- [2] H. P. Schwan, “Electrical Properties of Tissue and Cell Suspensions,” in *Advances in Biological and Medical Physics* (J. H. Lawrence and C. A. Tobias, eds.), vol. 5, pp. 147–209, Elsevier, Jan. 1957.
- [3] H. Ayliffe, A. Frazier, and R. Rabbitt, “Electric impedance spectroscopy using microchannels with integrated metal electrodes,” *Journal of Microelectromechanical Systems*, vol. 8, pp. 50–57, Mar. 1999.
- [4] C. K. Fuller, J. Hamilton, H. Ackler, P. Krulevitch, B. Boser, A. Eldredge, F. Becker, J. Yang, and P. Gascoyne, “Microfabricated multi-frequency particle impedance characterization system,” in *Micro Total Analysis Systems 2000*, pp. 265–268, Springer, 2000.
- [5] S. Gawad, L. Schild, and P. Renaud, “Micromachined impedance spectroscopy flow cytometer for cell analysis and particle sizing,” *Lab on a Chip*, vol. 1, no. 1, pp. 76–82, 2001.
- [6] Y. Xu, X. Xie, Y. Duan, L. Wang, Z. Cheng, and J. Cheng, “A review of impedance measurements of whole cells,” *Biosensors and Bioelectronics*, vol. 77, no. October 2017, pp. 824–836, 2016.
- [7] J. Chen, C. Xue, Y. Zhao, D. Chen, M. H. Wu, and J. Wang, “Microfluidic impedance flow cytometry enabling high-throughput single-cell electrical property characterization,” *International Journal of Molecular Sciences*, vol. 16, no. 5, pp. 9804–9830, 2015.
- [8] C. Petchakup, H. Li, and H. W. Hou, “Advances in single cell impedance cytometry for biomedical applications,” *Micromachines*, vol. 8, no. 3, p. 87, 2017.
- [9] T. Sun and H. Morgan, “Single-cell microfluidic Impedance cytometry: A review,” *Microfluidics and Nanofluidics*, vol. 8, no. 4, pp. 423–443, 2010.
- [10] C. Bernabini, D. Holmes, and H. Morgan, “Micro-impedance cytometry for detection and analysis of micron-sized particles and bacteria,” *Lab on a Chip*, vol. 11, no. 3, pp. 407–412, 2011.
- [11] M. Di Berardino, M. Hebeisen, T. Hessler, A. Ziswiler, S. Largiadèr, and G. Schade, “Impedance microflow cytometry for viability studies of microorganisms,” *Imaging, Manipulation, and Analysis of Biomolecules, Cells, and Tissues IX*, vol. 7902, no. February 2011, p. 790212, 2011.
- [12] F. David, M. Hebeisen, G. Schade, E. Franco-Lara, and M. Di Berardino, “Viability and membrane potential analysis of *Bacillus megaterium* cells by impedance flow cytometry,” *Biotechnology and Bioengineering*, vol. 109, no. 2, pp. 483–492, 2012.

- [13] N. Haandbæk, S. C. Bürgel, F. Heer, and A. Hierlemann, “Characterization of sub-cellular morphology of single yeast cells using high frequency microfluidic impedance cytometer,” *Lab on a Chip*, vol. 14, no. 2, pp. 369–377, 2014.
- [14] M. T. Guler and I. Bilican, “Capacitive detection of single bacterium from drinking water with a detailed investigation of electrical flow cytometry,” *Sensors and Actuators A: Physical*, vol. 269, pp. 454–463, Jan. 2018.
- [15] D. C. Spencer, T. F. Paton, K. T. Mulrone, T. J. J. Inglis, J. M. Sutton, and H. Morgan, “A fast impedance-based antimicrobial susceptibility test,” *Nature Communications*, vol. 11, p. 5328, Dec. 2020.
- [16] S. Gawad, K. Cheung, U. Seger, A. Bertsch, and P. Renaud, “Dielectric spectroscopy in a micromachined flow cytometer: Theoretical and practical considerations,” *Lab on a Chip*, vol. 4, no. 3, pp. 241–251, 2004.
- [17] J. Cottet, O. Fabregue, C. Berger, F. Buret, P. Renaud, and M. Frénéa-Robin, “MyDEP: A New Computational Tool for Dielectric Modeling of Particles and Cells,” *Biophysical Journal*, vol. 116, no. 1, pp. 12–18, 2019.
- [18] M. Shaker, L. Colella, F. Caselli, P. Bisegna, and P. Renaud, “An impedance-based flow microcytometer for single cell morphology discrimination,” *Lab on a Chip*, vol. 14, no. 14, pp. 2548–2555, 2014.
- [19] T. E. Winkler, H. Ben-Yoav, and R. Ghodssi, “Hydrodynamic focusing for microfluidic impedance cytometry: a system integration study,” *Microfluidics and Nanofluidics*, vol. 20, no. 9, p. 134, 2016.
- [20] C. Grenvall, C. Antfolk, C. Z. Bisgaard, and T. Laurell, “Two-dimensional acoustic particle focusing enables sheathless chip Coulter counter with planar electrode configuration,” *Lab on a Chip*, vol. 14, no. 24, pp. 4629–4637, 2014.
- [21] D. Di Carlo, J. F. Edd, K. J. Humphry, H. A. Stone, and M. Toner, “Particle segregation and dynamics in confined flows,” *Physical Review Letters*, vol. 102, no. 9, p. 94503, 2009.
- [22] W. Tang, D. Tang, Z. Ni, N. Xiang, and H. Yi, “Microfluidic Impedance Cytometer with Inertial Focusing and Liquid Electrodes for High-Throughput Cell Counting and Discrimination,” *Analytical Chemistry*, vol. 89, no. 5, pp. 3154–3161, 2017.
- [23] C. H. Clausen, G. E. Skands, C. V. Bertelsen, and W. E. Svendsen, “Coplanar electrode layout optimized for increased sensitivity for electrical impedance spectroscopy,” *Micromachines*, vol. 6, no. 1, pp. 110–120, 2015.
- [24] D. Spencer, F. Caselli, P. Bisegna, and H. Morgan, “High accuracy particle analysis using sheathless microfluidic impedance cytometry,” *Lab on a Chip*, vol. 16, no. 13, pp. 2467–2473, 2016.
- [25] A. De Ninno, V. Errico, F. R. Bertani, L. Businaro, P. Bisegna, and F. Caselli, “Coplanar electrode microfluidic chip enabling accurate sheathless impedance cytometry,” *Lab on a Chip*, vol. 17, no. 6, pp. 1158–1166, 2017.

- [26] R. Reale, A. De Ninno, L. Businaro, P. Bisegna, and F. Caselli, “Electrical measurement of cross-sectional position of particles flowing through a microchannel,” *Microfluidics and Nanofluidics*, vol. 22, no. 4, p. 41, 2018.
- [27] F. Caselli and P. Bisegna, “A simple and robust event-detection algorithm for single-cell impedance cytometry,” *IEEE Transactions on Biomedical Engineering*, vol. 63, no. 2, pp. 415–422, 2016.
- [28] D. Spencer and H. Morgan, “Positional dependence of particles in microfluidic impedance cytometry,” *Lab on a Chip*, vol. 11, no. 7, pp. 1234–1239, 2011.
- [29] U. Hassan and R. Bashir, “Coincidence detection of heterogeneous cell populations from whole blood with coplanar electrodes in a microfluidic impedance cytometer,” *Lab on a Chip*, vol. 14, no. 22, pp. 4370–4381, 2014.
- [30] W. M. Cohen and D. A. Levinthal, “Absorptive Capacity: A New Perspective on Learning and Innovation,” *Administrative Science Quarterly*, vol. 35, no. 1, pp. 128–152, 1990. Publisher: [Sage Publications, Inc., Johnson Graduate School of Management, Cornell University].
- [31] R. Nazir, S. Rehman, M. Nisa, and U. a. Baba, “Chapter 7 - Exploring bacterial diversity: from cell to sequence,” in *Freshwater Microbiology* (S. A. Bandh, S. Shafi, and N. Shameem, eds.), pp. 263–306, Academic Press, 2019.
- [32] T. J. Silhavy, D. Kahne, and S. Walker, “The Bacterial Cell Envelope,” *Cold Spring Harbor Perspectives in Biology*, vol. 2, pp. a000414–a000414, May 2010.
- [33] K. Mitra, I. Ubarretxena-Belandia, T. Taguchi, G. Warren, and D. M. Engelman, “Modulation of the bilayer thickness of exocytic pathway membranes by membrane proteins rather than cholesterol,” *Proceedings of the National Academy of Sciences*, vol. 101, pp. 4083–4088, Mar. 2004.
- [34] J. D. Geyter, “Protein folding in the cell envelope of *Escherichia coli*,” *Nature Microbiology*, vol. 1, p. 13, 2016.
- [35] J. Abramson, “Structure and Mechanism of the Lactose Permease of *Escherichia coli*,” *Science*, vol. 301, pp. 610–615, Aug. 2003.
- [36] S. Park, Y. Zhang, T. H. Wang, and S. Yang, “Continuous dielectrophoretic bacterial separation and concentration from physiological media of high conductivity,” *Lab on a Chip*, vol. 11, no. 17, pp. 2893–2900, 2011.
- [37] W. Vollmer, D. Blanot, and M. A. De Pedro, “Peptidoglycan structure and architecture,” *FEMS Microbiology Reviews*, vol. 32, pp. 149–167, Mar. 2008.
- [38] D. Joseleau-Petit, J.-C. Liébart, J. A. Ayala, and R. D’Ari, “Unstable *Escherichia coli* L Forms Revisited: Growth Requires Peptidoglycan Synthesis,” *Journal of Bacteriology*, vol. 189, pp. 6512–6520, Sept. 2007.
- [39] J. Postgate, “Chapter XVIII Viable counts and Viability,” in *Methods in Microbiology*, vol. 1, pp. 611–628, Elsevier, 1969.

- [40] T. Nyström, “Not quite dead enough: On bacterial life, culturability, senescence, and death,” *Archives of Microbiology*, vol. 176, 2001.
- [41] M. Fakruddin, K. S. B. Mannan, and S. Andrews, “Viable but Nonculturable Bacteria: Food Safety and Public Health Perspective,” *ISRN Microbiology*, vol. 2013, pp. 1–6, 2013.
- [42] M. J. Allen, S. C. Edberg, and D. J. Reasoner, “Heterotrophic plate count bacteria - What is their significance in drinking water?,” *International Journal of Food Microbiology*, vol. 92, no. 3, pp. 265–274, 2004.
- [43] A. S. Kaprelyants, J. C. Gottschal, and D. B. Kell, “Dormancy in non-sporulating bacteria,” *FEMS Microbiology Reviews*, vol. 10, pp. 271–285, Apr. 1993.
- [44] L. G. Wayne, “Dormancy of *Mycobacterium tuberculosis* and latency of disease,” *European Journal of Clinical Microbiology and Infectious Diseases*, vol. 13, pp. 908–914, Nov. 1994.
- [45] H. M. Davey, “Life, Death, and In-Between: Meanings and Methods in Microbiology,” *Applied and Environmental Microbiology*, vol. 77, pp. 5571–5576, Aug. 2011.
- [46] G. A. Cangelosi and J. S. Meschke, “Dead or alive: Molecular assessment of microbial viability,” *Applied and Environmental Microbiology*, vol. 80, 2014.
- [47] R. G. Green and W. P. Larson, “Conductivity of bacterial cells,” *Journal of Infectious Diseases*, vol. 30, pp. 550–558, May 1922.
- [48] A. F. Huxley, “Kenneth Stewart Cole, 10 July 1900 - 18 April 1984,” *Biographical Memoirs of Fellows of the Royal Society*, vol. 38, pp. 97–110, Nov. 1992. Publisher: Royal Society.
- [49] K. R. Foster, “Herman P. Schwan: A Scientist and Pioneer in Biomedical Engineering,” *Annual Review of Biomedical Engineering*, vol. 4, pp. 1–27, Aug. 2002.
- [50] H. Morgan and N. G. Green, *AC electrokinetics: colloids and nanoparticles*. No. 2 in Microtechnologies and microsystems series, Baldock: Research Studies Press, 2003.
- [51] W. Bai, K. Zhao, and K. Asami, “Dielectric properties of *E. coli* cell as simulated by the three-shell spheroidal model,” *Biophysical Chemistry*, vol. 122, pp. 136–142, July 2006.
- [52] K. Asami, T. Hanai, and N. Koizumi, “Dielectric approach to suspensions of ellipsoidal particles covered with a shell in particular reference to biological cells,” *Japanese Journal of Applied Physics*, vol. 19, no. 2, pp. 359–365, 1980.
- [53] I. Popov, P. B. Ishai, A. Khamzin, and Y. Feldman, “The mechanism of the dielectric relaxation in water,” *Physical Chemistry Chemical Physics*, vol. 18, no. 20, pp. 13941–13953, 2016.
- [54] L. Fumagalli, A. Esfandiari, R. Fabregas, S. Hu, P. Ares, A. Janardanan, Q. Yang, B. Radha, T. Taniguchi, K. Watanabe, G. Gomila, K. S. Novoselov, and A. K. Geim, “Anomalously low dielectric constant of confined water,” *Science*, vol. 360, pp. 1339–1342, June 2018.

- [55] N. Lloret, R. S. Frederiksen, T. C. Møller, N. I. Rieben, S. Upadhyay, L. De Vico, J. H. Jensen, J. Nygård, and K. L. Martinez, “Effects of buffer composition and dilution on nanowire field-effect biosensors,” *Nanotechnology*, vol. 24, p. 035501, Jan. 2013.
- [56] D. a. Borkholder, *Cell Based Biosensors using Microelectrodes*. PhD Thesis, 1998.
- [57] A. Ebrahimi and M. A. Alam, “Evaporation-induced stimulation of bacterial osmoregulation for electrical assessment of cell viability,” p. 6.
- [58] H. Morgan, T. Sun, D. Holmes, S. Gawad, and N. G. Green, “Single cell dielectric spectroscopy,” *Journal of Physics D: Applied Physics*, vol. 40, no. 1, pp. 61–70, 2007.
- [59] H. Bruus, *Theoretical microfluidics*. Oxford University Press, 2007.
- [60] E. Shashi Menon, “Chapter Five - Fluid Flow in Pipes,” in *Transmission Pipeline Calculations and Simulations Manual* (E. Shashi Menon, ed.), pp. 149–234, Boston: Gulf Professional Publishing, Jan. 2015.
- [61] D. Di Carlo, D. Irimia, R. G. Tompkins, and M. Toner, “Continuous inertial focusing, ordering, and separation of particles in microchannels,” *Proceedings of the National Academy of Sciences*, vol. 104, no. 48, pp. 18892–18897, 2007.
- [62] D. Di Carlo, “Inertial microfluidics,” *Lab on a Chip*, vol. 9, no. 21, pp. 3038–3046, 2009.
- [63] M. Urdaneta and E. Smela, “Multiple frequency dielectrophoresis,” *Electrophoresis*, vol. 28, no. 18, pp. 3145–3155, 2007.
- [64] J. H. Scofield, “Frequency-domain description of a lock-in amplifier,” *American Journal of Physics*, vol. 62, no. 2, pp. 129–133, 1994.
- [65] N. Wiener, *Extrapolation, Interpolation, and Smoothing of Stationary Time Series: With Engineering Applications*. M.I.T. Press, 1964.
- [66] E. Billaur, “peakdet: Peak detection using MATLAB (non-derivative local extremum, maximum, minimum).” 2021-04-26, <http://billauer.co.il/peakdet.html>.
- [67] S. Węglarczyk, “Kernel density estimation and its application,” *ITM Web of Conferences*, vol. 23, p. 00037, 2018.
- [68] S. J. Sheather and M. C. Jones, “A Reliable Data-Based Bandwidth Selection Method for Kernel Density Estimation,” *Journal of the Royal Statistical Society: Series B (Methodological)*, vol. 53, pp. 683–690, July 1991.
- [69] B. Herigstad, M. Hamilton, and J. Heersink, “How to optimize the drop plate method for enumerating bacteria,” *Journal of Microbiological Methods*, vol. 44, pp. 121–129, Mar. 2001.
- [70] G. Reshes, S. Vanounou, I. Fishov, and M. Feingold, “Cell Shape Dynamics in *Escherichia coli*,” *Biophysical Journal*, vol. 94, pp. 251–264, Jan. 2008.

- [71] S. B. Almasaudi, "Acinetobacter spp. as nosocomial pathogens: Epidemiology and resistance features," *Saudi Journal of Biological Sciences*, vol. 25, pp. 586–596, Mar. 2018.
- [72] A. N. Hassan and J. F. Frank, "Microorganisms associated with milk," in *Encyclopedia of Dairy Sciences (Second Edition)* (J. W. Fuquay, ed.), pp. 447–457, San Diego: Academic Press, Jan. 2011.
- [73] C. A. Batt, "LISTERIA | *Listeria monocytogenes*," in *Encyclopedia of Food Microbiology (Second Edition)* (C. A. Batt and M. L. Tortorello, eds.), pp. 490–493, Oxford: Academic Press, Jan. 2014.
- [74] Y. Du, Z. Xu, G. Yu, W. Liu, Q. Zhou, D. Yang, J. Li, L. Chen, Y. Zhang, C. Xue, and Y. Cao, "A Newly Isolated *Bacillus subtilis* Strain Named WS-1 Inhibited Diarrhea and Death Caused by Pathogenic *Escherichia coli* in Newborn Piglets," *Frontiers in Microbiology*, vol. 10, 2019. Publisher: Frontiers.
- [75] T. Foster, "Staphylococcus," in *Medical Microbiology* (S. Baron, ed.), Galveston (TX): University of Texas Medical Branch at Galveston, 4th ed., 1996.
- [76] P. D. Fey and M. E. Olson, "Current concepts in biofilm formation of *Staphylococcus epidermidis*," *Future microbiology*, vol. 5, pp. 917–933, June 2010.
- [77] I. Chatterjee, G. A. Somerville, C. Heilmann, H. G. Sahl, H. H. Maurer, and M. Herrmann, "Very low ethanol concentrations affect the viability and growth recovery in post-stationary-phase *Staphylococcus aureus* populations," *Applied and Environmental Microbiology*, vol. 72, pp. 2627–2636, Apr. 2006.
- [78] M. Hartmann, M. Berditsch, J. Hawecker, M. F. Ardakani, D. Gerthsen, and A. S. Ulrich, "Damage of the bacterial cell envelope by antimicrobial peptides gramicidin S and PGLa as revealed by transmission and scanning electron microscopy," *Antimicrobial Agents and Chemotherapy*, vol. 54, no. 8, pp. 3132–3142, 2010.
- [79] F. Braet, R. De Zanger, and E. Wisse, "Drying cells for SEM, AFM and TEM by hexamethyldisilazane: a study on hepatic endothelial cells," *Journal of Microscopy*, vol. 186, pp. 84–87, Apr. 1997.
- [80] H. D. Smyth and A. J. Hickey, eds., *Controlled Pulmonary Drug Delivery*. New York, NY: Springer New York, 2011.
- [81] J. Castillo-León, W. E. Svendsen, and M. Dimaki, *Micro and Nano Techniques for the Handling of Biological Samples*. CRC Press, Aug. 2011.
- [82] W. H. Organization, "WHO report on surveillance of antibiotic consumption: 2016–2018 early implementation," 2018. Publisher: World Health Organization.
- [83] J. O'Neill, "Tackling drug-resistant infections globally: final report and recommendations," report, Government of the United Kingdom, May 2016.
- [84] C. L. Ventola, "The antibiotic resistance crisis: part 1: causes and threats," *Pharmacy and therapeutics*, vol. 40, no. 4, p. 277, 2015. Publisher: MediMedia, USA.

- [85] K. Syal, M. Mo, H. Yu, R. Iriya, W. Jing, S. Guodong, S. Wang, T. E. Grys, S. E. Haydel, and N. Tao, “Current and emerging techniques for antibiotic susceptibility tests,” *Theranostics*, vol. 7, no. 7, p. 1795, 2017. Publisher: Ivyspring International Publisher.
- [86] J.-L. Ramos and R. C. Levesque, *Pseudomonas: Volume 4: Molecular Biology of Emerging Issues*, vol. 4. Springer Science & Business Media, 2006.
- [87] G. M. Rossolini, F. Arena, P. Pecile, and S. Pollini, “Update on the antibiotic resistance crisis,” *Current Opinion in Pharmacology*, vol. 18, pp. 56–60, Oct. 2014.
- [88] J. M. Conly and B. L. Johnston, “Colistin: the phoenix arises,” *Canadian Journal of Infectious Diseases and Medical Microbiology*, vol. 17, no. 5, pp. 267–269, 2006. Publisher: Hindawi.
- [89] H. Zhang, M. Hou, Y. Xu, S. Srinivas, M. Huang, L. Liu, and Y. Feng, “Action and mechanism of the colistin resistance enzyme MCR-4,” *Communications biology*, vol. 2, no. 1, pp. 1–14, 2019. Publisher: Nature Publishing Group.
- [90] N. Jochumsen, R. L. Marvig, S. Damkiær, R. L. Jensen, W. Paulander, S. Molin, L. Jelsbak, and A. Folkesson, “The evolution of antimicrobial peptide resistance in *Pseudomonas aeruginosa* is shaped by strong epistatic interactions,” *Nature Communications*, vol. 7, p. 13002, Oct. 2016. Number: 1 Publisher: Nature Publishing Group.
- [91] G. D. Wright, “Molecular mechanisms of antibiotic resistance,” *Chemical communications*, vol. 47, no. 14, pp. 4055–4061, 2011. Publisher: Royal Society of Chemistry.
- [92] A. Z. Bialvaei and H. Samadi Kafil, “Colistin, mechanisms and prevalence of resistance,” *Current medical research and opinion*, vol. 31, no. 4, pp. 707–721, 2015. Publisher: Taylor & Francis.
- [93] R. C. D. Furniss, M. Kostrzewa, D. A. Mavridou, and G. Larrouy-Maumus, “The clue is in the lipid A: Rapid detection of colistin resistance,” *PLoS pathogens*, vol. 16, no. 4, p. e1008331, 2020. Publisher: Public Library of Science San Francisco, CA USA.
- [94] J. M. Benarroch and M. Asally, “The Microbiologist’s Guide to Membrane Potential Dynamics,” *Trends in Microbiology*, vol. 28, pp. 304–314, Apr. 2020.
- [95] L. D. Mosgaard, K. A. Zecchi, and T. Heimburg, “Mechano-capacitive properties of polarized membranes,” *Soft Matter*, vol. 11, pp. 7899–7910, Oct. 2015. Publisher: The Royal Society of Chemistry.
- [96] G. V. Lowry, R. J. Hill, S. Harper, A. F. Rawle, C. O. Hendren, F. Klaessig, U. Nobbmann, P. Sayre, and J. Rumble, “Guidance to improve the scientific value of zeta-potential measurements in nanoEHS,” *Environmental Science: Nano*, vol. 3, no. 5, pp. 953–965, 2016.
- [97] R. L. Soon, R. L. Nation, S. Cockram, J. H. Moffatt, M. Harper, B. Adler, J. D. Boyce, I. Larson, and J. Li, “Different surface charge of colistin-susceptible and -resistant *Acinetobacter baumannii* cells measured with zeta potential as a function

- of growth phase and colistin treatment,” *Journal of Antimicrobial Chemotherapy*, vol. 66, pp. 126–133, Jan. 2011.
- [98] J. Shephard, A. J. McQuillan, and P. J. Bremer, “Mechanisms of Cation Exchange by *Pseudomonas aeruginosa* PAO1 and PAO1 wbpL, a Strain with a Truncated Lipopolysaccharide,” *Applied and Environmental Microbiology*, vol. 74, pp. 6980–6986, Nov. 2008.
- [99] M. R. Lima, G. F. Ferreira, W. R. Nunes Neto, J. d. M. Monteiro, . R. C. Santos, P. B. Tavares, . M. L. Denadai, M. R. Q. Bomfim, V. L. dos Santos, S. G. Marques, and A. de Souza Monteiro, “Evaluation of the interaction between polymyxin B and *Pseudomonas aeruginosa* biofilm and planktonic cells: reactive oxygen species induction and zeta potential,” *BMC Microbiology*, vol. 19, p. 115, Dec. 2019.
- [100] S. Halder, K. K. Yadav, R. Sarkar, S. Mukherjee, P. Saha, S. Haldar, S. Karmakar, and T. Sen, “Alteration of Zeta potential and membrane permeability in bacteria: a study with cationic agents,” *SpringerPlus*, vol. 4, Nov. 2015.
- [101] D. Mietchen, T. Schnelle, T. Müller, R. Hagedorn, and G. Fuhr, “Automated dielectric single cell spectroscopy - temperature dependence of electrorotation,” *Journal of Physics D: Applied Physics*, vol. 35, pp. 1258–1270, May 2002. Publisher: IOP Publishing.
- [102] A. Walkty, M. DeCorby, K. Nichol, J. A. Karlowsky, D. J. Hoban, and G. G. Zhanel, “In vitro activity of colistin (polymyxin E) against 3,480 isolates of gram-negative bacilli obtained from patients in Canadian hospitals in the CANWARD study, 2007–2008,” *Antimicrobial Agents and Chemotherapy*, vol. 53, no. 11, pp. 4924–4926, 2009.
- [103] P. J. Bergen, J. Li, and R. L. Nation, “Dosing of colistin—back to basic PK/PD,” *Current opinion in pharmacology*, vol. 11, no. 5, pp. 464–469, 2011. Publisher: Elsevier.
- [104] S. Chevalier, E. Bouffartigues, J. Bodilis, O. Maillot, O. Lesouhaitier, M. G. J. Feuilloley, N. Orange, A. Dufour, and P. Cornelis, “Structure, function and regulation of *Pseudomonas aeruginosa* porins,” *FEMS Microbiology Reviews*, vol. 41, pp. 698–722, Sept. 2017.
- [105] Y. Yu and J. B. Klauda, “Modeling *Pseudomonas aeruginosa* inner plasma membrane in planktonic and biofilm modes,” *The Journal of Chemical Physics*, vol. 149, p. 215102, Dec. 2018. Publisher: American Institute of Physics.
- [106] A. Akbarzadeh, R. Rezaei-Sadabady, S. Davaran, S. W. Joo, N. Zarghami, Y. Hanifepour, M. Samiei, M. Kouhi, and K. Nejati-Koshki, “Liposome: classification, preparation, and applications,” *Nanoscale Research Letters*, vol. 8, p. 102, Feb. 2013.
- [107] D. Carugo, E. Bottaro, J. Owen, E. Stride, and C. Nastruzzi, “Liposome production by microfluidics: potential and limiting factors,” *Scientific Reports*, vol. 6, p. 25876, May 2016.

- [108] A. P. Costa, X. Xu, M. A. Khan, and D. J. Burgess, “Liposome Formation Using a Coaxial Turbulent Jet in Co-Flow,” *Pharmaceutical Research*, vol. 33, pp. 404–416, Feb. 2016.
- [109] M. Kanášová and K. Nesměrák, “Systematic review of liposomes’ characterization methods,” *Monatshefte für Chemie - Chemical Monthly*, vol. 148, pp. 1581–1593, Sept. 2017.
- [110] M. Checa, R. Millan-Solsona, N. Blanco, E. Torrents, R. Fabregas, and G. Gomila, “Mapping the dielectric constant of a single bacterial cell at the nanoscale with scanning dielectric force volume microscopy,” *Nanoscale*, vol. 11, no. 43, pp. 20809–20819, 2019. Publisher: Royal Society of Chemistry.
- [111] F. Zhang, S. Wang, Y. Yang, J. Jiang, and N. Tao, “Imaging Single Bacterial Cells with Electro-optical Impedance Microscopy,” *ACS Sensors*, vol. 6, pp. 348–354, Feb. 2021.

A Appendix

A.1 Variation between chips

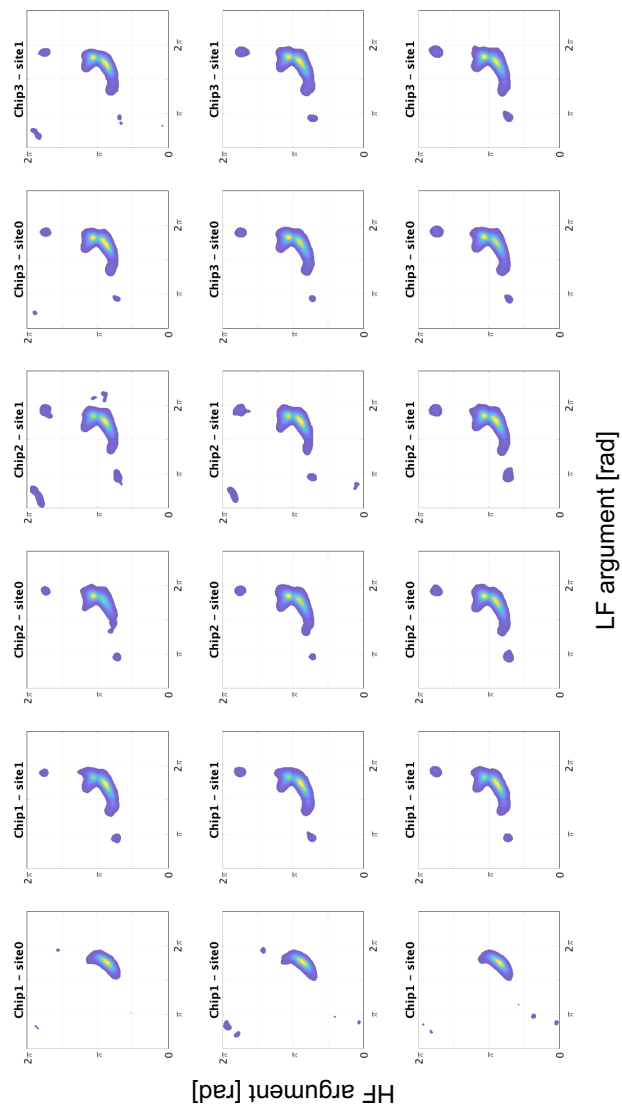


Figure A.1: Kernel density plots of *E. coli* measurements, 3 repetitions, from 3 chips, each with 2 measurement sites. Note that site0 on Chip1 one is known to be broken.

B Appendix

B.1 Six bacteria species

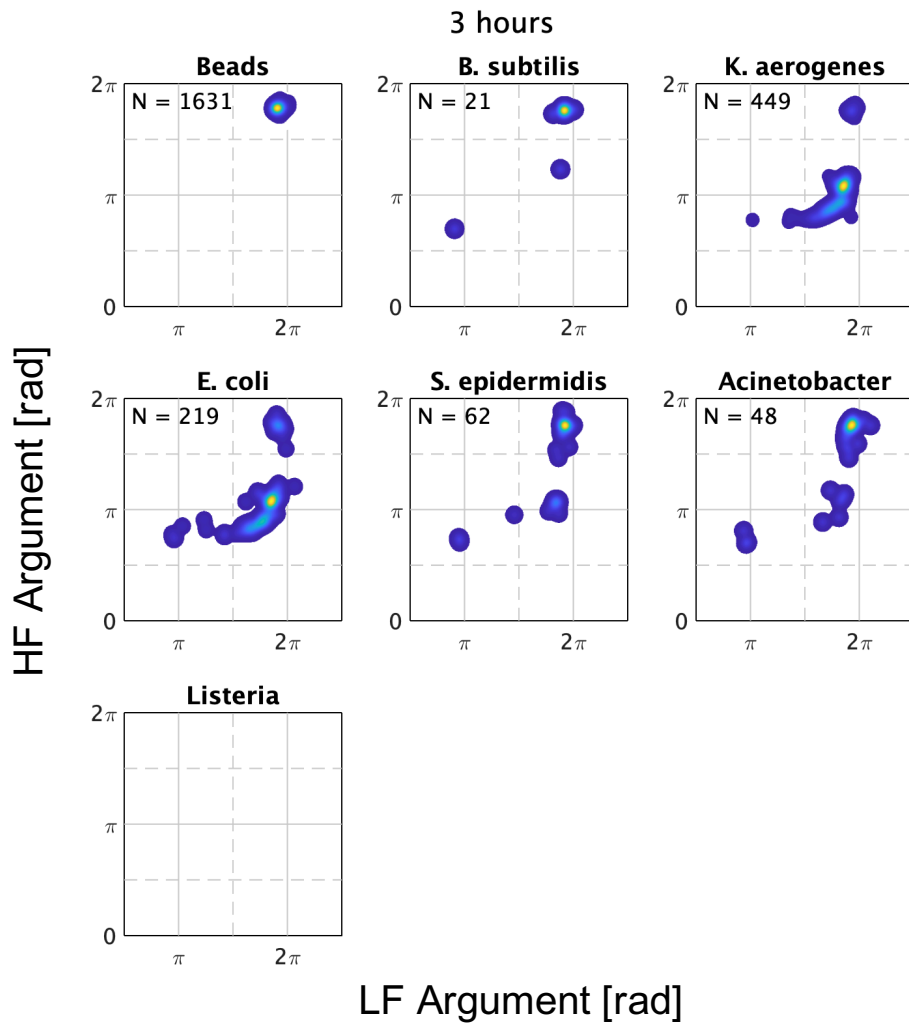


Figure B.1: Kernel density plot of the low (366 kHz) and high (6.9 MHz) frequency differential argument from measurements of 6 species after 3 hours of growth

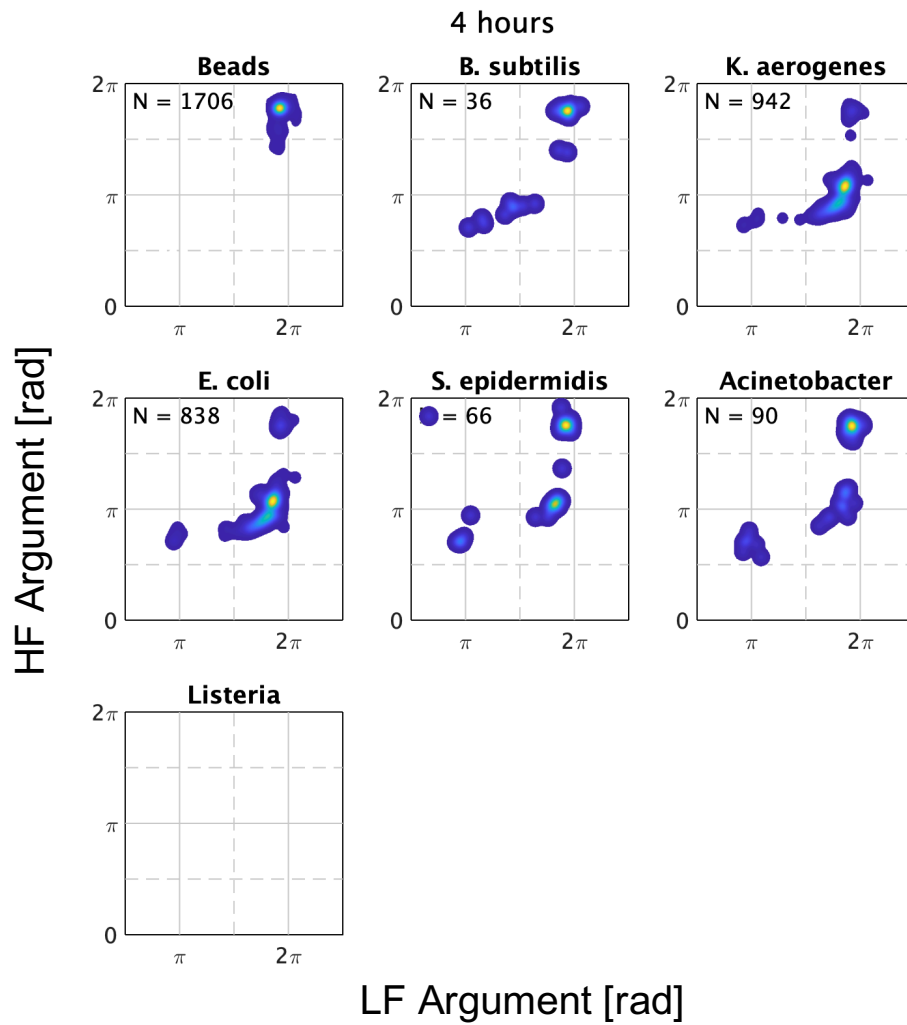


Figure B.2: Kernel density plot of the low (366 kHz) and high (6.9 MHz) frequency differential argument from measurements of 6 species after 4 hours of growth

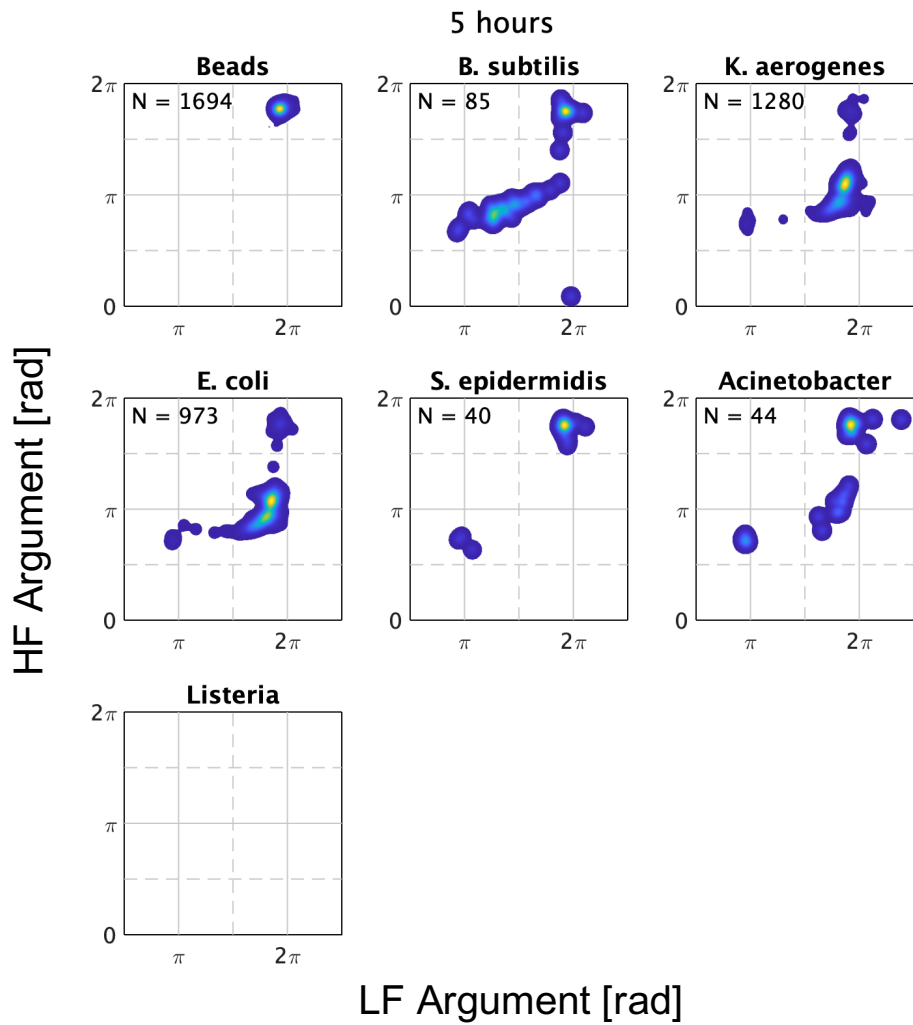


Figure B.3: Kernel density plot of the low (366 kHz) and high (6.9 MHz) frequency differential argument from measurements of 6 species after 5 hours of growth

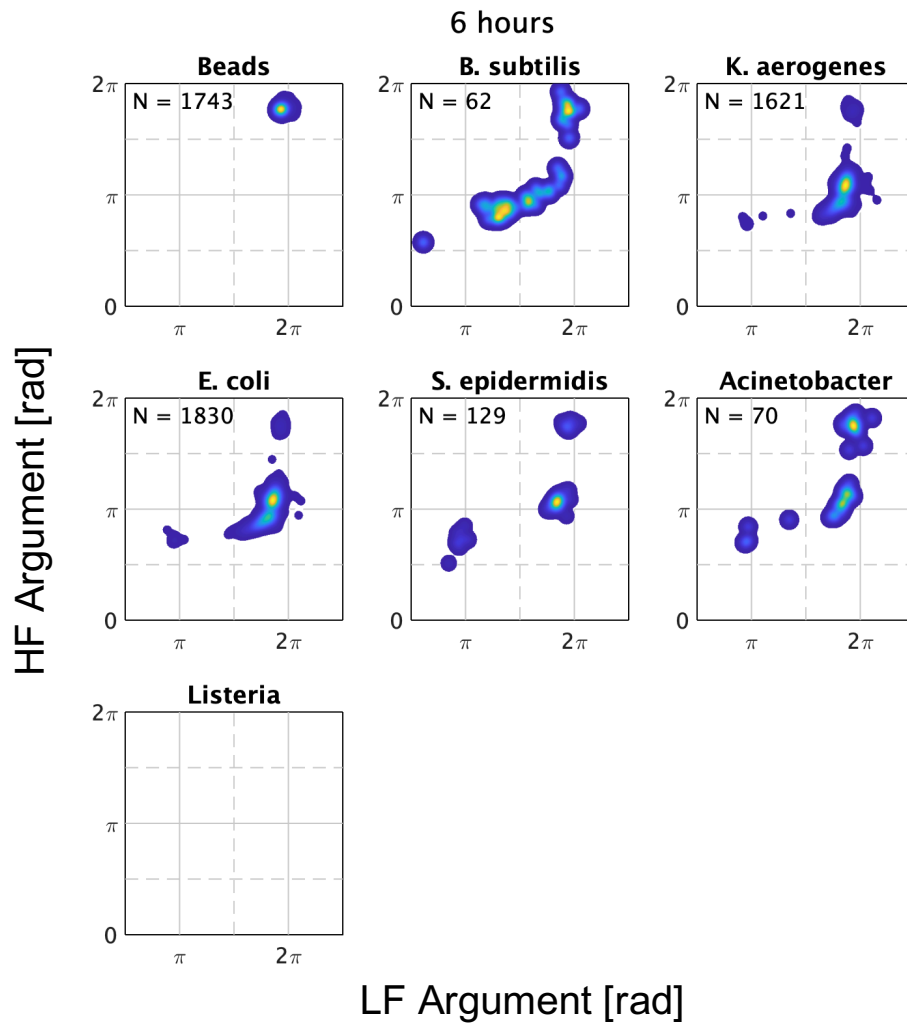


Figure B.4: Kernel density plot of the low (366 kHz) and high (6.9 MHz) frequency differential argument from measurements of 6 species after 6 hours of growth

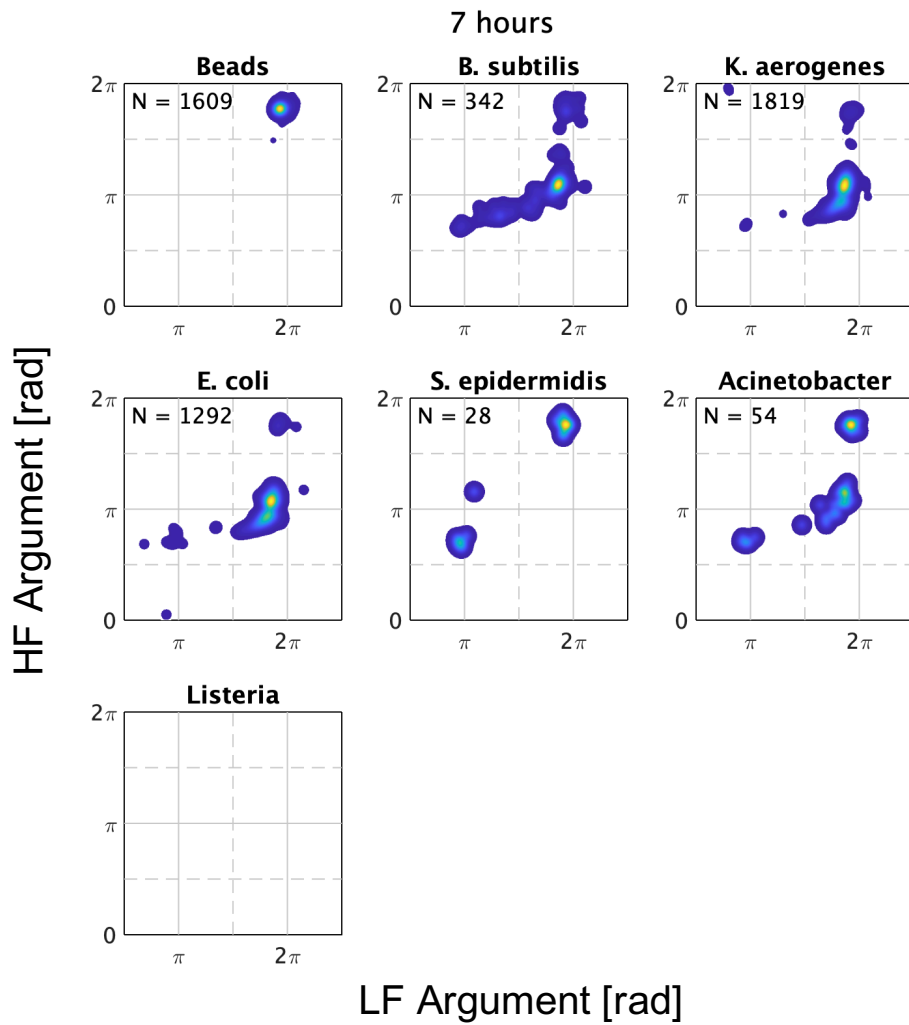


Figure B.5: Kernel density plot of the low (366 kHz) and high (6.9 MHz) frequency differential argument from measurements of 6 species after 7 hours of growth

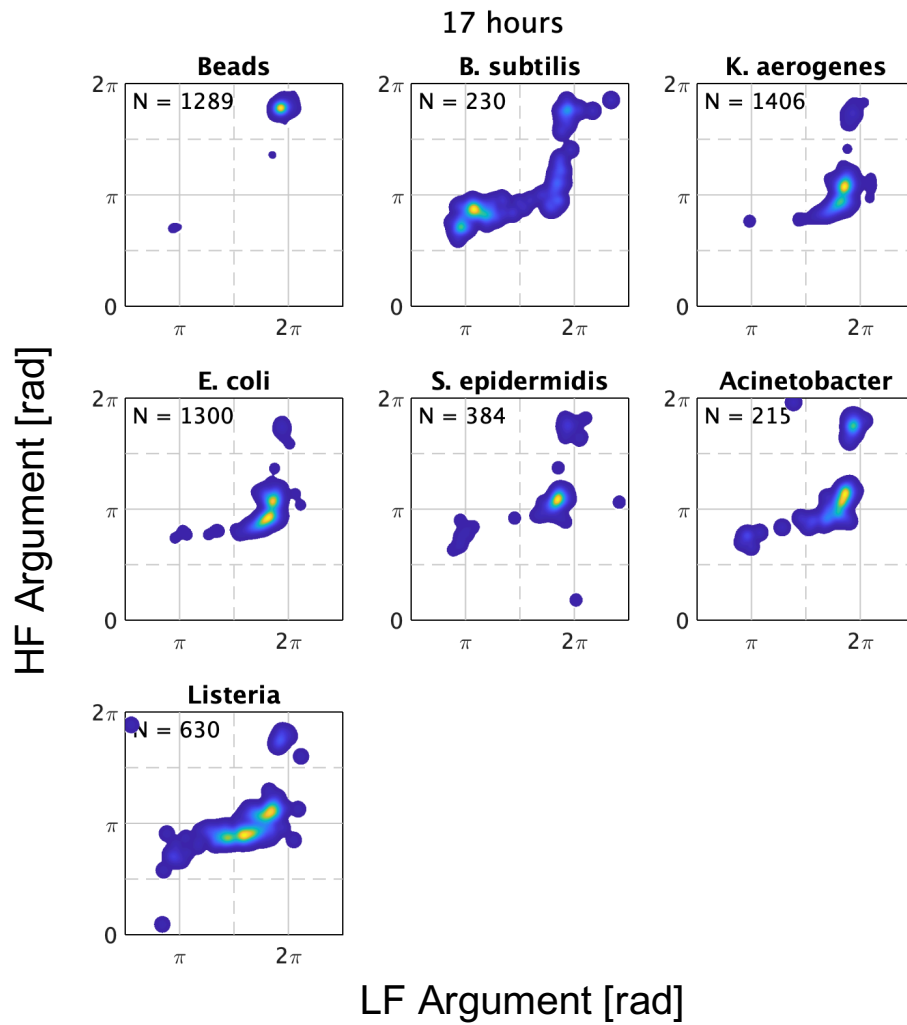


Figure B.6: Kernel density plot of the low (366 kHz) and high (6.9 MHz) frequency differential argument from measurements of 6 species after 17 hours of growth

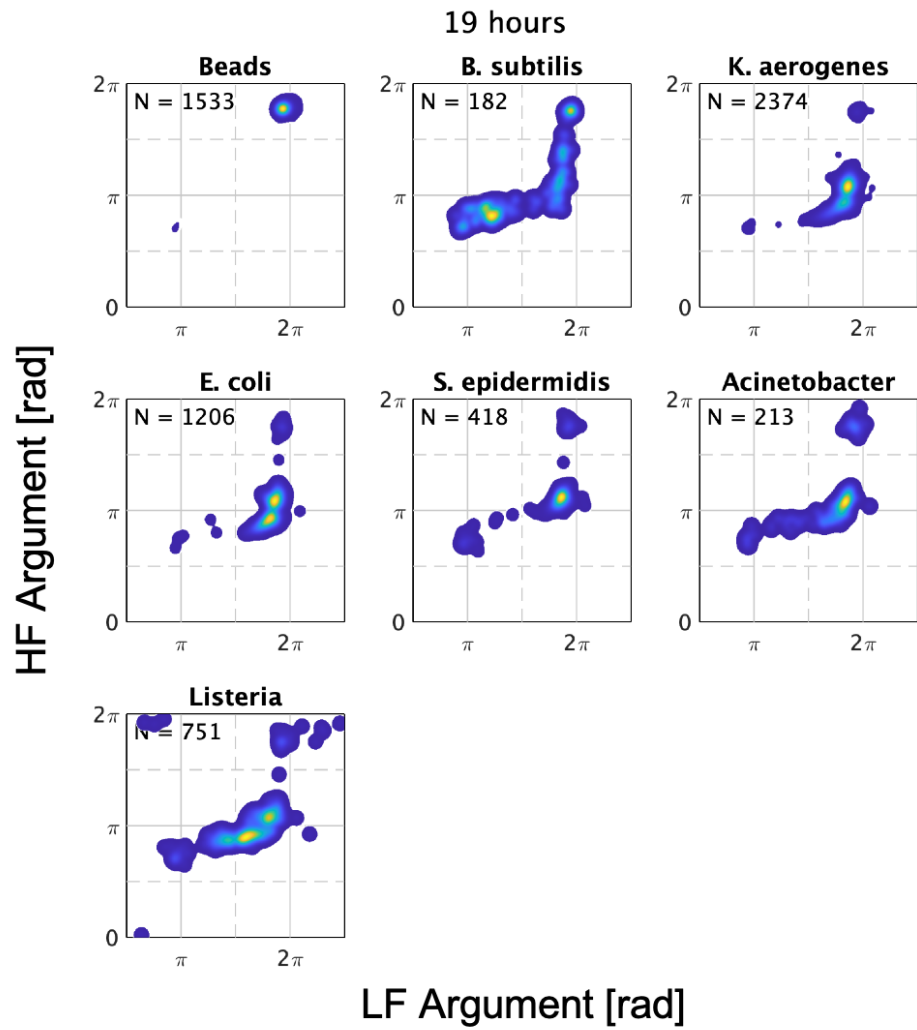


Figure B.7: Kernel density plot of the low (366 kHz) and high (6.9 MHz) frequency differential argument from measurements of 6 species after 19 hours of growth

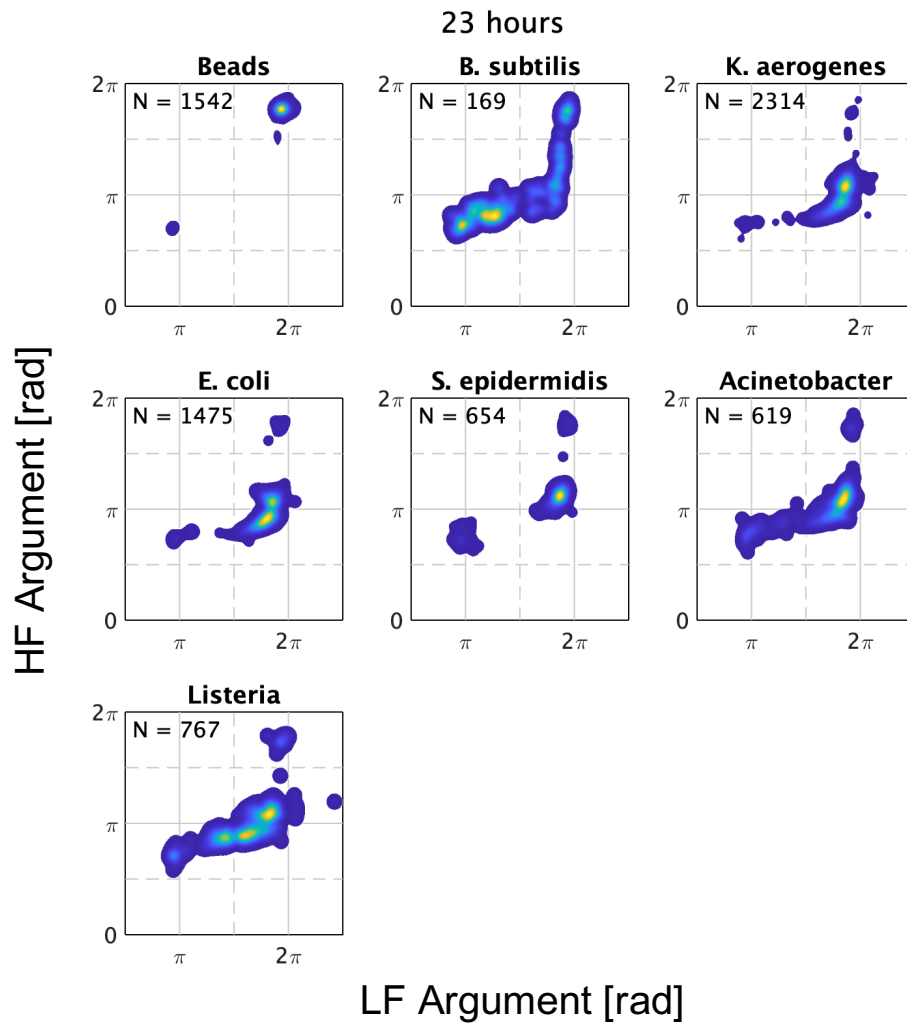


Figure B.8: Kernel density plot of the low (366 kHz) and high (6.9 MHz) frequency differential argument from measurements of 6 species after 23 hours of growth

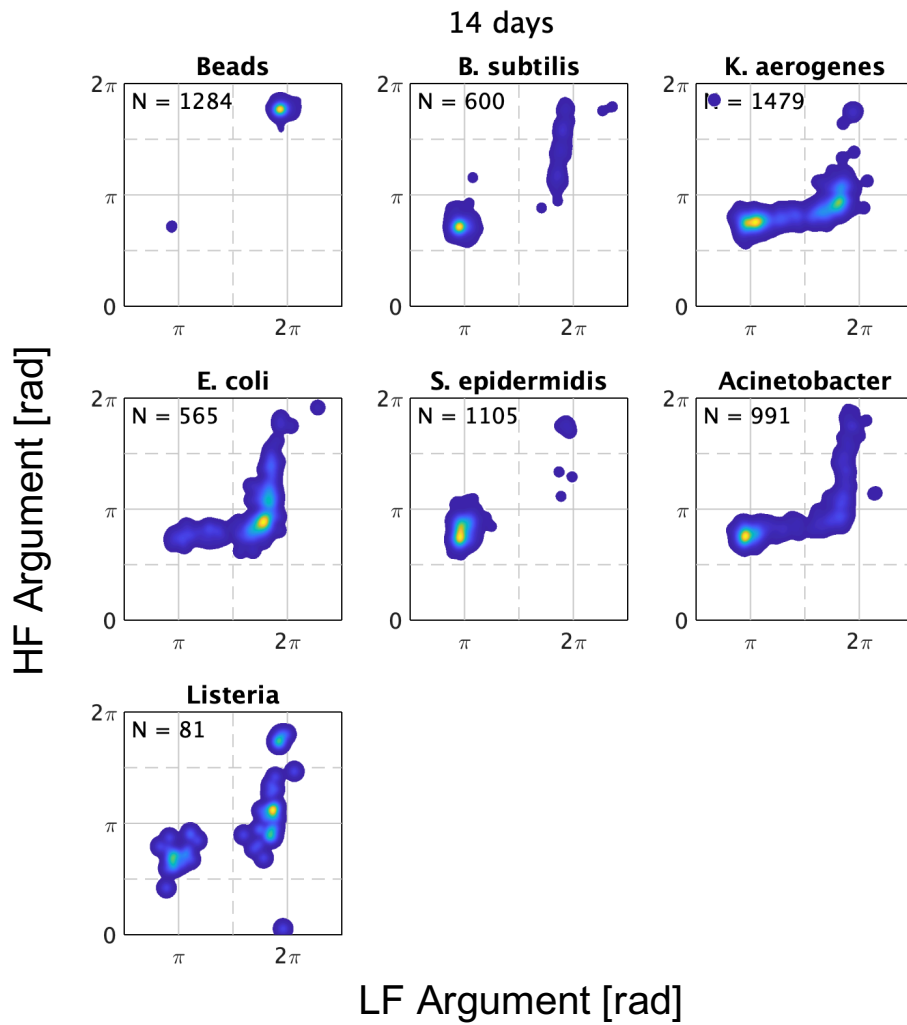


Figure B.9: Kernel density plot of the low (366 kHz) and high (6.9 MHz) frequency differential argument from measurements of 6 species after 14 days of growth

B.2 ROC comparison of gram-types - Moduli

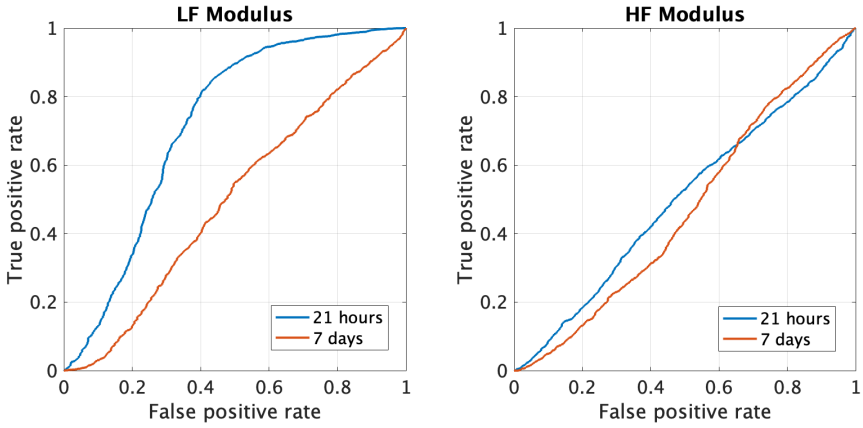


Figure B.10: ROC curves for gram-type classification (ie. gram-positive: *Bacillus*, *Staph. ep.*, *Listeria* and gram-negative: *E. coli*, *Klebsiella* *Acinetobacter*) based on the modulus for low and high frequency data (366 kHz and 6.9 MHz).

C Appendix

C.1 Drop plate images

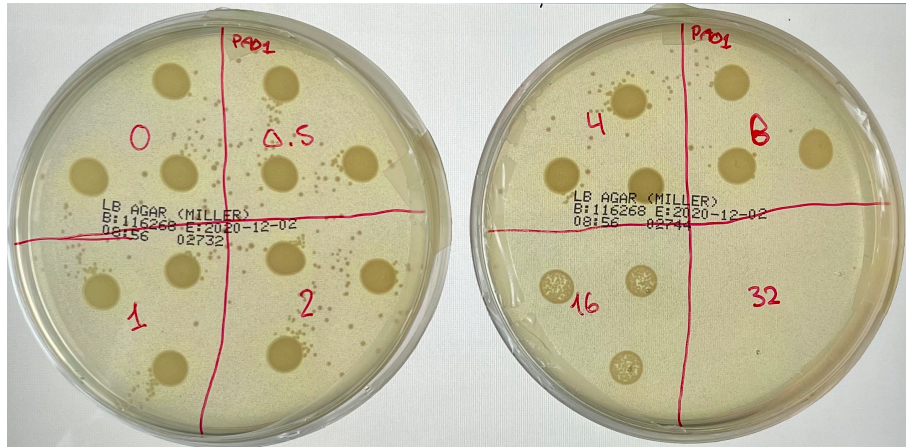


Figure C.1: Drop plating of samples of *P. aeruginosa* PAO1 after 3 hours exposure to colistin, after 24 hours at 37C



Figure C.2: Drop plating of samples of *P. aeruginosa* Q5 after 3 hours exposure to colistin, after 24 hours at 37C

Technical
University of
Denmark

Søltofts Plads 221
2800 Kgs. Lyngby
Tlf. 4525 1700

www.bio.dtu.dk